Institute of Fundamental Technological Research,
Polish Academy of Sciences

Semi-active control of energy transfer between vibration modes in mechanical structures

mgr inż. Mariusz Ostrowski

Supervisor
dr hab. inż. Bartłomiej Błachowski, prof. IPPT PAN
Assistant supervisor
dr inż. Grzegorz Mikułowski

Warsaw, Poland

2024-October

Publications related to the thesis

Journal articles

1. **Ostrowski M**, Błachowski B, Popławski B, Pisarski D, Mikułowski G, Jankowski Ł. *Semi-active modal control of structures with lockable joints: general methodology and applications.* Structural Control and Health Monitoring. 2021;28(5):e2710. Available from: `https://doi.org/10.1002/stc.2710`.

2. Błachowski B, Świercz A, **Ostrowski M**, Tauzowski P, Olaszek P, Jankowski Ł. *Convex relaxation for efficient sensor layout optimization in large-scale structures subjected to moving loads.* Computer-Aided Civil and Infrastructure Engineering. 2020;35(10):1085—1100. Available from: `https://doi.org/10.1111/mice.12553`.

3. **Ostrowski M**, Błachowski B, Bocheński M, Piernikarski D, Filipek P, Janicki W. *Design of nonlinear electromagnetic energy harvester equipped with mechanical amplifier and spring bumpers.* Bulletin of the Polish Academy of Sciences: Technical Sciences. 2020;68(6):1373—1383. Available from: `https://doi.org/10.24425/bpasts.2020.135384`.

4. **Ostrowski M**, Mikułkowski G, Błachowski B, Jankowski Ł. *Experimental assessment of Bayesian and mode matching approaches for parametric identification of bolted connections.* Mechanical Systems and Signal Processing. 2023;201:110652. Available from: `https://doi.org/10.1016/j.ymssp.2023.110652`.

5. **Ostrowski M**, Błachowski B, Mikułowski G, Jankowski Ł. *Influence of Noise in Computer-Vision-Based Measurements on Parameter Identification in Structural Dynamics.* Sensors. 2023;23(1):291. Available from: `https://doi.org/10.3390/s23010291`. This is an invited paper belonging to a special issue entitled: *Intelligent Sensing Technologies in Structural Health Monitoring.*

Conference articles

1. **Ostrowski M**, Błachowski B, Mikułowski G, Jankowski Ł. *Semi-active control of modal energy transfer by means of lockable joints: theory and applications.*

In: International Conference on Noise and Vibration Engineering / International Conference on Uncertainty in Structural Dynamics, ISMA - USD; 2024. (*in press*)

2. Mikułowski G, **Ostrowski M**, Błachowski B, Jankowski Ł. *Semi-active control of modal energy transfer by means of lockable joints: experimental verification.* In: International Conference on Noise and Vibration Engineering / International Conference on Uncertainty in Structural Dynamics, ISMA - USD; 2024. (*in press*)
3. **Ostrowski M**, Błachowski B, Mikułowski G, Jankowski Ł. *Semi-active modal control based on the energy transfer between structural vibration modes.* In: 10th ECCOMAS Thematic Conference on Smart Structures and Materials, SMART, 2023; p. 526–537. Available from: `https://doi.org/10.7712/150123.9807.444377`.
4. Mikułowski G, **Ostrowski M**, Błachowski B, Jankowski Ł. *Experimental verification of a semi-active modal control algorithm for structures with lockable joints.* In: 10th ECCOMAS Thematic Conference on Smart Structures and Materials, SMART; 2023. p. 572–581. Available from: `https://doi.org/10.7712/150123.9811.446236`.
5. Błachowski B, **Ostrowski M**, Mikułowski G, Jankowski Ł. *Mode matching vs Bayesian approach for model updating of frame structure with uncertain bolted connection.* In: International Conference on Noise and Vibration Engineering / International Conference on Uncertainty in Structural Dynamics, ISMA - USD; 2022. p. 1325–1334. Available from: `https://past.isma-isaac.be/downloads/isma2022/proceedings/Contribution_539_proceeding_3.pdf`.
6. Błachowski B, Świercz A, **Ostrowski M**, Tauzowski P, Jankowski Ł. *Multi-type sensor placement for structural health monitoring of tied-arch bridges.* In: 10th European Workshop on Structural Health Monitoring, EWSHM; 2021. p. 286–297. Available from: `https://doi.org/10.1007/978-3-030-64594-6_29`
7. Błachowski B, **Ostrowski M**, Tauzowski P, Świercz A, Jankowski Ł. *Sensor placement for structural damage identification by means of topology optimization.* In: 4th Polish Congress of Mechanics and 23rd International Conference on Computer Methods in Mechanics, PCM-CMM; 2020. p. 020002–1–11. Available from: `https://doi.org/10.1063/5.0007817`.
8. **Ostrowski M**, Błachowski B, Jankowski Ł, Pisarski D. *Inverse Lyapunov based method for semi-active control of energy transfer between vibration modes.* In: 9th ECCOMAS Thematic Conference on Smart Structures and Materials, SMART, 2019; p. 345–356. Available from: `https://congress.cimne.com/smart2019/frontal/doc/EbookSMART2019.pdf`.

Book chapters

1. **Ostrowski M**, Błachowski B, Jankowski Ł, Pisarski D. *Structural vibration control using semi-actively switched lockable joints*. In: Mańka M, Mendrok K. *Projektowanie i dynamika urządzeń mechatronicznych*. Cracow: Katedra Robotyki i Mechatroniki AGH; 2019. p. 221–228.

Acknowledgements

I would like to express special gratitude to Jehovah, the God of armies, especially for His creations, which we humans can marvel at, learn and study. Because of His inconceivable wisdom and the great love that went into the creation, we will never fully fathom them, as Solomon said:

> "*He has made everything beautiful in its time. He has even put eternity in their heart; yet mankind will never find out the work that the true God has made from start to finish.*"
>
> (Ecclesiastes 3:11; NWT).

I would like to thank my supervisor, Professor Bartłomiej Błachowski, in particular for his enormous contribution to my scientific development. Professor Błachowski not only guided me in learning about the issues of dynamics and control of structures, sharing his extensive experience and knowledge with me, but also taught me appropriate values referring to scientific ethics. On many occasions, he reminded me that science is not about points, statistics and citations, but about hard work resulting in deepening knowledge and understanding of the phenomena studied.

I would like to thank my assistant supervisor, Doctor Grzegorz Mikułowski, for his dominant contribution to the experiments described in Chapter 5 of this dissertation and the hardware implementation of the proposed control strategy. This work required great persistence, which resulted in obtaining unique experimental results and deepening knowledge on the proposed strategy. I also thank for instructive thoughts and conversations on scientific research methodology.

I would also like to thank Doctor Dominik Pisarski and Professor Łukasz Jankowski for helping me, together with the Professor Błachowski, to choose novel and interesting direction of research at the very beginning of my doctoral studies. Seminars given by Doctor Pisarski were an inspiration for implementation of the instantaneously optimal approach in the control strategy proposed in this thesis.

I would like to thank Professor Łukasz Jankowski also for creating a favourable atmosphere in Department of Intelligent Technologies, for his management and invaluable advice on scientific issues.

Thanks are also due to my wife, Małgorzata, for encouraging me to finish my dissertation, supporting me in my professional and private life, taking care of the warmth of our home and for being patient with me.

Streszczenie rozszerzone

Niniejsza rozprawa skupia się na nowej strategii półaktywnego sterowania modalnego, pozwalającego na precyzyjne przenoszenie energii pomiędzy poszczególnymi postaciami drgań konstrukcji mechanicznej. Sterowanie realizowane jest za pomocą blokowanych połączeń rotacyjnych – blokowanych węzłów – zainstalowanych w wybranych miejscach konstrukcji ramowej. Połączenie takie może być dynamicznie zablokowane i przenosić moment gnący między belkami konstrukcji lub być odblokowane i pracować jak zawias. Przenoszony moment gnący odpowiada za sprzężenie modalne, co skutkuje wymianą energii mechanicznej między postaciami drgań. Sterowanie ma zastosowanie zarówno w tłumieniu drgań, jak i usprawnianiu procesu pozyskiwania energii z drgań (ang. *energy harvesting*). Praca obejmuje również inne aspekty strategii sterowania, takie jak optymalne rozmieszczenie sensorów do filtracji modalnej oraz optymalne rozmieszczenie blokowanych połączeń. Nowa strategia sterowania została zweryfikowana zarówno numerycznie, jak i eksperymentalnie.

Wstęp, przegląd literatury i motywacja Przegląd literaturowy będący częścią niniejszej rozprawy pokazał, że choć zagadnienie sterowania drganiami konstrukcji jest badane od dekad, nadal jest aktualne z uwagi fakt, że drgania są często szkodliwe, a nawet mogą być źródłem niebezpieczeństw [1]. Z drugiej strony coraz większym zainteresowaniem cieszy się również pozyskiwanie energii z drgań i konwertowanie jej na energię elektryczną [2].

Z ważniejszych prac w kontekście niniejszej rozprawy należy wymienić te opisujące nieliniowe urządzenia (ang. nonlinear energy sink, NES), które nie tylko pochłaniają energię drgań, ale powodują zmianę jej rozkładu spektralnego w dziedzinie częstotliwości [3–7]. W dużej większości są to urządzenia pasywne. Zmiana udziału energetycznego w poszczególnych częstościach drgań powodowana jest przez sprzężenie modalne wywołane nieliniowymi charakterystykami pracy tych urządzeń. Powoduje to przeniesienie energii do postaci drgań wyższego rzędu, które zazwyczaj charakteryzują się dużym tłumieniem w porównaniu do podstawowych postaci drgań. Efekt ten można również uzyskać poprzez półaktywnie sterowanie lokalnymi zmianami sztywności konstrukcji. Onoda i inni zaproponowali sterowanie konstrukcjami kratownicowymi wyposażonymi w człony o zmiennej sztywności [8]. Podczas ruchu konstrukcja ulega deformuji, co powoduje akumulację energii potencjalnej w odkształceniach. Nagłe zmniejszenie sztywności powoduje wtedy uwolnienie części tej energii w wysokoczęstotliwościowych drganiach swobodnych odpowiadających postaciom drgań wyższych rzędów. Następnie energia ta jest efektywnie tłumiona w materiale konstrukcji. Ten rodzaj strategii sterowania jest rozwijany również dzisiaj z zastosowaniem do konstrukcji ramowych wyposażonych w blokowane rotacyjne węzły lub w konstrukcjach warstwowych, gdzie zmiana sztywności odbywa się poprzez delaminację [9–14]. Z uwagi na charakterystyczne dla tej grupy strategii akumulowanie i uwalnianie nagromadzonej energii odkształceń są one nazywane „Prestress Accumulation–Release" (PAR). Mimo, że lokalna zmiana sztywności wywołuje efekt sprzężenia modalnego, a w efekcie wymianę energii między postaciami drgań, sterownik nie ma informacji o stanie konstrukcji wyrażonym za pomocą amplitud, czy prędkości modalnych. w związku z tym PAR jest heurystycznym podejściem.

Głównym problem w pozyskiwaniu energii z drgań mechanicznych jest nie tylko zwiększanie efektywności, ale również poszerzenie szerokości roboczego pasma częstotliwości, w którym przetwornik elektromechaniczny wydajnie pracuje [15]. Aby uzyskać jak najlepszy kompromis między szerokością pasma roboczego a szczytową wydajnością przetworników celowo wprowadza się nieliniowości do charakterystyki tych urządzeń, np.: sprężyste zderzenia ciał w celu zmiany prędkości magnesu oddziałującego na cewkę elektromagnetyczną [16,17] lub wprowadzenie zderzaków sprężynowych ograniczających skok magnesu [18]. Testowane są również przetworniki o więcej niż jednym stopniu swobody zaprojektowane tak, aby uzyskać kilka pików rezonansowych [19]. W ostatnim czasie intensywnie badany jest również wpływ rezonansu wewnętrznego w nieliniowych przetwornikach mechanicznych na poszerzenie roboczego pasma częstotliwościowego oraz możliwość pracy urządzenia w wielu postaciach drgań [20]. Rezonans wewnętrzny i jego wpływ na wymianę energii między postaciami drgań jest często badany analitycznie, podobnie jak inne nieliniowości wprowadzone do przetworników.

W przeciwieństwie do zagadnienia odzyskiwania energii oraz wielu pasywnych nieliniowych układów (np. NES) sprzężenie modalne i jego wpływ na tłumienie drgań nie zostały dokładnie przebadane w strategiach półaktywnego sterowania, jak np. PAR. W szczególności mało znany jest mechanizm przenoszenia energii między postaciami drgań. Było to motywacją do podjęcia badań nad nową strategią półaktywnego sterowania modalnego. Proponowana strategia wykorzystuje rotacyjne blokowane węzły do precyzyjnego przenoszenia energii mechanicznej między wybranymi postaciami drgań. Umożliwia to nie tylko tłumienie drgań z narzuceniem priorytetu na poszczególne postacie, ale też usprawnienie procesu odzyskiwania energii z drgań. W drugim przypadku odbywa się to poprzez przeniesienie energii drgań do wybranej (docelowej) postaci, która współpracuje optymalnie z zamontowanym na konstrukcji przetwornikiem elektromechanicznym.

Dynamika konstrukcji z blokowanymi połączeniami Zablokowanie lub odblokowanie węzła jest odwzorowane poprzez narzucenie lub odrzucenie więzów kinematycznych na odpowiednie rotacyjne stopnie swobody konstrukcji. W związku z tym zmienia się efektywna liczba stopni swobody sterowanej konstrukcji, jej właściwości dynamiczne oraz baza wektorów własnych reprezentujących postacie drgań, jak i jej wymiar (rys. 2.1 na str. 33).

Zauważono, że aby sterować konstrukcją wystarczy opisać jej ruch w bazie wektorów własnych uzyskanej dla wszystkich węzłów w stanie odblokowanym. Jest to możliwe ze względu na największy i wystarczający wymiar tej bazy. Konieczne jest natomiast uwzględnienie efektu sprzężenia modalnego w modalnych równaniach ruchu opisanych w tej bazie, aby prawidłowo odwzorować efekt zablokowania i jego wpływ na zachowanie konstrukcji. Sprzężenie modalne pozwala również opisać wymianę energii między postaciami drgań. Aby wprowadzić czytelnika w te zagadnienia najpierw omówiono je na przykładzie prostego układu o dwóch stopniach swobody, a później zagadnienie rozszerzono na konstrukcje ramowe o dowolnej liczbie stopni swobody.

W celu ułatwienia obliczeń zaproponowano również używanie osłabionych więzów kinematycznych, gdy węzeł jest zablokowany. Takie więzy są realizowane za pomocą sterowanego współczynnika tłumienia wiskotycznego między rotacyjnymi stopniami swobody opisującymi blokowane węzły (rys. 2.11 na str. 2.11). Gdy węzeł jest zalokowany, współczynnik tłumienia osiąga bardzo dużą wartość efektywnie usztywniając blokowane połączenie. W rezultacie otrzymujemy biliniowe równania ruchu, a uwzględniając ograniczenia nałożone na stan węzłów (całkowicie odblokowany lub całkowicie zablokowany) układ jest liniowy przedziałami (co po uwzględnieniu pętli sprzężenia zwrotnego stanowi klasę układów nieliniowych).

Mierzone wielkości fizyczne, optymalne rozmieszczenie sensorów i blokowanych węzłów Algorytm sterowania oparty jest na oszacowaniu chwilowej wartości przepływu energii między postaciami drgań, który nie może być mierzony bezpośrednio. Wielkość tą można oszacować znając prędkości modalne oraz momenty gnące przenoszone przez zablokowane węzły. Prędkości modalne monitorowanych postaci drgań estymowane są za pomocą filtracji modalnej. Momenty gnące natomiast estymowane są na podstawie pomiarów odkształceń w pobliżu każdego blokowanego węzła.

Aby ograniczyć wpływ szumu pomiarowego oraz wpływ postaci drgań wyższego rzędu na filtrację modalną sensory rozmieszczono tak aby uzyskać maksymalną wartość wyznacznika macierzy informacji Fishera. Jest to zadanie o charakterze kombinatorycznym, stąd aby zredukować nakład obliczeniowy posłużono się nową metodą przybliżoną opartą na wypukłej relaksacji (zastąpieniu problemu dyskretnego jego ciągłym odpowiednikiem) [21].

W celu zapewnienia efektywnego działania sterowania zaproponowano również miarę sterowalności poszczególnych postaci drgań stosowaną w niniejszej pracy do optymalnego rozmieszczenia blokowanych węzłów. Standardowe miary sterowalności poszczególnych postaci drgań, jak np. gramian sterowalności, nie odzwierciedlają dokładnie zdolności węzłów do przenoszenia energii między postaciami drgań.

Prawo i algorytm sterowania, możliwe aplikacje Zaproponowano chwilowo optymalne prawo sterowania, które w każdej chwili czasu zapewnia najbardziej stromy spadek funkcji celu. Funkcja celu jest ważoną sumą energii stowarzyszonych z poszczególnymi monitorowanymi postaciami drgań. Dobór wag ma kluczowe znaczenie i zależy od aplikacji proponowanej strategii sterowania.

W przypadku zastosowania do tłumienia drgań wszystkie wagi są dodatnie. Wtedy minimalizacja funkcji celu wymusza przepływ energii z monitorowanych postaci drgań do pozostałych (niemonitorowanych) postaci – zazwyczaj wyższych rzędów. Odpowiedni dobór wag pozwala również na wymuszenie przepływu z każdej postaci drgań z pożądanym priorytetem.

W przypadku zastosowania do usprawnienia procesu odzyskiwania energii z drgań, waga odpowiadająca docelowej postaci drgań ma wartość ujemną. Minimalizowanie funkcji celu będzie zatem wymuszać przepływ energii do tej postaci. Zakładając, że przetwornik elektromechaniczny jest dostrojony to docelowej postaci drgań, będzie on pracował zawsze w rezonansie, nawet jeżeli wymuszenie zewnętrzne pobudza konstrukcję w postaciach drgań dalekich od częstotliwości drgań własnych przetwornika. Węzły blokując się nie wykonują pracy nad układem, zatem sterowanie takie nie destabilizuje układu podczas drgań swobodnych.

Zaproponowany algorytm sterowania pomaga zaimplementować prawo sterowania z uwzględnieniem ograniczeń sprzętowych. Wykazano, że naturalną własnością tego algorytmu jest blokowanie węzłów, gdy odpowiednie rotacyjne stopnie swobody mają równe prędkości (lub równe w przybliżeniu), co pozwala unikać udarów.

Weryfikacja numeryczna Weryfikacja numeryczna obejmuje badania symulacyjne zarówno dla zastosowania strategii sterowania do tłumienia drgań, jak i usprawniania odzyskiwania energii. Do testów wykorzystano autorskie oprogramowanie oraz komputerowe modele MES płaskich konstrukcji ramowych. Prędkości w różnych punktach konstrukcji służą później do filtracji modalnej celem oszacowania prędkości modalnych. Pomiar odkształceń odwzorowany z funkcji kształtu belowych elementów skończonych i znanych wymiarów przekroju służy oszacowaniu momentu gnącego przenoszonego przez każdy blokowany węzeł. Lokalizacje pomiarów prędkości są znalezione za pomocą algorytmu opartego na wypukłej relaksacji.

W weryfikacji numerycznej skuteczności w tłumieniu drgań rozważane były dwie konfiguracje konstrukcji: (1) z węzłami umieszczonymi optymalnie wg. miary sterowalności zaproponowanej w niniejszej pracy oraz (2) z węzłami umieszczonymi nieoptymalnie, celem sprawdzenia odporności algorytmu na nieoptymalne rozmieszczenie węzłów (np. z uwagi na ograniczenia konstrukcyjne). W obydwu konfiguracjach proponowana strategia sterowania była porównana ze strategią PAR dla drgań swobodnych, wymuszenia harmonicznego oraz losowego. Choć obie metody dawały zadowalające wyniki, proponowane sterowanie umożliwiało narzucenie priorytetu tłumienia poprzez odpowiedni dobór wag dla poszczególnych monitorowanych postaci drgań. Dzięki temu sterowanie modalne lepiej tłumiło drgania pierwszej postaci drgań. Proponowane sterowanie modalne wymaga również mniejszej liczby przełączeń stanu blokowanych węzłów. Różnice w efektywności tłumienia drgań z użyciem porównywanych metod były bardziej widoczne dla konfiguracji drugiej (nieoptymalnie rozmieszczone węzły).

W przypadku testowania możliwości usprawniania odzyskiwania energii z drgań węzły zostały umiejscowione tak, aby wszystkie monitorowane postacie drgań były dobrze sterowalne. Uwzględniony również został model przetwornika elektromechanicznego konwertującego energię drgań na energię elektryczną. Rozważano dwie konfiguracje układu, gdzie przetwornik elektromechaniczny jest dostrojony do: (1) pierwszej postaci drgań oraz (2) drugiej postaci drgań sterowanej konstrukcji. W tym przypadku energia mechaniczna miała być przenoszona odpowiednio do pierwszej lub drugiej postaci. W obydwu konfiguracjach konstrukcja była poddawana różnym rodzajom wymuszeń kinematycznych. Wykazano, że przenoszenie energii w obu kierunkach – w kierunku niższych, jak i wyższych częstotliwości – poprawia wydajność pracy przetwornika elektromechanicznego. W przypadku szerokopasmowych wymuszeń rekomendowane jednak jest zaprojektowanie całego układu tak, aby najbardziej podstawowa postać drgań była jednocześnie docelową.

Walidacja eksperymentalna Walidację eksperymentalną proponowanej strategii przeprowadzono na laboratoryjnym demonstratorze drgań, którym jest rama wysięgnikowa wyposażona w sześć blokowanych węzłów. Rama i jej wymiary przedstawione są na rysunku 5.1. Efekt zablokowania/odblokowania był realizowany przez piezo stos zmieniający siłę docisku między powierzchniami ciernymi węzła. Aby wyznaczyć niezbędne dla algorytmu parametry modalne oraz mieć możliwość porównania wyników eksperymentalnych z symulacją komputerową przygotowano model MES konstrukcji. Model MES został skalibrowany z użyciem zidentyfikowanych eksperymentalnie postaci drgań konstrukcji. Algorytm sterowania zaimplementowano na sterowniku FPGA. Z uwagi na jego ograniczoną pamięć możliwe było sterowanie jedną parą węzłów na raz – pozostałe były w tym czasie pasywnie zablokowane. Monitorowane były pierwsze trzy postacie drgań demonstratora.

Przetestowano skuteczność tłumienia drgań swobodnych oraz wymuszonych (przemiatanie częstotliwości wzbudnikiem modalnym). Drgania swobodne analizowano w dziedzinie czasu, natomiast wymuszone – w dziedzinie częstotliwości za pomocą funkcji odpowiedzi częstotliwościowej oraz funkcji widmowej gęstości mocy. Charakteryzowane były zarówno przemieszczenia, jak i przyśpieszenia swobodnego końca konstrukcji. W zależności od dobieranych wag algorytmu możliwe było selektywne tłumienie poszczególnych postaci drgań. Eksperymentalnie wykazano przeniesienie energii do drgań w postaciach wyższego rzędu poza zakresem wzbudzenia konstrukcji przez wzbudnik. Widoczne jednak były rozbieżności między wynikami symulacyjnymi a eksperymentem, głównie ze względu na fakt, że węzły są prototypami i mają istotne wady: w stanie odblokowanym pozostaje resztkowa siła docisku między okładzinami ciernymi, a w stanie zablokowanym następuje poślizg między

okładzinami ciernymi z uwagi na przekroczenie maksymalnego momentu przenoszonego przez węzły.

Walidacja przenoszenia energii drgań między wybranymi postaciami została zweryfikowana tylko w drganiach wymuszonych. Testowane było przenoszenie energii do pierwszej oraz do drugiej postaci drgań. W obu przypadkach wzbudnik modalny nie pobudzał docelowych postaci drgań, co pozwalało na wyraźne zademonstrowanie możliwości przenoszenia energii między postaciami drgań w obu kierunkach. Wyniki przedstawiono w postaci funkcji widmowej gęstości mocy – z uwagi na zawężony zakres wzbudzenia. W obu przypadkach wykazano wyraźne zwiększenie poziomu przemieszczeń i przyśpieszeń docelowych postaci drgań kosztem tych wzbudzanych przez wzbudnik. Towarzyszyło temu również niezamierzone przeniesienie części energii do postaci drgań wyższego rzędu.

Konkluzje Zaproponowano sterowanie umożliwiające precyzyjne przenoszenie energii między wybranymi postaciami drgań poprzez blokowanie półaktywnie sterowanych węzłów. Bazuje ono na autorskich wyprowadzeniach opisujących wpływ zablokowania węzła na efekt sprzężenia modalnego skutkującego przepływem energii między postaciami drgań. Zaproponowano również dedykowaną metodę optymalnego rozmieszczania węzłów i sensorów. Sterowanie pozwala nie tylko efektywnie tłumić niskoczęstotliwościowe drgania poprzez przeniesienie ich energii do lepiej tłumionych postaci drgań wyższego rzędu, ale również pozwala przenosić energię do wybranej postaci drgań, co ma zastosowanie w odzyskiwaniu energii z drgań. W tłumieniu drgań sterowanie pozwala narzucać priorytet na wybrane postacie drgań oraz wymaga mniejszej liczby przełączeń stanu węzła, niż metoda PAR. Eksperymentalnie pokazano, że pomimo znacznych niedoskonałości blokowanych węzłów nieujętych w modelu konstrukcji, sterowanie nadal działa, co udowadnia jego odporność na błędy modelowania.

Abstract

This thesis is devoted to a new semi-active modal control methodology of frame structures. The control allows for precise transfer of the mechanical energy between structural vibration modes. It is realised by the lockable joints connecting structural beams. These joints can be dynamically locked and work as rigid connections, transmitting the bending moments between the adjacent beams, or can be unlocked and work as hinges. The locking effect introduces modal coupling that results in energy exchange between the vibration modes. The proposed control methodology has two potential applications: attenuation of low-frequency vibration and enhancement of the energy harvesting process. In the former application the vibration energy is transferred into the high-frequency vibration modes and then effectively dissipated due to the higher damping coefficients of these modes. In the latter possible application the energy harvester is attached to the controlled structure. Then, the energy is transferred from the currently excited structural vibration modes into the preselected one that cooperates well with the energy harvester in terms of installation location and natural frequency.

This research is motivated by the fact that existing semi-active control strategies which aim at inducing the energy transfer are heuristic and usually are able to transfer the energy only towards higher vibration frequencies. They do not employ any feedback from the state expressed in terms of modal parameters. Furthermore, any knowledge about the influence of the locking effect on modal coupling and modal energy transfer is very limited. Additional motivation of the research are efforts recently devoted to improve the trade-off between peak efficiency and operational frequency bandwidth of energy harvesters by introducing intentional nonlinearities, studying internal resonance phenomena and designing of the adaptive devices.

Investigation of the locking effect focuses on the fact that locking and unlocking of the joints changes dynamic properties of the structure, effective number of structural degrees of freedom, modal basis and its dimension. It is shown that the highest-dimension modal basis that is obtained for all joints in the unlocked state can be adopted for investigation of the structural behaviour even if joints become locked. Then, modal coupling effect is included for proper description of the structural behaviour. It allows for investigation of the energy exchange between the vibration modes. These derivations are later used to develop the instantaneously optimal control law and control algorithm as well as to select the measured quantities. Moreover, the control methodology includes dedicated metric of controllability of the energy transfer to/from particular vibration modes, which is used for selection of locations of lockable joints providing their efficient operation. Also a new convex-relaxation-based method for efficient sensor layout optimisation for the purpose of modal filtering is adopted.

Control strategy has been validated both numerically and experimentally. It is demonstrated that due to the insight into modal coupling effects the proposed methodology mitigates low-frequency vibration requiring significantly less number of the joint state switches than prestress accumulation–release (PAR) method that was adopted as a benchmark. Moreover, the proposed modal approach allowed for damping of particular vibration modes with assigned various priority levels, which is not possible in PAR method. Proposed control algorithm also allows for significant enhancement of the energy harvesting process. It has been shown both numerically and experimentally that the control allows for precise energy transfer both towards lower frequencies and vice-versa.

Contents

Chapter 1

Introduction

This chapter introduces the Reader into the thesis. First, a state of the art is provided by the literature review in the first section. This literature review discusses various techniques and aspects of broad field of vibration control ending with discussion on advances in vibration-based energy harvesting. Later, aims, scope and the stated thesis are specified in Section 1.2. Section 1.3 summarises novelty of the control methodology proposed in this thesis and contributions into the current state of the science. This chapter is ended with short summary of the content referring to each chapter.

1.1 Literature review

Vibration is usually undesired phenomenon in mechanical engineering and civil structures. It can cause decrease of efficiency of industrial processes such as machining or robot arm manipulation. Vibration can cause also fatigue damages of mechanical parts or even emergency situations that are dangerous for people as e.g. famous collapse of the Tacoma Narrows Bridge in 1940. Thus, vibration reduction was intensively researched for decades and many different approaches for structural vibration control have been developed. The most important control strategies and their applications until 1997 have been discussed in extensive review done by Housner et al. [22]. The authors concluded that despite of the significant progress in structural control and various engineering applications still large effort is required and will be put into development of methods of vibration attenuation, especially in fields: algorithms and controlling devices, modelling of nonlinear dispersed structures, smart materials, structural health monitoring and damage detection, sensor technology, near-field-earthquake problems and improved collaboration for comparison of large-scale tests. Indeed, the intensive effort in these topics has not decreased until today and still there are aspects that need further study, e.g. modelling of nonlinear structural behaviour, experimental validation of some control strategies aiming at their implementation, development of control strategies tolerant of malfunctions and semi-active as well as hybrid control strategies that are not only fault-tolerant to some degree but also relatively cheap [23]. Additional reason for the amount of work done in the field of vibration control is its multidisciplinary nature. Vibration control includes: control algorithm, optimal placement of sensors and actuators as well as their design and integration with the remaining parts of the control system and the controlled structure. It causes that the structure equipped with such a control system is often called “smart structure” [24]. Various devices intended for actuation of the state of controlled structure, e.g. active mass dampers, dampers with negative stiffness, shape memory and piezoelectric materials or semi-active devices was reviewerd by Ghaedi et al. [1]. Vibration attenuation methods can be divided into three groups according to the way of working and required energy consumption: passive damping working without any external power supply, active control supplied with the energy from the external source and semi-active control required usually a little amount of energy. They are discussed in subsections 1.1.1-1.1.3.

During vibration mitigation the mechanical energy is usually dissipated. However, it is also possible to recover some part of the energy and convert it into other usable form, e.g. electrical one. This process is called energy harvesting. Sometimes vibration is even desired phenomenon as the source of energy in the energy harvesting process. Due to development of the modern energy-saving electronics the energy harvesting is the topic of the growing importance [2]. Methods of enhancement of the energy harvesting process are discussed in subsection 1.1.5.

1.1.1 Passive versus active vibration control

The most common vibration reduction methods are passive ones such as stiffening, damping or isolation with use of e.g. viscous fluids, passive piezoelectrics [25] or tuned mass dampers (TMDs) [26]. Simplicity of this approach often is the main advantage of the passive systems. It determines that they are more reliable than active control systems. Hence, they can work together with active control systems as a hybrid control not only decreasing the costs of the installation but also providing some level of vibration energy dissipation in the case of the failure of the active control system [27]. Due to this valuable properties passive systems are utilised in large scale structures such as e.g. the Millenium Bridge, equipped with tuned mass dampers and viscous fluid dampers [28, 29] and the CN Tower in Toronto equipped in tuned mass dampers in the form of rings [30]. This method of vibration attenuation is employed since XIX century. First noticed passive device similar to the TMD was described and published in 1883 [31]. First TMD device was patented in 1911 [32]. However, it can be observed the ease of designing linear TMDs comes at a cost of the trade-off between peak efficiency occuring at the resonance frequency and operational frequency bandwidth. Thus, many researchers have attempted to expand the frequency and improve the overall efficiency of the TMDs using nonlinear components, e.g. Gatti showed that nonlinear stiffness of the TMD affects one of the peaks of the frequency response function (FRF) introduced usually by the TMD that improve the bandwidth [33]. Pisal researched influence of the dry friction in the TMD on vibration reduction of seismically excited system [34]. Analogous rule of working can be found in the tuned liquid column dampers (TLCD), where instead of mass on spring the liquid moving in a U-shaped pipe attenuates vibration. Range of applications of the TLCDs is similar as for TMDs, e.g. Alkimim et al. showed how to optimise parameters of the TLCD for reducing vibration of a wind turbine based on an arbitrary stochastic wind model with known power spectral density [35]. Adaptable TLDCs discussed in subsection 1.1.2 as sub-class of the semi-active control systems.

It is also possible to expand operational frequency bandwidth of the damping device by nonlinear absorbers called in the literature nonlinear energy sinks (NESes). In addition to the ability to local dissipation of the energy, the NES can provide nonlinear coupling between the vibration modes of usually linear structure and redistribute the energy among different vibration modes, enhancing effectiveness of the vibration mitigation [36]. Simple example of the vibro-impact NES (VI-NES) attached to a single-degree-of-freedom (SDOF) system is discussed in [3]. Due to single-DOF modal coupling is not possible, however a similar idea employing multi degree of freedom (MDOF) system is described in [4]. Here the energy is dissipated not only in the impact but also transferred to the higher-order vibration modes of the structure, which are excited during the impact. These modes usually are characterised by greater material damping coefficients, hence after their excitation the mechanical energy is effectively dissipated. In the later studies performance of the single VI-NES and two VI-NESes system have been compared and discussed in [5]. It has been found that the use of two dissimilar VI-NESes provides better robustness of vibration suppression with respect to excitation amplitude and extends the operational frequency range of the vibration mitigation system. National Aeronautics and Space Administration (NASA) provided the experiment aiming at testing the influence of gaps in pin joints installed in the precise space truss structures on vibration damping under low-gravity conditions [37]. These joints operate similarly to NESes, as apart energy dissipated in friction also the higher-order vibration modes are induced by impacts caused by the interface clearance. Both friction and impacts are recognised as significant sources of damping of low-frequency vibrations. The investigated structure is of high precision and any preload, e.g. by the gravity, limits the damping effect due to the lack of relative motion of the parts within the joint interfaces. However, among the advantages of such damping system there are: low weight, simplicity and expected high durability, as well as the absence of any fluids what often is in demand in space applications. Effectiveness of the mechanism of the mechanical energy transfer to the higher-order vibration modes has been also reported by Motato et al. for the use of NES in a MDOF drive-train system [38]. Due to transferring of the energy from the lower-order vibration modes the first four vibration modes of the investigated drive-train system equipped with two NE-

Ses have significantly increased the normalised effective damping factor. Study of the effectiveness of strongly nonlinear absorber (SNA) that is also a kind of NES device in attenuation of nine-story building was investigated by Li et al. [6]. In this case SNA is mass damper with strongly nonlinear stiffness. The nonlinearity is purely geometrical. They studied both SDOF and two-DOF SNAs and observed that both SNAs cause the the quick redistribution of the energy from the excited low-order modes into the higher-order ones, however the two-DOF SNA is more effective. The energy transferred into higher frequencies is later effectively dissipated in the material damping. The intended modal energy transfer provided by NESes discussed above is recognised as very effective and promising in vibration attenuation method of low-frequency vibrations that are usually the most difficult to be damped. Thus, employment of this phenomenon in semi-active control is discussed also in Subsection 1.1.3.

Other example of passive damping system which can be used in applications requiring very small weight is piezoelectric patch with a shunted electrical circuit. Here, piezoelement is a device used to transform the mechanical energy into electrical one and dissipate it in the resistance of the shunted electrical circuit. First works describing this approach were published by Forward as well as Edwards and Miyakawa [39, 40]. First validated mathematical model describing effective mechanical impedance of the shunted piezoelectric was written by Hagood and von Flotow [41]. This topic of passive vibration damping still is researched. A fully passive nonlinear piezoelectric tuned vibration absorber that is able to adapt to nonlinearities of the structure was developed by Lossouarn et al. in 2018 [42]. In this work the electrical circuit of the absorber includes an electromagnetic coil that not only provides the electrical resonance, increasing effectiveness of the damping system, but also due to ferrite-material core of the coil it provides desired nonlinear characteristics of the electrical circuit. Due to proper design of the coil it is possible to compensate the nonlinearities of the structure, hence vibration are effectively mitigated in wider range of excitation amplitudes. Another concept of design of the electromagnetic coil with vary inductance was also adopted to compensate the temperature dependant variations of electrical circuit parameters [43]. Utility of the shunted piezoelectric transducers with two configurations of shunt circuits: resistive and resistive–inductive has been evaluated by Sales et al. [44]. It has been shown that due to possibility of miniaturization of the shunted circuit it is applicable in the spacecrafts but in the case of mitigation of low-frequency oscillations high value of inductance is in demand.

An interesting example of the passive vibration mitigation is shown in [45]. The authors proposed the passive damping system aiming at preventing an impact when displacement capacity is limited – it is activated only in the cases when displacement is beyond preselected threshold. Proposed approach is to calculate the optimal control forces and trajectories (like in active control) and design passive system that will have similar characteristics. The problem of the near-fault kinematic excitation is considered also during the design of seismic isolation system. Near-fault displacements in seismic isolation system were taken into consideration by Tsai et al. [46]. They proposed friction pendulum system with curvature lengthened with the displacement. Also finite element formulation was proposed for this isolation system. Shahbazi and Taghikhany evaluated 120 cases of polynomial functions describing the variable curvature of friction pendulum aiming at minimisation of the floor accelerations and displacements [47].

Contrary to the passive vibration reduction, the active control provides high performance at the expense of much higher application costs caused by the need of use of the efficient power supply, a controller with uploaded algorithm and a set of sensors and actuators. In one of the first studies of structural active control Swigert and Forward showed that for two orthogonal modes of a cylindrical mast two electronic circuits are required [48], which additionally increase cost of the installation. It suggests that application of the active control techniques can be difficult and require deepened knowledge. Well-systematised guidelines about active control have been collected by Fuller et al. [49]. This book among other important topics discusses the feedback and feedforward control architectures, which are considered as two main approaches in design of the active vibration control, as indicated also by Alkhatib and Golnaraghi in the review paper [50]. Other excellent book written by Preumont describes the active control of structures modelled with aid of the finite element method (FEM), the controllability and obsrvability problems, collocated and optimal control and other important topics related to the control theory [51].

Feedback control architecture is used commonly in many engineering applications because of the relative ease of designing process. It does not require a reference signal depending on the disturbance, nor the accurate mathematical model of the controlled object, even for certain optimal approaches. Zhang et al. proposed sliding mode control of a 76-story building by means of the rotational active mass damper (AMD), where for the controller design purposes model of the building has been simplified to the single-story structure [52]. Zhang et al. compared proposed control strategy with benchmark results obtained by Yang et al. linear quadratic regulator (LQR) employing 12 DOF reduced model for controller design purposes [53]. Despite much simpler model used to design the controller sliding mode control achieved performance close to the LQR control that is optimal in sense the Pontryagin's maximum principle.

Feedforward control approach require mathematical model of the controlled plant or at least knowledge about its basic properties. The reason is that in purely feedforward-based control system the control signal is applied to the controlled plant based only on the reference (set point) signal or known disturbance – without any information about current plant state. Feedforward control is the most beneficial when it is combined with other control strategies. Such approaches are often used in set-point tracking problems where fast control of the rigid-body modes causes residual vibrations in the flexible modes. Bruijnen and Dijk showed feedforward control with assistance of input shaping filter and feedback loop for damping of residual vibration aiming at improving tracking accuracy [54]. Dhanda et al. proposed solution of similar problem with near time-optimal control of flexible modes by means of the input shaping filters [55]. Very interesting example of modern control utilising measurement of excitation in the form of earthquake and feedback with respect to Kalman's filter-based observation has been proposed by Wasilewski et al. [56]. In this case the authors proposed optimal control approach in the sense of the Pontryagin's maximum principle, where measurement of the ground acceleration is used to calculate autoregression-based prediction which is included in the optimal control problem.

Strong disadvantage of the active control is possibility of destabilisation of the controlled plant, especially when the control is sensitive to the measurement noises, modelling errors or communication time delays [22, 57]. Hence, the attention is paid to the resistance of the control to the modelling errors, measurement noises or delays. This property of the control system is called robustness. Among many approaches in robust control, a branch based on pole-placement should be noticed, e.g. with aid of singular value or QR decomposition [58]. Here, robustness is referred as insensitivity of the closed-loop eigenvalues with respect to system parameters or modelling errors. An interesting example of robust pole placement for structural control using receptance data has been proposed proposed by Tehrani et al. [59]. The pole placement is robust with respect to noise in the measured receptances. They proposed method of pole placement for subsequent modes in the way that each next column in the input matrix changing poles for current vibration mode does not affect pole placement related to all modes in previous steps of the procedure. Other example of commonly used control approaches characterised by the robustness is sliding mode control. It allows for the state of the structure to "slide" along designed sliding surface in the state space due to discontinuous control signal. However, there appears a phenomenon of chattering, which often causes the wear of the system components or even possibility of fatigue damage. There are numerous algorithms reducing the chattering phenomenon and one of the simplest is time-dependent reduction the sliding gain function, simultaneously with decreasing amplitude of vibration [60].

The robustness can be also improved by suitable arrangement of sensors and actuators. Apart maximisation of various measures of the controllability and observability of vibration modes dominant in structural response (which are discussed in Subsection 1.1.4) the robustness with respect to the stability can be provided also by collocated architecture of the control system [51]. The pair sensor-actuator is collocated if they are attached to the same degree of freedom (DOF) of the structure. Then, single-input-single-output (SISO) control loop is characterised by the root locus plot insensitive to changes in the structural parameters and does not go beyond the complex left half plane indicating the stability. However, due to present practical limitations the pairs sensor-actuator sometimes cannot be collocated or despite the same location they are not collocated according to the DOF type, e.g. sensor measures translational DOF and actuator acts on rotational DOF at the same location. In such a situation system is only conditionally stable and there are required more advanced control algorithms or intentional structural modifications as proposed by Gatti et al., where concentrated mass added at sensor location improved the system stability [61].

The term "collocated" relates to the placement of sensors and actuator and should not be mistook with decentralised control as it was emphasized in [62]. The term "centralised" refers to the control architecture, where all actuators and sensors are operated by one controller. In other cases the control is called non-centralised that is not always the same as decentralised. Pisarski et al. compared the newly proposed scalable distributed optimal control, where the control system is divided into sub-modules that can communicate with neighboring sub-modules with two other control approaches: (1) a decentralised control system, where the modules do not communicate with other ones and (2) a centralised control [63]. All three compared strategies were based on LQR approach. The conclusion was that the proposed scalable control combines the advantages of the decentralised control that are reliability of the whole system in the case of any module failure with high performance close to centralised control due to the possibility of the communication.

In the case of presence of significant parameter uncertainties of used plant model or unmodeled dynamics adaptive intelligent control (AIC) can be used. Control algorithms classified as AIC due to its adaptability and capability to learning are suitable for these design problems. The AIC control methods can be categorised into machine learning, evolutionary game theory, reasoning systems and adaptive filters [64]. Good example of machine learning in structural control is artificial neural network-based controller, called neuro-controller, proposed by Błachowski and Pnevmatikos [65]. They compared the neuro-controller with classical LQR approach on two numerical examples of structures: a SDOF structure and realistic example of 12-story tall building. They found that the neuro-controller effectively attenuates vibration caused by an earthquake. Example of 12-story building was adopted from other excellent work done by Jiang and Adeli, where they shown that the proposed structural control fuzzy wavelet neural network was able to manage both geometric and material nonlinearities of irregular building structures [66]. Interesting example of reasoning system based on fuzzy logic used to control a composite plate has been proposed by Zorić et al. [67]. The authors also used a heuristic method called particle-swarm optimisation to find sizes and places of the actuators as well as controller membership function parameters and output matrices. An example of intelligent model identification meant for nonlinear problems can be found in [68], where the authors proposed filter structure including the neural finite impulse response modules and the tapped-delay-line linear combiner can be learned more effectively than two other benchmark examples.

Concluding this section the active vibration control provides better performance than passive vibration mitigation, however it is more difficult and expensive in practical implementations. It needs efficient power source and awareness of possible destabilisation of the controlled plant is required during the control system design. Thus, often sophisticated mathematical apparatus is required to provide stability – especially when model uncertainties are present.

1.1.2 Semi-active control

The semi-active control is the compromise between passive damping and active control. In this approach controlled plant is equipped with semi-active devices able to dynamically modify local parameters of the system, e.g. stiffness or damping coefficient. Contrary to fully active control it does not require efficient power supply but simultaneously is sufficient to mitigate vibration with efficiency close to the active vibration control [69]. Hence, the semi-active control systems can be much less expensive, what sometimes is more important than the control performance [62]. Detailed review and comparison of classical semi-active control systems with passive and active control systems was provided in paper [70]. Similarly to the active control the semi-active one also requires law and dedicated semi-active devices able to modify structural properties [71]. This class of devices usually cannot add energy to the controlled plant but rather dissipate it only so, naturally, the semi-active strategies cannot destabilise the object, as contrary to the active control. The effort made into design of variety semi-active devices was motivation for some works about measure estimating the potential achievable performance of the semi-active device. This problem was discussed in [72], where the authors proposed procedure based on constrained optimal control.

Semi-active dampers based on controlled damping properties mostly can be divided into viscous-based and friction-based devices. The first group of the devices is widely accepted to use for car suspension control as well as in other vibrating structures. One of most popular types of the viscous-based dampers are magnetorheological fluid dampers (MR dampers). In this type of damper the fluid contains magnetisable particles that when subjected to the external magnetic field can change parameters of the fluid resulting in vary damping coefficient of the MR damper. Due to the highly nonlinear characteristics of the MR dampers and inherent dynamics variety of the mathematical models has been developed. Among many works about modelling of MR dampers behaviour we should distinguish a paper describing a phenomenological model proposed by Spencer et al. based on Bouc-Wen hysteresis model comparing the proposed model with several others [73]. MR dampers can be used in many mechanical systems due to their relatively small dimensions and possibility of fast change of the controlled properties. A control scheme based on H_∞ methods realised by the MR damper was proposed by Du at al. [74]. It was shown that the semi-actively controlled MR damper presented similar effectiveness as the active damper. Yang et al. proposed recently a new semi-active suspension control strategy with aid of the negative stiffness included to the suspension in parallel to the MR damper and spring [75]. Negative stiffness is realised by magnets. Strong nonlinearities of such a system pursued the use of advanced control algorithm based on Takagi-Sugeno fuzzy logic approach. Negative stiffness force and controlled always-resistant MR damper force allowed to achieve characteristics like for the active suspension system but still keeping advantages of the semi-active systems. It has been verified both numerically and experimentally. An interesting industrial example o the use of the MR damper has been proposed by Michajłow et al. [76]. They proposed optimal semi-active control strategy in the sense of the Pontryagin's maximum principle for attenuation of torsional vibration of a drivetrain system driven by an electrical motor. Proposed in this research semi-analytical procedure allows for finding the optimal control function for mitigation of steady-state vibration. Capability of semi-active MR damping devices transmission of loads occurring during vibrations of civil structures has been demonstrated in design considerations by Li et al. [77]. In the further research Li and Jianchun studied characteristics of the device and proposed computationally effective model [78]. Usefulness of the MR dampers due to their low power consumption and desirable characteristics for seismic events what was demonstrated with clipping-optimal control algorithm by Dyke et al. [79]. Ha et al. showed that despite the nonlinear character of the MR dampers the design of the controller employing Lyapunov function and direct control of the current supplying MR damper coils is possible [80]. To this end they used the hysteresis model of the MR damper behaviour that does not involve the internal dynamics of the device [81]. The possibility of generation of relatively large forces by semi-active dampers with simultaneous low power consumption was employed to mitigate vibration of a beam structure subjected to a travelling load, as demonstrated first time by Bogacz and Bajer [82]. As this approach was recognised as effective, later it was investigated also by other authors, e.g. Wasilewski and Pisarski proposed methodology for development of the near-optimal control based on the algebraic Lyapunov equation [83]. Effectiveness of the control was demonstrated numerically on simply supported beam subjected on the load moving with vary velocity.

Regarding decentralised control approach an interesting semi-active device, the switching oil damper, intended for such a control architectures was proposed by Kurino et al. [84]. This device is represented by the Maxwell model, consisting of spring and switching (controlled) damper connected in series. The way of working can be described by three following steps: (1) during the structural motion the damping factor of the device is switched into its maximal value, (2) the deformation across the device increases along with structural motion, hence the strain energy is accumulated in the spring element, (3) at the time instance when the strain energy achieves its local maximum the damping factor is switched into its minimal value resulting in the release of the energy accumulated in the spring and its quick local dissipation in the viscous damping. Effectiveness of this method of vibration attenuation was confirmed by real applications as reported in [85]. This control strategy is similar to the prestress acumulation–release (PAR) [86] method which is treated as a benchmark for the control strategy proposed in this thesis. The difference is that PAR method results in release of the structural strain energy in high-frequency oscillation in higher-order modes of the controlled structure contrary to the decentralised device proposed by Kurino et al. that dissipates the energy locally. PAR method is discussed in detail in Subsection 1.1.3.

The friction-based damping modification also found its wide-range applications. One of such devices was controllable friction-based sliding isolation system proposed by Feng et al. [87]. Vary friction force was realised by chamber connected to the pressure control system. Feng et al. indicated that because of the nonlinear character of the friction force the linear control theory cannot be applied to design the control algorithm for such a device. Thus, they proposed also two control algorithms for their device based on: instantaneous optimality and bang-bang approach. Later Inaudi proposed simply and effective approach called modulated homogeneous friction [88]. The contact force between frictional surfaces is assumed to be piece-wise constant and proportional to the last peak value of the deformation of the friction-based damping device. As the amplitude of vibration decreases the values of the contact force also is downsized stepwise. The friction-based device controlled in such a way exhibits rectangular hysteresis loop whose area is proportional to the square of the device deformation. Laflamme et al. developed friction-based semi-active device intended for large-scale structures capable to transmit force of 200 kN with power source voltage of 12 V [89]. The device transmits forces through stiffness element, viscous damper and the friction-based breaking mechanism, composed in parallel. The friction-based breaking mechanism is responsible for providing the control force while viscous damper and stiffness elements serve as fail-save mechanism in the case of failure of the breaking mechanism. Aiming at simulation of the friction phenomenon, appearing in the breaking mechanism, exhibiting its strongly nonlinear nature the LuGre model was used. Laflamme et al. suggested that their device can be controlled by two decoupled controllers. The first, LQR in this case, calculates required friction force. The second, termed "intrernal", controller calculates required clamping force allowing the device to achieve the required friction force which is treated as a setpoint signal. Zhang et al. proposed optimal robust control strategy of building isolation system [90]. This control system also is based on combination of two controllers: LQR and robust compensator. The former one pursues optimality, however it is restricted to the linear control plants. Hence, the later controller compensates nonlinearity resulting from the frictional base isolation system. The control pressure force is calculated in such a way that the friction force is equal to sum of the LQR component and robust compensator component. More examples of friction-based control strategies dedicated to flexible truss-like structures are discussed in section 1.1.3.

Regarding passive TMDs from the previous section, Hrovat et al. showed that due to variability of the damping in semi-actively controlled TMD it is possible to achieve both smaller structural displacements and accelerations as well as TMD stroke [91]. Semi-actively controlled TMD with ground-hook control approach was compared with passive TMD by Setareh [92]. One of the limitations of TMDs designed for buildings is related to required space for their motion for efficient operation. The problem of the influence of the limited stroke on efficiency of various algorithms controlling semi-active TMDs was studied by Demetriou et al. [93]. Chu et al. proposed a leverage-type variable stiffness mechanism for semi-active TMD reducing both the stroke demand of the semi-active TMD as well as energy consumption comparing to the hybrid TMD [94]. Liu et al. described the concept design of a tall building with division of the structure on substructure separated from a superstructure by a semi-active mid-story isolation system [95]. Superstructure in this case acts as semi-actively controlled TMD, although it is also usable for people and mass rations between super and superior structure are different than for "traditional" TMDs, thus the problem of the space limitations is overcomed.

Interesting result can be obtained by an arbitrary change of the natural frequency of the TMD device keeping it always well-tuned to the frequency of oscillations. Brzeski et al. introduced concept of an adaptable TMD, where change of its mechanical properties is realised by an inerter connected through continuously variable transmission system [96]. In further research the authors shown experimentally that due to variable inertance the TMD is able to mitigate vibration of the host structure at almost each frequency with peak-efficiency of the traditional TMD [97]. Other TMD-like device intended for high-rise structures with adaptable natural frequency as well as damping factor is U-shaped semi-active liquid column damper proposed by Altay and Klinkel [98]. Here, the natural frequency is adapted by change of the cross-sectional area of the columns, whereas damping factor is modified by change by movable panels in the horizontal segment of the U-shaped tank.

Another possibility for controlled modification of the structure properties is the use of magnetorheological elastomers (MR elastomers). The change of the magnetic flux density across the MR elastomer contrary to the MR fluid in the MR damper modifies the shear modulus rather than the damping properties. Moreover, dependence of the shear modulus on magnetic flux density is near-linear until magnetic field saturation does not occur [99]. This valuable property makes the design of the controller easier. Dyniewicz et al. researched the semi-active damping control strategy for a layered beam (some times called also sandwich beam in the literature) equipped with MR elastomers between the beam layers [100]. They considered both damping and stiffness factors modifications, however they suggested that the sudden change of the share stiffness of the MR elastomers in appropriate time instances is suitable approach for effective vibration attenuation. Pisarski et al. proposed Lyapunov method-based control strategy for vibration mitigation of the double layered beam equipped with MR elastomers [101]. They discretized the system with aid of FEM receiving bilinear equations of motion. According to the near-linear dependence of the MR elastomer properties on the magnetic flux density the bilinear form in the equation of motion allowed for both properly describing MR elastomer behaviour and keeping the ease of the design process of an instantaneously optimal controller. Later Pisarski studied the influence of the decentralised architecture of the control system on its effectiveness of vibration reduction [102]. It has been concluded that the ability of the local controllers to collect the structure state information in their neighbourhood – not only at their locations – increases performance of the decentralised system to the level comparable with the centralised control system. MR elastomers can be used also for applications other than layered beam structures e.g. vibration isolation, absorbers, base or sensors. These application along with critical review of the advances in the field of MR elastomers were presented by Li et al. [103].

An interesting approach for semi-active control also was proposed recently by Lu et a. [7]. They developed VI-NES controlled semi-actively (called in this paper “semi-active impact damper”) which is devoted for civil structures subjected to earthquakes. Similarly to the passive VI-NESes the semi-active one also allows for transfer of the vibration energy from low-order vibration modes into the higher-order ones and further its quick dissipation in material damping. Here, semi-active VI-NES consists of controlled slider and linear slide. Control strategy imposes the impact at particular position of the slide due to controlled pawl. The impact moment is selected in such a way that momentum exchange between slider and primary structure is maximised.

1.1.3 Semi-active control for light-weight structures

In this subsection the attention is paid on the semi-active vibration control of light-weight structures e.g. telecommunications masts or flexible space structures equipped with measurement apparatus. Light-weight structures are usually weakly damped because of their flexibility and the increase of the energy dissipation ability can be required for their proper operation [104]. Hence, vibration mitigation in these systems often requires dedicated approach. In this section various semi-active control strategies intended for truss-like structures are discussed.

One of the most accepted approaches is dissipation of the energy in friction joints, because it does not increase the weight significantly nor the complexity of the controlled structure. One of the first examinations of this local energy dissipation approach was conduced by Ferri and Heck on a simple structure consisting of two beams interconnected by the friction joint [105]. Later Gaul and Nitsche demonstrated on similar structure that semi-acive control of the clamping force in friction joint allows for significant increase of the damping efficiency compared to its purely passive counterpart [106]. The semi-active joint was controlled by means of the instantaneous minimization of the Lyapunov function equal to the mechanical energy of the system. The contact force between the frictional surfaces is realised with piezo stack actuator. Later Gaul et al. conduced research on semi-active vibration control methodology for space truss-like structures [107,108]. This methodology includes control algorithm as well as sensor and semi-active joint placement based on employed FE model of the structure. Two control algorithms were tested. The first one was based on decentralised approach employing the local-loop control of each joint independently on each other and instantaneous minimisation of the Lyapunov function. The second control approach was the clipped-optimal control. In the later case the control is composed of two sub-controllers similarly to strategies intended for friction-based devices discussed in section 1.1.2 [89,90]. The LQR controller generates signal representing optimal control forces like in fully active control. Later, the local controllers responsible for appropriate values of the contact force in friction interface in each joint treat the LQR signals as the set-point values. The use of the controllability and observability gramians were proposed to formulate the criterion of optimality for distribution of the set of the sensors and actuators. The combination of the LQR approach with an algorithm calculating required control signal for nonlinear semi-active device was also proposed by Onoda et al. [109]. However, such a control strategy was dedicated for a semi-active control device equipped with electro-rheological fluid damper (ER damper). The working principle of the ER dampers is similar as for MR dampers but the electric field is applied to vary damping properties of the damper instead of the magnetic field. The disadvantage of this ER dampers is that they often require high voltages, hence they are less popular. The semi-active device proposed by Onoda et al. controlled by their algorithm essentially works similarly to the device proposed by Kurino et al. [84] that is described in section 1.1.2. The potential energy is accumulated in the spring and released in appropriate moment to be dissipated in the damper which are inherent parts of the device. However, as Onoda et al. intended their control strategy to the light-weight space truss structures which usually are more flexible and have lower material damping than civil structures thus excitation of the higher-frequency vibrations is visible. It is due to the fact that the potential energy is accumulated during the increasing structural deformation both in the ER damper and structural members. Hence, when the ER damper switches its state suddenly reducing its effective stiffness then the accumulated energy is partially released also in the free vibration of the higher-order modes. The control strategy has great potential in vibration attenuation in light-weight structures, however an experimental verification exhibited that at the current stage of this research it is not possible to suppress the residual vibration of very small amplitude. The reason is that the prototype ER damper effectively always remains some residual stiffness and for sufficiently low vibration level works as the passive truss member.

The use of the advanced control algorithms represented by the term generating the setpoint value and term following-up this value by regulation of the contact force in the semi-active joints results from the complex and nonlinear nature of the friction phenomenon. Thus, modelling of the friction-based structural joints is important topic and significant effort has been devoted also to this problem. Segalman in a review paper indicated that linear approximations of the joint connection behaviour are restricted to loads range to which the linear model was tuned and the data for calibration of the device are required [110]. Hence, nonlinear phenomenological models are widely used. Various approaches to describe the nonlinear behaviour of the friction joints as well as applications are discussed in the review paper by Gaul and Nitsche [111]. They concluded that for the control design and simulation purposes phenomenological models e.g. LuGre model are good choice. These models have reduced number of DOFs but still provide ability to estimate energy dissipation rates in the friction interfaces.

The control strategies described above are designed to enhance the dissipation of the mechanical energy in semi-active devices, i.e. locally. However, the semi-active control also covers strategies, where energy dissipation in the whole volume of the structure is controlled by means of the dynamic modifications of local properties of the structure. One of the first of such semi-active control strategies was proposed by Onoda et al. [8]. A semi-actively controlled friction device was proposed to allow local modification of the structural stiffness. It is possible due to the clamping force that is sufficiently large for locking relative motion between the friction parts. Truss members equipped with this device were called “variable-stiffness members”. If the device is locked the variable-stiffness member behaves like regular beam of the structure but if the device is unlocked, relative motion between ends of the variable-stiffness member is possible and the local stiffness of the structure is switched to the lower value. Onoda et al. tested three control strategies intended for the use of variable-stiffness members. All of them are based on the principle that the potential energy accumulated in strains during the structural motion can be suddenly released into free vibration of the higher-order structural modes after dynamic unlocking the variable-stiffness members. The high-frequency oscillations in these modes decreases very quick because the higher-order modes are characterised by greater inherent material damping. Moreover, the higher-order modes usually have very small amplitudes of motion so the release of the strain energy in these modes does not disturb significantly the overall motion of the structure. This rule provides very effective mechanism of the dissipation of the energy in the volume of the structure. The strategies tested by Onoda et al. differ only in the type of the signal fed-back and criterion of the unlocking the variable-stiffness members. In the first strategy the variable-stiffness member is unlocked for short time when the structure tip displacement riches maximal displacement (zero velocity) which is assumed to approximately correspond with maximal potential energy of the structure while the part of this energy is to be released in free vibration of the higher-order modes. The second control strategy uses fed-back signal from the strain gauges placed on variable-stiffness members. The assumption is that square of these strains (representing load transmitted by the lockable member) is proportional to the energy accumulated by these members and their neighbourhood that is to be released in the higher-order modes. The variable-stiffness member is suddenly unlocked when the measured strain has its maximal value (zero derivative). This control strategy can be easily implemented as the decentralised control. Finally, the third control strategy unlocks the semi-active device at time instant when the estimated energy to be released has the maximal value. However the third control strategy was evaluated only numerically as opposed to the two remaining ones validated both experimentally and numerically.

Minesugi and Kondo were conducing a research to develop this approach with use of the modal control theory, however the fact that the variable-stiffness member has ability to be locked at arbitrary relative displacement of the friction surfaces was ignored by them in the equations of motion of the system [112]. It is manifested by lack of the static-force term resulting from the lock of the variable-stiffness member at non-zero relative displacement, hence these equations of motion do not describe the system dynamics properly – especially the crucial energy prestress-release mechanism. This mechanism has been well described on illustrative example of the spring-mass system in the continuation of the research stated by Onoda et al. [9, 10]. The spring-mass system was equipped with two springs set in parallel: one uncontrolled and one detachable (controlled). The control strategy is as follows. During the motion both springs accumulate the strain energy. When mass reaches a maximal displacement detachable spring is disconnected for short time moment. It causes the release of the strain energy into the spring vibration and its dissipation. After short time the spring is reattached and the whole process is repeated, however the equilibrium point of the spring mass system is changed due to the fact that the detachable spring is attached in other position than for the previous reattachment due to strain relaxation during the disconnection. This changing equilibrium point manifesting in the piece-wise constant term in equation of motion enhances efficiency of the damping strategy. The simple explanation is that reattaching the spring immediately after earlier its detaching allows for earlier beginning of accumulation of strains in the controlled spring. Authors of such a strategy called it "prestress accumulation–release" (PAR) and demonstrated the effectiveness of the PAR approach using both the numerical model and experimental setup of the layered beam structure [10]. Change of the stiffness analogous to introductory SDOF example is achieved by the delamination of the layers the structure. Sudden delamination at suitable time moment causes the release of the strain energy in free vibration of the higher-order modes of the structure. This mechanism corresponds to the energy dissipation in the detachable spring. In this paper it was indicated that PAR method has applications in pedestrian bridges, pipeline systems, truss-like structures – including space industry and small-scale mechanisms. Indeed, Mróz et al. proposed later PAR approach for control of the space structures, however instead of stiffness change by delamination mechanism they used dedicated semi-active joints. Such joints have ability to be locked and transmit the bending moment between structural members or unlocked and work as hinges [11]. In this case the principle of working also is analogous to the introductory SDOF example.

The motion of truss-like structure with currently locked joints causes accumulation of the strains. When strain responsible for the bending moment near the semi-active joint achieves its maximal value, it the joint dynamically unlocked resulting in the release of the strain energy in free vibration of higher-order modes and its quick dissipation in the associated material damping. The vibration can be suppressed with PAR method in its several lowest-mode cycles. Performance of the PAR was also demonstrated by Popławski et al. both in numerical model of a multi-bay structure as well as experimental tests on the frame structure demonstrator equipped with two lockable joints [12, 13]. The level of 66-94 % of the forced vibration amplitude reduction in the first natural frequency during experiments was reported in [13]. Orłowska et al. investigated the possibility of employing PAR approach also in structures where instead of lumped or local change of the structural properties (such as locking/unlocking of the joint) it is provided by a smart material [14]. They studied layered beam structure equipped with a controllable core between two outside beam layers. Particular sections of the core material change its damping properties depending on the control signal that provides dynamical effect similar to delamination of the layers and results in the release of the accumulated strain energy in high-frequency vibrations. Applicability of various smart materials such as MR elastomers or pneumatically controlled granular structure in vibration mitigation of layered beam structures was investigated with other semi-active control laws also in [100, 113]. The variety of the structures and possible ways to change the structural properties which are described above demonstrates the possible range of applications of semi-active control strategies transferring the energy into the higher-order vibration modes.

It should be noted that for the control techniques described in [8–14, 112] realised by the lockable joints or variable-stiffness members it was sufficient to replace the complex and nonlinear model of the friction interfaces with imposing of constraints on the DOFs describing the current state of the device. It is due to the fact that contrary to the vibration attenuation based on the local energy dissipation approaches, the semi-active device here have only two steady states: fully locked or fully unlocked. Any transient states are assumed to be very short. Thus, any significant energy dissipation does not appear in the semi-active device interface.

The second important note to works [8–14] is that they describe the methods that due to controlled structural modifications allow for the transfer of the mechanical energy from lower-order, weakly damped, vibration modes to the high-frequency modes resulting in efficient vibration suppression due to their higher inherent material damping. This mechanism is recognised to be very effective in vibration attenuation, especially for the light-weight truss-like flexible structures. However, these control methodologies do not take the full advantage of the shifting of the energy into the higher modes because the control algorithms do not receive information about the current state of the structure in terms of the modal coordinates nor modal velocities. Control strategies processing such information are discussed in general in the next subsection.

1.1.4 Modal control

The modal control approach allows for taking the advantage from representation of the controlled system in eigenvalue-eigenvector formulation. Inman indicated that modal control was developed in two scientific disciplines: structural dynamics and control theory [114]. Regarding the later one the state space equations are transformed into decoupled first-order ordinary differential equations allowing for lower computational effort. Control strategies refer to the pole placement problem [115]. The desired change of the poles (system eigenvalues) associated with particular vibration modes of the closed system, i.e. including control loop, can be achieved during design of the feedback controller. The possibility of decoupling the state equations makes the design of the controlled easier, especially for large-scale MDOF structures. Extensive review of the robust design of the modal control strategies using control theory-based formulation has been given in a tutorial book by Magni [116]. The book contains review and description of the tools for the robust design and examples of their use with MATLAB® functions belonging to the accompanying toolbox for use with MATLAB® software. Regarding modal control developed the former scientific discipline, Gould and Murray-Lasso proposed modal control for structures in 1966 [117]. In this class of modal control strategies the equations of motion describing structural behaviour in physical coordinates are decoupled with the aid of modal analysis. Hence, each vibration mode can be considered, well understood, SDOF oscillator represented by second-order oscillator which is decoupled in free vibration from other ones. Of course, eigenvectors representing mode shapes obtained from modal analysis provide the same information on vibration modes as ones used in the control theory but formulation is different.

Modelling of the continuous or MDOF systems exactly requires including infinite or large number of vibration modes, respectively, whereas it is possible also to model only several ones because of practical reasons. The reasonable strategy is to model only lowest-order vibration modes usually taking significant participation in the structural motion and use only these modes during the design of the controller. The reason is that they are naturally weakly damped and easy to excite by external loads. Nevertheless, such a modal truncation of the investigated system can lead the controller designed only for these, controlled, vibration modes to excite vibration in higher-order, residual, vibration modes causing instability of the system. This phenomenon was investigated by Balas [118]. Balas shown that necessary condition for such a instability is the presence both control spillover and measurement spillover. The first type of spillover is undesired excitation of the residual modes by the actuators controlling intentionally the set of the controlled modes. Measurement spillover is the disturbance of measurement of the controlled modes by the presence of residual modes at the sensor locations. The control spillover does not cause instability issues itself yet. It rather only decrease control performance. However, if additionally measurement spillover effect is present, then the closed-loop system provides bidirectional coupling between controlled and residual modes. It can lead to excitation residual vibration modes with corresponding negative damping coefficients provided by the controller. Such a phenomenon does not appear always but, as Balas indicated, each modal controller should be designed with a special attention on this effect.

Later the active control methodology termed "independent modal-space control" was introduced and developed by Meirovitch and Coauthors [119–121]. The idea of this methodology was to control a set vibration modes of the structure in such a way that each particular mode is controlled independently on each other. In other words control does not couple modal equations or this effect is not significant. It requires at least as many actuators as many modes are to be controlled. This control methodology reduces control spillover effects, i.e. remaining modes are affected by the actuators very weakly. It allows concentrate the control effort on the preselected set of the controlled modes that usually are characterised by low material damping and high participation in the structural response. Process of extraction of the corresponding modal coordinates or velocities, providing information about the instant participation of the modes in the structural behaviour, from measured data is called modal filtering. Meirovitch and Baruch also proposed concept of a modal filter operator. It is represented by matrix reciprocal to the matrix collecting controlled mode shapes at sensor locations. In this case it is kind of spatial filtration that is equivalent to fitting particular mode shapes into measured displacement or velocities with the least squares method. If sensors are properly arranged on the controlled structure, then modal filtering allows for avoiding contamination of modal quantities by the noise and reduces measurement spillover effect. Various approaches in optimal sensor placement for modal filtering purposes are discussed later in this section. Control spillover is reduced by suitable distribution of the forces corresponding to each controlled mode among the actuators. Meirovitch and Baruh also showed that the use of the independent modal-space control with aid of modal filtering is robust with respect to the system uncertainties [122].

Lu proposed an active modal control with direct output feedback dedicated for the mitigation of seismically excited structural vibration [123]. Lu demonstrated that the modal control allows for vibration mitigation when limited information about state of the structure is available with performance close to the control with full-state knowledge. It is valuable property of the modal control. Later, Lu adopted active modal control concept in semi-active control capable to generate dissipative control forces characterised by hysteresis loops similar to its active counterpart pursuing greater values of the modal damping factors for the controlled vibration modes [124]. It is due to the fact that active control forces often are also mainly dissipative, i.e. they have opposite direction to the increments of actuator deformation. Hence, semi-active modal control proposed by Lu has almost the same performance as for the active control. Moreover, both modal approaches proposed by Lu [123, 124] are resistant to measurement noise.

Basu and Nielsen proposed a modal control algorithm combining pole placement technique and integral resonant controller [125]. Such a control methodology allows for broadening the set of the controlled vibration modes. Pole placement that is used to achieve the desired modal damping factors of the higher controlled modes whereas the integral-resonant term effectively attenuates low-order vibration modes. Performance of this control strategy was demonstrated both numerically and experimentally on a cantilever beam equipped with a single strain-gauge and piezoelectric actuator.

Belyaev et al. compared the modal control approach with a local one in experiment on cantilever beam equipped with two collocated pairs of piezoelectric sensor and actuator [126]. In this case the sensor-actuator pairs were located at the points at which the two controlled mode shapes have extreme modal deformations. These two first modes were to be controlled by such an instrumentation with the aid of the modal control characterised by designed transfer function – similarly for the benchmark local controller. The superiority of the modal approach over the local one was shown. The presented modal control was able to effectively reduce vibration for both resonances: of the first mode and of the second one while the local approach was able to suppress effectively only first or only second resonance.

Very interesting example of the control based on the concept of independent modal-space control with example of application to mitigate response of a tall building excited by an earthquake was proposed by Etedali [127]. The control of the preselected set of modes was proposed to be realised with modal proportional–integral–derivative (PID) controller. It was demonstrated that the modal PID outperforms the well known LQR control that was also implemented within the methodology of independent modal-space control. Parameters of the modal PID controller were optimised with cuckoo search algorithm searching for the trade-off in multi-objective optimisation problem for each controlled mode. Moreover, Etedali showed that the modal PID controller is more robust against structural stiffness uncertainties than the benchmark LQR control example.

Modal coordinates describe deformation of the whole structure, of course with some loss of the accuracy related to the modal truncation error. However, modal approach can be also adopted to minimise vibration amplitude at particular location of the structure – e.g. at the location of measurement equipment. To this end, a new approach of semi-active sliding mode control employing the lockable joints was investigated by Ostrowski et al. [128]. In this control approach a hyperplane is formulated in modal space in such a way that any modal displacement within this plane results in zero structural displacement at the preselected location within the structure. Then, lockable joints are controlled aiming at minimisation of the distance of the actual modal displacements from the hyperplane. The advantage of formulation of the problem in modal coordinates is possibility of reduction of the problem to only few modal coordinates since only several first vibration modes participate predominantly in the structural displacements. This approach provides satisfactory preliminary results, where full state of the system is known.

Regarding the mentioned earlier influence of the sensor and actuator placement on the measurement and control spillover reduction, respectively, it is one of the key aspects of the modal control. Sensor placement can be related to various measures of observability, e.g. observability gramian which was adopted by Gaul et al. in earlier discussed work [108]. However, as the attention is paid to modal control approaches not only in this subsection but also in the research undertaken in the present thesis, sensor placement techniques referring directly to modal filtering, identification of modal parameters and modal control are further discussed. One of the simplest approaches for sensor placement is their location at highest amplitudes, inclinations or deformations (depending on the sensor type) of particular mode shapes belonging to set of controlled modes. An example of such an approach is shown in the work of Belyaev et al. that is mentioned earlier [126]. This method is suitable only for simple structures and for small set of only several controlled modes. Here only two first modes of cantilever thin beam were controlled. In practice FE models with a large number of DOFs often are used where usually much smaller subset of DOFs is selected as sensor locations. In this case optimal sensor placement becomes a combinatorial task requiring tremendous computational effort. Thus, variety of criteria and methods of approximation of the optimal sensor locations were invented and developed. Chepuri and Leus [129] discussed optimisation criteria based on the covariance matrix of the error of estimated parameters. It was noticed that calculation of the covariance matrix and using it in numerical procedures during optimisation can be difficult or even practically impossible. Hence, a weaker criterion based on Cramér-Rao bound was considered. Here, instead of the covariance matrix the Fisher information matrix (FIM) can be used. Therefore, optimality criteria for selection of sensor locations relate to the maximisation of FIM norms, e.g. its trace or determinant. Papadimitriou and Beck showed that the use of the norm of the FIM other than determinant is not recommended in some cases [130]. In the case of estimation of the modal coordinates the determinant of FIM represents a trade-off between values of mode shapes (related motion amplitudes) at sensor locations and their linear independence. After selection of appropriate optimality criteria the algorithm allowing for obtaining near-optimal solution is required. One of the simplest approaches for sensor placement referring to the independence of the mode shapes was proposed by Schedlinski and Link [131]. They did not formulate Fisher information matrix explicitly but proposed to use vector basis composed of rows of the modal matrix, where rows correspond to particular DOFs of the structure, that also finds near-maximal determinant of FIM. First, the row vector with the highest norm is selected. Later, vector whose projection on plane perpendicular to all vectors selected yet has the biggest norm is selected in iterative manner until desired number of rows (sensors) is not achieved. This method is also used in solving under-determined linear equation sets using QR decomposition with pivoting to select the most representative solution basis, e.g. in MATLAB® software. Kammer proposed famous Effective Independence method (EFI) whose formulation is explicitly based on FIM [132]. This method removes particular sensor locations from the set of the candidate sensor locations in iterative manner providing the lowest decrease of the determinant of FIM. The algorithm is stopped when the number of desired sensor locations decrease to the number of available sensors. Recently, very efficient convex-relaxation-based algorithm to maximise the determinant of FIM was proposed by Błachowski et al. [21]. In this method the discrete problem is replaced with its continuous counterpart. During optimisation process instead removing candidate sensor locations a sensor density vector is obtained. Elements of this vector that converge to ones denote that the corresponding candidate locations are selected to be sensor locations, whereas elements converging to zeros denote rejected candidate sensor locations. This method has been selected to be used for sensor placement in the present research – more details can be found in Section 3.2.

Proper actuator placement is related to the controllability of the structure. Controllability condition proposed by Kalman used classically in the control theory allows to investigate if the system is controllable or not. In the case of optimal actuator placement other mathematical tools are employed. Additionally for large MDOF systems often used in the engineering practice Kalman's criterion may lead to numerical difficulties. A Popov-Belevitch-Hautus eigenvector test (PBH test) allows for indicating both the observability of the mode from the particular sensor location and its controllability from the particular actuator avoiding the numerical problems [51]. In both cases the mode shapes must have nonzero values at sensor/actuator location and corresponding eigenvalues must have unique values, i.e. there must not be any multiple eigenvalue. PBH test provides also some metric about controllability and observability. The bigger displacement of the mode shape at sensor/actuator location is the greater is the associated observability/controllability. However they do not include dynamic properties associated with modes such as modal damping coefficients or natural frequencies in quantifying the controllability, since higher-order modes that are strongly mitigated by inherent material damping are usually less controllable. Hence, an alternative approach to quantify the controllability of the vibration modes can be obtained with the controllability gramians [133]. This controllability metric was used by Gaul et al. in multicriteria problem of optimal placement of the semi-active joints [108]. Gaul et al. also used controllability and observability gramians to calculate the Hankel singular values providing information about simultaneously most controllable and observable modes [107]. Indication of these modes allowed to reduce structural model for the purpose of controller design. Interesting example of robust optimal actuator placement was proposed by Li et al. [134]. Uncertainties of the structural parameters that affect eigenvalues of the controllability gramian were taken into account during optimisation of the actuator positions. Optimisation problem is formulated in such a way that it is possible to choose the trade-off between pure optimality and robustness with respect to the uncertainties of the structural parameters.

Summarising this subsection, literature on modal control shows that this approach has several important advantages in relation control approaches based on the feedback from the state expressed in the form of physical coordinates. Superiority in terms of both performance and frequency bandwidth of the modal control over local approaches can be achieved due to the physical insight resulting from modal analysis (e.g. Belyaev et al. [126]). Additionally, modal control can achieve performance close to the full-state feedback (e.g. Lu [123]), whereas it keeps the ease of the design process, lower computational effort and robustness with respect to the structural parameter uncertainties.

1.1.5 Energy harvesting

As it was mentioned, energy harvesting technology has growing importance in both science and industry, e.g. it can be used for battery-less supplying wireless sensors and other devices connected to the Internet of Things crucial for e.g. predictive maintenance, real-time data processing and collection, monitoring of supply chains and other approaches belonging to the Industry 4.0 [135]. Energy harvesting technologies allow for not only energy salvage but also can reduce costs of applications requiring network of devices, e.g. such as sensors, due to avoid the wired power source. There is variety of devices scavenging energy from its various environmental sources, among others: the well known photo voltaic cells and wind turbines, thermoelectric, friction-based mechanisms and, finally, vibration-based technologies. In this subsection the attention is focused on the vibration-based energy harvesting. In this area there exist many different types of EHs whose principle of working is based on different physical phenomena, e.g. electrostatics or magnetostriction phenomenon, however mainly the two the most popular are: electromagnetic energy harvesters (EMEHs), based on the Farady's law, and piezoelectric energy harvesters (PEHs), based on piezoelectricity phenomenon [136]. EMEHs often operate at lower operational frequencies than PEHs. Usually vibration-based energy harvesting is associated with small-scale applications allowing for lower-rates of generated power used in supplying e.g. sensors or micro electromechanical systems (MEMS), however also bigger or even large-scale applications are possible, e.g. in human motion, automotive industry and buildings [137, 138].

In recent times significant effort has been devoted to improve operation of EHs not only in terms of efficiency and size, but also expanding operational frequency bandwidth. Interesting example of shape modifications aiming at enhancement of the device operation was proposed by Kundu and Nemade [139]. In this PEH the beam structure was designed with vary cross-section in such a way that uniform stress along the length. It increased the produced power by 20 % comparing with conventional PEH having uniform cross-section. Other example of PEH with application in medicine was proposed by Anand and Kundu [140]. The proposed PEH is dedicated for pacemaker. Due to spiral shape of the cantilever-beam structure the natural frequency of PEH is reduced to the frequency of the heart beat allowing work under resonance while simultaneously keeping small size. Regarding expanding of the operational frequency bandwidth, it can be achieved with collection of several oscillators in the MDOF structure resulting in several frequency peaks. Such an EMEH device containing three electromagnetic coils and moving magnets connected through V-shape plate was discussed by El-Hebeary et al. [19]. The device allows for operation in three frequency-different vibration modes. Chen and Fan discussed recent advances in the utilisation of the internal resonance phenomena in enhancing nonlinear EH operational characteristics [20]. Internal resonance allows for operation of nonlinear EH in wider operational bandwidth due to the coupling of the vibration modes and their energy exchange, possibility of multi-mode and multi-directional operation.

If EH is to be installed between two bodies that relatively move then a mechanism called mechanical amplifier can be employed [141]. Principle of working of such mechanisms is that relative motion between bodies is transmitted on the attached EH simultaneously magnifying the amplitude. Hence, velocities and accelerations acting on the EH also are increased.

Zhang et al. showed that for the EHs exhibiting linear behaviour the expanded operational frequency bandwidth can be achieved only at the expense of the peak-efficiency at the resonance [15]. Hence, the designer of the EH must consider the trade-off between these two criteria of the device performance. On the other hand, nonlinear EH are difficult to be analysed, e.g. the highest vibration amplitude does not have to cause the biggest produced output power. Due to the nonlinearities the EH can return some amount of the energy to the excitation above certain vibration amplitude level. To tackle this problem Zhang et al. proposed using the condition of the global resonance for maximisation of EH effectiveness. This condition is satisfied when excitation does not perform negative work over EH at any time instant. This condition is related to the shaping of the EH potential well and can be used for single-frequency vibration source and multi-frequency one. Ostrowski et al. considered both vary electromechanical coupling coefficient and vary inductance of the electromagnetic coil [18]. Both of them depend on the moving magnet position. For the vibration amplitude above certain level the nonlinearities and the influence of internal dynamics of electrical circuit are strongly exhibited in EMEH behaviour. Then, increasing the excitation amplitude can even decrease the produced power. It allowed to determine untypical U-shaped characteristics of the generated power in dependence on amplitude and frequency of excitation. For each value of the excitation frequency one particular value of excitation amplitude could be found for which generated power was maximal. Size of the device was limited by spring bumpers between which the magnet was moving. This additional mechanical nonlinearity expands the operational frequency bandwidth.

Cottone et al. proposed the use of elastic collisions of the magnet with the moving mass to amplify the velocity of the magnet that was moving inside the coil [16]. Such an intentional mechanical nonlinearity introduced to the system increased the generated power level by 33 times comparing to the device based on single mass. Broadened operational frequency bandwidth was the additional benefit. Collision phenomenon can be used in frequency-up conversion in energy harvesting. Halim et al. proposed EMEH device employing collision-driven frequency-up mechanism dedicated for human-limb excitation [17]. Frequency-up mechanism is similar to velocity amplification proposed by Cottone et al. due to the principle of conservation of momentum. In this case mass freely moves between two magnets mounted on springs. These magnets interact with electromagnetic coils. They vibrate with high frequency after collision with the moving free mass. Due to this possible to convert low frequency human motion into high frequency oscillations of the moving magnets allowing enhanced power generation and simultaneously keeping relatively small size of the device. Other example of the impact-driven frequency-up conversion was discussed by Wang et al. [142]. In this device freqency-up mechanism was realised by collision of the mass on the beam tip with piezoelectric beams. Operational frequency bandwidth was additionally expanded with the aid of magnets in vicinity of the moving mass. These two types of intentional nonlinearities affecting the potential well of the EH increased significantly the level of generated power. The problem of the tread-off between peak efficiency and operational frequency range can be avoided with adaptable EH. Alevras and Theodossiades proposed a self-tunable EMEH intended for rotating structures, e.g. shafts, operating with vary rotational velocities resulting in vary excitation frequencies for the EMEH [143]. Natural frequency of the proposed EMEH is tuned to the expected vibration frequency due to the centrifugal force acting on a tuning mass. Such a structure allows the proposed EMEH to operate under resonance in the wide frequency range.

Literature on vibration-based energy harvesting shows that significant effort is devoted aiming at expanding operational frequency range and increase the effectiveness of the EHs. To tackle the trade-off between frequency range of efficient operation and resonance peak efficiency various nonlinear devices are developed and studied, including modal coupling phenomena driven by the internal resonance.

1.2 Motivation, aims, assumptions and scope of the thesis

From the literature review it is concluded that the known attempts to dampen vibrations have been made for a century and a half, however, due to the often harmful impact of vibrations, this topic is intensively researched to this day. Despite of the effectiveness of active vibration control mainly the passive approaches are employed. It is due higher costs of the active control systems related to the power source and actuators, and the fact that the active control system does not work in the case of the power source failure. Semi-active control provides a reasonable trade-off between passive and active vibration control, requiring relatively small amount of energy to change the state of the semi-active devices turning in the dynamic change of the local properties of the controlled structure. It can result in effectiveness close to the purely active approach simultaneously keeping the advantages of the passive systems. Thus, attention of the present author was focused on semi-active vibration control. However, instead of local dissipation of the vibration energy in the controlled semi-active devices the control strategies stimulating global damping mechanism are considered. Here, vibration energy associated with the lower-order vibration modes that are usually the most participating in structural motion can be transferred into the higher-order vibration modes and quickly dissipated in the structural volume due to material damping. This mechanism is recognised as very efficient in suppressing of the structural vibration due to the fact that the higher-order vibration modes have significantly higher damping coefficients than the lower-order ones, which in turn, are usually the most difficult to be attenuated.

As the mechanism of the modal coupling in the case of passive systems and resulting in nonlinear interaction between vibration modes is well researched in the literature, the semi-actively controlled modal energy transfer is less investigated. There are only a little works explaining the theoretical basis of the modal coupling effect caused by switching of the local stiffness properties realised by locking or unlocking the relative motion between structural DOFs. E.g. PAR method, despite of its high effectiveness, is heuristic approach based on local strain measurements. It does not take the advantage from information about the structural behaviour expressed in terms of modal coordinates. The literature review shows also that modal control approaches can have performance close to control strategies employing the full-state knowledge but still keep the advantages carried by modal truncation: low computational effort and the ease of the design process. Thus, an investigation of modal interactions during semi-actively controlled energy exchange between vibration modes and its potential application in the controller design process seems to be very interesting and important problem.

Regarding the vibration-based energy harvesting, as the literature review shows, significant effort is devoted to enhance the operation of the EHs in terms of among others: expanding of the operational frequency bandwidth, dealing with the trade-off between the operational frequency bandwidth and EH peak efficiency, providing multi-modal and multi-directional operation of EHs or amplify the EH motion. Intentionally introduced nonlinearities, including internal resonance phenomenon resulting in the energy transfer between the coupled vibration modes, aim at achieving these enhancements. These directions in the research on energy harvesting lead to the question: Is it possible to develop semi-active control strategy allowing for effective and precise transferring of the energy from currently excited vibration modes into the vibration mode whose vibration provides EH peak-efficiency?

The considerations described above motivated the author of the thesis to conduce research on the novel semi-active modal control strategy that is able to precisely transfer the mechanical energy to or out from the selected structural vibration modes. Transfer of the energy is induced by the modal coupling effect resulting from locking/unlocking of the lockable joints installed in the controlled frame structure. Such a methodology can be potentially applied both for vibration mitigation and energy harvesting.

In the former case the vibration damping of light-weight structures is considered. Similarly to PAR method, the proposed control strategy also allows for the transfer of the energy into the high-frequency vibration modes and its efficient dissipation in material damping. Due to the semi-active character of the control it does not require efficient energy source that is great advantage for light-weight structures. The proposed control methodology is especially attractive to be used in space structures. Apart possible lower weight, this control strategy has also other advantages valued in this field. First, the locking effect of the joints can be realised by friction-based interface with vary clamping force that is more preferred in space industry than other solutions, e.g. containing fluids. It allows for operation of the vibration mitigation systems in high-cleanliness or vacuum environment to which fluid-based solutions are sensitive. Second, the control is of semi-active type, thus it cannot destabilise the structure in free vibration. Third, the joints can be designed in a way increasing the reliability of the overall system. In the case of any failure of the control system, e.g. controller or actuator within semi-actively controlled lockable joint, the clamping force can be kept at the level providing friction-based local damping within the joint. Then, despite of the lower effectiveness of the system, it still can reduce vibration. And the last advantage is related to the results reported in [37]. Passive pinned joints intended for space structure, which have similar advantages and attenuate low-frequency vibration by both friction and transferring the vibration energy towards higher-order vibration modes, unfortunately are very sensitive to any preload of the structure. Their use requires high-precision of the truss assembly and constant operational conditions. It is due to the fact these joints provide these two damping effects due to the clearance between the interface parts which can be eliminated when the structural geometry is even slightly changed. The proposed semi-active control allows for avoiding of this problem as the joints can be locked/unlocked at any rotational positions between adjacent structural members and still operate properly.

Regarding the energy harvesting applications the mechanical energy is to be transferred from the currently excited vibration modes into the preselected (targeted) vibration mode. Here, it is assumed that EH is attached to the controlled structure and is tuned with the targeted mode of this structure. In this situation EH works under resonance conditions even if frequency of external excitation is far from that, being within resonance range of any other monitored vibration mode of the structure.

The control methodology described above require deep insight into the behaviour of vibration modes interacting with each other during modal energy exchange. These problems undertaken have been led to formulation of the following thesis:

Dynamic reconfiguration of frame structures by locking and unlocking rotational joints can be used for precise transfer of mechanical energy between selected vibration modes in a chosen direction. Such a reconfiguration is a generalization of the "Prestress Accumulation–Release" (PAR) strategy and, in addition to being used to mitigate vibrations, can increase the efficiency of energy harvesting when necessary.

Aiming at proving the stated thesis the main goal of the present work is to propose and validate a new methodology of the semi-active modal control that allows for precise and efficient energy transfer between vibration modes (as opposed to PAR approach which allows the transfer only from lower-order to higher-order vibration modes, in practice only in heuristic manner). The proposed control strategy at the current preliminary stage of the research is limited to flat frame structures and is to be realised by controlled lockable joints. Depending on the control signals such joints can be locked and transmit the bending moments between adjacent structural members or can be unlocked and work as a hinge. The methodology described in this thesis consists of:

- Theoretical analysis of the influence of the locking effect on modal coupling effect and modal energy transfer, aiming at: designing of the controller, better understanding the control strategy and allowing for its eventual further improvements and its application for structures different from ones proposed in the thesis. Here, a special attention is paid to the fact that when any joint becomes locked a reconfiguration of the system occurs that results in the change of no. of structural DOFs and modal basis.

- Selection of the physical quantities required to estimate the instant value of the modal energy transfer rate required for operation of the control algorithm.

- Methods of optimal placement of both sensors required for modal filtering and lockable joints controlling the structural behaviour.

- Control law which is directly based on the theoretical analysis and control algorithm that additionally includes equipment limitations and other practical issues. The control algorithm instantaneously maximises weighted transfer rate between particular monitored structural vibration modes in desired direction.

The following assumptions are made in the present thesis for analysing reconfigurable structures to be controlled:

1. Beams of flexible frame structures are made from linear-elastic and isotropic material, whereas lumped members of relatively large stiffness (e.g. lockable joints, their components) are modelled as ideally rigid components, e.g. by using lumped mass parameters and offsets. The exception is illustrative example of two degrees of freedom system, introduced for clarify of the dynamics of reconfigurable systems, where rods (that are not lumped members) also are ideally rigid.

2. Small vibration is assumed, thus apart the usefulness of the above assumption also the geometrical nonlinearities are neglected.

3. Flexible frame structures are discretized with aid of FEM, which results in relatively big but finite number of DOFs of the structure.

4. Proportional model of material damping is assumed or omitted.

5. The transient state during locking of the joint is assumed to be very short and later the coupled rotational DOFs involved in the joint have common rotational velocity, thus it is modelled with aid of the law of conservation of angular momentum and kinematic constraints imposed on appropriate rotational DOFs or with aid of relaxed constraint represented by viscous joint model.

6. Additional assumptions for modelling of the EMEH in numerical study are made: stiffness of the spring providing the restoring force for the moving magnet is constant, damping of the magnet motion inside the electromagnetic coil is viscous, inductance of the electromagnetic coil and electromechanical coupling coefficient are constant.

Apart the current chapter allowing for determination how this work relates to the current state of the art, the scope of the further part of the thesis is as follows:

Chapter 2 This chapter describes the influence of the locking of the joint on the structural dynamics. Locking/unlocking of the joint is treated as a kind of reconfiguration resulting in removing/restoring kinematic constraints that results in changing of number of structural DOFs, the modal basis and structural properties. Useful relaxation of the kinematic constraints provided by the joint lock is described by employing viscous-based joint model with large damping coefficient. These issues are introduced first using a simple two-DOF system and later derivations for MDOF structures are served. Modal coupling effect and modal energy transfer which result from the locking of the joints are described. Additionally, suitable method of integration of equations of motion is recommended.

Chapter 3 In this part of the thesis various aspects of the control strategy devoted for the structures from the previous chapter are introduced and discussed. First, physical quantities that are to be measured for proper operation of the control are indicated and some specific issues related to the measurement in reconfigurable structure are discussed. Later, optimal placement of sensors and lockable joints is studied. Novel method of finding optimal sensor layout providing maximal determinant of the Fisher information matrix is described. This method is based on convex relaxation that allows for replacement of the discrete optimisation problem with its continuous counterpart. Novel controllability measures are introduced aiming at indication of optimal locations of the lockable joint. Finally, the novel control law based on instantaneous maximisation of the weighted modal energy transfer rates in desired direction is proposed for both vibration attenuation and energy harvesting application. The control law serves as a basis to a control algorithm that is adapted to equipment limitations and other practical issues.

Chapter 4 Effectiveness of the proposed methodology is verified numerically for both kinds of applications: vibration attenuation and energy harvesting. In both of these cases the controlled structures are subjected to various excitations. The performance of the proposed control strategy in vibration attenuation is compared with PAR approach for each excitation. Moreover optimal and non-optimal (e.g. in the case of construction limitations) placement of the lockable joints is considered. In the numerical testing concerning the energy harvesting application a small-scale frame structure with the attached EMEH is investigated.

Chapter 5 Applicability and the performance of the method in control of real frame structures is validated experimentally on laboratory frame demonstrator. Both the ability to dampen vibration and transfer the energy to preselected vibration mode (here without any EH) is studied. Free (hook release) and forced (frequency sweeps) vibrations are controlled during the experiments. FE model of the controlled structure is updated to experimentally identified modal data and later used to calculation of the parameters used in the control algorithm as well as to make numerical simulations aiming at comparison of the numerical results with the experimental ones. During this comparison an attention is paid to the imperfectness of the prototypes of the lockable joints employed in the tests, which is mainly responsible for the differences in control performance in simulation and experiment. Despite of this fact, the experimental results are satisfactory and proof the applicability and effectiveness of the developed control strategy.

Chapter 6 In the last chapter of the thesis the conclusions on each aspect of the proposed methodology and its validation, both numerical and experimental, are drown. It is followed by comments on unresolved issues and future research.

1.3 Contributions

The contributions of this thesis are summarised as follows:

1. Author's analysis of the reconfiguration effect provided by the locking and unlocking of the joints of plane frame structures, and its influence on kinematics of the structure and its dynamic properties.

2. Author's derivations inspired by fast nonlinear analysis (FNA) [144] for describing the influence of operation of semi-actively controlled lockable joints of plane frame structures on modal coupling effect and resulting energy exchange between vibration modes.

3. Selection of the physical quantities to be measured for operation of the control algorithm under realistic conditions.

4. Co-authorship in development of novel method based on convex relaxation for optimal sensor placement in the sense of maximisation of determinant of the Fisher information matrix for modal filtering.

5. Proposition and development of method for optimal placement of the lockable joints which is dedicated for the proposed control methodology and allows for maximisation of energy exchanged between vibration modes during joint lock.

6. Development of the control strategy providing instantaneous optimality of the modal energy transfer rates to/from particular structural vibration modes consisting of: control law based on derivations indicated in the second point and the control algorithm developed with taking into account measured quantities and equipment limitations.

7. Extensive numerical evaluation of the performance of the proposed control methodology and its comparison with PAR method in vibration attenuation for various excitations as well as optimal and non-optimal placement of the lockable joints.

8. Extensive numerical evaluation of the performance of the proposed control methodology in enhancement of the energy harvesting process for various excitations and two different cases of the targeted mode. Simulations include model of EMEH.

9. Extensive experimental verification of the proposed control methodology based on experimental data provided by Doctor Grzegorz Mikułowski, using laboratory frame demonstrator equipped with lockable joints. Comparison of experimental results with simulations employing the FE model updated to the modal data of the real structure was conduced both for vibration attenuation and energy harvesting applications (EH was not included into the experiment). Free and forced (frequency sweeps) vibration cases were investigated.

The contributions enumerated above are described in publications: five articles in widely respected journals, eight conference papers in prestigious international conferences and one book chapter. All these publications are listed in pages i–iii.

Chapter 2

Dynamics of the reconfigurable structure equipped with lockable joints

In this chapter dynamics of structures equipped with lockable joints is considered. Locking of the joints causes that local stiffness is increased, natural frequencies and mode shapes are modified and one rotational DOF per each locked joint is effectively removed. Such a possibility of dynamic reconfiguration causes that a special attention should be paid to description of the structural motion in terms of the modal coordinates. Modal basis obtained for the system with currently locked joints differs from one obtained for the unlocked ones. It is illustrated in Figure 2.1, where three mode shapes of some three-DOF system equipped with lockable joint form, namely, unlocked modal basis $\{\boldsymbol{\phi}^{(1)}, \boldsymbol{\phi}^{(2)}, \boldsymbol{\phi}^{(3)}\}$. When the joint is locked the system has only two DOFs. Then, namely, locked modal basis is reduced to two eigenvectors $\{\widetilde{\boldsymbol{\phi}}^{(1)}, \widetilde{\boldsymbol{\phi}}^{(2)}\}$ that are different from the unlocked ones. Moreover, equilibrium point can shift from point $\mathbf{0}$ into $\widetilde{\mathbf{q}}_{l}$ if the joint is locked when structure is deformed (non-zero rotational displacement at DOFs involved in the joint) as demonstrated in Fig. 2.1. An important observation is that vectors of locked modal

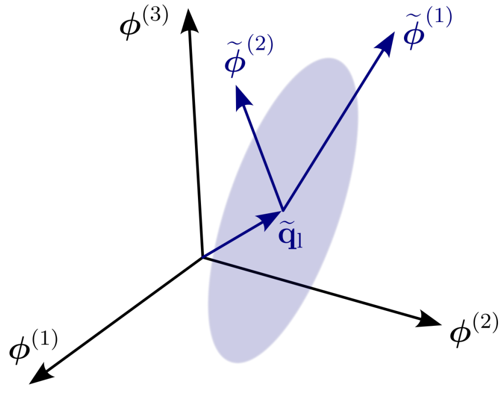

Figure 2.1: Example of possible relation between modal spaces of a reconfigurable three-DOF system which are obtained for the joint in the unlocked and locked states

basis can be described in terms of vectors of the unlocked modal basis that, generally, has as many more dimensions as many joints are currently locked. Thus, it is possible to describe structural behaviour using only unlocked modal basis, even if joints are locked, by employing modal coupling effect.

To understand dynamics of structures equipped with lockable joints these issues are discussed step-by-step in the present chapter. Derivations shown in this chapter allow in the further part of the thesis for:

- formulation of an efficient numerical model of semi-actively controlled lockable joint,
- derivation of the energy transfer rates between vibration modes of the structure serving as a basis for development of the control law, and
- optimal placement of sensors and lockable joints within structure of various kinds of topology.

2.1 Dynamics of a reconfigurable system with two degrees of freedom

Before discussion on general case of multi-degree of freedom structures with lockable joints a simple illustrative example of a reconfigurable system with two degrees of freedom (two-DOF system) is considered. This example allows for understanding crucial issues of dynamics of the structures equipped with the lockable joints. These issues are:

- locking/unlocking of the joint is some kind of reconfiguration of the system, thus it changes system characteristics, e.g. local stiffness of the structure, natural frequencies, no. of DOFs in the system (Subsections 2.1.2-2.1.4),
- dynamical effects caused by the sudden lock of the joints (Subsection 2.1.3),
- modal coupling effect and choice of the modal basis (for locked or unlocked joints) to describe the structural motion (Subsection 2.1.5).

These problems are described in detail using a kinematic constraint first. However, this approach causes additional difficulties in calculations that can be omitted with a relaxed constraint representing the locking effect, as shown in Subsection 2.1.6.

2.1.1 Reconfigurable system with 2 DOFs

Considered two-DOF system is shown in Figure 2.2a. It consists of two rigid rods of mass $M = 1$ kg and $l = 1$ m. The rods are connected together via lockable joint and rotational spring of stiffness $k = 5000$ Nm/rad. First rod is connected to the

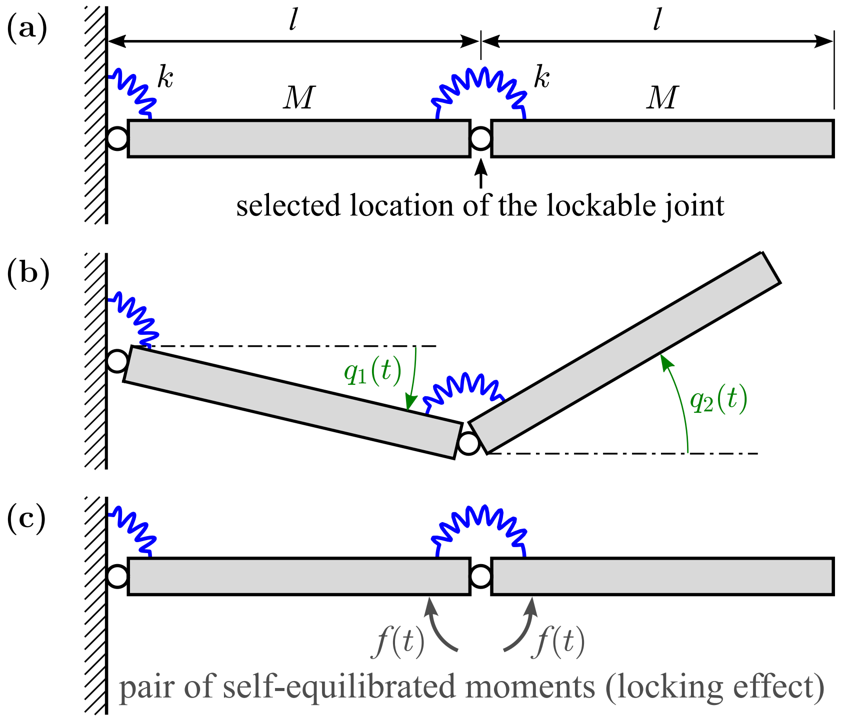

Figure 2.2: Two-DOF system equipped with lockable joint: (a) schematic view, (b) coordinates describing system displacements and (c) pair of self-equilibrated moments representing the locking effect of the joint

support via rotational node characterised by the same rotational stiffness k. It is assumed that the system is undamped and vibration is within small amplitudes.

Motion of the two-DOF system is described by the equation of motion

$$\begin{cases} \underbrace{\begin{bmatrix} I_{11} & I_{12} \\ I_{21} & I_{22} \end{bmatrix}}_{\mathbf{M}} \begin{bmatrix} \ddot{q}_1(t) \\ \ddot{q}_2(t) \end{bmatrix} + \underbrace{\begin{bmatrix} k_{11} & k_{12} \\ k_{21} & k_{22} \end{bmatrix}}_{\mathbf{K}} \underbrace{\begin{bmatrix} q_1(t) \\ q_2(t) \end{bmatrix}}_{\mathbf{q}(t)} = \begin{bmatrix} 1 \\ -1 \end{bmatrix} f(t), \quad t > 0 \\ \mathbf{q}(0) = \mathbf{q}_0, \\ \dot{\mathbf{q}}(0) = \dot{\mathbf{q}}_0 \end{cases} \tag{2.1}$$

where:

$$\mathbf{M} = Ml^2 \begin{bmatrix} 4/3 & 1/2 \\ 1/2 & 1/3 \end{bmatrix}, \qquad \mathbf{K} = k \begin{bmatrix} 2 & -1 \\ -1 & 1 \end{bmatrix},$$

are mass[1] and stiffness matrices, respectively, $q_1(t)$ and $q_2(t)$ are rotations of rigid rods as shown in Figure 2.2b and $f(t)$ is current value of the bending moment transmitted by the lockable joint. It is equal to zero, when the joint is in the unlocked state. Then, only rotational spring transmits the bending moment. In the locked state a pair of self-equilibrated moments acts on the connected structural

---

[1] In further part of the thesis "mass matrix" refers to generalised mass matrix $\mathbf{M}$ corresponding to both translational and rotational DOFs of MDOF structure. Thus, seeking for simplicity matrix in Equation (2.1) also is termed as "mass matrix".

(a) $\omega^{(1)} = 41.3$ rad/s, $\phi_1^{(1)} = -0.556$ rad, $\phi_2^{(1)} = -0.734$ rad

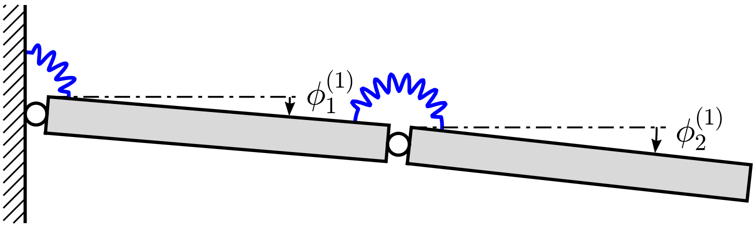

(b) $\omega^{(2)} = 274.7$ rad/s, $\phi_1^{(2)} = -1.185$ rad, $\phi_2^{(2)} = 2.514$ rad

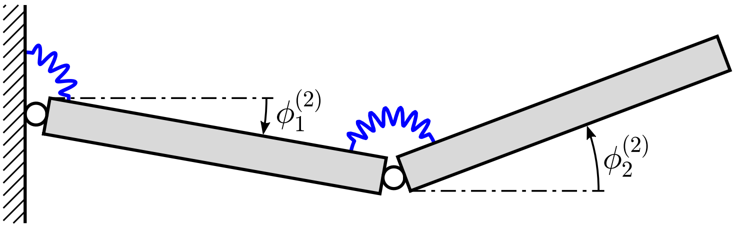

Figure 2.3: Vibration modes of the two-DOF system for the joint in the unlocked state

members as shown in Figure 2.2c, keeping the connection rigid. The lockable joint can be locked at any time instant t_l and any relative rotational displacement between the connected structural members.

Below system dynamics is described for: motion when the joint is unlocked, joint being locked, and when the lockable joint is being unlocked again.

2.1.2 Phase 1: unlocked joint

When the joint is in the unlocked state, i.e. $f(t) = 0, t \in [0, t_\mathrm{l}]$, where t_l is time instant when the joint is being locked, the system described in Equation (2.1) has two vibration modes satisfying the eigenvalue problem:

$$\left(-\begin{bmatrix} I_{11} & I_{12} \\ I_{21} & I_{22} \end{bmatrix} \omega^{(m)2} + \begin{bmatrix} k_{11} & k_{12} \\ k_{21} & k_{22} \end{bmatrix}\right) \underbrace{\begin{bmatrix} \phi_1^{(m)} \\ \phi_2^{(m)} \end{bmatrix}}_{\boldsymbol{\phi}^{(m)}} = \mathbf{0}, \quad m = 1, 2, \tag{2.2}$$

where $\omega^{(m)}$ and $\boldsymbol{\phi}^{(m)}$ are mth natural frequency and mode shape, respectively. Mode shapes are normalised with respect to the mass matrix. Vibration modes of the structure shown in Figure 2.2 are shown in Figure 2.3. Vibration modes $(\omega^{(m)}, \boldsymbol{\phi}^{(m)})$ and basis $\{\boldsymbol{\phi}^{(m)}\}$, $m = 1, 2$, are further called “unlocked vibration modes” and “unlocked modal basis”, respectively.

2.1.3 Phase 2: locking effect

Motion of the structure with currently locked joint is subjected to the constraint:

$$q_2(t) - q_1(t) = \Delta q, \qquad t \in (t_\mathrm{l}, t_\mathrm{u}], \tag{2.3}$$

where:

$$\Delta q = q_2(t_\mathrm{l}) - q_1(t_\mathrm{l}) = \mathrm{const}$$

is the difference of rotational displacements at the time instant t_l, when the joint is being locked, and t_u is time instant of the joint unlocking. In the consequence one DOF is lost after the joint lock. Then, we have:

$$\begin{bmatrix} q_1(t) \\ q_2(t) \end{bmatrix} = \underbrace{\begin{bmatrix} 1 \\ 1 \end{bmatrix}}_{\mathbf{B}_0} q(t) + \underbrace{\begin{bmatrix} 0 \\ 1 \end{bmatrix}}_{\mathbf{B}_1} \Delta q, \qquad t \in (t_\mathrm{l}, t_\mathrm{u}]. \tag{2.4}$$

For matrices $\mathbf{B}_0$ and $\mathbf{B}_1$ selected as shown in equation above

$$q(t) = q_1(t), \qquad t \in (t_\mathrm{l}, t_\mathrm{u}]. \tag{2.5}$$

If the constraint in Equation (2.4) is satisfied it follows that its derivative also is satisfied, then the corresponding constraint imposed on rotational velocities should be noticed:

$$\dot{q}_2(t) - \dot{q}_1(t) = 0, \qquad t \in (t_\mathrm{l}, t_\mathrm{u}]. \tag{2.6}$$

The joint can be locked at any time instant t_l, thus we assume that rotational velocities when the joint is being locked have not to be equal:

$$\dot{q}_2(t_\mathrm{l}) \neq \dot{q}_1(t_\mathrm{l}). \tag{2.7}$$

Thus, there is a discontinuity of rotational velocities at time instant t_l. When the joint is locked rotational velocities can be described by one common rotational velocity as follows:

$$\begin{bmatrix} \dot{q}_1(t) \\ \dot{q}_2(t) \end{bmatrix} = \begin{bmatrix} 1 \\ 1 \end{bmatrix} \dot{q}(t), \qquad t \in (t_\mathrm{l}, t_\mathrm{u}]. \tag{2.8}$$

Due to the discontinuity the common rotational velocity $\dot{q}(t)$ is to be found after the joint lock, i.e. at the time instant $t_\mathrm{l} + \varepsilon_t$, where ε_t is infinitesimal time interval.

Independently on the realisation of the locking effect the law of conservation of angular momentum can be used to find the rotational velocity common for both rotational DOFs (Eq. (2.8)). Due to the fact that both rotational DOFs have the same rotational velocity after the locking it can be treated as ideally inelastic collision. Knowing that angular momentum of the system before and after locking of the joint is the same and taking into account Equation (2.8) we have the following equation:

$$\underbrace{\begin{bmatrix} 1 & 1 \end{bmatrix} \mathbf{M} \begin{bmatrix} 1 \\ 1 \end{bmatrix}}_{I_\mathrm{l}} \dot{q}^+ = \begin{bmatrix} 1 & 1 \end{bmatrix} \mathbf{M} \begin{bmatrix} \dot{q}_1^- \\ \dot{q}_2^- \end{bmatrix}, \tag{2.9}$$

where: $\dot{q}^+ = \dot{q}(t_\mathrm{l} + \varepsilon_t)$ is the common rotational velocity after joint locking, whereas

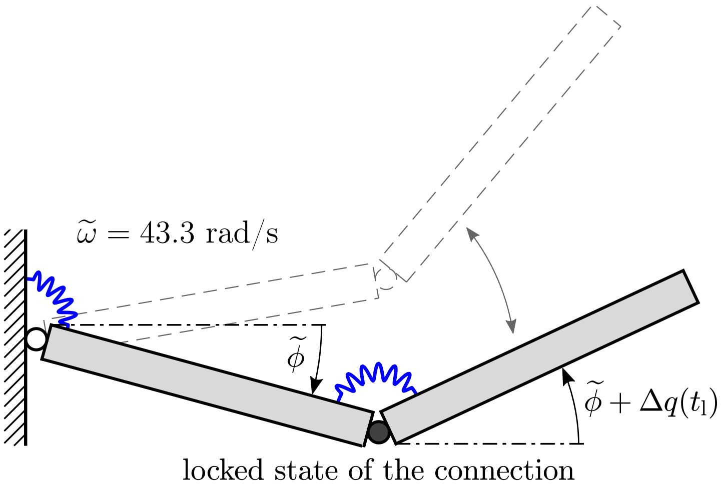

Figure 2.4: Vibration mode of the two-DOF system with currently locked joint; $\widetilde{\phi}$ is insufficient to describe full state of the system

$\dot{q}_1^- = \dot{q}_1(t_l)$ and $\dot{q}_2^- = \dot{q}_2(t_l)$ are rotational velocities before joint locking. Thus

$$\dot{q}^+ = \frac{1}{I_l}\begin{bmatrix} I_{11} + I_{21} & I_{12} + I_{22} \end{bmatrix}\begin{bmatrix} \dot{q}_1^- \\ \dot{q}_2^- \end{bmatrix} = \mathbf{A}_l \dot{\mathbf{q}}^- \tag{2.10}$$

Due to the fact that rotational velocity $\dot{q}^+$ is common for both DOFs after the lock of the joint some amount of kinetic energy is lost (converted to its other forms, e.g. the heat, as analogy to inelastic collision) when the rotational velocities are different before locking.

By substitution of Equation (2.4) into Equation (2.1) and left-multiplying by $\mathbf{B}_0^{\mathrm{T}}$ we receive:

$$\begin{aligned} &\underbrace{\mathbf{B}_0^{\mathrm{T}}\begin{bmatrix} I_{11} & I_{12} \\ I_{21} & I_{22} \end{bmatrix}\mathbf{B}_0}_{I_l}\,\ddot{q}(t) + \underbrace{\mathbf{B}_0^{\mathrm{T}}\begin{bmatrix} k_{11} & k_{12} \\ k_{21} & k_{22} \end{bmatrix}\mathbf{B}_0}_{k_l = k}\,q(t) + \\ &\qquad + \underbrace{\mathbf{B}_0^{\mathrm{T}}\begin{bmatrix} k_{11} & k_{12} \\ k_{21} & k_{22} \end{bmatrix}\mathbf{B}_1}_{0}\,\Delta q(t) = \underbrace{\mathbf{B}_0^{\mathrm{T}}\begin{bmatrix} 1 \\ -1 \end{bmatrix}}_{0} f(t), \quad t \in (t_l, t_u]. \end{aligned} \tag{2.11}$$

Finally, the motion of the two-DOF system when the joint is locked is described, including initial conditions for the considered range of time, as follows:

$$\begin{cases} I_l \ddot{q}(t) + k_l q(t) = 0, \quad t \in (t_l, t_u] \\ q(t_l + \varepsilon_t) = q(t_l) \\ \dot{q}(t_l + \varepsilon_t) = \mathbf{A}_l \dot{\mathbf{q}}^- \end{cases}. \tag{2.12}$$

After the transformation between configuration spaces shown in Equation (2.11) the information about angle Δq and potential energy stored in the second spring is lost in the resulting equation. Δq should be then stored separately. Furthermore, reduction of the configuration space by one DOF due to locking effect reduces modal basis into one, single-DOF mode shape, denoted as $\widetilde{\phi}$, and one natural frequency:

$$\widetilde{\omega} = \sqrt{\frac{k_l}{I_l}} \tag{2.13}$$

that usually is different from both $\omega^{(1)}$ and $\omega^{(2)}$. This modal basis is insufficient to describe full state of the two-DOF system due to the lost information about Δq. This issue is illustrated in Figure 2.4. Vibration mode $(\widetilde{\omega}, \widetilde{\phi})$ and single-dimensional modal basis $\{\widetilde{\phi}\}$ are further called “locked vibration mode” and “locked modal basis”, respectively.

If information about Δq is available then current displacements of the structure with the joint in the locked state can be expressed in terms of the unlocked modal basis (even if this basis does not describe dynamical properties of the system for the locked joint). It is due to the fact that locked vibration mode illustrated in Figure 2.4 can be expressed as superposition of two unlocked vibration modes. Similar relationship between locked and unlocked modal basis for some three-DOF system is shown in Figure 2.1, where unlocked modal basis has greater dimensionality than the locked one. For the two-DOF system this relation is as follows:

$$\mathbf{B}_0 \underbrace{\widetilde{\phi}\widetilde{\eta}(t)}_{q(t)} + \mathbf{B}_1 \Delta q = \underbrace{\begin{bmatrix} \phi_1^{(1)} & \phi_1^{(2)} \\ \phi_2^{(1)} & \phi_2^{(2)} \end{bmatrix}}_{\mathbf{\Phi}} \underbrace{\begin{bmatrix} \eta_1(t) \\ \eta_2(t) \end{bmatrix}}_{\boldsymbol{\eta}(t)}, \tag{2.14}$$

where $\mathbf{\Phi}$ is called modal matrix that collects unlocked mode shapes and $\boldsymbol{\eta}(t)$ is vector of corresponding modal coordinates. Then:

$$\boldsymbol{\eta}(t) = \mathbf{\Phi}^{-1} \left(\mathbf{B}_0 q(t) + \mathbf{B}_1 \Delta q \right). \tag{2.15}$$

Analogous derivations for modal velocities lead to the following equation:

$$\dot{\boldsymbol{\eta}}(t) = \mathbf{\Phi}^{-1} \mathbf{B}_0 \dot{q}(t). \tag{2.16}$$

In the equations above the modal coordinates $\boldsymbol{\eta}(t)$ and velocities $\dot{\boldsymbol{\eta}}(t)$ do not change in time as for the system with the unlocked joint. Their time histories are affected by the modal coupling effect that is discussed in detail in Subsection 2.1.5. It is also discussed in Subsection 2.1.6 for the relaxed kinematic constraint representing locking effect.

2.1.4 Phase 3: unlocking of the joint

When the lockable joint is unlocked at time instant t_u then there is no any discontinuities. Motion of two-DOF system is described again in two dimensional configuration space. Initial conditions for time interval $(t_\mathrm{u}, t_\mathrm{l}]$, where t_l is time instant of eventual next joint locking, are computed from Equations (2.4) and (2.8). Finally we have:

$$\begin{cases} \begin{bmatrix} I_{11} & I_{12} \\ I_{21} & I_{22} \end{bmatrix} \begin{bmatrix} \ddot{q}_1(t) \\ \ddot{q}_2(t) \end{bmatrix} + \begin{bmatrix} k_{11} & k_{12} \\ k_{21} & k_{22} \end{bmatrix} \begin{bmatrix} q_1(t) \\ q_2(t) \end{bmatrix} = \mathbf{0}, \quad t \in (t_\mathrm{u}, t_\mathrm{l}] \\ \mathbf{q}(t_\mathrm{u} + \varepsilon_t) = \mathbf{B}_0 q(t_\mathrm{u}) + \mathbf{B}_1 \Delta q \\ \dot{\mathbf{q}}(t_\mathrm{u} + \varepsilon_t) = \mathbf{B}_0 \dot{q}(t_\mathrm{u}) \end{cases} . \tag{2.17}$$

The two-DOF system again is characterised by two unlocked vibration modes as discussed in Subsection 2.1.2.

2.1.5 Selection of the modal basis

From the considerations above it follows that modal basis of the structure depends on its actual configuration. Locked modal basis cannot be used to describe full state of the system due to reduced dimension. However, as demonstrated in Subsection 2.1.3, it is possible to describe structural motion using only unlocked modal basis $\{\boldsymbol{\phi}^{(1)}, \boldsymbol{\phi}^{(2)}\}$ both for locked and unlocked state of the joint, since the dimension of this basis is equal to the maximal dimension of the configuration space of the system. To this end, modal coupling effect is to be taken into account.

Motion of the two-DOF system is expressed in terms of unlocked modal basis $\{\boldsymbol{\phi}^{(1)}, \boldsymbol{\phi}^{(2)}\}$ according to the transformation:

$$\mathbf{q}(t) = \boldsymbol{\Phi}\boldsymbol{\eta}(t). \tag{2.18}$$

By substitution of Equation (2.18) into Equation (2.1) and left-multiplication by $\boldsymbol{\Phi}^\mathrm{T}$ we receive:

$$\underbrace{\boldsymbol{\Phi}^\mathrm{T} \begin{bmatrix} I_{11} & I_{12} \\ I_{21} & I_{22} \end{bmatrix} \boldsymbol{\Phi}}_{\mathbf{I}} \ddot{\boldsymbol{\eta}}(t) + \underbrace{\boldsymbol{\Phi}^\mathrm{T} \begin{bmatrix} k_{11} & k_{12} \\ k_{21} & k_{22} \end{bmatrix} \boldsymbol{\Phi}}_{\boldsymbol{\Omega}^2} \boldsymbol{\eta}(t) = \boldsymbol{\Phi}^\mathrm{T} \begin{bmatrix} 1 \\ -1 \end{bmatrix} f(t), \quad t \in \mathbb{R}_+, \tag{2.19}$$

where $\mathbf{I}$ is identity matrix and $\boldsymbol{\Omega}^2$ is diagonal matrix collecting squares of unlocked natural frequencies. Finally we have:

$$\begin{bmatrix} \ddot{\eta}_1(t) \\ \ddot{\eta}_2(t) \end{bmatrix} + \begin{bmatrix} \omega^{(1)} & 0 \\ 0 & \omega^{(2)} \end{bmatrix} \begin{bmatrix} \eta_1(t) \\ \eta_2(t) \end{bmatrix} = \begin{bmatrix} \Delta\phi^{(1)} \\ \Delta\phi^{(2)} \end{bmatrix} f(t), \quad t \in \mathbb{R}_+, \tag{2.20}$$

where $\Delta\phi^{(m)} = \phi_1^{(m)} - \phi_2^{(m)}$ is the relative angle between structural members at the joint for mth unlocked mode shape (normalised with respect to the mass matrix).

In the equation above unlocked vibration modes are decoupled when $f(t) = 0$ (joint unlocked). In the opposed case these vibration modes are coupled through the right-hand-side of this equation. Then, the two-DOF system vibrates with frequency

$\widetilde{\omega}$ and modal coordinates $\eta_1(t)$ and $\eta_2(t)$ have such a values at each $t \in (t_\mathrm{l}, t_\mathrm{u}]$ that constraints (2.4) and (2.8) are satisfied.

Value of $f(t)$, when different from zero, depends on configuration coordinates, thus it can be expressed in terms of modal coordinates. To this end, Equation (2.4) is substituted into Equation (2.1) that is later left-multiplied by $\mathbf{B}_1^\mathrm{T}$. Then we have:

$$\begin{split}\underbrace{\mathbf{B}_1^\mathrm{T}\begin{bmatrix} I_{11} & I_{12} \\ I_{21} & I_{22}\end{bmatrix}\mathbf{B}_0}_{I_{21}+I_{22}}\,\ddot{q}(t) + \underbrace{\mathbf{B}_1^\mathrm{T}\begin{bmatrix} k_{11} & k_{12} \\ k_{21} & k_{22}\end{bmatrix}\mathbf{B}_0}_{k_{21}+k_{22}=0}\,q(t) + \\ + \underbrace{\mathbf{B}_1^\mathrm{T}\begin{bmatrix} k_{11} & k_{12} \\ k_{21} & k_{22}\end{bmatrix}\mathbf{B}_1}_{k_{22}}\,\Delta q = \underbrace{\mathbf{B}_1^\mathrm{T}\begin{bmatrix} 1 \\ -1\end{bmatrix}}_{-1} f(t), \quad t \in (t_\mathrm{l}, t_\mathrm{u}].\end{split} \tag{2.21}$$

Hence, finally:

$$f(t) = -(I_{21} + I_{22})\ddot{q}(t) - k_{22}\Delta q, \qquad t \in (t_\mathrm{l}, t_\mathrm{u}]. \tag{2.22}$$

Aiming at expression of $f(t)$ in terms of the unlocked modal basis the following substitutions are to be made in the equation above using Equation (2.18):

$$\Delta q = -\Delta\phi^{(1)}\eta_1(t_\mathrm{l}) - \Delta\phi^{(2)}\eta_2(t_\mathrm{l}) \tag{2.23}$$

and, taking into account Equations (2.4) and (2.5),

$$\ddot{q}(t) = -\frac{k_\mathrm{l}}{I_\mathrm{l}}q(t) = -\frac{k_\mathrm{l}}{I_\mathrm{l}}\left(\phi_1^{(1)}\eta_1(t) + \phi_1^{(2)}\eta_2(t)\right), \quad t \in (t_\mathrm{l}, t_\mathrm{u}]. \tag{2.24}$$

By substitution of Equations (2.22)-(2.24) into Equation (2.20) finally we receive:

$$\ddot{\boldsymbol{\eta}}(t) + \left(\boldsymbol{\Omega}^2 + \boldsymbol{\Theta}_1\right)\boldsymbol{\eta}(t) + \boldsymbol{\Theta}_2\boldsymbol{\eta}(t_\mathrm{l}) = \mathbf{0}, \qquad t \in (t_\mathrm{l}, t_\mathrm{u}], \tag{2.25}$$

where:

$$\boldsymbol{\Theta}_1 = -\frac{(I_{11} + I_{22})k_\mathrm{l}}{I_\mathrm{l}}\begin{bmatrix} \Delta\phi^{(1)}\phi_1^{(1)} & \Delta\phi^{(1)}\phi_1^{(2)} \\ \Delta\phi^{(2)}\phi_1^{(1)} & \Delta\phi^{(2)}\phi_1^{(2)}\end{bmatrix}$$

and

$$\boldsymbol{\Theta}_2 = -k_{22}\begin{bmatrix} \Delta\phi^{(1)2} & \Delta\phi^{(1)}\Delta\phi^{(2)} \\ \Delta\phi^{(2)}\Delta\phi^{(1)} & \Delta\phi^{(2)2}\end{bmatrix}$$

are matrices representing locking effect of the joint. They are not diagonal that provides the modal coupling effect.

As it can be seen, Equation (2.25) has the same dimension as for the unlocked joint. This allows us to describe system dynamics using one equation of motion for both configurations of the system. To this end, control signal $u(t) \in \{0, 1\}$ is introduced. When the joint is unlocked $u(t) = 0$ and when locked then $u(t) = 1$.

Finally we have:

$$\begin{cases} \ddot{\boldsymbol{\eta}}(t) + \left(\boldsymbol{\Omega}^2 + u(t)\boldsymbol{\Theta}_1\right)\boldsymbol{\eta}(t) + u(t)\boldsymbol{\Theta}_2\boldsymbol{\eta}(t_\mathrm{l}) = \mathbf{0}, & t \in \mathbb{R}_+ \\ \dot{\boldsymbol{\eta}}^+ = \mathbf{A}_\mathrm{l}^\Phi \dot{\boldsymbol{\eta}}^- \\ \boldsymbol{\eta}(0) = \boldsymbol{\Phi}^{-1}\mathbf{q}_0 \\ \dot{\boldsymbol{\eta}}(0) = \boldsymbol{\Phi}^{-1}\dot{\mathbf{q}}_0 \end{cases}, \tag{2.26}$$

where:

$$\dot{\boldsymbol{\eta}}^+ = \dot{\boldsymbol{\eta}}(t_\mathrm{l} + \varepsilon_t) = \boldsymbol{\Phi}^{-1}\mathbf{q}^+, \quad \dot{\boldsymbol{\eta}}^- = \dot{\boldsymbol{\eta}}(t_\mathrm{l}) = \boldsymbol{\Phi}^{-1}\mathbf{q}^-, \quad \mathbf{A}_\mathrm{l}^\Phi = \boldsymbol{\Phi}^{-1}\left(\begin{bmatrix}1\\1\end{bmatrix}\mathbf{A}_\mathrm{l}\right)\boldsymbol{\Phi}$$

for each time instant t_l when the joint is being locked.

Using of unlocked modal basis along with modal coupling terms to describe structural motion is not only more convenient. It also provides physical insight to the concept of energy transfer between vibration modes, since off-diagonal elements of coupling matrices allow for the exchange of the mechanical energy between unlocked vibration modes. This phenomenon is discussed in detail in Section 2.2.4 using unlocked modal basis.

The drawback of Equation (2.26) is that for each locking of the joint there is required calculation of: (1) term depending on t_l that needs to be computed for each locking of the joint and (2) modal velocities representing common rotational velocity for DOFs coupled by locked joint. Next subsection discusses relaxed kinematic constraint allowing for avoiding these problems.

2.1.6 Relaxed kinematic constraints with (equivalent) viscous model of the joint

In this subsection four key aspects of the replacement of the exact kinematic constraints with their relaxed counterpart are discussed. They are: viscous joint model, its influence on dynamics of the two-DOF system, modal coupling effect and comparison between exact and relaxed constraint on example of free vibration of the two-DOF system.

Viscous joint model

Relaxed counterpart of kinematic constraints (see: Eq.: (2.3) and (2.6)) is pursued:

$$q_2(t) - q_1(t) \approx \Delta q, \qquad t \in (t_\mathrm{l}, t_\mathrm{u}], \tag{2.27}$$

and

$$\dot{q}_2(t) - \dot{q}_1(t) \approx 0, \qquad t \in (t_\mathrm{l}, t_\mathrm{u}]. \tag{2.28}$$

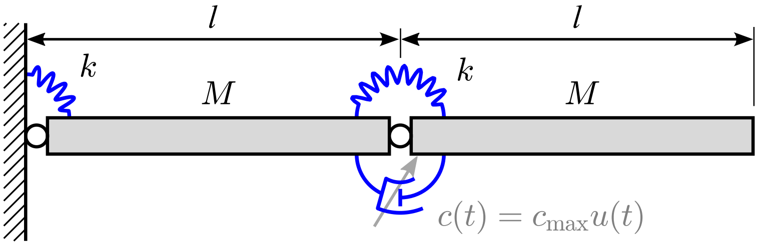

Figure 2.5: Two-DOF system equipped with lockable joint represented by controllable viscous damper with large damping factor

It is done with viscous model of the lockable joint explicitly describing the dependence between locking moment $f(t)$ on actual state of the system. This model is schematically shown in Figure 2.5, where rotational DOFs are coupled/decoupled by the controlled large viscous damping factor $c(t)$. The moment $f(t)$ is then described as:

$$f(t) = -\underbrace{u(t)c_{\max}}_{c(t)} \begin{bmatrix} 1 & -1 \end{bmatrix} \begin{bmatrix} \dot{q}_1(t) \\ \dot{q}_2(t) \end{bmatrix}, \tag{2.29}$$

where $c_{\max}$ is constant large damping factor and $u(t) \in \{0, 1\}$, as previously. When the joint is in the unlocked state, i.e. $u(t) = 0$, then also $f(t) = 0$ and rotational DOFs are decoupled. When $u(t) = 1$ the joint behaves closely to rigid connection due to large $c_{\max}$ and the relaxed constraint in Equation (2.28), and in consequence (2.27), is satisfied, despite of the fact that Equation (2.29) does not provide explicitly any constraint.

After substitution of Equation (2.29) into Equation (2.1) the bilinear equation of motion is obtained:

$$\begin{cases} \begin{bmatrix} I_{11} & I_{12} \\ I_{21} & I_{22} \end{bmatrix} \begin{bmatrix} \ddot{q}_1(t) \\ \ddot{q}_2(t) \end{bmatrix} + u(t) \underbrace{c_{\max} \begin{bmatrix} 1 & -1 \\ -1 & 1 \end{bmatrix}}_{\tilde{\mathbf{C}}} \begin{bmatrix} \dot{q}_1(t) \\ \dot{q}_2(t) \end{bmatrix} + \\ \qquad + \begin{bmatrix} k_{11} & k_{12} \\ k_{21} & k_{22} \end{bmatrix} \begin{bmatrix} q_1(t) \\ q_2(t) \end{bmatrix} = \begin{bmatrix} 0 \\ 0 \end{bmatrix}, \quad t \in \mathbb{R}_+ \\ \mathbf{q}(0) = \mathbf{q}_0 \\ \dot{\mathbf{q}}(0) = \dot{\mathbf{q}}_0 \end{cases} \tag{2.30}$$

The equation of motion above is sufficient to describe behaviour of the two-DOF system for both states of the lockable joint. Due to given explicitly $f(t)$ (Equation (2.29)) the law of conservation of angular momentum then is not needed (but still is satisfied) to calculate the common velocity of rotational DOFs when the joint is being locked. Moreover, there is no any piecewise-constant terms depending on t_1.

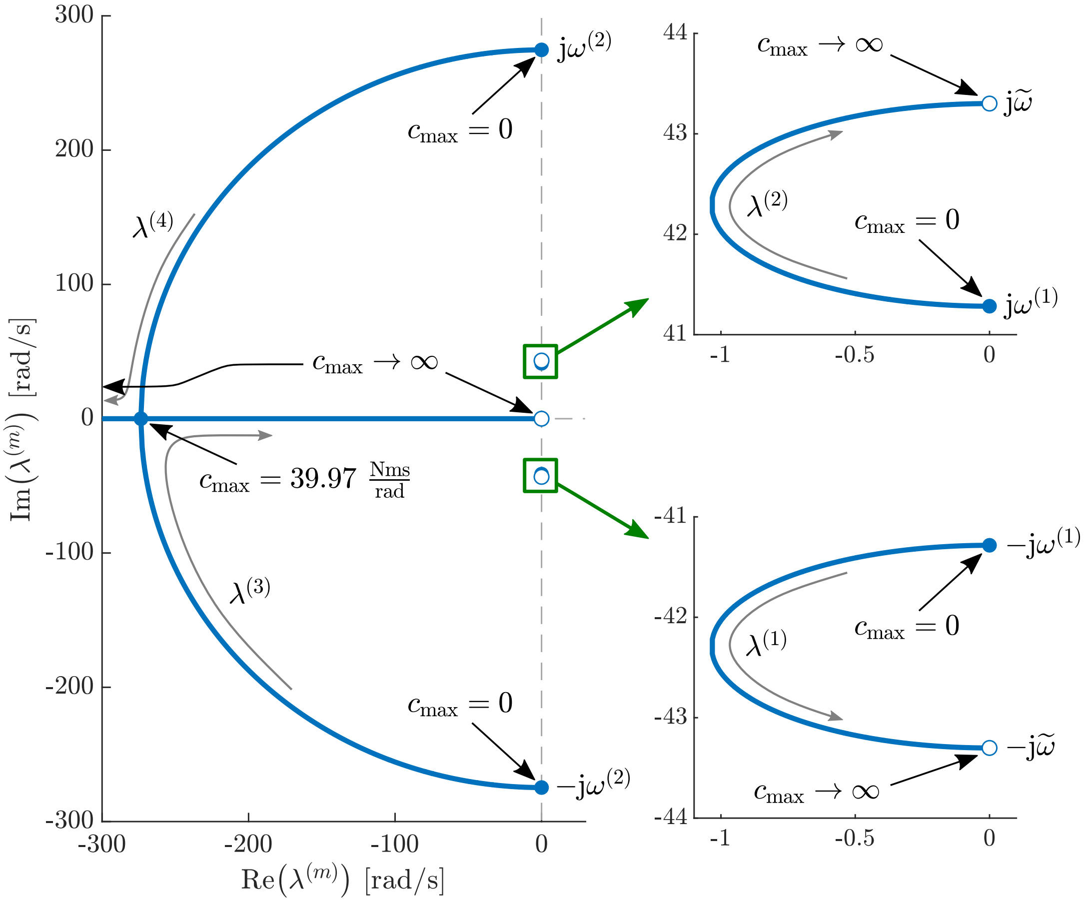

Figure 2.6: Eigenvalues of two-DOF system with the viscous joint model in the locked state in dependence on damping factor $c_{\max}$

The influence of the viscous joint model on dynamics of the two-DOF system

Modal parameters provide the insight into structural dynamics for both locked and unlocked joint of the two-DOF system. For unlocked joint ($u(t) = 0$) the two-DOF system described by Equation (2.30) is characterised by two unlocked vibration modes as described in Subsection 2.1.2. For the locked joint ($u(t) = 1$) non-proportional damping is provided by matrix $\widetilde{\mathbf{C}}$. Then, we have eigenvalue problem in the following form:

$$(\mathbf{A} - \lambda \mathbf{I}_{4\times 4})\,\boldsymbol{\xi} = \mathbf{0}, \tag{2.31}$$

where: λ is eigenvalue sought, $\mathbf{I}_{4\times 4}$ is identity matrix of appropriate dimension,

$$\mathbf{A} = \begin{bmatrix} \mathbf{0}_{2\times 2} & \mathbf{I}_{2\times 2} \\ -\mathbf{M}^{-1}\mathbf{K} & -\mathbf{M}^{-1}\widetilde{\mathbf{C}} \end{bmatrix} \tag{2.32}$$

is system matrix in state space representation obtained for the two-DOF system with locked joint ($u(t) = 1$), and $\boldsymbol{\xi}$ is eigenvector sought. For system matrix of the

(a) $\lambda^{(1)} = -43.3\mathrm{j}$ rad/s, $\phi_{\mathrm{c1}}^{(1)} \approx \phi_{\mathrm{c2}}^{(1)} = -0.612$ rad

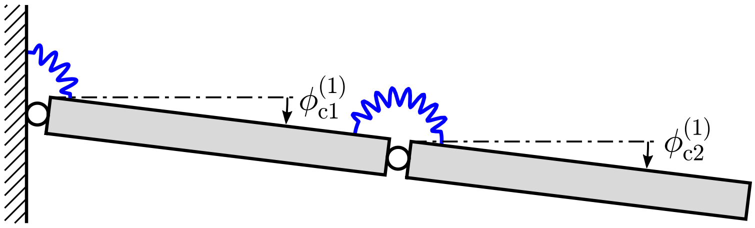

(b) $\lambda^{(2)} = 43.3\mathrm{j}$ rad/s, $\phi_{\mathrm{c1}}^{(2)} \approx \phi_{\mathrm{c2}}^{(2)} = -0.612$ rad

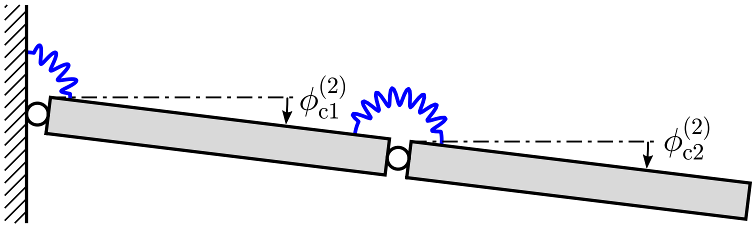

(c) $\lambda^{(3)} = -0.01$ rad/s, $\phi_{\mathrm{c1}}^{(3)} = -2.9 \cdot 10^{-8} \approx 0$ rad, $\phi_{\mathrm{c2}}^{(3)} = 1.732$ rad

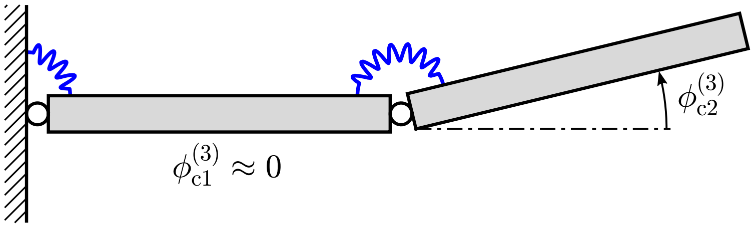

(d) $\lambda^{(4)} = -6.9 \cdot 10^{6}$ rad/s, $\phi_{\mathrm{c1}}^{(4)} = -1.157$ rad, $\phi_{\mathrm{c2}}^{(4)} = 2.546$ rad

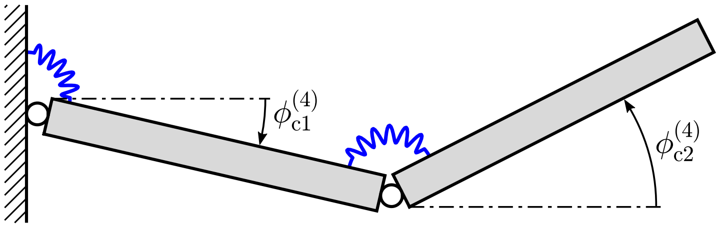

Figure 2.7: Eigenvalues and eigenvectors of the two-DOF system for currently locked joint with viscous model for $c_{\max} = 5 \cdot 10^5$ Nms/rad

structure as shown in Equation (2.32) $\boldsymbol{\xi}$ has the form:

$$\boldsymbol{\xi} = \begin{bmatrix} \boldsymbol{\phi}_{\mathrm{c}} \\ \lambda \boldsymbol{\phi}_{\mathrm{c}} \end{bmatrix}, \tag{2.33}$$

thus for simplicity $\boldsymbol{\phi}_{\mathrm{c}}$ also are called eigenvectors in the further part of the present subsection.

Eigenvalue problem in Equation (2.31) has four solutions. The eigenvalues (transfer function poles) depend on $c_{\max}$ (see: Eq. (2.30)). This dependence is shown in Figure 2.6. For $c_{\max} = 0$ the eigensolutions, as obviously, correspond to vibration modes of the unlocked system (Figure 2.3):

$$\text{for } c_{\max}=0: \qquad \begin{aligned} \lambda^{(1)} &= \lambda^{(2)*} = -\mathrm{j}\omega^{(1)}, & \boldsymbol{\phi}_{\mathrm{c}}^{(1)} &= \boldsymbol{\phi}_{\mathrm{c}}^{(2)*} = \boldsymbol{\phi}^{(1)}, \\ \lambda^{(3)} &= \lambda^{(4)*} = -\mathrm{j}\omega^{(2)}, & \boldsymbol{\phi}_{\mathrm{c}}^{(3)} &= \boldsymbol{\phi}_{\mathrm{c}}^{(4)*} = \boldsymbol{\phi}^{(2)}, \end{aligned} \tag{2.34}$$

where: $\mathrm{j}=\sqrt{-1}$ is imaginary unit and $(\cdot)^*$ denotes complex conjugate.

The increase of $c_{\max}$ results in shifting of the eigenvalues towards negative real numbers. Moreover, due to not-proportional damping provided by matrix $\widetilde{\mathbf{C}}$ eigenvectors contain elements relatively shifted in phase. In other words: $\arg \phi_{\mathrm{c}i}^{(m)} \neq \arg \phi_{\mathrm{c}j}^{(m)}$, $\boldsymbol{\phi}_{\mathrm{c}}^{(m)} \in \mathbb{C}^2$, $i \neq j$. For $c_{\max} > 39.97$ Nms/rad eigenvalues $\lambda^{(3)}$ and $\lambda^{(4)}$ related to the second vibration mode for the unlocked joint become real numbers. It is due to overdamping provided by the increasing $c_{\max}$ coefficient. Then the two-DOF system is represented by one vibration mode related to eigensolutions: $\left(\lambda^{(1)}, \boldsymbol{\phi}_{\mathrm{c}}^{(1)}\right)$, $\left(\lambda^{(2)}, \boldsymbol{\phi}_{\mathrm{c}}^{(2)}\right)$ and second order system represented by the chain of two first-order systems. These first-order systems are characterised by the poles $\lambda^{(3)}$, $\lambda^{(4)}$ and eigenvectors $\boldsymbol{\phi}_{\mathrm{c}}^{(3)}$, $\boldsymbol{\phi}_{\mathrm{c}}^{(4)}$, respectively.

When $c_{\max}$ becomes large and tends to the infinity eigenvalues $\lambda^{(1)}$ and $\lambda^{(2)}$ tend to complex counterpart of natural frequency of the two-DOF system with locked joint $\widetilde{\omega}$. These values are denoted by empty dots in the zoomed areas in Figure 2.6. $\lambda^{(3)}$ tends to zero representing constant solution reproducing rigidity of the locked joint and $\lambda^{(4)}$ tends to $-\infty$ representing short transient behaviour after locking of the joint. Then, also phase shifts between elements of vectors $\boldsymbol{\phi}_{\mathrm{c}}^{(m)}$ tend to zero (or $-\pi$ that occurs also for real eigenvectors) and, in result, they can be closely reproduced using only real numbers.

For selected $c_{\max} = 5 \cdot 10^5$ Nms/rad eigenvalues and eigenvectors as shown in Figure 2.7 are obtained. Imaginary part of elements of the first and second eigenvector is below 0.01 % of the corresponding real part, thus imaginary part is neglected. The third and fourth eigenvector are real due to damping damping introduced the system (see: Fig. 2.6). Eigenvectors are normalised with respect to mass matrix $\mathbf{M}$ but not orthogonal with respect to it.

The first two eigensolutions (Fig. 2.7a and b) correspond to periodic component of motion of the two-DOF system with the locked joint. The third eigenvector (Fig. 2.7c) corresponds to eigenvalue that can be considered as negligible in relation to remaining ones ($\lambda^{(3)}$ tends to zero when $c_{\max}$ tends to ∞). Thus, if $c_{\max}$ is sufficiently large, this pair of eigenvector and eigenvalue represents constant component of motion related to the relative angle Δq. Due to this eigensolution and the first two ones the structural motion can be represented similarly as shown in Figure 2.4. Small absolute value of $\lambda^{(3)}$ causes that Equations (2.27) and (2.28) are satisfied. The last eigenvector (Fig. 2.7d) is related to large negative eigenvalue. The corresponding time constant is then negligibly small and relates to quick braking of relative motion between structural DOFs when the joint is being locked. After this transient state the rotational coordinates satisfy the relaxed kinematic constraints.

It is worth to notice that elements of eigenvector $\boldsymbol{\phi}_{\mathrm{c}}^{(4)}$ are near-proportional to reciprocal elements of matrix $\mathbf{A}_{\mathrm{l}}$ (see: Eq. (2.10)). Negligible disproportions result from the fact that selected $c_{\max}$, despite of its large value, still is finite and dynamics of the system also is affected by stiffness k.

Modal coupling effect

Modal coupling effect resulting from the interaction between rotational DOFs through rotational controllable viscous damper is discussed below. Here, modal equation of motion is obtained by substitution of Equation (2.18) into Equation (2.30) and left-multiplying by $\boldsymbol{\Phi}^{\mathrm{T}}$ analogously to Equation (2.19). It also can be received by substitution of Equation (2.29) expressed in terms of modal coordinates (Eq. (2.18)) into Equation (2.20). Finally we receive

$$\begin{cases} \ddot{\boldsymbol{\eta}}(t) + u(t)\boldsymbol{\Gamma}\dot{\boldsymbol{\eta}}(t) + \boldsymbol{\Omega}^2\boldsymbol{\eta}(t) = \mathbf{0}, \qquad t \in \mathbb{R}_+ \\ \boldsymbol{\eta}(0) = \boldsymbol{\Phi}^{-1}\mathbf{q}_0 \\ \dot{\boldsymbol{\eta}}(0) = \boldsymbol{\Phi}^{-1}\dot{\mathbf{q}}_0 \end{cases}, \tag{2.35}$$

where:

$$\boldsymbol{\Gamma} = \begin{bmatrix} \gamma_{11} & \gamma_{12} \\ \gamma_{21} & \gamma_{22} \end{bmatrix} = \boldsymbol{\Phi}^{\mathrm{T}}\widetilde{\mathbf{C}}\boldsymbol{\Phi} = c_{\max}\begin{bmatrix} \Delta\phi^{(1)2} & \Delta\phi^{(1)}\Delta\phi^{(2)} \\ \Delta\phi^{(2)}\Delta\phi^{(1)} & \Delta\phi^{(2)2} \end{bmatrix} \tag{2.36}$$

is matrix representing modal coupling effect resulting from the joint lock. Similarly to matrices $\boldsymbol{\Theta}_1$ and $\boldsymbol{\Theta}_2$ in Equation (2.26) $\boldsymbol{\Gamma}$ also is not diagonal matrix.

It is worth to notice that Equation (2.35) has advantages similar to Equation (2.30) that are the avoidance of additional constant terms depending on the time instant of the joint locking and additional equation employing the law of conservation of angular momentum.

Comparison with the exact constraints

The ability of the viscous lockable joint model to reproduce dynamics of the considered reconfigurable system demonstrated in Figure 2.8. This figure shows free vibration of two-DOF system for initial condition $\mathbf{q}_0 = \begin{bmatrix} -2.89^\circ & -2.65^\circ \end{bmatrix}^{\mathrm{T}}$ and $\dot{\mathbf{q}}_0 = \mathbf{0}$. The lockable joint is locked at $t_{\mathrm{l}} = 0.1525$ s. Both initial conditions and time instant of the joint locking is selected aiming at demonstration of interesting dynamical effects. E_{p} and E_{k} in Figure 2.8d relate to the potential energy of the system that is accumulated in both springs and to total kinetic energy of the two-DOF system, respectively.

In all time histories shown in Figure 2.8 continuous lines denote behaviour of the two-DOF system for the locking effect reproduced with the viscous damper, whereas dashed lines relate to the system behaviour subjected to the exact kinematic constraint when the joint is locked. It is evident that the corresponding lines overlap

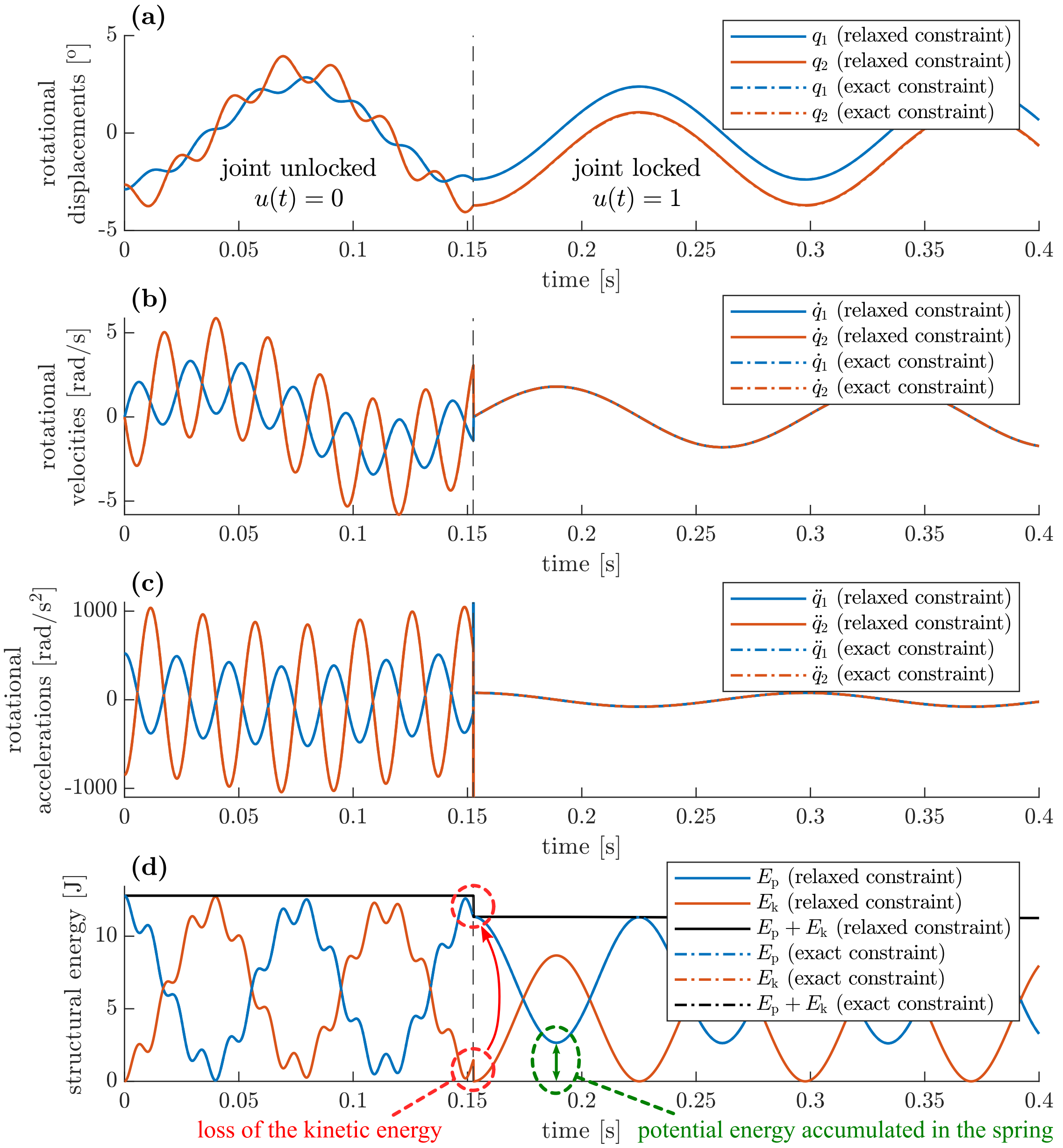

Figure 2.8: Time histories representing structural behaviour before and after reconfiguration via joint lock using relaxed constraint (viscous damper) and exact constraint: (a) rotational displacements, (b) rotational velocities, (c) rotational accelerations and (d) structural energy: potential energy E_p, kinetic energy E_k and total energy $E_\mathrm{p} + E_\mathrm{k}$

within entire time history of various types of structural response depicted in the figure.

Unconstrained motion of two DOFs of the considered system is clearly visible in Figure 2.8 until the joint is unlocked. When the joint is locked the two-DOF system behaves like single DOF oscillator with natural frequency $\widetilde{\omega}$ for exact constraint and $\widetilde{\omega}_\mathrm{c} = -\mathrm{Im}\lambda^{(1)} = \mathrm{Im}\lambda^{(2)} \approx \widetilde{\omega}$ for the relaxed constraint. Varying component of motion of the two-DOF system is represented by the first and second eigenvectors (Fig. 2.7a and b). Difference between rotational displacements of two DOFs is constant for exact kinematic constraint case, as shown in Figure 2.8a, whereas for relaxed constraint quasi-constant. Due to selected large $c_{\max}$ the drift of the rotational DOFs is negligibly small and slow. It relates to near-zero eigenvalue $\lambda^{(3)}$ and corresponding eigenvector $\boldsymbol{\phi}_{\mathrm{c}}^{(3)}$ (see: Fig 2.7c) describing behaviour of the two-DOF system with locked joint after locking.

Rotational velocities become common after the joint lock (Fig. 2.8b). For exact constraint they are exactly equal for $t > t_{\mathrm{l}}$ and have discontinuity at $t = t_{\mathrm{l}}$. Their value after the lock of the joint results from the law of conservation of angular momentum. For the relaxed constraint a quasi-common velocity is achieved in continuous manner but very quickly as related to eigenvalue $\lambda^{(4)}$ and eigenvector $\boldsymbol{\phi}_{\mathrm{c}}^{(4)}$ reproducing the inelastic collision.

Locking of the joint causes large acceleration peak (Fig. 2.8c). In the case of exact constraint it is infinite and can be represented by Dirac delta due to discontinuity of the rotational velocities at $t = t_{\mathrm{l}}$. In the case of relaxed constraint the acceleration peaks are finite but achieve large values which depend on selected $c_{\max}$. These values of the accelerations follows from the assumption that the joint is immediately locked. However, as it will be shown in Section 3.4 the proposed control locks the joints when relative rotational velocity of the DOFs involved in the joint is zero or have very small values resulting in lower level of accelerations for relaxed constraint. In MDOF structure such a sudden lock of the joint can induce higher-order vibration modes. Also depending on the engineering realisation of the lockable joint a short slip between the rotational DOFs is possible.

The two-DOF system is assumed undamped. Thus, before locking the total mechanical energy is constant, as shown in Figure 2.8d. After locking of the joint energy is also is constant for the exact constraint and quasi-constant for the relaxed constraint. It demonstrates that for sufficiently large $c_{\max}$ the viscous damper can reproduce locking effect and closely reproduce the exact kinematic constraint without adding any significant damping to the system. Moreover, it also reproduces the amount of kinetic energy lost in the inelastic collision as shown in red dashed ovals in Fig. 2.8d. This energy lost takes place when rotational velocities of DOFs involved in the joint are not equal during locking of the joint. When the joint is locked at nonzero Δq then the potential energy of value $\frac{1}{2}k\Delta q^2(t_{\mathrm{l}})$ is stored in the second spring. This energy is not dissipated in any way for the exact constraint, whereas for the relaxed constraint the dissipation is negligibly slow in relation to the vibration period and considered duration of the structural motion. After the joint unlock potential energy accumulated in the second spring will be released into vibration energy.

Behaviour of the structure described in terms of the unlocked modal basis $\{\boldsymbol{\phi}^{(1)}, \boldsymbol{\phi}^{(2)}\}$ both for exact and relaxed constraint is shown in Figure 2.9. It is evident that for both types of constraints the results are very close. Thus, only the influence of the locking effect on behaviour of the structure in the modal space is discussed.

It is evident that before locking of the joint vibration modes are not coupled.

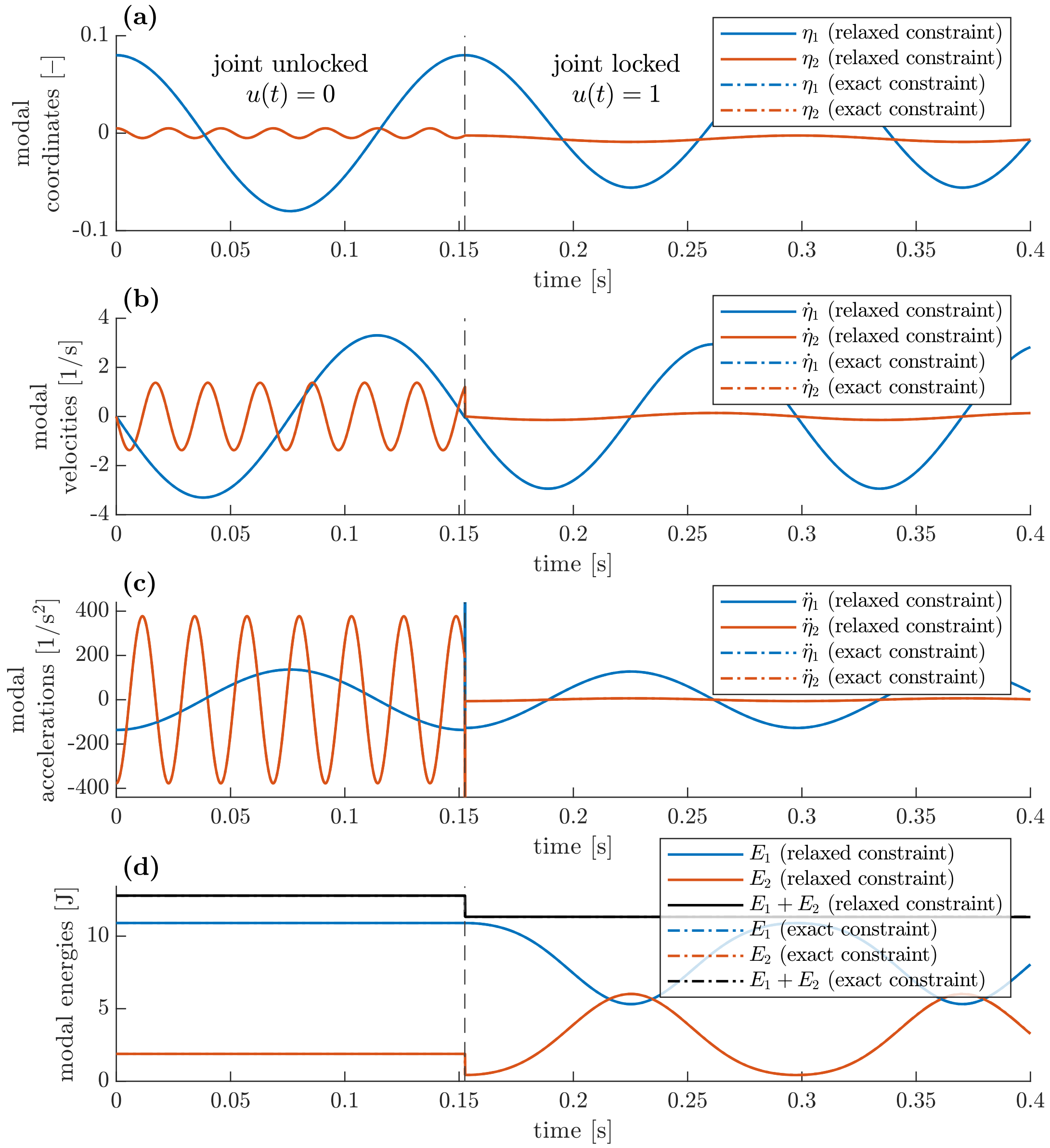

Figure 2.9: Time histories representing structural behaviour before and after reconfiguration via joint lock using relaxed constraint (viscous damper) and exact kinematic constraint in terms of unlocked modal basis: (a) modal coordinates, (b) modal velocities, (c) modal accelerations and (d) modal energies

They vibrate with their individual natural frequencies (see: Fig 2.9a-c) and mechanical energies associated with these modes, namely: modal energies, are constant (Fig. 2.9d). Modal energies in MDOF structure are defined in Equation (2.67) which also relates to the two-DOF system. When the joint is in the locked state modal coordinates, velocities and accelerations oscillate with the frequency equal to $\widetilde{\omega}$ (or $\widetilde{\omega}_c$ for relaxed constraint). It is due to the fact that superposition of the unlocked modes gives corresponding state variables of the two-DOF system (shown in Fig. 2.8a-c) also for the locked joint due to the modal coupling effect. After the joint lock both the equilibrium point and amplitudes of oscillation of modal coordinates are changed (Fig 2.9a).

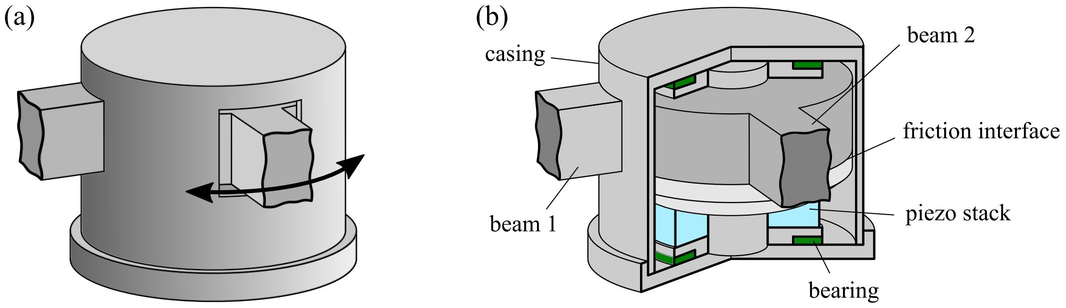

Figure 2.10: Example of realisation of the lockable-joint concept [145]: (a) outside view and (b) internal components arranged as proposed by Nitche and Gaul [106]

The joint lock causes sudden change of the modal velocities – mainly the second one (Fig. 2.9b). Second vibration mode $\boldsymbol{\phi}^{(2)}$ is highly correlated with the fourth eigenvector $\boldsymbol{\phi}_{\mathrm{c}}^{(4)}$ representing transient component structural velocities that is lost during lock as the consequence of the law of conservation of angular momentum (compare Figures 2.3b and 2.7d). Sudden change of the first modal velocity is negligible in this case. For exact constraint discontinuities are present at $t = t_1$.

After the joint lock system vibrates with one frequency the and second modal acceleration reduces its value. Peak modal accelerations during the joint lock are noticeable analogously to the rotational accelerations in configuration space (Fig. 2.8c).

Finally, the most important observation is that after the joint lock vibration energy is exchanged between unlocked vibration modes due to the modal coupling effect. When the joint is continuously locked the modal energy transfer is periodic and alternating. However, locking and unlocking the joint in suitable time instances allows for directed energy flow between vibration modes. This essential observation is a foundation for the proposed control strategy that is developed in Chapter 3. Before that the dynamics of MDOF structures is described in further sections in the current chapter.

2.2 Dynamics of reconfigurable MDOF structures

In this section implementation of the lockable joint concept allowing for reconfiguration of flexible MDOF structure is introduced and resulting dynamical effects are discussed. The effect of change of the modal basis, modal coupling effect known from the two-DOF system are extended for MDOF structures. Additionally, derivation of modal energy transfer rates between vibration modes are served. These considerations and derivations of modal energy transfer rates are a basis for development of the control strategy introduced in the next chapter. As opposed to the two-DOF system, here the energy is exchanged between relatively big number of unlocked vibration modes including not-monitored ones which are usually of higher-order. At the end of this section efficient method for numerical integration is suggested.

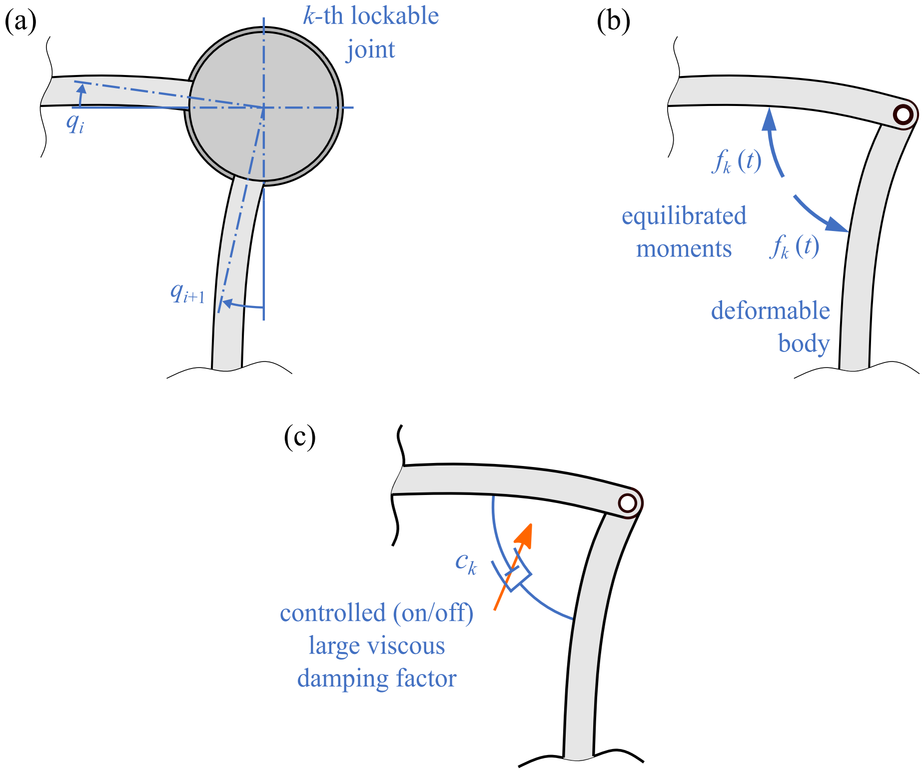

Figure 2.11: Mathematical description of the lockable joint [145]: (a) independent rotation of the connected flexible structural members, (b) pair of self-equilibrated moments involved in kth lockable joint and (c) simplified model employing controlled viscous damper

2.2.1 Lockable joints in MDOF structure

Similarly to the two-DOF system, the lockable joints installed in MDOF, depending on the control signal, can be dynamically locked and transmit bending moment between connected structural members or they can be dynamically unlocked working as a hinges. One of possible realisations of the concept of lockable joint is friction clutch with vary clamping force generated by a piezo stack as shown in Figure 2.10. The lockable joint is designed in such a way that clamping force is sufficiently large to lock relative rotation between friction surfaces. When the joint becomes unlocked, the friction surfaces are detached and free relative rotation between the connected structural members is possible. Such a semi-active joint allows for locking rotational motion between adjacent beams at arbitrary opening angle, as described in the previous section.

The locking effect, analogously to the previous section, imposes kinematic constraint on rotational DOFs involved in the joint which are shown in Figure 2.11a:

$$\dot{q}_i(t) - \dot{q}_{i+1}(t) = 0, \qquad t \in (t_{\mathrm{l}k}, t_{\mathrm{u}k}], \tag{2.37}$$

where in equations above $q_i(t)$ and $q_{i+1}(t)$ are rotational displacements at the time instant t involved in kth lockable joint and $(t_{\mathrm{l}k}, t_{\mathrm{u}k}]$ is time interval within the kth joint is locked.

The constraint in Equation (2.37) is kept by the action of pair of self-equilibrated moments on friction surfaces in the lockable joint that are equal to the transmitted bending moment $f_k(t)$ as it is schematically shown in Figure 2.11b. Generally, bending moment transmitted through the kth lockable joint can be nonlinear function of the kth control signal $u_k(t)$ and local state of the structure:

$$f_k(t) = f(u_k(t), q_i, q_{i+1}(t), \dot{q}_i(t), \dot{q}_{i+1}(t), t). \tag{2.38}$$

Selection of the function $f(u_k(t), q_i, q_{i+1}, \dot{q}_i, \dot{q}_{i+1}, t)$ plays important role in simulation of the vibration damping process if vibration energy is to be dissipated in the semi active-joints as e.g. in [108]. However, contrary to such approaches the friction surfaces do not move relatively in the proposed implementation when the lockable joint is fully locked, thus energy is dissipated not in the lockable joints but rather in the volume of the structure after shifting the energy into the higher-order vibration modes. It is assumed that the friction surfaces slides on each other only for negligibly short transient state and operate mainly in the two stable states: fully unlocked or fully locked. Moreover, the proposed control algorithm (Section 3.4) has natural property to locking the joints when the relative rotational velocity between DOFs involved in the joints is vary small, limiting the sliding effect. Thus, behaviour of the lockable joint in the MDOF structure can be simplified analogously to joint in the two-DOF system. Taking into account the reliability of the viscous model of the lockable joint and the ease of its use demonstrated Subsection 2.1.6 one can adopt this model for reproduction of the locking effect in reconfigurable MDOF structure and use for further derivations. Then, lockable joint is represented by controlled viscous damper as shown in Figure 2.11c. Equation (2.38) can be replaced with

$$f_k(t) = -u_k(t) c_{\max} \left(\dot{q}_i(t) - \dot{q}_{i+1}(t)\right), \qquad t > 0, \tag{2.39}$$

where: $u_k(t) = 0$ when the joint is unlocked and $u_k(t) = 1$ when the joint is locked and $c_{\max}$ is large viscous damping coefficient. Such model ensures that when the joint is locked constraint in Equation (2.37) is closely satisfied:

$$\dot{q}_i(t) \approx \dot{q}_{i+1}(t), \qquad t \in (t_{\mathrm{l}k}, t_{\mathrm{u}k}]. \tag{2.40}$$

Also it is worth to notice that this approach was validated experimentally with other control strategy in which lockable joints also work in only two stable states: fully locked and fully unlocked [12, 13], despite of the fact that in these works the viscous joint model was not investigated theoretically aiming at comparison with exact kinematic constraints.

2.2.2 Structure dynamics

Equation of motion of the MDOF structure

In this subsection mathematical description of behaviour of a flexible MDOF structure equipped with lockable joints is described. Small amplitudes of motion are assumed. Vibration of the MDOF is described by the equation of motion (2.41).

$$\begin{cases} \mathbf{M}\ddot{\mathbf{q}}(t) + \mathbf{C}\dot{\mathbf{q}}(t) + \mathbf{K}\mathbf{q}(t) = \mathbf{L}\mathbf{f}(t) + \mathbf{d}(t) \\ \mathbf{q}(0) = \mathbf{q}_0 \\ \dot{\mathbf{q}}(0) = \dot{\mathbf{q}}_0 \end{cases} \tag{2.41}$$

In the equation above $\mathbf{M}$, $\mathbf{C}$, $\mathbf{K} \in \mathbb{R}^{N_\mathrm{d} \times N_\mathrm{d}}$ are mass, material damping and stiffness matrices, respectively, $\mathbf{q}(t) \in \mathbb{R}^{N_\mathrm{d}}$ is displacement vector collecting both translational and rotational DOFs, N_d is the number of structural DOFs for all joints unlocked, vector

$$\mathbf{f}(t) = \begin{bmatrix} f_1(t) & f_2(t) & \cdots & f_{N_k}(t) \end{bmatrix}^\mathrm{T} \tag{2.42}$$

contains bending moments transmitted by N_k lockable joints, $\mathbf{L} = \begin{bmatrix} \mathbf{l}_1 & \mathbf{l}_2 & \cdots & \mathbf{l}_{N_k} \end{bmatrix} \in \mathbb{R}^{N_\mathrm{d} \times N_k}$ is transformation matrix collecting vectors $\mathbf{l}_k$ selecting DOFs involved in lockable joints in the way ensuring self-equilibrium of the moments acting on the adjacent structural members (Fig. 2.11b):

$$\mathbf{l}_k = \begin{bmatrix} 0 & \cdots & 0 & 1 & 0 & \cdots & 0 & -1 & 0 & \cdots & 0 \end{bmatrix}^\mathrm{T},$$

and $\mathbf{d}(t) \in \mathbb{R}^{N_\mathrm{d}}$ is vector of external disturbances. In this work only proportional material damping is considered.

Viscous joint model in MDOF structure

Substitution of the transmitted bending moments $f_k(t)$ in Equation (2.41) with the right hand side of Equation (2.39) results in the bilinear form of Equation of motion:

$$\mathbf{M}\ddot{\mathbf{q}}(t) + \left(\mathbf{C} + \sum_{k=1}^{N_k} u_k(t) \widetilde{\mathbf{C}}_k \right) \dot{\mathbf{q}}(t) + \mathbf{K}\mathbf{q}(t) = \mathbf{d}(t) \tag{2.43}$$

where matrix

$$\widetilde{\mathbf{C}}_k = c_\mathrm{max} \mathbf{l}_k \mathbf{l}_k^\mathrm{T}$$

couples rotational DOFs involved in the kth lockable joint in the sense of Equation (2.40) when corresponding control signal $u_k(t) = 1$.

Some important advantages of the use of matrices $\widetilde{\mathbf{C}}_k$ as above should be noticed. Such method of coupling is straightforward in implementation. It does not require additional equations as opposed to coupling the DOFs by imposing kinematic constraints as demonstrated in Section 2.1. Moreover, Equation (2.43) remains piece-wise linear, as the control signals are piece-wise fixed.

State-space representation of MDOF structural behaviour and its simulation

The last advantage indicated above is helpful in the simulation process. Since local truncation error is common problem in the integration of differential equations it can significantly slow down simulation due to the fact that higher-order vibration modes are also included into the simulation. In other words, model reduction with modal truncation is not used in the proposed control methodology because higher-order modes are responsible for energy dissipation mechanism. Thus, they require sufficiently small integration step if not appropriate solver is used. Piece-wise linear character of Equation (2.43) allows for using zero-order hold method to avoid this problem.

First, equation of motion is transformed into the state-space representation, as follows:

$$\begin{cases} \dot{\mathbf{x}}(t) = \mathbf{A}(\mathbf{u}(t))\mathbf{x}(t) + \mathbf{B}\mathbf{d}(t) \\ \mathbf{y}(t) = \mathbf{C}_{\mathrm{y}}\mathbf{x}(t) + \mathbf{D}\mathbf{u}(t) + \mathbf{v}(t) \end{cases}, \tag{2.44}$$

where:

$$\mathbf{x}(t) = \begin{bmatrix} \mathbf{q}(t) \\ \dot{\mathbf{q}}(t) \end{bmatrix}, \quad \mathbf{A}(\mathbf{u}(t)) = \begin{bmatrix} \mathbf{0} & \mathbf{I} \\ -\mathbf{M}^{-1}\mathbf{K} & -\mathbf{M}^{-1}\left(\mathbf{C} + \sum_{k=1}^{N_k} u_k(t)\widetilde{\mathbf{C}}_k\right) \end{bmatrix},$$

$$\mathbf{u}(t) = \begin{bmatrix} u_1(t) & u_2(t) & \cdots & u_{N_k}(t) \end{bmatrix}^{\mathrm{T}} \in \{0,1\}^{N_k}, \quad \mathbf{B} = \begin{bmatrix} \mathbf{0} \\ \mathbf{M}^{-1} \end{bmatrix},$$

$\mathbf{I}$ is the identity matrix of appropriate dimension and $\mathbf{v}(t)$ is vector of the measurement noise. The structure of matrices $\mathbf{C}_{\mathrm{y}}$, $\mathbf{D}$ and vector $\mathbf{v}(t)$ is discussed in Chapter 3. For particular piece-wise constant control signals $\mathbf{u}$ within a time interval of length Δt the state-space equation can be replaced with its discrete counterpart:

$$\mathbf{x}_{\mathrm{d}}[l+1] = \mathbf{A}_{\mathrm{d}}^{\mathbf{u}}\mathbf{x}_{\mathrm{d}}[l] + \mathbf{B}_{\mathrm{d}}^{\mathbf{u}}\mathbf{d}_{\mathrm{d}}[l], \tag{2.45}$$

where:

$$\mathbf{A}_{\mathrm{d}}^{\mathbf{u}} = \mathrm{e}^{\mathbf{A}(\mathbf{u})\Delta t}, \quad \mathbf{B}_{\mathrm{d}}^{\mathbf{u}} = \mathbf{A}^{-1}(\mathbf{u})\left(\mathbf{A}_{\mathrm{d}}^{\mathbf{u}} - \mathbf{I}\right)\mathbf{B}, \quad \mathbf{u} = \mathrm{const\ in}\ \left[l\Delta t, (l+1)\Delta t\right),$$

and e is the Euler's number. In the case of free vibration ($\mathbf{d} \equiv \mathbf{0}$) $\mathbf{x}_{\mathrm{d}}[l+1]$ is exact solution of differential Equation (2.44) for initial condition taken as $\mathbf{x}_{\mathrm{d}}[l]$. Hence, the local truncation error is avoided even for time-steps Δt longer than period of any higher-order vibration mode. In the case of forced vibration ($\mathbf{d} \neq \mathbf{0}$) the time step must be appropriately smaller than period of the highest harmonic component of the excitation. To avoid calculation of matrices $\mathbf{A}_{\mathrm{d}}^{\mathbf{u}}$ and $\mathbf{B}_{\mathrm{d}}^{\mathbf{u}}$ at each time step they can be computed for each possible control signal vector $\mathbf{u}$ before simulation process and later appropriately selected for substitution in Equation (2.45) depending on the current control signals u_k indicated by the controller. If excitation $\mathbf{d}$ does not contain high-frequency components then the use of the Equation (2.45) provides time-effective and accurate simulation.

2.2.3 Unlocked and locked modal basis, modal coupling effect

In this subsection an insight into structural dynamics is provided by description of the influence of the locking effect on the modal basis. Modal coupling effect in MDOF structure caused by the action of lockable joints is introduced. It is used to describe energy transfer between the unlocked vibration modes and derive the control law in the next chapter.

All joints in the unlocked state

Vibration modes obtained for all joints in the unlocked state are referred as "unlocked vibration modes". Eigenvalue problem formulated for all joints unlocked is formulated as follows:

$$\left(\mathbf{K} - \omega^2\mathbf{M}\right)\boldsymbol{\phi} = \mathbf{0}. \tag{2.46}$$

The solution of the eigenvalue problem are unlocked natural frequencies $\omega^{(m)}$ and unlocked mode shapes $\boldsymbol{\phi}^{(m)} \in \mathbb{R}^{N_\mathrm{d}}$, $m = 1, 2, \ldots N_\mathrm{d}$ denotes index of unlocked vibration mode. N_d also is equal to the maximal number of DOFs (when all joints are unlocked). Motion of the structure can be expressed in modal coordinates $\boldsymbol{\eta}(t) \in \mathbb{R}^{N_\mathrm{d}}$ by the use of the transformation below

$$\mathbf{q}(t) = \boldsymbol{\Phi}\boldsymbol{\eta}(t). \tag{2.47}$$

In the equation above matrix $\boldsymbol{\Phi} = \begin{bmatrix}\boldsymbol{\phi}^{(1)} & \boldsymbol{\phi}^{(2)} & \cdots & \boldsymbol{\phi}^{(N_\mathrm{d})}\end{bmatrix}$ collects unlocked mode shapes normalised with respect to the mass matrix, i.e.

$$\boldsymbol{\Phi}^\mathrm{T}\mathbf{M}\boldsymbol{\Phi} = \mathbf{I}. \tag{2.48}$$

Locking effect and locked vibration modes

Here, behaviour of the MDOF structure for any joint locked is investigated. Rotational velocities of beam ends coupled by the joint fulfill the law of conservation of angular momentum. However, having adopted viscous joint model it is not required using this law to calculate the common rotational velocity of the DOFs invlolved in the joint, as discussed in Section 2.1. Hence, mainly the influence of the locking effect on structural modal parameters is discussed below.

First, to understand the changes in structural dynamics the exact kinematic constraint in Eq. (2.37) is recalled for any combination of currently locked joints:

$$\begin{aligned} \mathbf{q}(t) &= \mathbf{B}_0\widetilde{\mathbf{q}}(t) + \mathbf{B}_1\boldsymbol{\Delta}\mathbf{q}, \\ \dot{\mathbf{q}}(t) &= \mathbf{B}_0\dot{\widetilde{\mathbf{q}}}(t), \\ \ddot{\mathbf{q}}(t) &= \mathbf{B}_0\ddot{\widetilde{\mathbf{q}}}(t), \qquad\qquad t \in (t_\mathrm{l}, t_\mathrm{u}]. \end{aligned} \tag{2.49}$$

In equation above t_l and t_u are time instants of locking and unlocking of any joint, respectively, i.e. they limit the time interval within which vector $\mathbf{u}(t)$ is constant. $\mathbf{B}_0 \in \{0,1\}^{N_\mathrm{d}\times(N_\mathrm{d}-N_\mathrm{l})}$, where N_l is no. of currently locked joints, is transformation matrix obtained from identity matrix, where each two columns related to rotational DOFs involved in currently locked joint are summed and putted replacing one of them and remaining one is removed, e.g. for single locked joint coupling DOFs i and j this matrix has the following form:

$$\mathbf{B}_0 = \begin{bmatrix} \mathbf{s}_1 & \mathbf{s}_2 & \cdots & \mathbf{s}_{i-1} & \mathbf{s}_i + \mathbf{s}_j & \mathbf{s}_{i+1} & \cdots & \mathbf{s}_{j-1} & \mathbf{s}_{j+1} & \cdots & \mathbf{s}_{N_\mathrm{d}} \end{bmatrix}, \tag{2.50}$$

where $\mathbf{s}_i \in \{0,1\}^{N_\mathrm{d}}$ is Boolean vector indicating ith DOF. This matrix depends on the control signal vector $\mathbf{u}$, including the change of no. of its columns. Matrix $\mathbf{B}_1 \in \{0,1\}^{N_\mathrm{d}\times N_\mathrm{l}}$ contains columns removed from matrix $\mathbf{B}_0$ (for the example above $\mathbf{B}_1 = \mathbf{s}_j$) and vector $\boldsymbol{\Delta}\mathbf{q}$ collects terms describing differences of rotational displacements of DOFs involved in each kth of currently locked joint:

$$\Delta q_k = \mathbf{l}_k^\mathrm{T}\mathbf{q}(t_\mathrm{l}) = \text{const in } (t_\mathrm{l}, t_\mathrm{u}]. \tag{2.51}$$

Matrices $\mathbf{B}_0$ and $\mathbf{B}_1$ in Equation (2.4) also fulfill the above definitions.

By substitution of Equation (2.49) into Equation (2.41) and left-multiplying by $\mathbf{B}_0^\mathrm{T}$ we receive equation below. For better clarity the matrix describing material damping and the initial conditions are omitted.

$$\underbrace{\mathbf{B}_0^\mathrm{T}\mathbf{M}\mathbf{B}_0}_{\widetilde{\mathbf{M}}_{00}}\ddot{\widetilde{\mathbf{q}}}(t) + \underbrace{\mathbf{B}_0^\mathrm{T}\mathbf{K}\mathbf{B}_0}_{\widetilde{\mathbf{K}}_{00}}\widetilde{\mathbf{q}}(t) + \underbrace{\mathbf{B}_0^\mathrm{T}\mathbf{K}\mathbf{B}_1}_{\widetilde{\mathbf{K}}_{01}}\boldsymbol{\Delta}\mathbf{q} = \underbrace{\mathbf{B}_0^\mathrm{T}\mathbf{L}\mathbf{f}(t)}_{\mathbf{0}} + \underbrace{\mathbf{B}_0^\mathrm{T}\mathbf{d}(t)}_{\widetilde{\mathbf{d}}(t)} \tag{2.52}$$

In the equation above $\widetilde{\mathbf{M}}_{00}$, $\widetilde{\mathbf{K}}_{00} \in \mathbb{R}^{(N_\mathrm{d}-N_\mathrm{l})\times(N_\mathrm{d}-N_\mathrm{l})}$ are mass and stiffness matrices, respectively, representing dynamical properties of the structure with locked particular joints at $\Delta q_k = 0$, whereas matrix $\widetilde{\mathbf{K}}_{01} \in \mathbb{R}^{(N_\mathrm{d}-N_\mathrm{l})\times N_\mathrm{l}}$ is responsible for piece-wise static forces provided by locking of the joints at nonzero Δq_k. As opposed to the two-DOF system investigated in Section 2.1, here this matrix usually is nonzero. It means that locking of any kth joint at nonzero Δq_k causes deformation in the entire structure and changes equilibrium point of the system also in the configuration space reduced to the minimal number of DOFs. This equilibrium point can be calculated by substituting $\ddot{\widetilde{\mathbf{q}}}(t) = \mathbf{0}$ and $\widetilde{\mathbf{d}}(t) = \mathbf{0}$ in Equation (2.52) as:

$$\widetilde{\mathbf{q}}_\mathrm{l} = -\widetilde{\mathbf{K}}_{00}^{-1}\widetilde{\mathbf{K}}_{01}\boldsymbol{\Delta}\mathbf{q}. \tag{2.53}$$

After substitution of

$$\widetilde{\mathbf{q}}(t) = \widetilde{\mathbf{q}}_{\mathrm{eq}}(t) + \widetilde{\mathbf{q}}_{\mathrm{l}}, \tag{2.54}$$

where $\widetilde{\mathbf{q}}_{\mathrm{eq}}(t)$ is structural displacement with respect to the equilibrium point, into Equation (2.52) the constant term disappears. Then, free vibration with respect to the equilibrium point $\widetilde{\mathbf{q}}_{\mathrm{l}}$ can be investigated using eigenvalue problem:

$$\left(\widetilde{\mathbf{K}}_{00} - \widetilde{\omega}_0^2 \widetilde{\mathbf{M}}_{00}\right) \widetilde{\boldsymbol{\phi}}_0 = \mathbf{0}. \tag{2.55}$$

The above eigenvalue problem is the same as one obtained for the structure with particular joints locked at $\Delta q_k = 0$. Thus, modes describing vibration for $\Delta q_k = 0$ also are the same.

Finally, for the subset of currently locked joints structural displacement depends on modal parameters as follows:

$$\mathbf{q}(t) = \mathbf{B}_0 \left(\widetilde{\boldsymbol{\Phi}}_0 \widetilde{\boldsymbol{\eta}}_0(t) + \widetilde{\mathbf{q}}_{\mathrm{l}}\right) + \mathbf{B}_1 \boldsymbol{\Delta}\mathbf{q}, \qquad t \in (t_{\mathrm{l}}, t_{\mathrm{u}}], \tag{2.56}$$

where: $\widetilde{\boldsymbol{\Phi}}_0 \in \mathbb{R}^{(N_{\mathrm{d}}-N_{\mathrm{l}})\times(N_{\mathrm{d}}-N_{\mathrm{l}})}$ is modal matrix collecting all mode shapes obtained by solving eigenvalue problem in Equation (2.55) for particular subset of joints that are currently locked and $\widetilde{\boldsymbol{\eta}}_0$ is corresponding vector of the modal coordinates. The equation above allows for understanding that analogously to the two-DOF system the modal basis formed by $\widetilde{\boldsymbol{\Phi}}_0$ is insufficient to describe full state of the structure. Information about the opening angles between beam ends coupled by the currently locked joints contained by $\boldsymbol{\Delta}\mathbf{q}$ is required. Moreover, as opposed to the two-DOF system, in this case it affects also equilibrium point $\widetilde{\mathbf{q}}_{\mathrm{l}}$ related to the structural deformation described in the reduced configuration space (whereas for the two-DOF system changed equilibrium is visible in the configuration space with full dimension only).

Corresponding vibration modes obtained from eigenvalue problem in Equation (2.55) differ for different joints selected to be locked:

$$\mathbf{B}_0 \widetilde{\boldsymbol{\phi}}_0^{(m)}\Big|_{\mathbf{u}=\mathbf{u}_1} \neq \mathbf{B}_0 \widetilde{\boldsymbol{\phi}}_0^{(m)}\Big|_{\mathbf{u}=\mathbf{u}_2} \quad \text{if} \quad \mathbf{u}_1 \neq \mathbf{u}_2, \tag{2.57}$$

where mode shapes obtained for both combinations of the locked joints (indicated by the control signals) are referred as “corresponding” in the sense that they are most correlated, e.g. accordingly to the highest modal assurance criterion (MAC). Moreover, mode shape obtained for any combination of the currently locked joints is different also from the corresponding unlocked mode shape:

$$\mathbf{B}_0 \widetilde{\boldsymbol{\phi}}_0^{(m)} \neq \boldsymbol{\phi}^{(m)}. \tag{2.58}$$

The exception is only if joints are placed in such a way that they do not transmit any bending moments in mth mode shape even in the locked state.

Vibration modes obtained only for subset of joints that are locked ($N_\mathrm{l} < N_k$) are not further used in this thesis because they are insufficient to describe the full state of the structure. However, vibration modes obtained for all joints in the locked state ($N_\mathrm{l} = N_k$) are further referred as “locked vibration modes” and are used to indicate optimal locations of the lockable joints (Section 3.3). The locked vibration modes and other corresponding quantities related to all joints in the locked state are denoted by symbols with omitted subscript “0”. Then, the eigenvalue problem is:

$$\left(\widetilde{\mathbf{K}} - \widetilde{\omega}^2\widetilde{\mathbf{M}}\right)\widetilde{\boldsymbol{\phi}} = \mathbf{0}, \tag{2.59}$$

where:

$$\widetilde{\mathbf{K}} = \mathbf{B}^\mathrm{T}\mathbf{K}\mathbf{B}, \qquad \widetilde{\mathbf{M}} = \mathbf{B}^\mathrm{T}\mathbf{M}\mathbf{B},$$

$\widetilde{\omega}$ and $\widetilde{\boldsymbol{\phi}} \in \mathbb{R}^{N_\mathrm{d}-N_k}$ are mth locked natural frequency and mth locked mode shape, respectively, and $\mathbf{B} \in \{0,1\}^{N_\mathrm{d}\times(N_\mathrm{d}-N_k)}$ is defined as $\mathbf{B}_0$ for all joints locked.

Similarly to the two-DOF system the vibration of the MDOF structure always can be described in the unlocked modal basis due its dimension equal to the highest dimension of the configuration space:

$$\boldsymbol{\eta}(t) = \boldsymbol{\Phi}^{-1}\left(\mathbf{B}_0\left(\widetilde{\boldsymbol{\Phi}}_0\widetilde{\boldsymbol{\eta}}_0(t) + \widetilde{\mathbf{q}}_\mathrm{l}\right) + \mathbf{B}_1\boldsymbol{\Delta}\mathbf{q}\right), \qquad t \in (t_\mathrm{l}, t_\mathrm{u}]. \tag{2.60}$$

Then time histories of modal coordinates in the unlocked modal basis $\boldsymbol{\eta}(t)$ are affected by the modal coupling effect which changes not only equilibrium point, as illustrated in Figure 2.1, but also frequencies which in this case are related to the vibration modes obtained for current combination of the locked joints. Modal coupling effect and description of structural behaviour in the unlocked modal basis are discussed below.

Modal coupling effect in the unlocked modal basis

Based on the considerations above and ones in Section 2.1 vibration modes calculated for all joints unlocked are used because of two reasons. The first is appropriate dimension of the eigenvector basis, equal to the maximal dimension of the configuration space. The second reason is the ease of mathematical description of the modal coupling effect allowing further derivation of equations of the modal energy transfer and development of the control algorithm.

Description of structural motion in terms of the unlocked modal basis derived below is similar to fast nonlinear analysis (FNA) method described by Wilson [144]. FNA was intended for reduce the model order and quick simulation of nonlinear structures, where the nonlinearity is provided locally and only by a finite number of structural nonlinear members (whereas the remaining structure is linear itself). Structure described by Equation (2.43) fulfills this requirement, since the number of summed bilinear terms is finite (N_k) and they represent locking effect that couples usually only two rotational DOFs. However, contrary to approach adopted in this thesis FNA usually employs basis formed from load-dependent Ritz vectors instead of the structural mode shapes. The forces provided by nonlinear members can be treated as external loads acting on a linear structure (similarly to Eq. (2.41) in this thesis). In this situation smaller number of load-dependent Ritz vectors is needed for suitable reconstruction of structural behaviour as opposed to the wider spectrum of linear vibration modes. However, the load-dependent Ritz vectors do not provide sufficient information about structural dynamics, e.g. resonance frequencies, modal damping factors. Hence, unlocked modal basis is further employed in this thesis for the investigation of the modal coupling effect, modal energy transfer phenomenon and design of the controller. Although the load-dependent Ritz vectors are not used in this thesis they can be adopted for simulation of large-scale structure equipped with lockable joints if reduction of the structural model order is required, however this is independent from the designing of the controller.

By substituting of transformation shown in Equation (2.47) into Equation (2.43) and its left-multiplying by $\mathbf{\Phi}^{\mathrm{T}}$ the modal form of equation of motion is received as shown below.

$$\ddot{\boldsymbol{\eta}}(t) + \left(2\mathbf{\Omega}\mathbf{Z} + \sum_{k=1}^{N_k} u_k(t)\mathbf{\Gamma}_k\right)\dot{\boldsymbol{\eta}}(t) + \mathbf{\Omega}^2\boldsymbol{\eta}(t) = \mathbf{\Phi}^{\mathrm{T}}\mathbf{d}(t) \tag{2.61}$$

In Equation (2.61) $\mathbf{Z} = \operatorname{diag}\left(\begin{bmatrix}\zeta^{(1)} & \zeta^{(m)} & \cdots & \zeta^{(N_\mathrm{d})}\end{bmatrix}^{\mathrm{T}}\right)$ is diagonal damping matrix, $\mathbf{\Omega} = \operatorname{diag}\left(\begin{bmatrix}\omega^{(1)} & \omega^{(m)} & \cdots & \omega^{(N_\mathrm{d})}\end{bmatrix}^{\mathrm{T}}\right)$ is diagonal matrix containing the unlocked natural frequencies and

$$\mathbf{\Gamma}_k = \mathbf{\Phi}^{\mathrm{T}}\widetilde{\mathbf{C}}_k\mathbf{\Phi} \tag{2.62}$$

is modal coupling matrix that is usually full matrix as opposed to $\mathbf{Z}$ and $\mathbf{\Omega}$, thus the lock of any joint causes coupling between the unlocked vibration modes. Equation (2.61) can be written in the index notation:

$$\ddot{\eta}_m(t) + 2\zeta^{(m)}\omega^{(m)}\dot{\eta}_m(t) + \sum_{k=1}^{N_k}\sum_{n=1}^{N_\mathrm{d}} u_k(t)\gamma_{kmn}\dot{\eta}_n(t) + \omega^{(m)2}\eta(t) = \sum_{i=1}^{N_\mathrm{d}} \phi_i^{(m)} d_i(t). \tag{2.63}$$

Element γ_{kmn} of the coupling matrix $\mathbf{\Gamma}_k$ provides coupling between individual modes m and n through the kth lockable joint.

By rewriting γ_{kmn} we receive

$$\gamma_{kmn} = \boldsymbol{\phi}^{(m)\mathrm{T}}\widetilde{\mathbf{C}}_k\boldsymbol{\phi}^{(n)} = c_{\max}\boldsymbol{\phi}^{(m)\mathrm{T}}\mathbf{l}_k\mathbf{l}_k^{\mathrm{T}}\boldsymbol{\phi}^{(n)} = c_{\max}\Delta\phi_k^{(m)}\Delta\phi_k^{(n)}, \tag{2.64}$$

where $\Delta\phi_k^{(m)}$ is the difference of rotations of mth unlocked mode shape at the DOFs involved in kth lockable joint when unlocked. It is evident that values of opening angles of unlocked mode shapes at the location of lockable joint provide information about degree of coupling of these modes.

Despite of the presence of squared unlocked frequencies collected $\boldsymbol{\Omega}^2$ in Equation (2.61) the structure vibrates with different frequencies if any joint is in the locked state. It is caused by the modal coupling term which is result of appearing of the pair of self-equilibrated moments representing the locking effect (see: Fig. 2.11b). These frequencies will be very similar (the same if c_max tends to the infinity) as frequencies obtained from eigenvalue equation (2.55) as demonstrated in Equation (2.60), where on the right hand side of the equation only $\widetilde{\boldsymbol{\eta}}_0$ depends on time. After moving the modal coupling term in Equation (2.63) into its right hand side we obtain modal coupling term expressed in terms of bending moments transmitted by the lockable joints (analogously to Eq. (2.20) for the two-DOF system):

$$\begin{aligned}&-\sum_{k=1}^{N_k}\sum_{n=1}^{N_\mathrm{d}} u_k(t)\gamma_{kmn}\dot{\eta}_n(t) = -\sum_{k=1}^{N_k} u_k(t)\boldsymbol{\gamma}_k^{(m)}\dot{\boldsymbol{\eta}}(t) = \\ &= -\sum_{k=1}^{N_k} u_k(t)\boldsymbol{\phi}^{(m)\mathrm{T}}\widetilde{\mathbf{C}}_k \underbrace{\boldsymbol{\Phi}\dot{\boldsymbol{\eta}}(t)}_{\dot{\mathbf{q}}(t)} = -\sum_{k=1}^{N_k}\underbrace{\boldsymbol{\phi}^{(m)\mathrm{T}}\mathbf{l}_k}_{\Delta\phi_k^{(m)}}\underbrace{u_k(t)c_\mathrm{max}\mathbf{l}_k^\mathrm{T}\dot{\mathbf{q}}(t)}_{-f_k(t)} = \\ &= \sum_{k=1}^{N_k}\Delta\phi_k^{(m)} f_k(t),\end{aligned} \tag{2.65}$$

where $\boldsymbol{\gamma}_k^{(m)}$ is mth row of matrix $\boldsymbol{\Gamma}_k$. It is evident that resultant modal force acting on mth mode can be expressed as sum of forces derived from all unlocked vibration modes (including the mth one) in all lockable joints or sum of modal forces derived directly from pair of self-equilibrated moments in all joints.

Equation (2.61) can be rewritten as shown in Equation (2.66).

$$\begin{aligned}&\begin{bmatrix}\ddot{\boldsymbol{\eta}}_\mathrm{M}(t)\\ \ddot{\boldsymbol{\eta}}_\mathrm{H}(t)\end{bmatrix} + \left(2\begin{bmatrix}\boldsymbol{\Omega}_\mathrm{M}\mathbf{Z}_\mathrm{M} & \mathbf{0}\\ \mathbf{0} & \boldsymbol{\Omega}_\mathrm{H}\mathbf{Z}_\mathrm{H}\end{bmatrix} + \sum_{k=1}^{N_k} u_k(t)\begin{bmatrix}\boldsymbol{\Gamma}_{\mathrm{MM}k} & \boldsymbol{\Gamma}_{\mathrm{MH}k}\\ \boldsymbol{\Gamma}_{\mathrm{HM}k} & \boldsymbol{\Gamma}_{\mathrm{HH}k}\end{bmatrix}\right)\begin{bmatrix}\dot{\boldsymbol{\eta}}_\mathrm{M}(t)\\ \dot{\boldsymbol{\eta}}_\mathrm{H}(t)\end{bmatrix} + \\ &\quad + \begin{bmatrix}\boldsymbol{\Omega}_\mathrm{M}^2 & \mathbf{0}\\ \mathbf{0} & \boldsymbol{\Omega}_\mathrm{H}^2\end{bmatrix}\begin{bmatrix}\boldsymbol{\eta}_\mathrm{M}(t)\\ \boldsymbol{\eta}_\mathrm{H}(t)\end{bmatrix} = \begin{bmatrix}\boldsymbol{\Phi}_\mathrm{M} & \boldsymbol{\Phi}_\mathrm{H}\end{bmatrix}^\mathrm{T}\mathbf{d}(t)\end{aligned} \tag{2.66}$$

The first row, denoted by subscript M, is related to monitored unlocked vibration modes, whereas the second row is related to higher-order unlocked vibration modes and is denoted by subscript H. It is evident that matrix blocks $\boldsymbol{\Gamma}_{\mathrm{HM}k}$ and $\boldsymbol{\Gamma}_{\mathrm{MH}k}$ are responsible for transferring the mechanical energy from monitored unlocked vibration modes to the higher-order ones and vice versa, respectively. In the case of vibration attenuation application of the proposed control methodology the transfer of the mechanical energy to the higher-order unlocked vibration modes is desired. However, in energy harvesting applications, where energy is to be transferred from the set of monitored modes to the particular one preselected within this set, transfer of the mechanical energy to the higher-order unlocked modes can be considered as the control spillover. It is due to the fact that this energy cannot be transferred back after the first joint unlock. After the joint unlock the energy accumulated in higher-order unlocked vibration modes is released in their free vibration and quickly dissipated in material damping. Moreover, the equipment limitations could be additional difficulties for transferring energy back from the higher-order unlocked vibration modes (modal velocities $\dot{\boldsymbol{\eta}}_\mathrm{H}(t)$ cannot be measured accurately). More details are provided in Section 3.2.

2.2.4 Energy transfer between vibration modes

Equations describing transfer of the mechanical energy between unlocked vibration modes caused by the modal coupling, namely: modal energy transfer, are required to understand the proposed methodology and design the controller that is explicitly based on these equations.

Modal energies and modal energy transfer

First, total mechanical energy of the structure $E(t)$ is decomposed into the energies $E_m(t)$ associated with particular unlocked vibration modes, namely: modal energies, as shown below.

$$\begin{aligned} E(t) &= \frac{1}{2}\dot{\mathbf{q}}^\mathrm{T}(t)\mathbf{M}\dot{\mathbf{q}}(t) + \frac{1}{2}\mathbf{q}^\mathrm{T}(t)\mathbf{K}\mathbf{q}(t) = \\ &= \frac{1}{2}\dot{\boldsymbol{\eta}}^\mathrm{T}(t)\underbrace{\boldsymbol{\Phi}^\mathrm{T}\mathbf{M}\boldsymbol{\Phi}}_{\mathbf{I}}\dot{\boldsymbol{\eta}}(t) + \frac{1}{2}\boldsymbol{\eta}^\mathrm{T}(t)\underbrace{\boldsymbol{\Phi}^\mathrm{T}\mathbf{K}\boldsymbol{\Phi}}_{\boldsymbol{\Omega}^2}\boldsymbol{\eta}(t) = \\ &= \sum_{m=1}^{N_\mathrm{d}} \frac{1}{2}\left(\dot{\eta}_m^2(t) + \omega^{(m)2}\eta_m^2(t)\right) = \sum_{m=1}^{N_\mathrm{d}} E_m(t). \end{aligned} \tag{2.67}$$

It is shown in this subsection that in free vibration any particular energy $E_m(t)$ can increase only at the expense of other modal energies when modal coupling is provided.

The derivative of mth modal energy is calculated:

$$\dot{E}_m(t) = \dot{\eta}_m(t)\left(\ddot{\eta}_m(t) + \omega^{(m)2}\eta_m(t)\right). \tag{2.68}$$

After substitution of Equation (2.63) into Equation (2.68) we have:

$$\begin{aligned} \dot{E}_m(t) &= \dot{\eta}_m(t)\left(-\sum_{k=1}^{N_k}\sum_{n=1}^{N_\mathrm{d}} u_k(t)\gamma_{kmn}\dot{\eta}_n(t) - 2\zeta^{(m)}\omega^{(m)}\dot{\eta}_m(t) + \sum_{r=1}^{N_\mathrm{d}}\phi_i^{(m)}d_i(t)\right) = \\ &= \underbrace{-\dot{\eta}_m(t)\sum_{k=1}^{N_k}\sum_{n=1}^{N_\mathrm{d}} u_k(t)\gamma_{kmn}\dot{\eta}_n(t)}_{\dot{W}_m(t)}\underbrace{-2\zeta^{(m)}\omega^{(m)}\dot{\eta}_m^2(t)}_{\dot{E}_m^\mathrm{loss}(t)} + \underbrace{\dot{\eta}_m(t)\sum_{r=1}^{N_\mathrm{d}}\phi_i^{(m)}d_i(t)}_{\dot{W}_m^\mathrm{ext}(t)}. \end{aligned} \tag{2.69}$$

In Equation (2.69) $W_m(t)$ is energy transferred to mth unlocked vibration mode from remaining ones – sign of this quantity indicates direction of the energy flow, $E_m^{\mathrm{loss}}(t)$ is energy dissipated in the material damping corresponding to mth unlocked mode and $W_m^{\mathrm{ext}}(t)$ is work done by external excitations on mth modal coordinate. Derivatives of these terms in Equation (2.69) are expressed in Watts. $\dot{W}_m(t)$ is further called modal energy transfer rate.

By taking into account derivations in Equation (2.65) the following calculations can be done on the modal energy transfer rate from Equation (2.69):

$$\begin{aligned}\dot{W}_m(t) &= -\dot{\eta}_m(t)\sum_{k=1}^{N_k}\sum_{n=1}^{N_\mathrm{d}} u_k(t)\gamma_{kmn}\dot{\eta}_n(t) = \dot{\eta}_m(t)\sum_{k=1}^{N_k}\Delta\phi_k^{(m)} f_k(t)\\ &= \sum_{k=1}^{N_k}\underbrace{\dot{\eta}_m(t)\Delta\phi_k^{(m)}}_{\Delta\dot{q}_k^{(m)}(t)} f_k(t) = \sum_{k=1}^{N_k}\Delta\dot{q}_k^{(m)}(t) f_k(t),\end{aligned} \tag{2.70}$$

where $\Delta q_k^{(m)}$ is relative rotational displacement of the beams connected at kth lockable joint related to mth mode. Due to the constraint shown in Equation (2.40) the condition that

$$u_k(t)\sum_{m=1}^{N_\mathrm{d}}\Delta\dot{q}_k^{(m)}(t) \approx 0, \tag{2.71}$$

is satisfied but $\Delta\dot{q}_k^{(m)}$ for particular vibration mode can be different from zero. Thus, it can be seen that energy transferred to the mth unlocked vibration mode is equal to the work done by self-equilibrated moments on relative rotational displacement resulting from this mode at all lockable joints. Similarly, the total modal energy transfer rate is the sum of modal energy transfer rates over all lockable joints.

Energetic balance between vibration modes

From Equation (2.71) one can derive that sum of all modal energy transfer rates is close to zero (when c_{max} goes to the infinity, then this sum goes to zero):

$$\sum_{m=1}^{N_\mathrm{d}}\dot{W}_m(t) = \sum_{m=1}^{N_\mathrm{d}}\sum_{k=1}^{N_k}\Delta\dot{q}_k^{(m)}(t) f_k(t) = \sum_{k=1}^{N_k} f_k(t)\sum_{m=1}^{N_\mathrm{d}}\Delta\dot{q}_k^{(m)}(t) \approx 0. \tag{2.72}$$

In other words when any kth joint is locked the total work of the pair of self-equilibrated moments $f_k(t)$ (Fig. 2.11b) done over the structure is equal to zero because the opening angle between the corresponding rotational DOFs is constant due to the constraint (2.40). The exception is only if rotational velocities of DOFs involved in the joints are different during the locking and the inelastic collision occurs. Then energy is shortly dissipated in the joint. However, after this transient state the energy transferred to any unlocked vibration mode is equal to the energy transferred out from the remaining unlocked vibration modes. In other words, lockable joints aim at exchange of energy between coupled unlocked vibration modes but they intentionally do not perform any work nor change the overall amount of the structural energy.

Similarly, the amount energy transferred to some subset of the unlocked vibration modes is equal to the energy transferred out from the all remaining ones. Taking notation as in Equation (2.66) the balance of the energy exchanged between monitored (lower-order) unlocked vibration modes and unmonitored (higher-order) ones can be written as follows:

$$\begin{aligned} \dot{W}_{\mathrm{H}}(t) &= -\dot{\boldsymbol{\eta}}_{\mathrm{H}}^{\mathrm{T}}(t) \sum_{k=1}^{N_k} u_k(t) \begin{bmatrix} \boldsymbol{\Gamma}_{\mathrm{HM}k} & \boldsymbol{\Gamma}_{\mathrm{HH}k} \end{bmatrix} \begin{bmatrix} \dot{\boldsymbol{\eta}}_{\mathrm{M}}(t) \\ \dot{\boldsymbol{\eta}}_{\mathrm{H}}(t) \end{bmatrix} \approx \\ &\approx \dot{\boldsymbol{\eta}}_{\mathrm{M}}^{\mathrm{T}}(t) \sum_{k=1}^{N_k} u_k(t) \begin{bmatrix} \boldsymbol{\Gamma}_{\mathrm{MM}k} & \boldsymbol{\Gamma}_{\mathrm{MH}k} \end{bmatrix} \begin{bmatrix} \dot{\boldsymbol{\eta}}_{\mathrm{M}}(t) \\ \dot{\boldsymbol{\eta}}_{\mathrm{H}}(t) \end{bmatrix} = -\dot{W}_{\mathrm{M}}(t) \end{aligned} \tag{2.73}$$

This is very important observation, because it follows that to control the modal energy transfer to the higher-order vibration modes it is sufficient to monitor only lower-order ones. The equation above can be written in equivalent form:

$$\dot{W}_{\mathrm{H}}(t) = \dot{\boldsymbol{\eta}}_{\mathrm{H}}^{\mathrm{T}}(t) \sum_{k=1}^{N_k} \boldsymbol{\Delta\phi}_{\mathrm{H}k} f_k(t) \approx -\dot{\boldsymbol{\eta}}_{\mathrm{M}}^{\mathrm{T}}(t) \sum_{k=1}^{N_k} \boldsymbol{\Delta\phi}_{\mathrm{M}k} f_k(t) = -\dot{W}_{\mathrm{M}}(t), \tag{2.74}$$

where:

$$\boldsymbol{\Delta\phi}_{\mathrm{M}k} = \begin{bmatrix} \Delta\phi_k^{(1)} & \Delta\phi_k^{(2)} & \cdots & \Delta\phi_k^{(N_p)} \end{bmatrix}^{\mathrm{T}} \tag{2.75}$$

for first N_p monitored unlocked vibration modes and

$$\boldsymbol{\Delta\phi}_{\mathrm{H}k} = \begin{bmatrix} \Delta\phi_k^{(N_p+1)} & \Delta\phi_k^{(N_p+2)} & \cdots & \Delta\phi_k^{(N_\mathrm{d})} \end{bmatrix}^{\mathrm{T}}. \tag{2.76}$$

It also should be noticed that energy transfer rate is the sum of energy transfer rates through each currently locked joint:

$$\dot{W}_{\mathrm{M}}(t) = \sum_{k=1}^{N_k} \dot{W}_{\mathrm{M}k}(t), \quad \dot{W}_{\mathrm{H}}(t) = \sum_{k=1}^{N_k} \dot{W}_{\mathrm{H}k}(t), \tag{2.77}$$

where $\dot{W}_{\mathrm{M}k}$ and $\dot{W}_{\mathrm{H}k}$ are energy transfer rates through the kth lockable joint to monitored vibration modes and the higher order ones, respectively. It follows that despite of information about global behaviour of the structure curried with modal velocities $\dot{\boldsymbol{\eta}}_{\mathrm{M}}$ each joint can be controlled independently on each other. $\dot{W}_{\mathrm{M}k}$ can be expressed as in equations below, whereas $\dot{W}_{\mathrm{H}k}$ is defined analogously.

$$\dot{W}_{\mathrm{M}k} = -u_k(t) \dot{\boldsymbol{\eta}}_{\mathrm{M}}^{\mathrm{T}}(t) \begin{bmatrix} \boldsymbol{\Gamma}_{\mathrm{MM}k} & \boldsymbol{\Gamma}_{\mathrm{MH}k} \end{bmatrix} \begin{bmatrix} \dot{\boldsymbol{\eta}}_{\mathrm{M}}(t) \\ \dot{\boldsymbol{\eta}}_{\mathrm{H}}(t) \end{bmatrix} \tag{2.78}$$

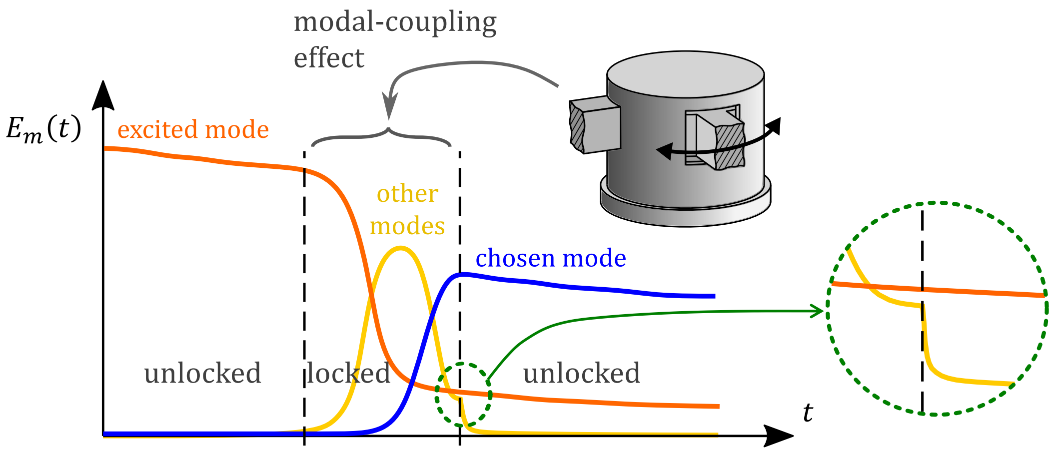

Figure 2.12: Illustrative example of typical flow of modal energies in energy harvesting application

$$\dot{W}_{\mathrm{M}k} = \dot{\boldsymbol{\eta}}_{\mathrm{M}}^{\mathrm{T}}(t)\boldsymbol{\Delta\phi}_{\mathrm{M}k} f_k(t) \tag{2.79}$$

Illustrative summary

Illustrative example of the modal energy transfer typical for energy harvesting application is shown in Figure 2.12. In this example energy is to be transferred from excited unlocked vibration mode (free vibration) to the chosen unlocked mode to which energy harvester is designed. Both of them are monitored (lower-order) unlocked vibration modes. First, when the joint is in unlocked state excited vibration is mitigated only by the material damping and energy is not transferred between vibration modes. Later, when the joint becomes locked, modal coupling resulting in the modal energy transfer is provided. Due to the fact that matrices $\boldsymbol{\Gamma}_k$ are full it causes energy exchange between all unlocked vibration modes, including the higher-order ones. At this stage the total structural energy is not dissipated quickly because the higher-order unlocked modes have mostly potential energy and become prestressed rather than vibrate freely. Finally, the joint is unlocked when the energy of chosen vibration mode stops increasing. At the same time instance the higher-order modes that are yet prestressed start to vibrate freely and their modal energies are quickly dissipated in material damping (see: zoomed area on the right hand side of Figure 2.12). In this case this amount of energy is inevitably lost.

In the case of vibration damping application of the proposed methodology it is desired phenomenon, hence the lockable joint could be dynamically unlocked, in simplest case, at the time instance in which higher-order modes (yellow line) have highest energy providing the biggest sudden energy decrease (analogously to the zoomed area but with greater amount).

Appropriate control algorithm with indicated quantities to be measured as well as sensor and joint placement are discussed in next chapter.

Chapter 3

Semi-active control strategy

Based on the derivations presented in Section 2.2.4 semi-active control methodology is developed. The proposed control methodology has feedback architecture. Its components are illustrated in the form of a block diagram shown in Figure 3.1. This chapter describes comprehensive methodology including not only control law and control algorithm but also measured quantities as well as methods for optimal placement of sensors and lockable joints.

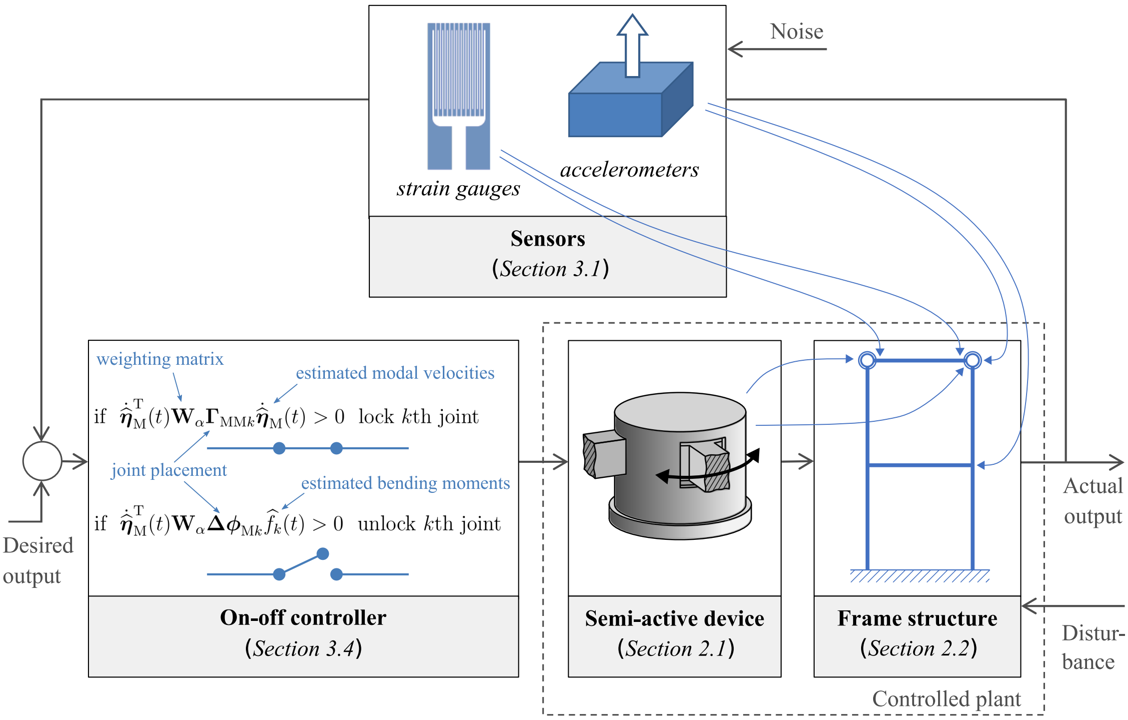

Figure 3.1: Semi-active control methodology [145]

3.1 Quantities required to be measured and hierarchical feedback architecture

3.1.1 Issues to be addressed and selected measured quantities

Since the higher-order vibration modes are characterised by significant damping coefficients and require relatively greater amount of energy to be excited by external forces, their participation in free vibration can be significant only within a short transient state and later, usually after the joint unlock, is negligible. However, in the reconfigurable structure this scheme is often not satisfied. As indicated at the end of Section 2.2.4, motion of higher-order unlocked modes cannot be characterised as free vibration when the joint is locked. The structure is rather prestressed in these vibration modes until the joint is unlocked. In other words superposition of all unlocked vibration modes (including the higher-order ones) gives motion of the structure with the joints in the locked state, even if only several fist locked vibration modes are induced. In this case cumulative total energy of the higher-order unlocked modes can be significant until their free, high-frequency, vibration is not induced by the joint unlock and later dissipated in material damping, as illustrated in Figure 2.12. Due to the character of the motion when the joints are locked it is mainly potential energy. On the other hand due to equipment limitations usually only lower-order modes can be monitored. The main limitation is restricted number of available sensors. Thus, the participation of the higher-order vibration modes in structural motion and operation of the lockable joints are issues in measurement technique that should be addressed.

As it is discussed in Section 3.4 the proposed control law for each joint requires estimation of current modal energy transfer rate (Eq. (2.78) and (2.79)) to make decision when the any joint should be locked/unlocked. Regarding the considerations above, the measurement of quantities required for this purpose when kth joint is in the locked state is considered first. In this case using of Equation (2.78) is impractical because $\dot{\boldsymbol{\eta}}_{\mathrm{H}}(t)$ is not measurable due to the equipment limitations. On the other hand it cannot be omitted as the higher-order unlocked vibration modes take significant participation in the structural response in this case – especially in bending moments $f_k(t)$. Additionally, estimation of whole vector $\dot{\boldsymbol{\eta}}_{\mathrm{H}}(t)$ using a state observer is too inaccurate when only vector $\dot{\boldsymbol{\eta}}_{\mathrm{M}}(t)$, which usually has much less elements, is available. These problems can be avoided using equation Equation (2.79), where $\dot{\boldsymbol{\eta}}_{\mathrm{H}}(t)$ is not explicitly used. Here, both $\dot{\boldsymbol{\eta}}_{\mathrm{M}}(t)$ and $f_k(t)$ are required to be estimated to calculate $\dot{W}_{\mathrm{M}k}(t)$, however moment $f_k(t)$ can be easily obtained e.g. via measurement of strains in vicinity of the kth lockable joint. Moments $f_k(t)$ contain sufficient information about the influence of the higher-order vibration modes on the modal energy transfer rate.

Next issue is that when the joint is unlocked $f_k(t) = 0$ and $\dot{W}_{\mathrm{M}k}(t) = 0$. In this case Equation (2.78) is used to estimate eventual modal energy transfer rate that could occur when kth joint is dynamically locked at time instant t by substitution $u_k(t) = 1$. In this case $\dot{W}_{\mathrm{M}k}(t)$ is estimated with assumption that $\dot{\boldsymbol{\eta}}_{\mathrm{H}}(t) \approx \mathbf{0}$. It follows from the fact that the higher-order unlocked vibration modes are damped after previous unlocking of the lockable joint.

Summarising, both $\dot{\boldsymbol{\eta}}_{\mathrm{M}}(t)$ and $f_k(t)$ are required to be estimated to determine when the currently locked kth joint should be unlocked and only $\dot{\boldsymbol{\eta}}_{\mathrm{M}}(t)$ is required when the currently unlocked joint state should be locked.

3.1.2 Realisation of measurement and its representation in the model

Taking into account the considerations above, output vector $\mathbf{y}$, matrices $\mathbf{C}_{\mathrm{y}}$, $\mathbf{D}$ and vector $\mathbf{v}(t)$ in Equation (2.44) take the following form:

$$\mathbf{y}(t) = \begin{bmatrix} \boldsymbol{\varepsilon}_{\mathrm{M}}(t) \\ \dot{\mathbf{q}}_{\mathrm{M}}(t) \\ \mathbf{u}(t) \end{bmatrix}, \quad \mathbf{C}_{\mathrm{y}} = \begin{bmatrix} \mathbf{L}_{\varepsilon} & \mathbf{0} \\ \mathbf{0} & \mathbf{L}_{\mathrm{q}} \\ \mathbf{0} & \mathbf{0} \end{bmatrix}, \quad \mathbf{D} = \begin{bmatrix} \mathbf{0} \\ \mathbf{0} \\ \mathbf{I} \end{bmatrix}, \quad \mathbf{v}(t) = \begin{bmatrix} \mathbf{v}_{\varepsilon}(t) \\ \mathbf{v}_{\dot{\mathrm{q}}}(t) \\ \mathbf{0} \end{bmatrix}, \tag{3.1}$$

where: $\boldsymbol{\varepsilon}_{\mathrm{M}}(t) = \begin{bmatrix} \varepsilon_{\mathrm{M}1}(t) & \varepsilon_{\mathrm{M}2}(t) & \cdots & \varepsilon_{\mathrm{M}N_k}(t) \end{bmatrix}^{\mathrm{T}} \in \mathbb{R}^{N_k}$ contain strains measured in vicinity of each lockable joint, $\dot{\mathbf{q}}_{\mathrm{M}}(t) = \begin{bmatrix} \dot{q}_{\mathrm{M}1}(t) & \dot{q}_{\mathrm{M}2}(t) & \cdots & \dot{q}_{\mathrm{M}N_{\mathrm{s}}}(t) \end{bmatrix}^{\mathrm{T}} \in \mathbb{R}^{N_{\mathrm{s}}}$ is vector containing measured velocities at N_{s} selected locations, $\mathbf{L}_{\varepsilon} \in \mathbb{R}^{N_k \times N_{\mathrm{d}}}$ is transformation matrix, $\mathbf{L}_{\mathrm{q}} \in \{0, 1\}^{N_{\mathrm{s}} \times N_{\mathrm{d}}}$ is Boolean matrix selecting appropriate DOFs of the structure. If FE mesh is not sufficiently dense then $\mathbf{L}_{\mathrm{q}} \in \mathbb{R}^{N_{\mathrm{s}} \times N_{\mathrm{d}}}$ estimates displacement from at point inside FE from the corresponding nodal displacements using shape functions. $\mathbf{v}_{\varepsilon}(t)$ and $\mathbf{v}_{\dot{\mathrm{q}}}(t)$ represent measurement noise corresponding to measured velocities and strains, respectively. $\boldsymbol{\varepsilon}_{\mathrm{M}}(t)$, $\dot{\mathbf{q}}_{\mathrm{M}}(t)$ and $\mathbf{u}(t)$ are used to estimate $\mathbf{f}(t)$, $\dot{\boldsymbol{\eta}}_{\mathrm{M}}(t)$ and determine if the joints are currently locked, respectively.

Estimation of the bending moments transmitted by the joint

Due to the fact that self-equilibrated moments at rotational DOFs of the kth lockable joint are equal to the bending moment transmitted through this joint $f_k(t)$ can be estimated using equation below.

$$\widehat{f}_k(t) = -\frac{2EI}{h} \varepsilon_{\mathrm{M}k}(t), \tag{3.2}$$

where: E, I and h are Young modulus, sectional moment of inertia and height of the cross section of the beam connected to the kth lockable joint, respectively, and

$$\varepsilon_{\mathrm{M}k}(t) = \frac{\varepsilon^{\mathrm{I}}_{\mathrm{M}k}(t) - \varepsilon^{\mathrm{II}}_{\mathrm{M}k}(t)}{2} \tag{3.3}$$

where $\varepsilon^{\mathrm{I}}_{\mathrm{M}k}(t)$ and $\varepsilon^{\mathrm{II}}_{\mathrm{M}k}(t)$ are strains measured on both sides of the beam (elongated and compressed) in vicinity of the lockable joint. Difference of these two signals that usually are obtained with strain gauges ensures that $\varepsilon_{\mathrm{M}k}(t)$ contains only the strain component resulting from bending of the beam, whereas strains resulting from longitudinal loads are rejected.

Transformation matrix that describes strain-displacement relation is defined using shape functions of the beam elements:

$$\mathbf{L}_\varepsilon = \begin{bmatrix} (\boldsymbol{\Psi}_1\mathbf{R}_1)^{\mathrm{T}} & (\boldsymbol{\Psi}_2\mathbf{R}_2)^{\mathrm{T}} & \cdots & (\boldsymbol{\Psi}_{N_k}\mathbf{R}_{N_k})^{\mathrm{T}} \end{bmatrix}^{\mathrm{T}}, \tag{3.4}$$

where: $\mathbf{R}_k$ is matrix transforming displacement vector $\mathbf{q}(t)$ to local coordinate system of the beam connected to the kth lockable joint and $\boldsymbol{\Psi}_k$ is row matrix containing first and second derivatives of the shape functions. If standard Euler-Bernoulli beam's model is assumed then matrix $\mathbf{R}_k \in \mathbb{R}^{6\times N_\mathrm{d}}$ and

$$\boldsymbol{\Psi}_k = \begin{bmatrix} \Psi_1'(\xi) & -\frac{h}{2}\Psi_2''(\xi) & -\frac{h}{2}\Psi_3''(\xi) & \Psi_4'(\xi) & -\frac{h}{2}\Psi_5''(\xi) & -\frac{h}{2}\Psi_6''(\xi) \end{bmatrix}\Big|_{\xi=\xi_k}, \tag{3.5}$$

where $\Psi_i(\xi)$ are beam's shape functions and ξ_k is location of the pair of the strain gauges in the local coordinate system of the beam.

Estimation of the monitored modal velocities (modal filtering)

$\dot{\boldsymbol{\eta}}_\mathrm{M}(t)$ is estimated using modal filtering technique. Estimate of $\dot{\boldsymbol{\eta}}(t)$ is calculated as

$$\hat{\dot{\boldsymbol{\eta}}}_\mathrm{M}(t) = \mathbf{F}\dot{\mathbf{q}}_\mathrm{M}(t), \tag{3.6}$$

where

$$\mathbf{F} = (\mathbf{L}_\mathrm{q}\boldsymbol{\Phi}_\mathrm{M})^{+} \in \mathbb{R}^{N_p\times N_\mathrm{s}} \tag{3.7}$$

is modal filter and $(\cdot)^{+}$ is Moore–Penrose inverse of the matrix. If number of selected sensor locations indicated by $\mathbf{L}_\mathrm{q}$ is greater than the number of measured vibration modes then $\hat{\dot{\boldsymbol{\eta}}}_\mathrm{M}(t)$ corresponds the least-square estimate of the modal velocities using mode shapes at sensor locations. It is evident that the number of sensors N_s cannot be lower than number of estimated modal velocities N_p. If $N_\mathrm{s} = N_p$ modal filter is square matrix reciprocal to matrix $\mathbf{L}_\mathrm{q}\boldsymbol{\Phi}_\mathrm{M}$.

Appropriate design of modal filter $\mathbf{F}$, i.e. selection of sensor locations described by the matrix $\mathbf{L}_\mathrm{q}$ and selection of the vibration modes to be monitored, can significantly reduce measurement spillover effect and impact of the noise on estimation of the modal velocities. This topic is discussed in the next section.

Hierarchical feedback architecture

Estimation of two quantities, i.e. modal velocities $\dot{\boldsymbol{\eta}}(t)$ and moments $\mathbf{f}(t)$ result in hierarchical architecture of the feedback control loop. As shown in Figure 3.2 each

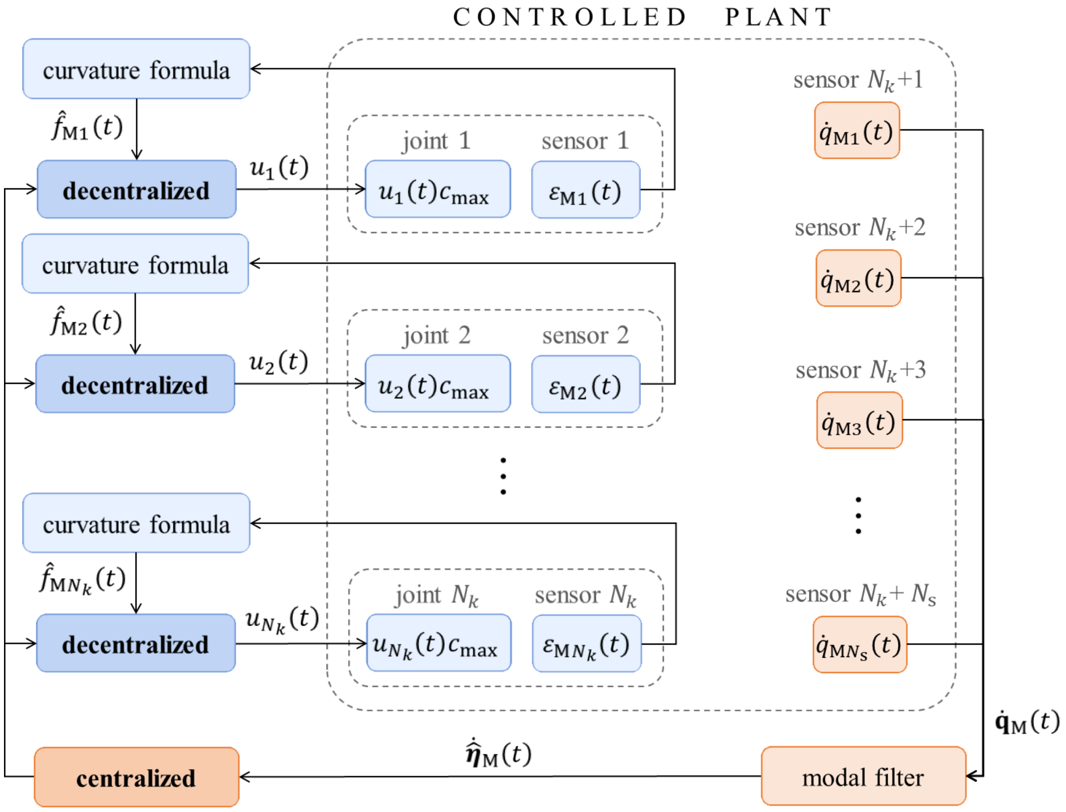

Figure 3.2: Diagram of hierarchical feedback architecture

lockable joint in local feedback loop, independently on the state of other lockable joints, using information about behaviour of the structure in the vicinity of particular lockable joint (bending moment) and global behaviour that is provided by modal velocities. Possibility of making the control independent for each lockable joint results from the fact that total modal energy transfer rate to/from selected vibration modes is the sum of the particular transfers via each lockable joint (see: Eqs (2.77)-(2.79)).

3.2 Optimal sensor placement

3.2.1 Error of the modal filter and its metrics

In this section a method for selection of optimal sensor locations to provide reliable estimation of $\dot{\boldsymbol{\eta}}_M(t)$ is described. Rows in Equation (3.1) related to the measured velocities can be rewritten into the following form:

$$\dot{\mathbf{q}}_M(t) = \mathbf{L}_q \begin{bmatrix} \boldsymbol{\Phi}_M & \boldsymbol{\Phi}_H \end{bmatrix} \begin{bmatrix} \dot{\boldsymbol{\eta}}_M(t) \\ \dot{\boldsymbol{\eta}}_H(t) \end{bmatrix} + \mathbf{v}_{\dot{q}}(t). \tag{3.8}$$

It is assumed that $\mathbf{v}_{\dot{q}}(t)$ is zero-mean and uncorrelated noise and standard deviation corresponding to each element of this vector is equal to σ_q. Seeking for the simplicity of further derivations let us denote by

$$\mathbf{\Phi}_{\mathrm{S}} = \mathbf{L}_{\mathrm{q}}\mathbf{\Phi}_{\mathrm{M}} \tag{3.9}$$

modal matrix truncated to the rows corresponding with measured DOFs and columns corresponding to the monitored vibration modes.

Taking estimate of $\dot{\boldsymbol{\eta}}_{\mathrm{M}}(t)$ as ordinary least square solution the following equation is received:

$$\begin{aligned}\hat{\dot{\boldsymbol{\eta}}}_{\mathrm{M}}(t) &= \mathbf{\Phi}_{\mathrm{S}}^{+}\dot{\mathbf{q}}_{\mathrm{M}}(t) = \\ &= \dot{\boldsymbol{\eta}}_{\mathrm{M}}(t) + \mathbf{\Phi}_{\mathrm{S}}^{+}\underbrace{\mathbf{L}_{\mathrm{q}}\mathbf{\Phi}_{\mathrm{H}}\dot{\boldsymbol{\eta}}_{\mathrm{H}}(t)}_{\dot{\mathbf{q}}_{\mathrm{H}}(t)} + \mathbf{\Phi}_{\mathrm{S}}^{+}\mathbf{v}_{\dot{\mathrm{q}}}(t).\end{aligned} \tag{3.10}$$

In Equation above the last two terms represent the influence of measurement spillover and measurement noise, respectively. Accordingly to the Gauss–Markov theorem the least-square estimator is unbiassed and efficient if error (here: $\dot{\mathbf{q}}_{\mathrm{H}}(t) + \mathbf{v}_{\dot{\mathrm{q}}}$) has zero mean and is uncorrelated. However, these assumptions may be invalid, as only $\mathbf{v}_{\dot{\mathrm{q}}}(t)$ is considered as random zero-mean variable with uncorrelated elements. Due to measurement spillover effect estimation error $\mathbf{e}_{\eta}(t)$ in general does not have zero expected value. The estimation error is given as:

$$\begin{aligned}\mathbf{e}_{\eta}(t) &= \hat{\dot{\boldsymbol{\eta}}}_{\mathrm{M}}(t) - \dot{\boldsymbol{\eta}}_{\mathrm{M}}(t) = \\ &= \mathbf{\Phi}_{\mathrm{S}}^{+}\left(\dot{\mathbf{q}}_{\mathrm{H}}(t) + \mathbf{v}_{\dot{\mathrm{q}}}(t)\right).\end{aligned} \tag{3.11}$$

As described at the beginning of Section 3.1 the higher-order unlocked vibration modes are quickly damped during their free vibration for unlocked state of the joints, whereas they can significantly participate in the strain (potential) energy when joints are in the locked state. It is due to relatively large higher-order unlocked natural frequencies $\omega^{(m)}$ (see: Eq. (2.67)). However, their participation in kinetic structural energy is negligible excepting short transient state after the joint unlock. It is due to the fact that for the locked joints these vibration modes correspond to the quasi-static motion in the sense that their current frequency of vibration is much smaller than natural frequencies $\omega^{(m)}$ characterising their free vibration (after joint unlock) as discussed in Chapter 2. Thus, in both cases participation in structural velocities can be considered as negligible in further derivations. For short transient states where high-frequency oscillations responsible for the error $\dot{\mathbf{q}}_{\mathrm{H}}(t)$ are present the control is stopped corresponding selected time interval, as described in Section 3.4.

On the other hand, $\dot{\mathbf{q}}_{\mathrm{H}}(t)$ depends on the excitation case, kind of the controlled structure and selected algorithm parameters, thus it is difficult to estimate $\dot{\mathbf{q}}_{\mathrm{H}}(t)$, since it is problem-dependent. Thus, calculation of the mean square error (MSE) of estimator $\hat{\dot{\boldsymbol{\eta}}}_{\mathrm{M}}(t)$ aiming at quantifying how the selected sensor locations affect modal filtering is very difficult. Covariance matrix that provide information about deviation from the expected value (as opposed to MSE measure quantifying deviation from the true value $\dot{\boldsymbol{\eta}}_{\mathrm{M}}(t)$) could be used, since higher-order unlocked vibration modes provide only small estimator bias that can be neglected.

Taking into account the considerations above a weaker formulation of the sensor placement problem than explicit minimisation of the MSE can be used. MSE of the estimator cannot be lower than corresponding variance that, accordingly to the Cramér–Rao bound, cannot be lower than reciprocal of the Fisher information matrix (FIM):

$$\mathrm{MSE}(\mathbf{e}_\eta(t)) \geq \mathbf{\Sigma}_\eta \geq \boldsymbol{\mathcal{I}}^{-1}, \tag{3.12}$$

where:

$$\mathrm{MSE}\left(\mathbf{e}_\eta(t)\right) = \mathrm{E}\left(\mathbf{e}_\eta(t)\mathbf{e}_\eta^{\mathrm{T}}(t)\right) \tag{3.13}$$

is MSE of estimator $\dot{\hat{\boldsymbol{\eta}}}_{\mathrm{M}}(t)$, where $\mathrm{E}(\cdot)$ is the expected value operator,

$$\begin{aligned}\mathbf{\Sigma}_\eta &= \mathrm{E}\left(\left[\mathbf{e}_\eta(t) - \mathrm{E}(\mathbf{e}_\eta(t))\right]\left[\mathbf{e}_\eta(t) - \mathrm{E}(\mathbf{e}_\eta(t))\right]^{\mathrm{T}}\right) = \\ &= \mathrm{E}\left(\left[\mathbf{e}_\eta(t) - \mathbf{\Phi}_{\mathrm{S}}^{+}\dot{\mathbf{q}}_{\mathrm{H}}(t)\right]\left[\mathbf{e}_\eta(t) - \mathbf{\Phi}_{\mathrm{S}}^{+}\dot{\mathbf{q}}_{\mathrm{H}}(t))\right]^{\mathrm{T}}\right) = \\ &= \sigma_{\mathrm{q}}^2\left(\mathbf{\Phi}_{\mathrm{S}}^{\mathrm{T}}\mathbf{\Phi}_{\mathrm{S}}\right)^{-1}\end{aligned} \tag{3.14}$$

is covariance matrix of estimator $\dot{\hat{\boldsymbol{\eta}}}_{\mathrm{M}}(t)$ and $\boldsymbol{\mathcal{I}}$ is FIM that in this particular case is equal to the reciprocal of the covariance matrix:

$$\boldsymbol{\mathcal{I}} = \sigma_{\mathrm{q}}^{-2}\left(\mathbf{\Phi}_{\mathrm{S}}^{\mathrm{T}}\mathbf{\Phi}_{\mathrm{S}}\right). \tag{3.15}$$

The inequality above or means that if $\mathbf{A} \geq \mathbf{B}$ then matrix $\mathbf{A}-\mathbf{B}$ is positive semidefinite. As σ_{q} is constant it does not play the role in the optimisation procedure, hence FIM further is represented by matrix $\boldsymbol{\mathcal{F}}$ written with omitted σ_{q} term:

$$\boldsymbol{\mathcal{F}} = \mathbf{\Phi}_{\mathrm{S}}^{\mathrm{T}}\mathbf{\Phi}_{\mathrm{S}}. \tag{3.16}$$

3.2.2 Effective Independence concept

Covariance matrix $\mathbf{\Sigma}_\eta$ provides information about the expected measurement error, hence its various norms, e.g. its trace, could be used as the objective function to be minimised. However, calculation of the characteristics in dependence of the selected sensor locations (rows of $\mathbf{\Phi}_{\mathrm{M}}$ that form matrix $\mathbf{\Phi}_{\mathrm{S}}$) is difficult. Hence, FIM is used in the optimisation process instead, as mentioned in Section 1.1.4. In this case determinant of FIM $\det\boldsymbol{\mathcal{F}}$ is to be maximised during the optimisation. It provides the trade-off between linear independence and norms of vectors formed from the mode shapes at sensor locations. One of methods searching near-optimal solution is famous Effective Independence (EFI) proposed by Kammer [132]. Since method used in this work in based on EFI method, EFI is introduced first.

In EFI method the optimisation problem below is solved.

$$\begin{array}{ll} \text{find} & \mathbf{s} \in \{0,1\}^{N_\mathrm{c}} \\ \text{to maximise} & \det \boldsymbol{\mathcal{F}}(\mathbf{s}) \\ \text{subject to} & \displaystyle\sum_{i=1}^{N_\mathrm{c}} s_i = N_p, \end{array} \tag{3.17}$$

where $\mathbf{s}$ is Boolean vector selecting DOFs to be sensor locations (corresponding rows of $\mathbf{\Phi}_\mathrm{M}$), N_c is number of DOFs candidating to be sensor locations. In simplest case $N_\mathrm{c} = N_\mathrm{d}$, however in some cases the set of candidate sensor locations can be restricted due to structural conditions, e.g. some locations can be not available for sensors (in this case corresponding rows of $\mathbf{\Phi}_\mathrm{M}$ also are removed initially). The constraint pursued on the cardinality of sensor locations follows from the fact that N_p sensors are required to monitor N_p vibration modes.

Kammer proposed that starting from full vector $\mathbf{s}$ (containing only ones), sensor locations that contribute the least to $\det \boldsymbol{\mathcal{F}}(\mathbf{s})$ are removed in iterative manner. Then, corresponding element of vector $\mathbf{s}$ is replaced with zero in each iteration step. Effective independence measure for all sensor locations is computed in the form of vector:

$$\mathbf{r}(\mathbf{s}) = \operatorname{diag}\left(\mathbf{\Phi}_\mathrm{S}(\mathbf{s})\boldsymbol{\mathcal{F}}^{-1}(\mathbf{s})\mathbf{\Phi}_\mathrm{S}^\mathrm{T}(\mathbf{s})\right) \tag{3.18}$$

after each sensor removal. If $r_i = 0$ then ith sensor location does not contribute to the $\det \boldsymbol{\mathcal{F}}(\mathbf{s})$ representing linear independence, whereas if $r_i = 1$ removal of this sensor cause that vectors in reduced modal matrix $\mathbf{\Phi}_\mathrm{S}(\mathbf{s})$ become not linearly independent and $\det \boldsymbol{\mathcal{F}} = 0$, i.e. this sensor location is crucial and cannot be removed. Poston and Tolson showed that determinants of FIM before and after the removal of ith sensor are related as follows [146]:

$$\det \boldsymbol{\mathcal{F}}(\mathbf{s}_\mathrm{next}) = (1 - r_i(\mathbf{s}_\mathrm{current})) \det \boldsymbol{\mathcal{F}}(\mathbf{s}_\mathrm{current}). \tag{3.19}$$

Thus, EFI method removes the candidate sensor locations in the way providing smallest decreases (the smallest r_i is selected) of determinant of FIM until N_p sensor locations are obtained. After each sensor removal number of rows in $\mathbf{\Phi}_\mathrm{S}(\mathbf{s})$ is reduced by one. Matrix $\mathbf{\Phi}_\mathrm{S}(\mathbf{s})\boldsymbol{\mathcal{F}}^{-1}(\mathbf{s})\mathbf{\Phi}_\mathrm{S}^\mathrm{T}(\mathbf{s})$ is idempotent, hence in each iteration step sum of elements of $\mathbf{r}(\mathbf{s})$ that is trace of $\mathbf{\Phi}_\mathrm{S}(\mathbf{s})\boldsymbol{\mathcal{F}}^{-1}(\mathbf{s})\mathbf{\Phi}_\mathrm{S}^\mathrm{T}(\mathbf{s})$ is equal to the number of monitored vibration modes:

$$\sum_{i=1}^{N_\mathrm{c}} r_i = N_p. \tag{3.20}$$

Thus, vector $\mathbf{r}$ satisfies constraint pursued on vector $\mathbf{s}$ in problem described in Equation (3.17).

3.2.3 Convex relaxation approach for sensor layout optimisation

EFI allows to find near-optimal solution of good quality without the need exhaustive search with all possible combinations of sensor locations that in practical applications with large N_c is not possible. However, the drawback of this method is that it performs $N_\mathrm{c} - N_p$ iterations to find sensor locations. Thus, in this thesis convex relaxation (CR) is employed to reduce the computational burden.

Taking the considerations above into account CR-based method is proposed that instead selecting the rows of $\mathbf{\Phi}_\mathrm{S}$ to be removed the sensor density vector $\boldsymbol{\rho} \in [0,1]^{N_\mathrm{c}}$ provides relaxed Boolean constraints as shown in Equation (3.21).

$$\mathbf{\Phi}_\rho = \mathrm{diag}(\boldsymbol{\rho})\mathbf{\Phi}_\mathrm{M}. \tag{3.21}$$

In the equation above rows of modal matrix $\mathbf{\Phi}_\mathrm{M}$ containing all candidate sensor locations are weighted by elements of the sensor density vector. On the other hand elements ρ_i provide information how much ith candidate sensor location is relevant analogously to vector $\mathbf{r}$ in Eqaution 3.18.

Taking into account the considerations above in CR-based approach continuous optimisation problem (3.22) that is relaxed counterpart of discrete problem (3.17) is solved.

$$\begin{array}{ll} \text{find} & \boldsymbol{\rho} \in [0,1]^{N_\mathrm{c}} \\ \text{to maximise} & \det\left(\mathbf{\Phi}_\rho^\mathrm{T}\mathbf{\Phi}_\rho\right) \\ \text{subject to} & \displaystyle\sum_{i=1}^{N_\mathrm{c}} \rho_i = N_p \end{array} \tag{3.22}$$

Procedure that searches for near-optimal solution of problem (3.22) is shown in the form of pseudo code below in Algorithm 1. In this approach N_p elements of vector $\boldsymbol{\rho}$ that contribute most to the linear independence converge to ones at the expense of the remaining elements that converge to zeros since condition (3.20) is always satisfied also for vector $\boldsymbol{\rho}$.

3.3 Optimal placement of the lockable joints

3.3.1 Controllability in the control of modal energy transfer – issues

Controllability metrics discussed in literature review such as value of mode shape at actuator location (as in PBH test) and controllability gramian are usually good measures of controllability of particular vibration modes when the controlled system is linear. However, in this work the controlled reconfigurable system belongs to the nonlinear class. Moreover, the aim of the proposed control methodology is to transfer the energy between unlocked vibration modes which interact with each

Algorithm 1 Pseudo code for CR-based sensor placement

Input: $\boldsymbol{\Phi}_{\mathrm{M}}$ related to monitored vibration modes and all candidate sensor locations and ϵ_{tol} for stop condition.

Output: indices i_{M} of DOFs to be measured.

```
$\boldsymbol{\rho} \leftarrow \frac{N_p}{N_c}\mathbf{1}_{N_c}$
Flag $\leftarrow 1$
while Flag do
    $\boldsymbol{\rho}_{\mathrm{prev}} \leftarrow \boldsymbol{\rho}$
    $\boldsymbol{\Phi}_{\rho} \leftarrow \mathrm{diag}(\boldsymbol{\rho})\boldsymbol{\Phi}_{\mathrm{M}}$
    $\boldsymbol{\rho} \leftarrow \mathrm{diag}\left(\boldsymbol{\Phi}_{\rho}\left(\boldsymbol{\Phi}_{\rho}^{\mathrm{T}}\boldsymbol{\Phi}_{\rho}\right)^{-1}\boldsymbol{\Phi}_{\rho}^{\mathrm{T}}\right)$
    if $\left\|\boldsymbol{\rho} - \boldsymbol{\rho}_{\mathrm{prev}}\right\| < \epsilon_{\mathrm{tol}}$ then
        Flag $\leftarrow 0$
    end if
end while
Select DOF indices $i_{\mathrm{M}}$ related to sensor densities close to 1, e.g. $\{i_{\mathrm{M}} : \rho_{i_{\mathrm{M}}} > 0.5\}$
```

other. These interactions are represented by the bilinear terms in the equations of motion, where the control forces do not depend only on the control signals but also directly on current state of the structure. Thus, calculation of controllability metric for particular vibration unlocked mode can be insufficient.

For the considered control methodology, in the simplest case one could take elements γ_{kmn} of matrix $\boldsymbol{\Gamma}_k$ as the metric of degree of coupling between mth and nth unlocked vibration mode through k lockable joint at its current location. Equation (2.64) shows that γ_{kmn}, analogously to PBH test, is proportional to rotational displacements of the unlocked mode shapes at DOFs involved in kth lockable joint that are entries for the self-equilibrated pair of moments illustrated in Figure 2.11b. However, similarly to the PBH test γ_{kmn} elements do not provide information about the amount of the energy that can be transferred from/to the monitored unlocked modes.

3.3.2 Proposed controllability metric

The proposed criterion is based on the assumption that locked mode shapes $\widetilde{\boldsymbol{\phi}}^{(m)}$ can be expressed in the basis formed from unlocked mode shapes $\boldsymbol{\phi}^{(m)}$. As discussed in Chapter 2 the additional information about relative rotational displacements at DOFs involved in the kth locked joint Δq_k is additionally required apart locked mode shapes to describe the state of the structure with locked kth joint. However, for the purpose of optimal placement of the lockable joints mode shapes $\widetilde{\boldsymbol{\phi}}^{(m)}$ obtained for the structure with joints locked at $\Delta q_k = 0$ for all k are sufficient (see Eq. (2.59)).

The ability of the lockable joints to transfer the energy between mth vibration mode and all remaining ones can be expressed as

$$g_m = \frac{\Delta \widetilde{E}_{\mathrm{p}m}}{\widetilde{E}_{\mathrm{p}m}}, \tag{3.23}$$

where

$$\widetilde{E}_{\mathrm{p}m} = \frac{1}{2} \widetilde{\boldsymbol{\phi}}^{(m)\mathrm{T}} \widetilde{\mathbf{K}} \widetilde{\boldsymbol{\phi}}^{(m)} = \frac{1}{2} \widetilde{\omega}^{(m)2} \tag{3.24}$$

is strain (potential) energy related to the mth locked vibration mode for unit modal displacement $\widetilde{\eta}_m(t) = 1$ and $\Delta \widetilde{E}_{\mathrm{p}m}$ represents the amount of strain energy that will be released into vibration in unlocked vibration modes other than mth one after sudden unlocking of the joints. It can be calculated as follows:

$$\begin{aligned} \Delta \widetilde{E}_{\mathrm{p}m} = \widetilde{E}_{\mathrm{p}m} - E_{\mathrm{p}m} = \widetilde{E}_{\mathrm{p}m} - \frac{1}{2} \vartheta_{mm}^2 \boldsymbol{\phi}^{(m)\mathrm{T}} \mathbf{K} \boldsymbol{\phi}^{(m)} = \\ = \frac{1}{2} \left(\widetilde{\omega}^{(m)2} - \vartheta_{mm}^2 \omega^{(m)2} \right), \end{aligned} \tag{3.25}$$

where coefficient ϑ_{mm} is the mth diagonal element of matrix $\boldsymbol{\Theta}$ that satisfies equation

$$\mathbf{B} \widetilde{\boldsymbol{\Phi}} = \boldsymbol{\Phi} \boldsymbol{\Theta}, \tag{3.26}$$

where matrix $\widetilde{\boldsymbol{\Phi}}$ collects locked mode shapes. $\boldsymbol{\Theta}$ is calculated simply as

$$\boldsymbol{\Theta} = \boldsymbol{\Phi}^{-1} \mathbf{B} \widetilde{\boldsymbol{\Phi}} \tag{3.27}$$

and contain information about participation of the unlocked mode shapes in structural deformation equal to the locked ones.

The greater the terms $\Delta \widetilde{E}_{\mathrm{p}m}$ are, the greater is the amount of energy distributed among all unlocked vibration modes when the structure vibrates in lower-order locked vibration modes. Thus, it is evident that the greater is $\Delta \widetilde{E}_{\mathrm{p}m}$ the better is the ability to transfer the energy between mth unlocked vibration mode and the remaining ones. Hence, g_m shown in Equation (3.23) can be considered as the controllability of the mth vibration mode in the sense of the energy transfer.

Usually only lower-order unlocked vibration modes are to be monitored. Their locked counterparts are less sensitive to local changes of the stiffness than the higher-order ones, hence corresponding coefficients $\vartheta_{mm} \approx 1$. Hence, for many practical cases the controllability metric can be simplified as shown below

$$g_m = \frac{\widetilde{\omega}^{(m)2} - \vartheta_{mm}^2 \omega^{(m)2}}{\widetilde{\omega}^{(m)2}} \approx \frac{\widetilde{\omega}^{(m)2} - \omega^{(m)2}}{\widetilde{\omega}^{(m)2}}. \tag{3.28}$$

Apart reflecting the ability of the lockable joints at their current locations to transfer the energy between vibration modes the proposed controllability metric it is also straightforward in calculation. It requires only modal parameters of the structure with all locked and all unlocked joints.

3.3.3 Implementation for various applications

Aiming at efficient vibration damping the controllability metrics g_m can be weighted by coefficients and summed as cumulative controllability metric:

$$G_1 = \sum_{p=1}^{N_p} \beta_p g_p, \tag{3.29}$$

where β_p are weights reflecting the priority of damping of the particular vibration modes in placement of the lockable joints. E.g. weights selected as $\beta_p = 1/\omega^{(p)}$ or $\beta_p = 1/\omega^{(p)2}$ pursue higher priority to mitigate vibration of the lower-order unlocked vibration modes that have lower material damping and are associated with greater vibration amplitudes.

If it is demanded to keep all monitored unlocked modes controllable, then the lockable joints should be located in such a way that no any g_p is close to zero. It applies to the energy harvesting application of the control methodology where the energy is transferred from all monitored vibration modes to the selected one. In this case cumulative controllability is reflected better by the product of the controllabilities associated with particular vibration modes rather than their sum:

$$G_2 = \prod_{p=1}^{N_p} g_p. \tag{3.30}$$

In cases where the mass of the lockable joints is not negligible Equation (3.29) or (3.30) is evaluated for each tested placement of the lockable joints. Then, exhaustive search method is employed to find the solution of such a combinatorial problem. In cases when the mass of the lockable joint can be treated negligible comparing to the mass of the structure the following simplification can be applied for seeking of the computational effectiveness. Controllability metrics $\beta_p g_{ip}$ can be aggregated in controllability matrix $\mathbf{G} \in [0,1]^{N_{\mathrm{Jc}} \times N_p}$, where g_{ip} is controllability metric of pth unlocked vibration mode for only one lockable joint placed at ith subsequent pair of rotational DOFs and N_{Jc} is the number of candidate locations of the lockable joints. Later, depending on the control purposes N_k rows (N_k joints to be placed) of $\mathbf{G}$ with the highest sum of contained elements are to be selected (analogously to the control metrics G_1) or with the highest product of the contained elements (analogously to the control metrics G_2). In the later case weights β_p do not affect the selected locations.

3.4 Semi-active control – potential applications

As indicated in [12] finding control functions $u_k(t)$ of semi-active structure equipped with the lockable joints that are optimal in the sense of Pontryagin's principle is very difficult. It is due to the fact that the costate equations contain negative damping.

Hence, integration of the state and costate equations is not stable. However, Pontryagin's principle provided an important information that optimal control is of the bang-bang type (fully locked/fully unlocked joint). Thus, PAR strategy is the simplification of the optimal approach (more details in Subsection 1.1.3). It uses only information about strains in vicinity of the lockable joints that can be visualised as local control loops in Figure 3.2 and is heuristic approach, whereas methodology developed in this thesis additionally employs information about global state of the controlled system that is provided by modal velocities (additional loop in Figure 3.2). It allows for explicit formulation of instantaneously optimal control related to the modal energies associated with monitored unlocked vibration modes.

Derivation of the control law, control algorithm and its implementation in vibration attenuation is discussed in Subsection 3.4.1. Later the control law is adopted for energy harvesting application by modyfing algorithm parameters, as discussed in Subsection 3.4.2. Both variants of the control law are based explicitly on instantaneous maximisation of the energy flow in desired direction derived and discussed earlier in Section 2.2.4. Basic properties of the proposed control strategy are illustrated on three control scenarios employing the two-DOF system in Subsection 3.4.3. It aims introducing the reader into the control strategy before more realistic numerical and experimental extensive studies which are shown in the next two chapters.

3.4.1 Implementation for vibration suppression

Objective function and instantaneous optimality

Formulating the control law for the energy transfer to the higher-order vibration modes we must remember that only the lower-order ones can be monitored due to equipment limitations (see: Section 3.1). Regarding Equations (2.73) and (2.74) the amount of the energy transferred to the higher-order unlocked vibration modes by operation of the lockable joints is equal to the energy transferred out from the monitored unlocked vibration modes. Hence, transferring the mechanical energy to the higher-order unlocked vibration modes is equivalent to pursuing energy transfer out from monitored unlocked modes only. Thus, in the case of the vibration attenuation Lyapunov function $V(t)$ is defined as the weighted sum of energies associated with monitored unlocked vibration modes:

$$V(t) = \sum_{p=1}^{N_p} \alpha_p E_p(t), \tag{3.31}$$

where α_p are weights that pursue priority in damping of particular vibration modes. In this subsection it is shown that instantaneous minimisation of $V(t)$ causes transfer of the energy to the higher-order unlocked vibration modes.

Selection of weights α_p is crucial for operation of the control algorithm. Since the lower-order unlocked modes usually are characterised by the lower inherent material damping and have the biggest participation in the structural motion, their energy should be transferred out into the higher-order modes with priority decreasing with the order of the monitored mode, e.g.:

$$\alpha_p = \frac{1}{\omega^{(p)2}}. \tag{3.32}$$

The control signals $\mathbf{u}(t)$ are sought at each time instant t aiming at providing the steepest descent of $V(t)$. It can be formally written as the instantaneous optimisation problem:

$$\begin{aligned} &\text{for current } t \text{ find} && \mathbf{u}(t) \in \{0,1\}^{N_k} \\ &\text{to minimise} && \dot{V}(t). \end{aligned} \tag{3.33}$$

The optimisation problem above is formulated for the current time instant as opposed to the optimisation problems formulated for some time interval (e.g. Pontryagin's maximum principle). In other words considered optimisation problem does not require variational calculus to be solved. Thus, no any constraints in the form of state equations are used here. As shown further, despite of the presence of derivatives with respect to time, only algebraic problem is solved to optimise the control.

From Equation (2.69) it follows that $\dot{V}(t)$ can be written as

$$\dot{V}(t) = \sum_{p=1}^{N_p} \alpha_p \left(\dot{W}_p(t) + \dot{E}_p^{\text{loss}}(t) + \dot{W}_p^{\text{ext}}(t) \right). \tag{3.34}$$

Only the modal energy transfer rates $\dot{W}_p(t)$ directly depend on control signals. Hence, equivalent optimisation problem can be solved:

$$\begin{aligned} &\text{for current } t \text{ find} && \mathbf{u}(t) \in \{0,1\}^{N_k} \\ &\text{to minimise} && \dot{V}_W(t), \end{aligned} \tag{3.35}$$

where

$$\dot{V}_W(t) = \sum_{p=1}^{N_p} \alpha_p \dot{W}_p(t). \tag{3.36}$$

Taking into account that the modal energy transfer rate is the sum of the modal energy transfer rates provided by each lockable joint (see: Eq. (2.70) and Eq. (2.77)) the calculations below are valid.

$$\dot{V}_W(t) = \sum_{p=1}^{N_p} \alpha_p \sum_{k=1}^{N_k} \dot{W}_{pk}(t) = \sum_{k=1}^{N_k} \sum_{p=1}^{N_p} \alpha_p \dot{W}_{pk}(t) = \sum_{k=1}^{N_k} \dot{V}_{Wk}(t) \tag{3.37}$$

$\dot{V}_{Wk}(t)$ represents weighted modal energy transfer rate to the monitored vibration modes through kth lockable joint. It should be noticed that the negative sign of $\dot{V}_{Wk}(t)$ means opposite direction of the energy flow, i.e. from the monitored vibration modes to the remaining ones.

It is evident that to minimise $\dot{V}_W(t)$ each kth component of the sum above can be instantaneously minimised independently on other components, accordingly to earlier considerations that each joint can be controlled independently on the other ones. It is visualised Figure 3.2 as local control loops for each lockable joint.

Control law and control algorithm employing measured quantities

Let $\dot{\widehat{V}}_{Wk}(t)$ denote estimated weighted modal energy transfer rate through kth joint after its locking. Then, taking into account the considerations above, the control law for each lockable joint

$$u_k = \begin{cases} 1 & \text{for } \dot{\widehat{V}}_{Wk}(t) < 0 \\ 0 & \text{otherwise} \end{cases} \tag{3.38}$$

is pursued. Regarding considerations in Section 3.1 $\dot{\widehat{V}}_{Wk}(t)$ can be estimated using estimated modal velocities when kth joint is currently unlocked or both modal velocities and bending moments when the joint is locked.

In the former case, making analogous calculations as in Equation (2.78) but using estimated modal velocities and employing weights α_p we receive

$$\dot{\widehat{V}}_{Wk}(t) = -\dot{\widehat{\boldsymbol{\eta}}}_{\mathrm{M}}^{\mathrm{T}}(t)\mathbf{W}_\alpha \boldsymbol{\Gamma}_{\mathrm{MM}k}\dot{\widehat{\boldsymbol{\eta}}}_{\mathrm{M}}(t), \tag{3.39}$$

where

$$\mathbf{W}_\alpha = \operatorname{diag}\left(\begin{bmatrix}\alpha_1 & \alpha_2 & \cdots & \alpha_{N_p}\end{bmatrix}^{\mathrm{T}}\right). \tag{3.40}$$

In Equation (3.39) the value of $\dot{\widehat{V}}_{Wk}(t)$ that could occur after eventual sudden lock of the kth joint is calculated. When it has positive sign the joint is not locked yet but if $\dot{\widehat{V}}_{Wk}(t)$ changes its sign into negative value then the joint is suddenly locked (see: (3.38)). Here, $\dot{\widehat{\boldsymbol{\eta}}}_{\mathrm{M}}$ is sufficient to calculate $\dot{\widehat{V}}_{Wk}(t)$ without the need estimation modal velocities related to the higher-order vibration modes if the condition for the joint lock is checked not earlier than after short time moment t_{unlock} after previous joint unlocking. It is assumed that this time interval allows to naturally mitigate higher-order vibration modes that were excited earlier by the operation of the joints.

In the later case, i.e. when joint is currently locked, calculations analogous to Equation (2.79) but with employed weights α_p are performed on estimated quantities as follows:

$$\dot{\widehat{V}}_{Wk}(t) = \dot{\widehat{\boldsymbol{\eta}}}_{\mathrm{M}}^{\mathrm{T}}(t)\mathbf{W}_\alpha \boldsymbol{\Delta\phi}_{\mathrm{M}k}\widehat{f}_k(t). \tag{3.41}$$

Here, the kth joint is unlocked when the estimated weighted modal energy transfer rate becomes positive, i.e. direction of the flow of mechanical energies associated with the monitored unlocked vibration modes becomes unprofitable. After the unlock of the kth joint Equation (3.39) is used again to check if the kth joint should

Algorithm 2 Pseudo code for implementation of the proposed semi-active modal control methodology

Input: selected modes to be monitored $p = 1, 2, \dots N_p$, weighting matrix $\mathbf{W}_\alpha$, modal filter $\mathbf{F}$, t_{unlock} and t_{lock}; calculated $\boldsymbol{\Gamma}_{\mathrm{MM}k}$ and $\boldsymbol{\Delta\phi}_{\mathrm{M}k}$, $k = 1, 2, \dots N_k$.
Measured quantities: velocities at sensor locations $\dot{\mathbf{q}}_{\mathrm{M}}(t)$, strains in vicinity of the lockable joints $\boldsymbol{\varepsilon}_{\mathrm{M}k}(t)$, $k = 1, 2, \dots N_k$.
Output: control signals $u_k(t)$, $k = 1, 2, \dots N_k$ for each lockable joint.

```
 1: $\dot{\hat{\boldsymbol{\eta}}}_{\mathrm{M}}(t) \leftarrow \mathbf{F}\dot{\mathbf{q}}_{\mathrm{M}}(t)$                          ▷ Global feedback loop
 2: for $k = 1, 2, \dots N_k$ do                          ▷ For each joint (local control loops)
 3:     $u_k^{\mathrm{prev}} \leftarrow u_k$
 4:     if $u_k(t) == 0$ then                                                ▷ Is unlocked?
 5:         $\dot{\hat{V}}_{Wk}(t) \leftarrow -\dot{\hat{\boldsymbol{\eta}}}_{\mathrm{M}}^{\mathrm{T}}(t)\mathbf{W}_\alpha\boldsymbol{\Gamma}_{\mathrm{MM}k}\dot{\hat{\boldsymbol{\eta}}}_{\mathrm{M}}(t)$
 6:         if $\dot{\hat{V}}_{Wk}(t) < -\kappa_1$ then
 7:             $u_k(t) \leftarrow 1$                                        ▷ Lock $k$th joint
 8:         end if
 9:     else
10:         $\hat{f}_k(t) \leftarrow -\frac{2EI}{h}\varepsilon_{\mathrm{M}k}(t)$
11:         $\dot{\hat{V}}_{Wk}(t) \leftarrow \dot{\hat{\boldsymbol{\eta}}}_{\mathrm{M}}^{\mathrm{T}}(t)\mathbf{W}_\alpha\boldsymbol{\Delta\phi}_{\mathrm{M}k}\hat{f}_k(t)$
12:         if $\dot{\hat{V}}_{Wk}(t) \geq \kappa_2$ then
13:             $u_k(t) \leftarrow 0$                                      ▷ Unlock $k$th joint
14:         end if
15:     end if
16: end for
17: if any($u_k^{\mathrm{prev}} == 1$ and $u_k == 0$) then                      ▷ Any joint unlocked
18:     Wait $t_{\mathrm{unlock}}$                ▷ Wait until higher-order modes are not mitigated
19: else if any($u_k^{\mathrm{prev}} == 0$ and $u_k == 1$) then                     ▷ Any joint locked
20:     Wait $t_{\mathrm{lock}}$                  ▷ Wait until higher-order modes are not mitigated
21: end if
22: Return to line no. 1
```

be locked.

A possible implementation of the control law is shown in the form of the pseudo code in Algorithm 2. This algorithm fulfills the scheme shown in Figure 3.2. $\dot{\hat{\boldsymbol{\eta}}}_{\mathrm{M}}$ carries information about global state of the structure, whereas iteration steps of the "for" loop correspond with the local collocated feedback loops for each lockable joint.

Thresholds κ_1 and κ_2 (lines no. 6 and 12) preselected with trial-and-error method prevent from redundant switches of the joint states (locking/unlocking) caused by measurement errors. Additionally, after any change of the state of the lockable joint algorithm waits t_{lock} or t_{unlock} required for mitigation of the higher-order vibration modes that could cause measurement spillover effect, also resulting in the redundant joint switches. Usually $t_{\mathrm{unlock}} \geq t_{\mathrm{lock}}$, hence unlocking is checked first (line no 17). Apart enhancing reliability of the lockable joints, these simple modifications in the control algorithm based on the control law described by Equation (3.38) significantly improve the control performance. Moreover, κ_1 and κ_2 are selected in such a way that allows to keep the joints locked if the vibration level (and thus possible weighted modal energy transfer rate from monitored vibration modes) is below certain value. In this situation joint operation is not required. If the structure is excited sufficiently the joints will be unlocked at profitable time instant (condition in line no. 6) and start to operate again to mitigate the vibration.

Jerking-preventing properties of the proposed control

It is assumed that lockable joints work in two steady state states: fully locked and fully unlocked, whereas transient states as e.g. slipping between friction parts are very short. This can cause large transient accelerations, especially using the idealised model of the lockable joint based on the viscous damper or exact kinematic constraints. Such a behaviour is demonstrated on two-DOF system in Section 2.1 (see: Fig. 2.8). However, Algorithm 2 implicitly prevents from jerking of the controlled structure in this way.

When the joint is unlocked Equation (3.39) is used for estimation of the weighted energy transfer rate if locking. The joint is to be locked when $\dot{\hat{V}}_{Wk}(t)$ crosses zero or small threshold as shown in 6th line of Algorithm 2. By substitution of Equations (2.64) and (2.75) into Equation (3.39) we receive:

$$\dot{\hat{V}}_{Wk}(t) = -\underbrace{\dot{\hat{\boldsymbol{\eta}}}^{\mathrm{T}}_{\mathrm{M}}(t)\mathbf{W}_{\alpha}\rlap{$\overbrace{\phantom{\boldsymbol{\Delta\phi}_{\mathrm{M}k}c_{\max}\boldsymbol{\Delta\phi}^{\mathrm{T}}_{\mathrm{M}k}}}^{\boldsymbol{\Gamma}_{kmn}}$}\boldsymbol{\Delta\phi}_{\mathrm{M}k}}_{\delta^{\alpha}_{k}(t)}\underbrace{c_{\max}\boldsymbol{\Delta\phi}^{\mathrm{T}}_{\mathrm{M}k}\dot{\hat{\boldsymbol{\eta}}}_{\mathrm{M}}(t)}_{c_{\max}\Delta\dot{q}^{N_p}_{k}(t)}, \tag{3.42}$$

where: $\Delta\dot{q}^{N_p}_k(t)$ is relative velocity between rotational DOFs involved in kth lockable joint obtained from superposition of monitored modal velocities only, whereas $-c_{\max}\Delta\dot{q}^{N_p}_k(t)$ would be bending moment transmitted by kth lockable joint if this joint is suddenly locked, and $\delta^{\alpha}_k(t)$ is function of monitored modal velocities (if all $\alpha_p = 1$ then $\delta^{\alpha}_k(t) = \Delta\dot{q}^{N_p}_k(t)$). As the higher-order vibration modes are naturally mitigated when the joints are in the unlocked state one can assume that $\Delta\dot{q}^{N_p}_k(t) \approx \mathbf{l}^{\mathrm{T}}_k\dot{\mathbf{q}}(t) = \dot{q}_i(t) - \dot{q}_j(t)$, $t \in (t_{\mathrm{u}}, t_{\mathrm{l}}]$. Thus, from the equation above it follows that Algorithm 2 locks kth joint only when relative rotational velocity between adjacent beam ends $\dot{q}_i(t) - \dot{q}_j(t)$ or term $\delta^{\alpha}_k(t)$ crosses zero (or is close to zero when $\kappa_1 \neq 0$ is selected in Algorithm 2). Passing zero by the function $\delta^{\alpha}_k(t)$ simultaneously when $\dot{q}_i(t)$ and $\dot{q}_j(t)$ are significantly different is not expected, as the higher-order unlocked vibration modes are quickly mitigated. This phenomenon can take place only within short time t_{unlock} after the unlocking of any joint but Algorithm 2 prevents from that (lines 17 and 18). Thus, the proposed control algorithm locks the joints only for zero or very small relative rotational velocities of the adjacent beam ends preventing from large peak accelerations or operational wear provided by slipping of the frictional parts during the locking of the lockable joints.

It is demonstrated in Subsection 3.4.3 (second control scenario) that for undamped vibration of the two-DOF system the control algorithm does not prevent from the problem described above. However, if material damping is considered and the set of monitored vibration modes is appropriately selected the control algorithm does not lock any joint when rotational velocities of the adjacent beam ends differ significantly. It is shown and commented in Section 4.1.

3.4.2 Implementation for energy harvesting

Objective function

In the case of application of the proposed control methodology for energy harvesting purposes the goal is to transfer the mechanical energy to the selected vibration mode r to which the energy harvester is tuned. Thus, in simplest case one could pursue condition that rth modal energy transfer rate must be non-negative:

$$\dot{W}_r(t) \geq 0. \tag{3.43}$$

Then, function $V(t)$ that is to be minimised is written with negative sign of the modal energy:

$$V(t) = -E_r(t). \tag{3.44}$$

The above objective function cannot be called Lyapunov function because now it is not positive. Moreover, the energy associated with the targeted vibration mode is to be maximised instead of minimisation. Despite of this the control cannot destabilise the controlled structure in free vibration. The proposed methodology is of semi-active type and employs devices (here the lockable joints) that cannot introduce any additional energy into the structural vibration. The lockable joints do not perform any work over the structure when they are in the steady state (fully locked or fully unlocked), whereas in the transient state the can only dissipate the energy, as demonstrated in Section 2.1. Thus, in free vibration pth modal energy can increase only at the expense of the remaining modal energies as described in Section 2.2.4.

Adaptation of the objective function and control algorithm for energy harvesting application

Condition in (3.44) based only on the selected vibration mode is theoretically sufficient to formulate the control law. $\dot{W}_r(t)$ depends on the targeted modal velocity and other monitored modal velocities or bending moments, analogously to Equation (2.70). However, in practice it can be insufficient to provide efficient energy flow to the targeted vibration mode. Hence, conditions pursued also on the remaining monitored vibration modes from which energy is to be transferred out also are employed. It results in the methodology described in previous subsection but with different weighting parameters in matrix $\mathbf{W}_\alpha$. In this case weight corresponding with the selected vibration mode is negative:

$$\mathbf{W}_\alpha = \operatorname{diag}\left(\begin{bmatrix}\alpha_1 & \cdots & \alpha_r & \cdots & \alpha_{N_p}\end{bmatrix}^{\mathrm{T}}\right), \quad \alpha_r < 0, \quad \text{all } \alpha_p \geq 0. \tag{3.45}$$

In this case the control can be realised as shown in Algorithm 2 with weighting matrix as in Equation (3.45).

Modified weighting matrix $\mathbf{W}_\alpha$ does not change the jerk-limiting properties of the control algorithm. Equation (3.42) is still valid.

3.4.3 Illustrative example of control of the system with two degrees of freedom

In this subsection several control scenarios of the two-DOF system that is described in detail in Section 2.1 are discussed. It allows for better understanding basic properties before considering control of more realistic models and control cases shown in Chapter 4 and laboratory frame demonstrator in Chapter 5.

Due to the equivalence between exact and relaxed kinematic constraints which is discussed and demonstrated in Subsection 2.1.6 the operation of the lockable joint is represented in here only by the relaxed constraint by means of the viscous joint model. Except negligible amount of the damping provided by the utilised model of the lockable joint the system is undamped. Equations of motion are integrated with zero-order hold method (see: Equation (2.45) in Subsection 2.2.2). Integration step $\Delta t = 0.1$ ms is selected. It is assumed that full state of the system is known in all considered control scenarios. Thus, all unlocked vibration modes are monitored: $N_p = N_\mathrm{d} = 2$. As all the unlocked vibration modes are available for the control algorithm both forms of the estimated weighted modal energy transfer rate (Eqs (3.39) and (3.41) or lines 5 and 11 in Algorithm 2, respectively) are equivalent according to Equation (2.70). Moreover, estimated weighted modal energy transfer rate $\dot{\widehat{V}}_W(t)$ is equal to its exact value $\dot{V}_W(t)$. κ_1, κ_2, t_lock and t_unlock are selected equal to zero.

Modal energy transfer to the first unlocked vibration mode

The first considered scenario is free vibration with initial condition: $\mathbf{q}_0 = 0.02\,\boldsymbol{\phi}^{(2)}$ and $\dot{\mathbf{q}}_0 = \mathbf{0}$ that means that the two-DOF system has potential energy in only second mode which is released in free vibration. The aim of the control is to transfer this energy to the first, targeted, unlocked vibration mode by locking and unlocking the joint in suitable time instances. To this aim the following weights are selected: $\alpha_1 = -1$ and $\alpha_2 = 0$ (see: Eq.: (3.40)). By pursuing only one non-zero weight α_1 the weighted modal energy transfer rate that is to be minimised has the following form:

$$\dot{V}_W(t) = -\dot{\eta}_1(t)\alpha_1 \begin{bmatrix}\gamma_{11} & \gamma_{12}\end{bmatrix} \begin{bmatrix}\dot{\eta}_1(t) \\ \dot{\eta}_2(t)\end{bmatrix} = \dot{\eta}_1(t)\alpha_1 \Delta\phi^{(1)} f(t). \tag{3.46}$$

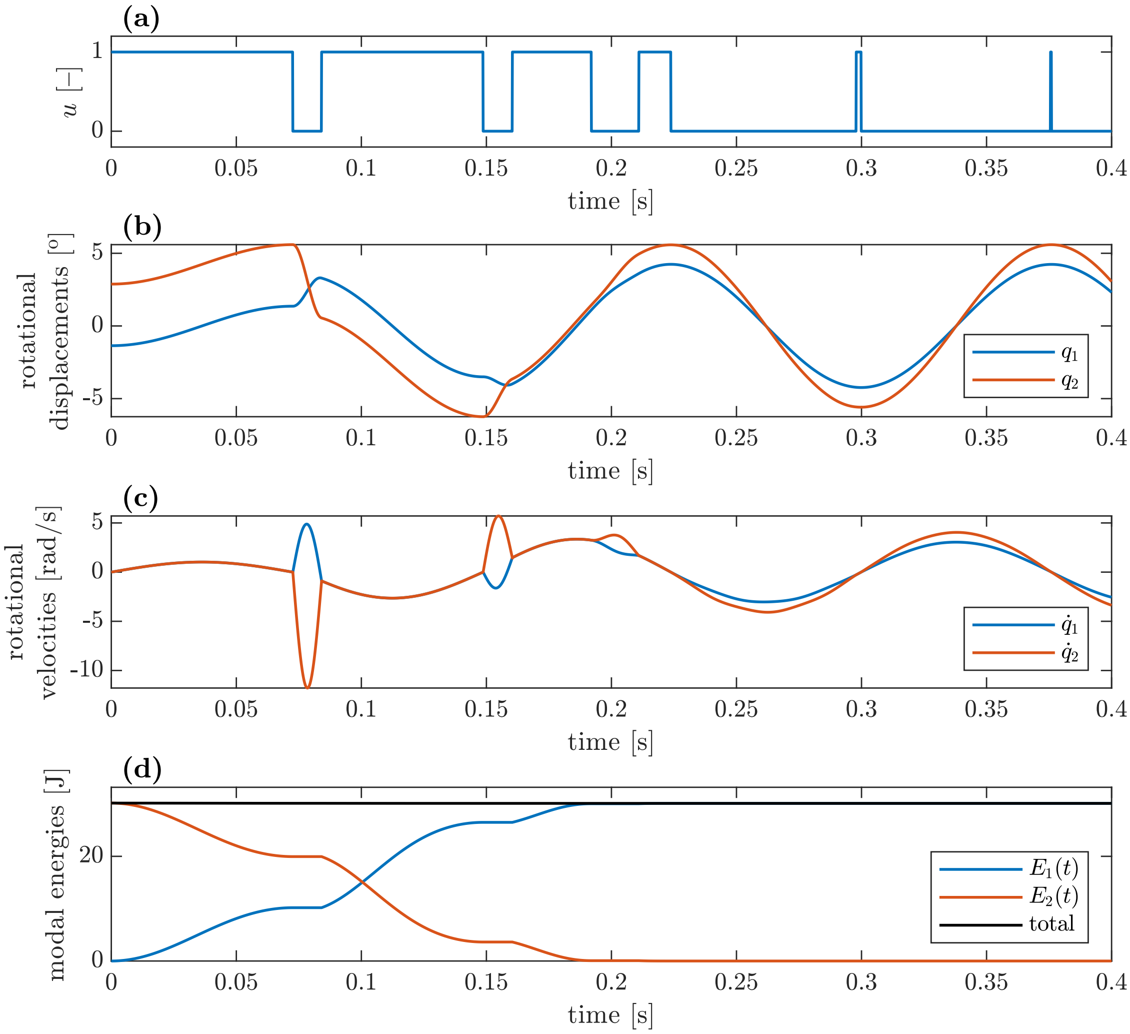

Figure 3.3: Energy transfer from the second unlocked mode (initial, $\alpha_2 = 0$) of the two-DOF system to the first one (targeted, $\alpha_1 = -1$); time histories of: (a) control signal, (b) rotational displacements, (c) rotational velocities and (d) participation of the modal energies in mechanical energy of the system

Results are shown in Figure 3.3. It is evident that locking effect of the joint causes modal coupling resulting in energy flow between unlocked vibration modes (compare Figs 3.3a and d). Due to the proposed control algorithm the joint is locked and unlocked in suitable time instances. The joint is locked when the modal energy transfer has profitable direction, whereas it is unlocked when the sign of the modal energy transfer rate changes. It allows for monotonic change of the modal energies as opposed to results shown in Figure 2.9, where joint once permanently locked allows for repetitive and alternate energy transfer between vibration modes.

It is also evident that the algorithm locks the joint when rotational velocities have the same value (Fig. 3.3c). Thus, in this case there is no any energy loss in the lockable joint resulting from the ideally inelastic collision (compare with Fig. 2.8), as mentioned in Subsection 3.4.1.

It is worth to notice that the most of the mechanical energy is transferred to

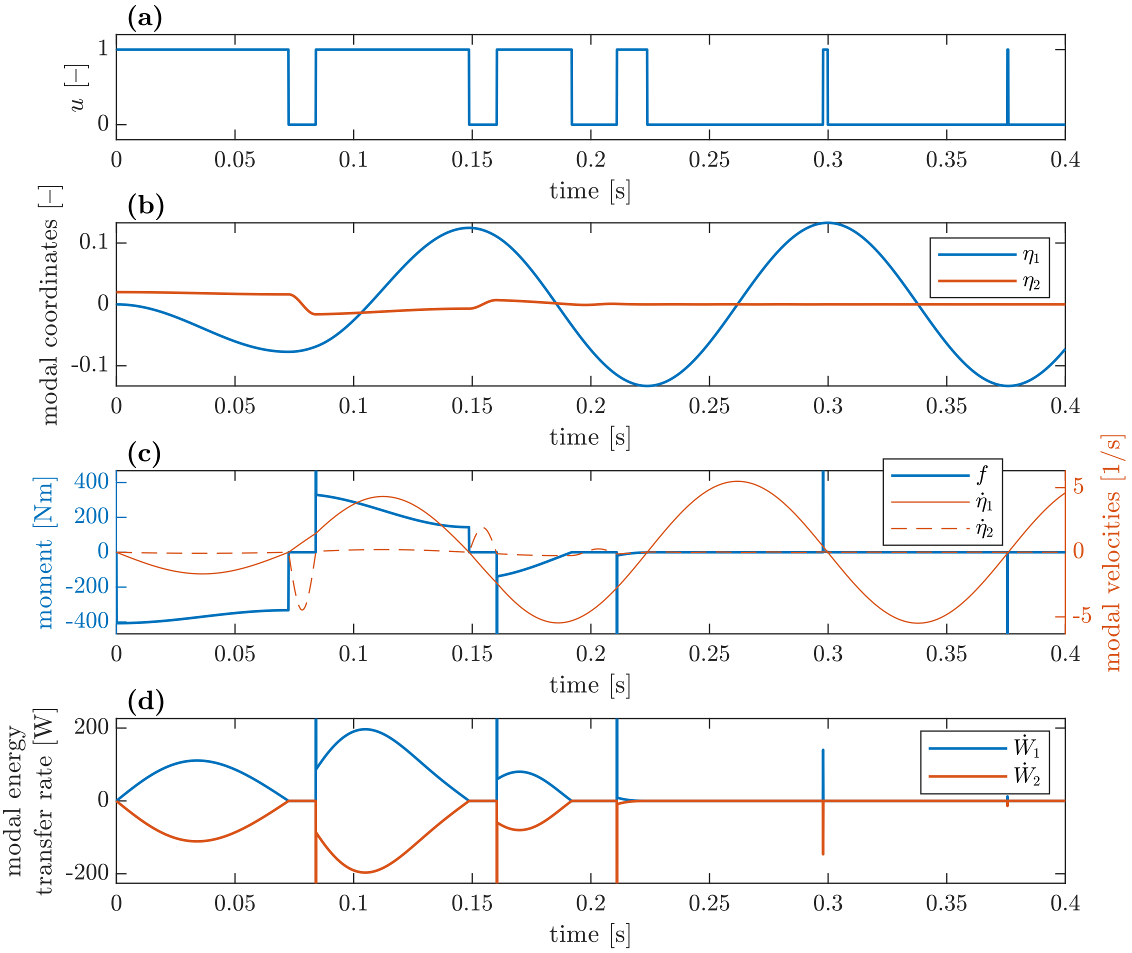

Figure 3.4: Energy transfer from the second unlocked mode (initial, $\alpha_2 = 0$) of the two-DOF system to the first one (targeted, $\alpha_1 = -1$); time histories of: (a) control signal, (b) modal coordinates, (c) bending moment transmitted via lockable joint along with modal velocities (d) modal energy transfer rates for both unlocked vibration modes

vibration in the first unlocked mode after two cycles (locking and unlocking) of the joint (Fig. 3.3d).

Figure 3.4 allows for better understanding the energy transfer phenomenon. Locking effect resulting in quasi-constant Δq (quasi-constant due to relaxed kinematic constraint) is especially visible in time history of the second modal coordinate in Figure 3.4b. (compare with Figure 3.3b).

Figure (3.4)c shows all "measured" quantities required for calculation of $\dot{V}_W(t)$ (see: Eq. (3.46)), whereas modal energy transfer rates to each particular vibration mode (see: Eq. (2.70)) also are shown in Figure 3.4d. It is evident that $\dot{W}_1(t) \approx -\dot{W}_2(t) > 0$ (if $c_{\max}$ tends to infinity then $\dot{W}_1 = -\dot{W}_2(t)$ would be satisfied) analogously to Equations (2.73) and (2.74) despite of the fact that only α_1 is selected nonzero.

Peak-like transient states visible in Figs (3.4)c and d is a numerical side-effect of the selected step size in the numerical integration. Numerical procedure cannot perfectly hit the point where $\dot{q}_1(t) = \dot{q}_2(t)$. This effect can be reduced by changing the step size towards smaller values. However, step sizes smaller than currently selected does not affect remaining parts of time histories.

Results shown in Figure 3.4c allows for better understanding why the control algorithm locks the joints when $\dot{q}_1(t) \approx \dot{q}_2(t)$. First, using analogous derivations as in Equation (3.42) the weighted modal energy transfer rate for the two-DOF system in Equation (3.46) can be rewritten into the form:

$$\dot{V}_W(t) = -\dot{\eta}_1(t)\alpha_1 c_{\max}\Delta\phi^{(1)} \underbrace{\begin{bmatrix}\Delta\phi^{(1)} & \Delta\phi^{(2)}\end{bmatrix}\begin{bmatrix}\dot{\eta}_1(t)\\ \dot{\eta}_2(t)\end{bmatrix}}_{\dot{q}_1(t)-\dot{q}_2(t)}. \tag{3.47}$$

Algorithm locks or unlocks the joint when the term above changes its sign. It takes place only when the targeted modal velocity $\dot{\eta}_1(t)$ or relative rotational velocity between rotational DOFs $\dot{q}_1(t) - \dot{q}_2(t)$ crosses zero. By comparing Figures 3.3c and Figure 3.4c one can see that only the former case occurs. The first case is possible but is not expected when the first modal velocity that corresponds to the nonzero weight participates significantly in the structural motion.

Step-like increments and decrements of the transmitted bending moment $f(t)$ result from the fact that the two-DOF system is consisted of two ideally rigid rods that are connected via rotational spring in parallel with the lockable joint (Fig. 2.2). If joint is locked at time instance when $\Delta q \neq 0$ then moment $f(t)$ not only balances the inertia forces in the system but also the moment provided by the second rotational spring. This results in piece-wise constant components of time history of $f(t)$, whereas the varying components relate to balancing the inertia forces. In the next chapter the transmitted bending moments represented by measured strains have not step-like character due to the fact that the considered structures do not contain any rotational spring connected in parallel to the lockable joint.

Modal energy transfer to the second unlocked vibration mode

Regarding the transfer of the energy in opposite direction, i.e. from the first unlocked vibration mode to the second one, it is allowable to pursue weights: $\alpha_1 = 0$ and $\alpha_2 = -1$. It provides efficient energy flow analogously to the case described above. However, to show that it is possible to transfer the energy between two vibration modes in both directions by changing the sign of only the first weight the following weights are selected: $\alpha_1 = 1$ and $\alpha_2 = 0$. In result, Equation (3.46) refers also to current selection of weights. Other parameters of the algorithm remain unchanged. The two-DOF system vibrates freely, where initial conditions are: $\mathbf{q}_0 = 0.1\,\boldsymbol{\phi}^{(1)}$ and $\dot{\mathbf{q}}_0 = \mathbf{0}$. Results for this case are shown in Figure 3.5.

It is evident that energy transfer from the first unlocked vibration mode to the second one is efficient until the third unlock of the joint (closely before $t = 0.2$ s). Within this time almost whole mechanical energy initially accumulated in the first

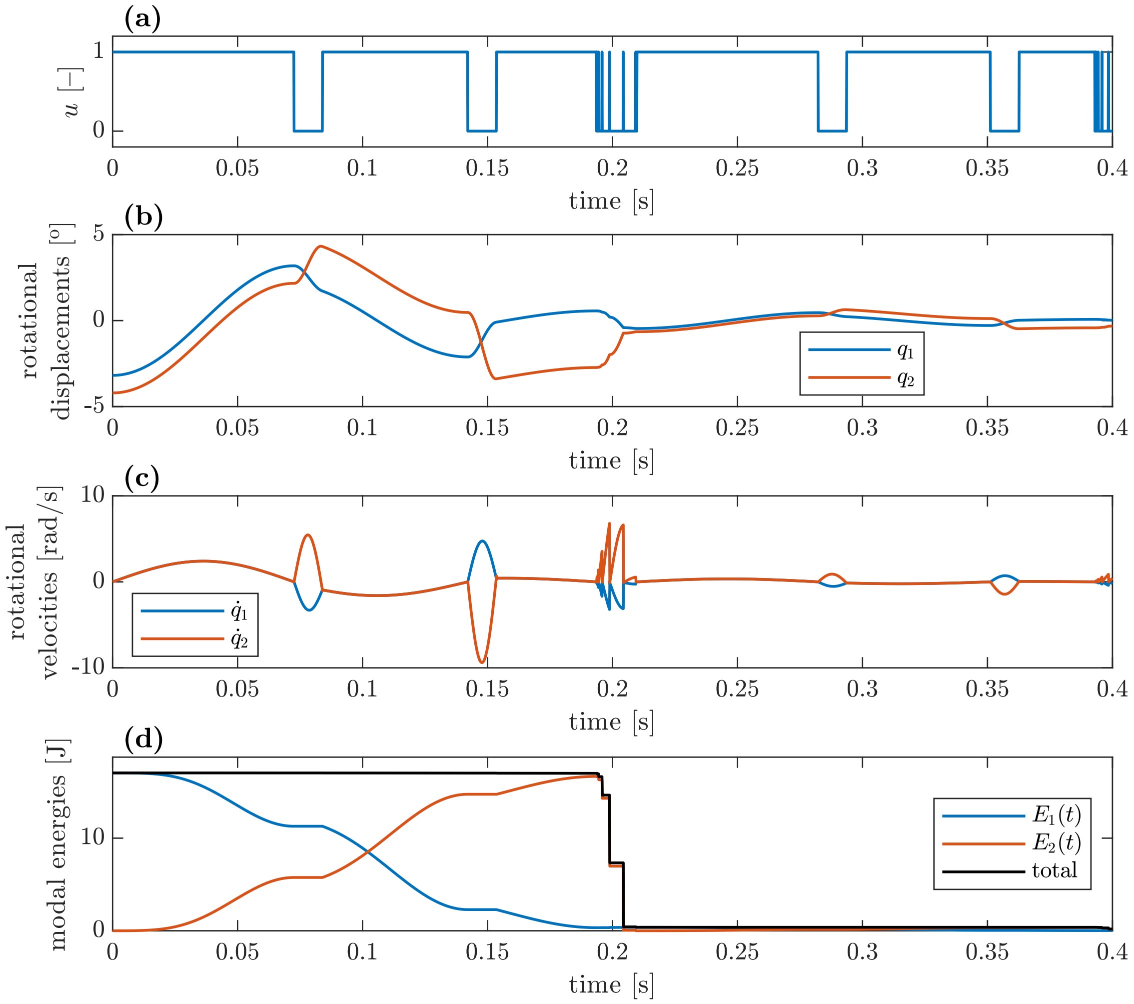

Figure 3.5: Energy transfer from the first unlocked mode (initial, $\alpha_1 = 1$) of the two-DOF system to the second one (targeted, $\alpha_2 = 0$); time histories of: (a) control signal, (b) rotational displacements, (c) rotational velocities and (d) participation of the modal energies in mechanical energy of the system

unlocked vibration mode is transferred out from this mode (accordingly to $\alpha_1 > 0$) and directed to the second vibration mode.

After the third joint unlock the control algorithm locks the joint at time instances when the structural members have significantly different rotational velocities (Fig. 3.5c). It results in the energy loss (Fig. 3.5d) in inelastic collisions at the lockable joint. This problem results from the fact that the unlocked vibration mode related to weight α_1 participate negligibly in the structural motion when the most of its energy is transferred out to the second unlocked vibration mode that then becomes predominant. Hence, it is highly probable that the first modal velocity crosses zero $\dot{\eta}_1(t) = 0$ when $\dot{\eta}_2(t)$ is significantly different from zero. It results in the change of sign of $\dot{V}_W(t)$ when $\dot{q}_1(t) \neq \dot{q}_2(t)$ is far from zero. This phenomenon is visible in Figure 3.6b (compare with Fig. 3.5c). Such a situation does not occur in the previous case of scenario (transfer to the first unlocked mode) because the nonzero weight is assigned to the targeted mode that is becomes predominant, as

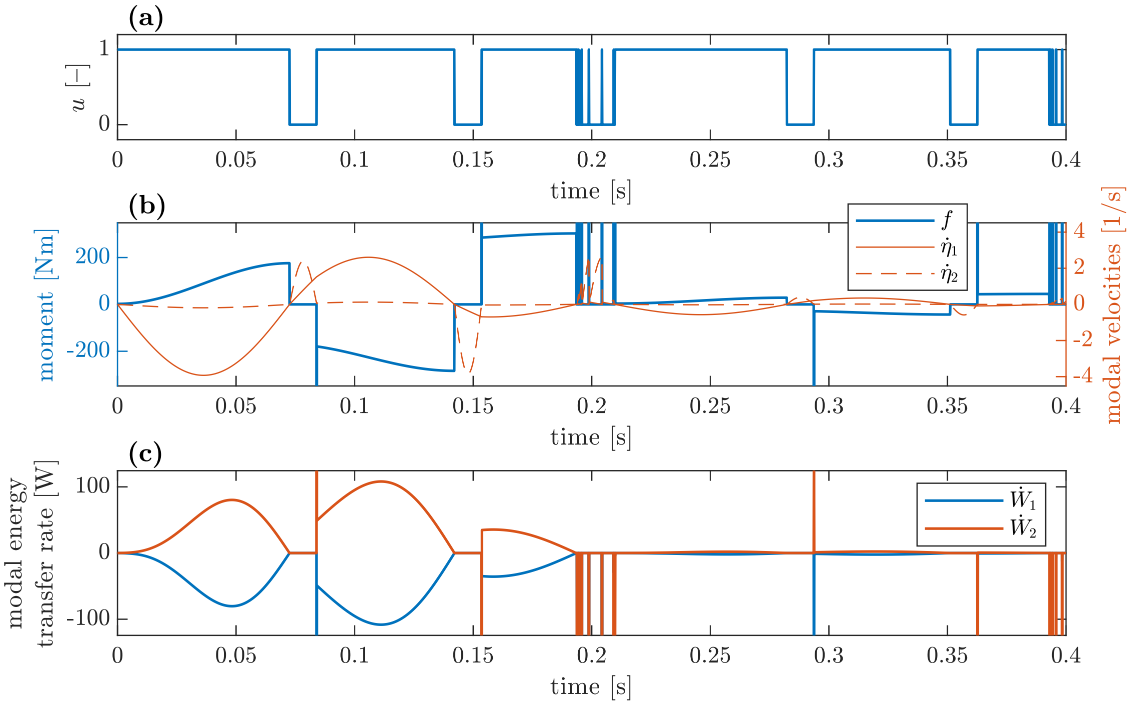

Figure 3.6: Energy transfer from the first unlocked mode (initial, $\alpha_1 = 1$) of the two-DOF system to the second one (targeted, $\alpha_2 = 0$); time histories of: (a) control signal, (b) bending moment transmitted via lockable joint along with modal velocities and (c) modal energy transfer rates for both unlocked vibration modes

opposed to the present case (Fig. 3.4b and c).

When significant amount of the energy is dissipated in the inelastic collisions, as shown in Figure 3.5d, the modal energy transfer rates can be unbalanced (their sum differs from zero) as shown in Figure 3.6d. The reason is that constraint in Equation 2.40 is not satisfied during these collisions. It turns in the fact that Equations (2.72)-(2.74), describing the balance of the modal energy transfer, also are not fulfilled. In other cases imbalance of the peaks of the modal energy transfer rates also can occur, but it does any significant impact on time histories of modal energies if joints are locked when $\dot{q}_1(t) \approx \dot{q}_2(t)$.

The locking of the joint when $\dot{q}_1(t) \neq \dot{q}_2(t)$ can be overcame in several ways. The first is setting parameters κ_1, κ_2, t_{lock} and t_{unlock} different from zero e.g. with the trial-and-error method. Also assigning the both weights nonzero, e.g. $\alpha_1 = 1$ and $\alpha_2 = -1$ allows for avoiding of locking the joint when $\dot{q}_1(t) \neq \dot{q}_2(t)$, as shown in Figure 3.7.

Problem of locking of the joint when $\dot{q}_1(t) \neq \dot{q}_2(t)$ does not occur in MDOF structures when the control aims at vibration damping. In this case, similarly to the above considerations, the vibration energy is transferred out from the monitored lower-order unlocked vibration modes (that have nonzero weights) into the remaining, higher-order ones that are not monitored. The problem is naturally avoided in those examples because after each unlock of the joint this energy is released in high-frequency vibration and then dissipated in the inherent material damping of

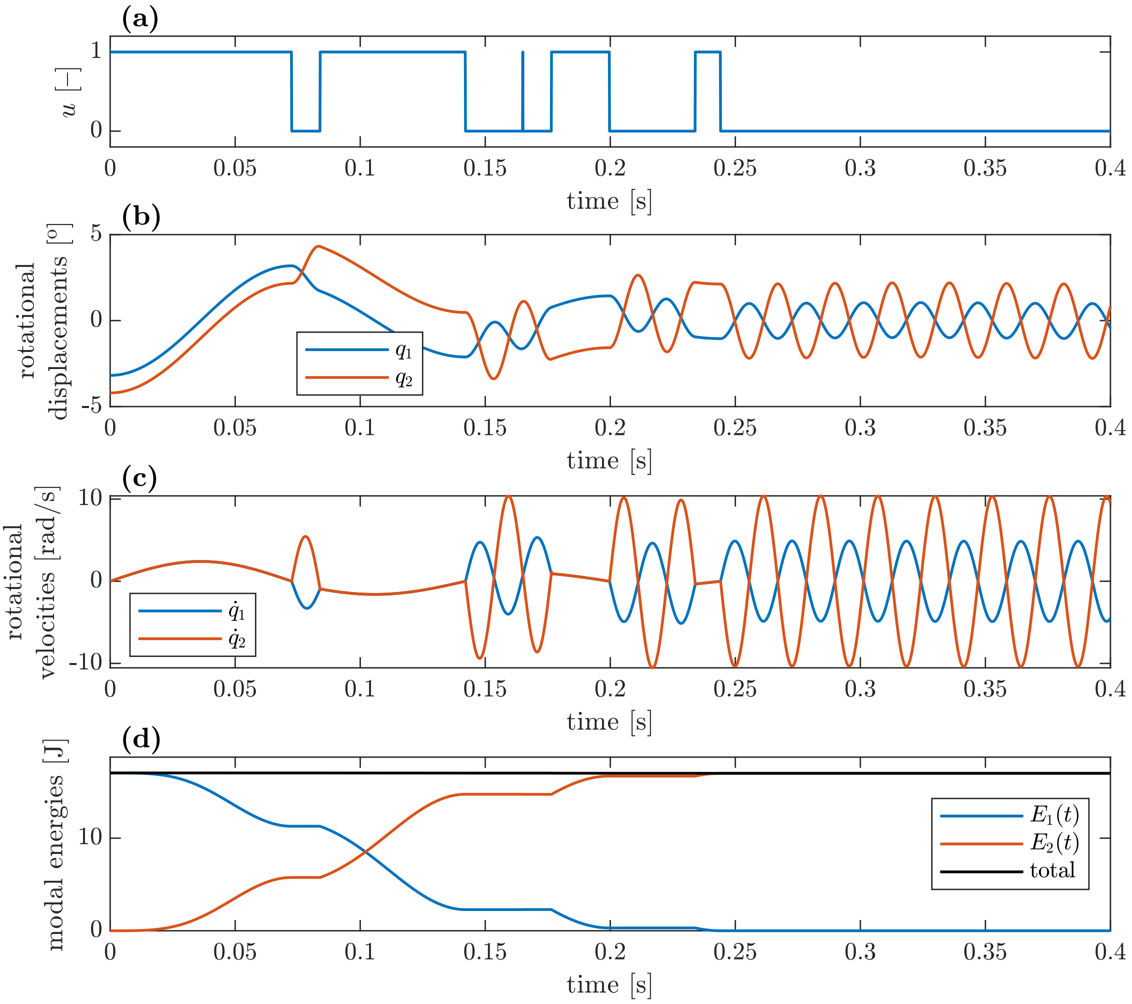

Figure 3.7: Energy transfer from the first unlocked mode (initial, $\alpha_1 = 1$) of the two-DOF system to the second one (targeted, $\alpha_2 = -1$); time histories of: (a) control signal, (b) rotational displacements, (c) rotational velocities and (d) participation of the modal energies in mechanical energy of the system

the structure. Due to the efficiency of this damping mechanism the high-frequency vibrations vanish after each joint unlock within the time usually shorter than preselected time interval t_{unlock} (see: line 18 in Algorithm 2). Thus, even if monitored modal velocities tend to zero in vibration mitigation process the unmonitored modes do not affect the control, since they are also mitigated as demonstrated in Subsection 4.1.

Illustrative examples above demonstrate that the proposed control methodology based on instantaneous minimisation of the weighted energy transfer rate can be effective and it is worth to be investigated on more complex and realistic examples as in next chapter. Experimental verification is provided in Chapter 5.

Chapter 4

Numerical study

The potential of the proposed methodology both in vibration attenuation and energy harvesting is illustrated in this chapter on various types of excitation. Section 4.1 compares performance of the proposed control in vibration damping with PAR approach on two configurations of the structure: with optimally and non-optimally placed lockable joints. Efficacy of the proposed control methodology in enhancing of the energy harvesting is tested for two configurations of relatively smaller structure with the attached EMEH in Section 4.2. In all tests the full state of the controlled structure is not known. Instead, measurement data as described in Section 3.1 are employed for control algorithms proposed in Section 3.4. Methods for sensor and lockable joint placement (see: Sections 3.2 and 3.3) ensuring efficient operation of the control algorithm also are adopted.

4.1 Vibration attenuation

In this section efficiency of Algorithm 2 for vibration attenuation is demonstrated. For comparison purposes PAR control strategy which is known as one providing efficient vibration damping by means of the lockable joints also is employed as a benchmark. It is described below. In further subsections both strategies are tested and compared on eight-bay frame structure equipped with one pair of the lockable joints with their two selected locations. In one case the pair of the lockable joints is placed optimally demonstrating potential performance of both compared methods (Subsection 4.1.2). In the next case the placement of the lockable joints is non-optimal allowing assessment the robustness of the vibration control approaches (Subsection 4.1.3). For both configurations of the lockable joints the structure is subjected to various excitations.

4.1.1 Prestress accumulation–release (PAR) as a benchmark

In PAR control only strains $\boldsymbol{\varepsilon}_{\mathrm{M}}(t)$ are measured as described in Subsection 3.1. Here, the lockable joints are kept mainly in the locked state. During the motion of

Table 4.1: Dimensions and properties of the eight-bay structure

Quantity	**Symbol**	**Unit**	**Value**
Bay side length	L	mm	600
Offset of the strain gauges	x_ε	mm	50
Young modulus	E	Pa	$210 \cdot 10^9$
Material density	ρ	kg/m^3	7860
Cross section: height × width	$h \times b$	mm	8×10
Mass of the lockable joint	m_J	kg	1.2

the structure the measured strains $\boldsymbol{\varepsilon}_\mathrm{M}(t)$ increase that corresponds with increasing potential energy. Some part of this energy is accumulated in the higher-order unlocked vibration modes. When the strains reach their maximum values the joints are unlocked for short time moment t_unlock. Then, strain energy is released in free vibration of higher-order unlocked vibration modes and quickly dissipated in material damping. Simultaneously, strains are relaxed. After re-locking of the joints the whole procedure is repeated.

The kth joint is unlocked if the condition below is satisfied.

$$\frac{\varepsilon^2_{\mathrm{M}k}(t) - \varepsilon^2_{\mathrm{M}k}(t - \Delta t)}{\Delta t} < -\kappa_\varepsilon \tag{4.1}$$

Δt is integration step or sampling period and κ_ε is selected threshold. $\varepsilon^2_{\mathrm{M}k}(t)$ is assumed to be near-proportional to the strain energy accumulated in the higher-order unlocked vibration modes and left hand side of Equation (4.1) represents its derivative.

4.1.2 Eight-bay smart structure equipped with two optimally placed lockable joints

The considered structure that is to be controlled is shown in scheme in Figure 4.1a. Characteristic dimensions and physical properties are listed in Table 4.1. FE model of the structure is shown in Figure 4.1b. The structure is discretized with one beam-type FE per each bay side. FEs are based on Euler-Bernoulli beam theory and have cubic shape functions. The beams are assumed to be non-extensible due to the fact that longitudinal vibration usually have significantly smaller participation than transversal vibration of the beams for the structure of such dimensions. The FE model has $N_\mathrm{d} = 26$ DOFs. Viscous damping coefficient $c_\mathrm{max} = 3 \cdot 10^4$ Nms/rad has been selected and allows for simulation of the joint in the locked state as rigid connection.

The first three unlocked vibration modes of the structure are selected to be monitored. Mode shapes calculated for the unlocked state of the joints are considered for the design of the controller. They are shown in Figure 4.2 along with modes obtained for the joints in the locked state.

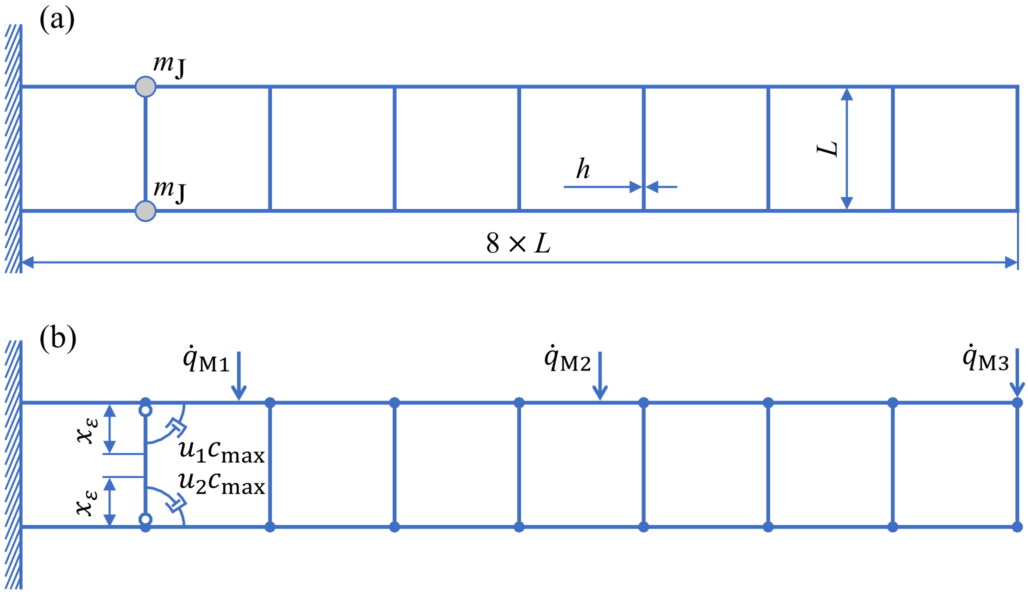

Figure 4.1: Eight-bay structure equipped with two lockable joints: (a) scheme of the structure and (b) FE model with indicated sensor locations [145]

Three sensor locations shown in Figure 4.1b are selected using Algorithm 1 described in Section 3.2. Measured strains at the distance x_ε from the joint axes are simulated from structural displacements with known shape functions of the FEs and dimensions of the cross section.

Optimal locations of the lockable joints, visible in Figure 4.1, have been selected according to the highest controllability metric G defined as in Equation (3.29), where weights β_p are selected as the reciprocals to the natural frequencies. Figure 4.3 shows mode controllability metrics for each transversal beam potentially equipped with lockable joints (including the selected one). For each beam that could be equipped with the lockable joints the mode shapes and natural frequencies are obtained and then Equation (3.29) is evaluated, since mass of the lockable joints in different locations affects dynamics of the structure.

Proportional material damping $\mathbf{C} = \alpha \boldsymbol{\Phi}^\mathrm{T}\mathbf{M}\boldsymbol{\Phi} + \gamma \boldsymbol{\Phi}^\mathrm{T}\mathbf{K}\boldsymbol{\Phi}$ is frequently used due to the property of keeping modes uncoupled. However, it is difficult to assign suitable damping level both for lower-order modes and the higher-order ones using this model. Hence, model combining classical proportional material damping and equal modal damping is used according to the equation below.

$$\mathrm{diag}(2\omega^{(m)}\zeta^{(m)}) = \boldsymbol{\Phi}^\mathrm{T}\mathbf{C}\boldsymbol{\Phi} = \underbrace{\alpha \mathbf{I}}_{\alpha \boldsymbol{\Phi}^\mathrm{T}\mathbf{M}\boldsymbol{\Phi}} + \beta \boldsymbol{\Omega} + \underbrace{\gamma \boldsymbol{\Omega}^2}_{\gamma \boldsymbol{\Phi}^\mathrm{T}\mathbf{K}\boldsymbol{\Phi}} \tag{4.2}$$

In this study $\alpha = 0$, $\beta = 0.015$ and $\gamma = 5.7278 \cdot 10^{-4}$ that results in modal damping ratios $\zeta^{(1)} = 1\%$, $\zeta^{(2)} = 1.55\%$ and $\zeta^{(3)} = 2.19\%$. Relation between modal damping ratios and natural frequencies is shown in Figure 4.4.

The structure described above is used to assess the proposed control methodology

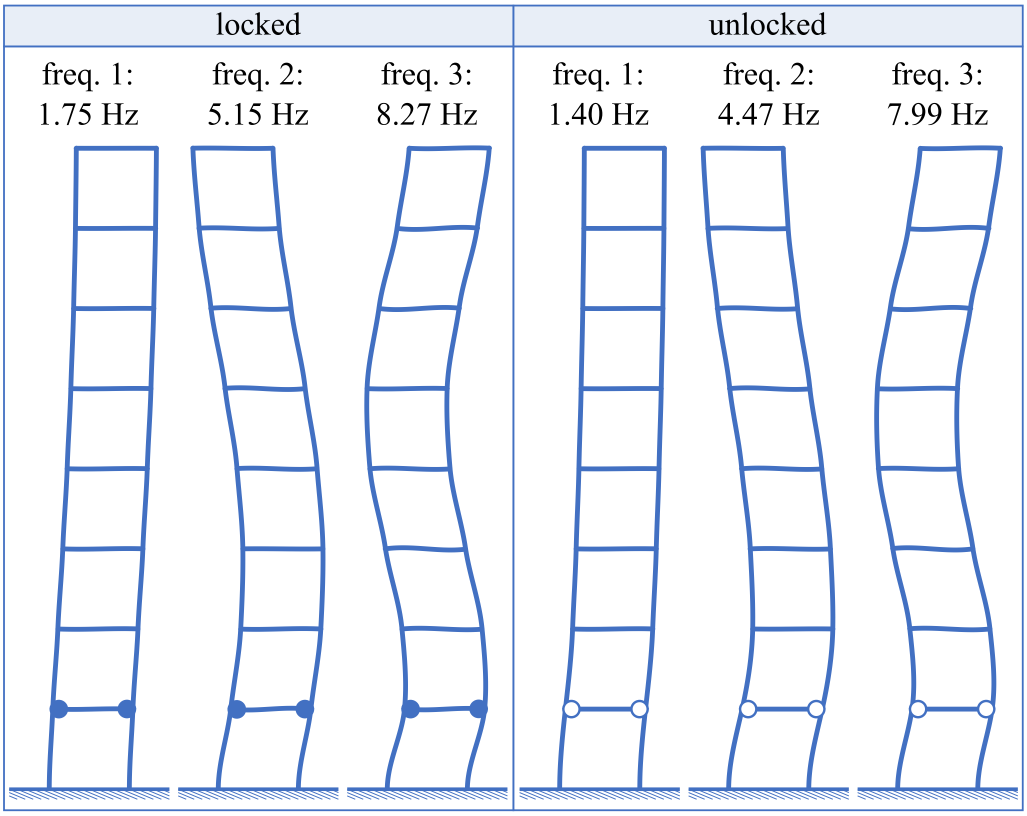

Figure 4.2: First three vibration modes for both locked and unlocked lockable joints

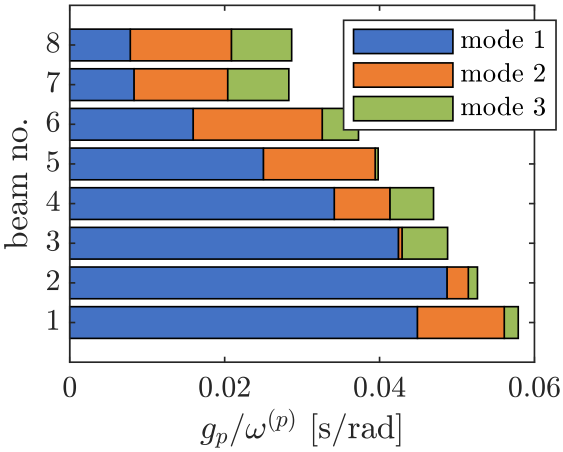

Figure 4.3: Controllability metrics of the monitored unlocked vibration modes for particular locations of the pair of the lockable joints

and compare it with PAR in three cases of excitation:

case 1 free vibration caused by sudden stop of the support motion,

case 2 harmonic force excitation and

case 3 kinematic noise excitation.

In all cases of excitation of the structure with optimally placed lockable joints the following parameters are selected to be used with Algorithm 2: $\alpha_p = 1/\omega^{(p)2}$,

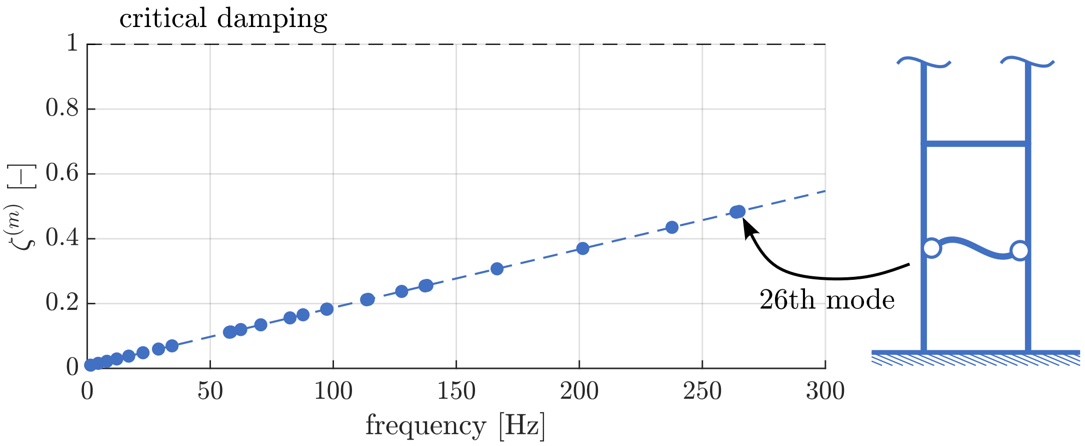

Figure 4.4: Modal damping factors in dependence of the natural frequencies of the structure

$t_{\mathrm{lock}} = t_{\mathrm{unlock}} = 12$ ms, $\kappa_1 = 0.03$ W and $\kappa_2 = 0.0005$ W. Remaining required parameters are calculated from modal data and structural dimensions. Parameter $\kappa_\varepsilon = 30$ and the same time interval $t_{\mathrm{unlock}} = 12$ ms for PAR method are selected. Equations of motion are rewritten into the state equations and integrated as shown in Equation (2.45) with time step $\Delta t = 1$ ms.

Case 1 In this case excitation represents sudden stop of motion of the structural support, while before this event the support along with the structure was in transversal motion. This kind of excitation can represent operation of many flexible mechanical systems, especially deployment of light-weight space structures which also are within the range of the potential applications. Initial condition on velocities

$$\dot{\mathbf{q}}_0 = -\mathbf{l}_{\mathrm{x}} v_0, \tag{4.3}$$

where $\mathbf{l}_{\mathrm{x}}$ is Boolean vector selecting DOFs representing horizontal displacements and v_0 is support velocity before the sudden stop, is applied. $v_0 = 0.5$ m/s is selected. Results of simulation with the proposed modal control are shown in Figure 4.5.

Lockable joints are controlled symmetrically (Fig. 4.5a) due to the fact that unlocked mode shapes have the same relative opening angles between beams connected via left and right lockable joint (Fig. 4.2, “unlocked”) and the fact that measured strains are also symmetric for this kind of excitation (Fig. 4.5c). Thus, also the response of the lockable joints for such a excitation is symmetric.

It is evident that when joints become locked ($u_k = 1$) modal energies of the monitored unlocked modes change their value due to the introduced modal coupling (Fig. 4.5b). Two following observations should be noticed. First, their energy is transferred to the higher-order unlocked vibration modes. The measured strains that are then increasing as shown in Figure 4.5c. It shows that the higher-order unlocked vibration modes accumulate mainly the potential energy. When total energy of the higher-order unlocked vibration modes has significant value (but not

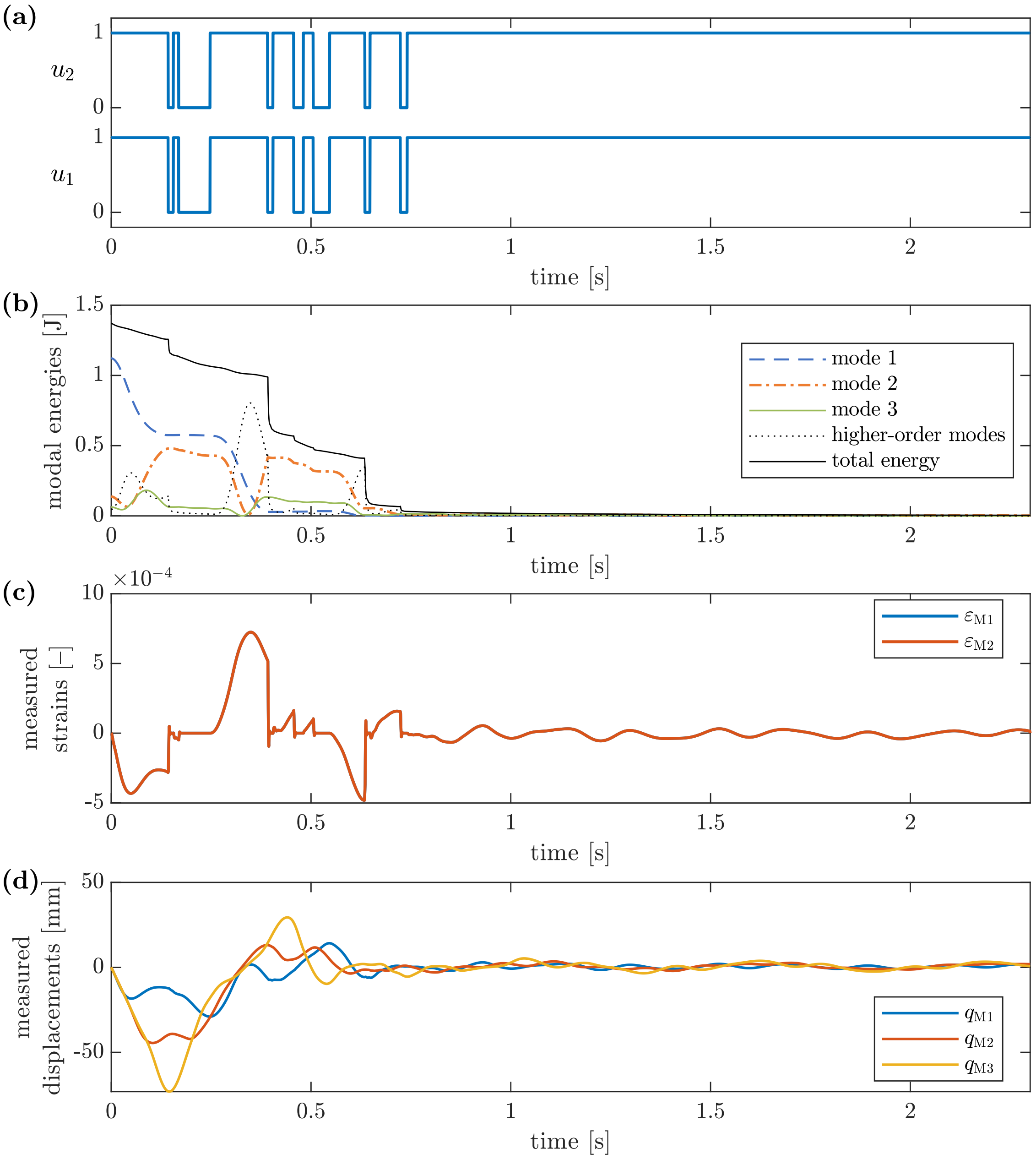

Figure 4.5: Time histories of: (a) control signals, (b) modal energies of the structure, (c) measured strains and (d) structural displacements at sensor locations for case 1 of excitation and modal control approach

necessary in the maximum) the joints are unlocked and the strain energy is released into free vibration of the structure in the higher-order unlocked vibration modes. Significant damping coefficients of these modes and their high frequencies cause quick dissipation of their energy and sudden decrease of the measured strains. The second observation is that energy is also transferred within monitored unlocked vibration modes from lower-order to higher-order ones (e.g. from the first to the second one) due to the weights α_p decreasing with the mode order. Thus, it is evident that weights α_p allow for imposing of the priority of particular vibration modes to be damped.

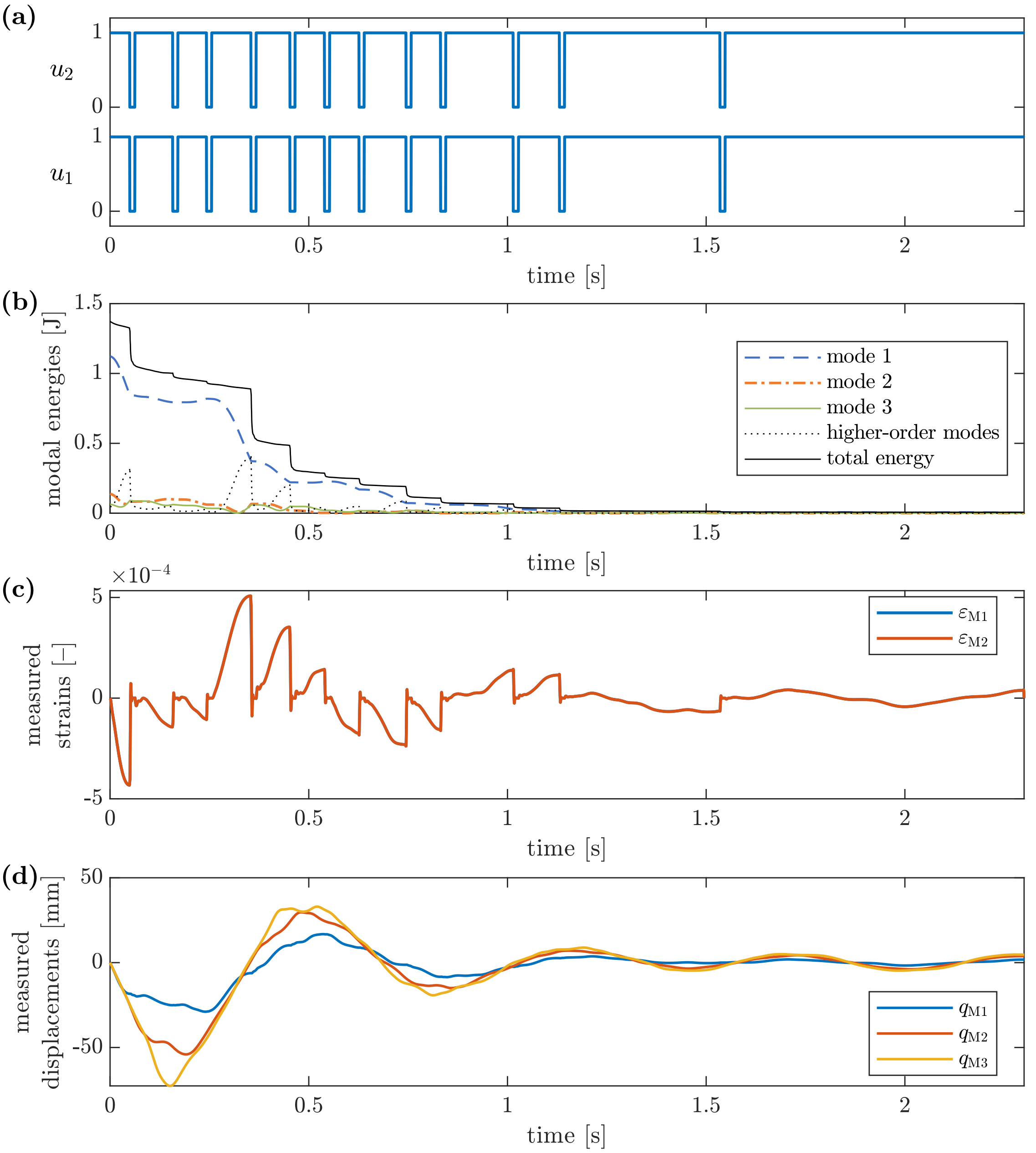

Figure 4.6: Time histories of: (a) control signals, (b) modal energies of the structure, (c) measured strains and (d) structural displacements at sensor locations for case 1 of excitation and PAR control approach

It is worth to notice that quick decrements of the structural energy occur only after joint unlock due to the mechanism described above. There is no any significant loss of the kinetic energy during the joint lock since control algorithm locks the joints when rotational velocities of the adjacent beam ends are equal or very close as commented in Subsection 3.4.1 (see: comments to Eq. (3.42)). The control algorithm locks the joint when the estimated weighted energy transfer rate crosses zero. It usually takes place when relative rotational velocity between beam ends connected via joint that is to be locked also crosses to zero. This property of the control algorithm allows for avoiding harmful effects like large transient accelerations which

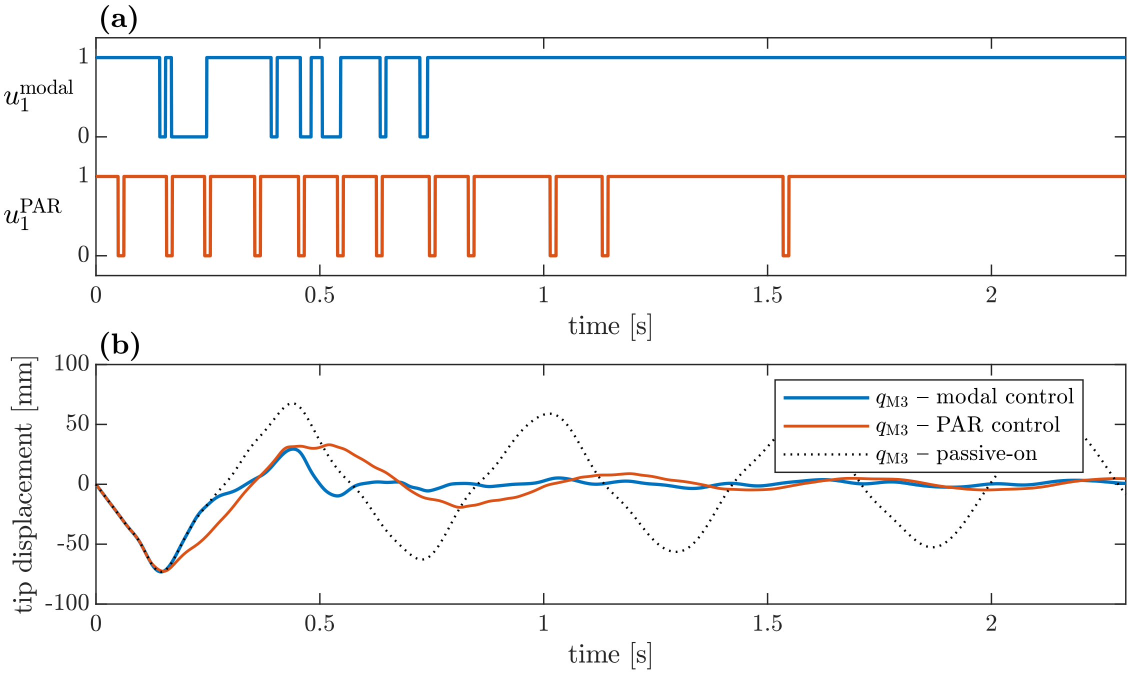

Figure 4.7: Comparison of modal and PAR control strategies for excitation case 1: (a) control signals and (b) structural tip displacements accompanied with the structure with locked joints

are demonstrated on the two-DOF system in Figures 2.8.

There are three reasons of assigning weights decreasing with the order of the monitored unlocked vibration modes. The first one is that the lower-order unlocked vibration modes are associated with weak material damping and thus they should be mitigated by the control with the higher priority. The second reason is lowest-order vibration modes usually have biggest participation in the structural motion and are easy to be excited by the external force. Hence, focusing on mitigation of the lower-order unlocked modes allows for effective mitigation of structural response, as shown in Figure 4.5d. Finally, such a selection of the weights results in smaller number of switches of the lockable joints due to the lower natural frequencies of lower-order unlocked vibration modes. It will be shown in the further part of the comparison of the modal control with PAR approach.

Analogous results for PAR control strategy are shown in Figure 4.6. Here, response of the lockable joints is also symmetric due to symmetric measured strains (Figs 4.6a and c).

Despite the fact that the control law is not based explicitly on the energy transfer phenomenon, PAR control also causes energy flow between unlocked vibration modes due to the modal coupling effect introduced by the lockable joints (Fig. 4.6b). However, PAR algorithm unlocks the joints in each local extreme of measured strains that is assumed to correspond with maximal energy of the higher-order unlocked vibration modes to be released in free vibration.

As opposed to modal approach, PAR algorithm does not use information about

Table 4.2: Comparison of various metrics of the control performance for modal and PAR approaches, and passively locked joints for the excitation case 1

Control type	RMS(q_{M1}) [mm]	RMS(q_{M2}) [mm]	RMS(q_{M3}) [mm]	$\overline{E}$ [J]	n_{J} [–]
Modal	7.36	12.51	16.13	0.260	28
PAR	9.53	17.07	20.47	0.227	48
Passive-on	11.54	29.59	38.54	0.896	0

global state of the structure in the form of modal velocities as well as does not use any weights assigned to particular unlocked vibration modes. It makes PAR approach simpler but also more sensitive to local strain maxima resulting in greater number of redundant joint unlocks. Additionally due to predominant participation of the first unlocked vibration mode in the whole vibration-mitigation process the displacements are greater in PAR approach despite similar total energy level.

Comparison of modal and PAR approach is shown in Figure 4.7 and in Table 4.2. The quantities in Table 4.2 are: RMS($q_{\mathrm{M}s}$) – root-mean-square value of the displacement, $\overline{E}$ – mean structural energy and n_{J} – total number of switches of all lockable joints.

It is evident that both methods compared effectively mitigate the vibration (Fig. 4.7b). Modal control achieves slightly greater mean energy of the structure (Tab. 4.2), but displacement RMS are significantly lower. It confirms that additional insight into structural state in the form of modal velocities and assigning the higher weights α_p to the lower-order unlocked vibration modes allows for better reduction of the low-frequency oscillations that usually are characterised by the biggest displacements. Moreover, due to these additional information used by the modal control it requires near two times less joint switches to mitigate vibration than PAR approach.

Case 2 In this case harmonic force excitation

$$f_{\mathrm{exc}}(t) = A_f \sin \Omega_f t, \tag{4.4}$$

acts on the structure at the point shown in Figure 4.8. This location allows for excitation of all three monitored unlocked vibration modes (see: Fig. 4.2), since it is not the node of any of these modes.

In this test the structure controlled with modal and PAR approaches, and with passively locked joints are excited in various excitation frequencies within range $\Omega_f \in 2\pi[1, 10]$ rad/s. Excitation amplitude $A_f = 4$ N. For each excitation frequency the vibration duration was calculated as

$$T(\Omega_f) = 45\ \mathrm{s} \cdot \widetilde{\omega}^{(1)}/\Omega_f. \tag{4.5}$$

Such a selection of duration time is adopted due to the faster stabilisation of the vibration amplitude for higher excitation frequencies. Duration time $T(\Omega_f)$ is selected in such a way that steady-state vibration of the structure with passively locked joints covers the time interval:

$$\mathbf{T}_{\text{steady}}(\Omega_f) = \Big[2/3 \cdot T(\Omega_f), \quad T(\Omega_f)\Big], \tag{4.6}$$

whereas operation of the controlled structure becomes near-steady much earlier. Only time interval $\mathbf{T}_{\text{steady}}(\Omega_f)$ is considered in calculation of results for modal and PAR approaches that are shown in Figures 4.9 and 4.10, respectively. The averaged no. of joint switches (Figs 4.9c and 4.10c) is calculated as:

$$\overline{n}_{\text{J}}^{\text{steady}} = n_{\text{J}}^{\text{steady}} / T_{\text{steady}}(\Omega_f) \tag{4.7}$$

where: $n_{\text{J}}^{\text{steady}}$ is sum of all joint switches within the time interval $\mathbf{T}_{\text{steady}}(\Omega_f)$ and $T_{\text{steady}}(\Omega_f)$ is its length. Such a metric gives information about expected mean frequency of joint switches.

Modal control has similar efficiency in damping vibration at the first resonance as PAR approach (Figs 4.9a, b and 4.10a, b). Averaged no. of switches $\overline{n}_{\text{J}}^{\text{steady}}$ for PAR control at the first resonance is slightly higher than for modal control. The second unlocked mode is better damped with the PAR approach due to the fact that weights α_p in the modal control are selected to mitigate mainly the first unlocked vibration mode. It results in worse but still satisfactory performance of the modal approach at the second resonance. The more important is that significantly smaller averaged number of joint switches and narrower frequency range exhibiting their work is achieved by the modal control. At the third resonance modal control does not mitigate the vibration due to the selected thresholds κ_1 and κ_2 and small that weight α_3. Possible level of the energy transfer rates from the third unlocked vibration mode weighted by α_3 is smaller than the selected thresholds for the present level of excitation. PAR control mitigates the third unlocked mode efficiently. However, in the passive-on (joints locked) state the third resonance corresponds with 30 times lower vibration energy for the employed excitation than the first resonance and requires the highest averaged number of joint switches – near to 65 Hz for PAR approach. Thus, the current selection of weights α_p in the modal approach can

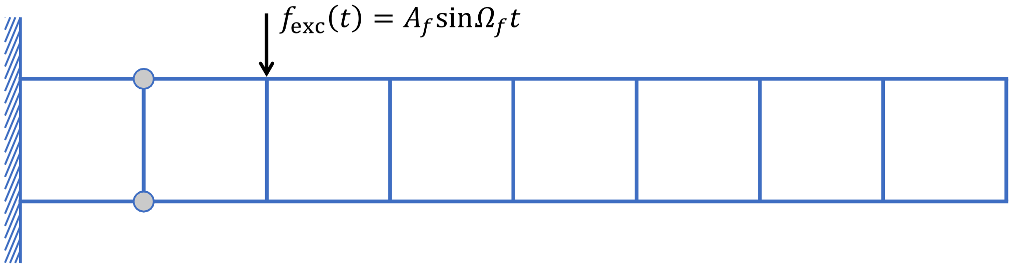

Figure 4.8: Location of the harmonic force excitation

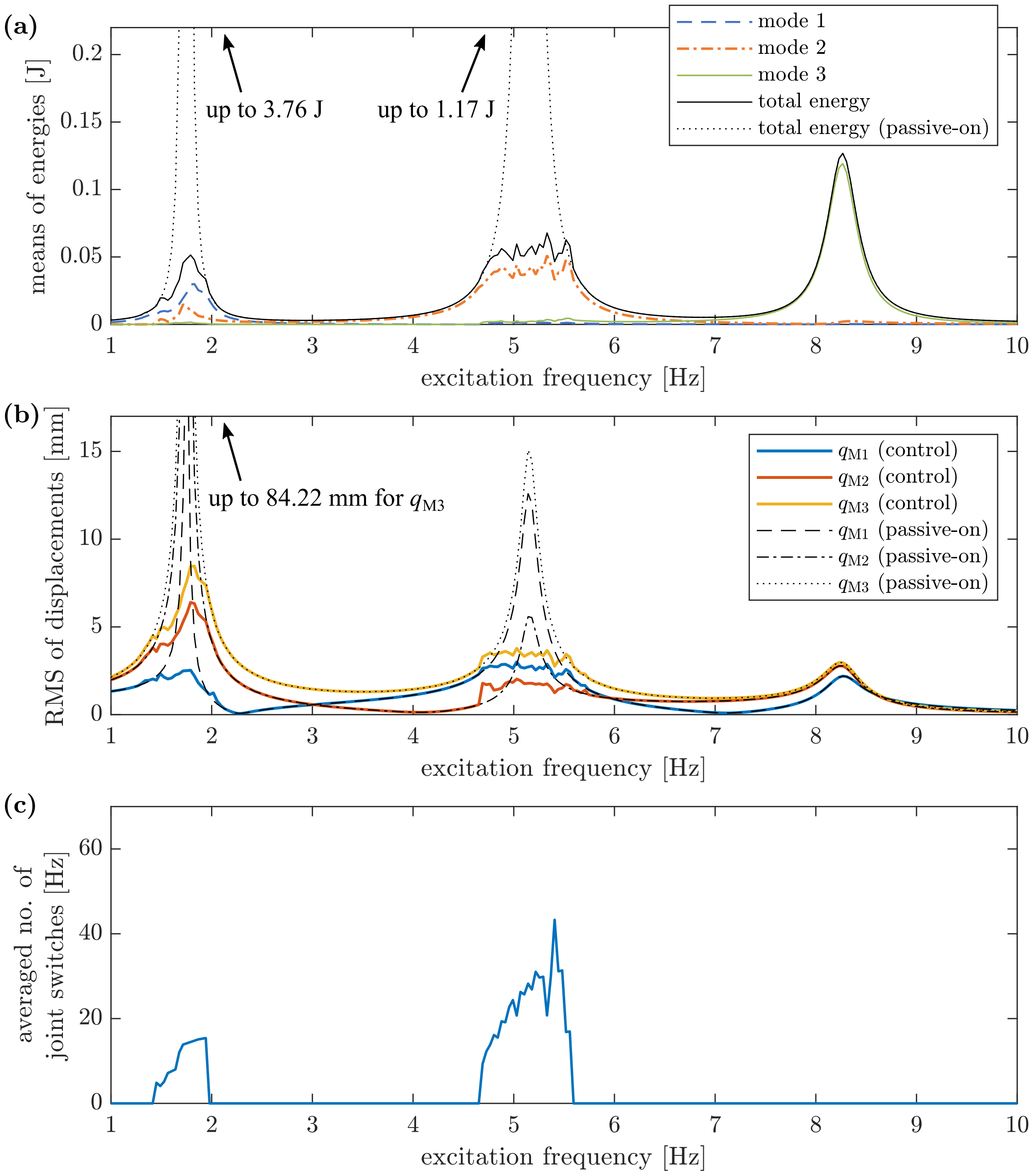

Figure 4.9: Various metrics of performance calculated for modal control in dependence of the excitation frequency (excitation case 2): (a) mean modal energies, (b) RMS displacement values and (c) mean no. of joint switches per second

be treated as one of possible ways of increasing durability of the lockable joints if damping of the third mode is not necessary. If it is, the weights can be changed even online, during the operation of the control algorithm.

Despite of the fact that the modal controller is designed using the unlocked modal parameters it efficiently damps also locked vibration modes as shown in Figure 4.9a and b. Hence, the difference in locked and unlocked natural frequencies (see: Fig. 4.2) does not affect efficiency of the proposed modal approach nor its operational bandwidth in any way. It is due to the fact the control algorithm is based

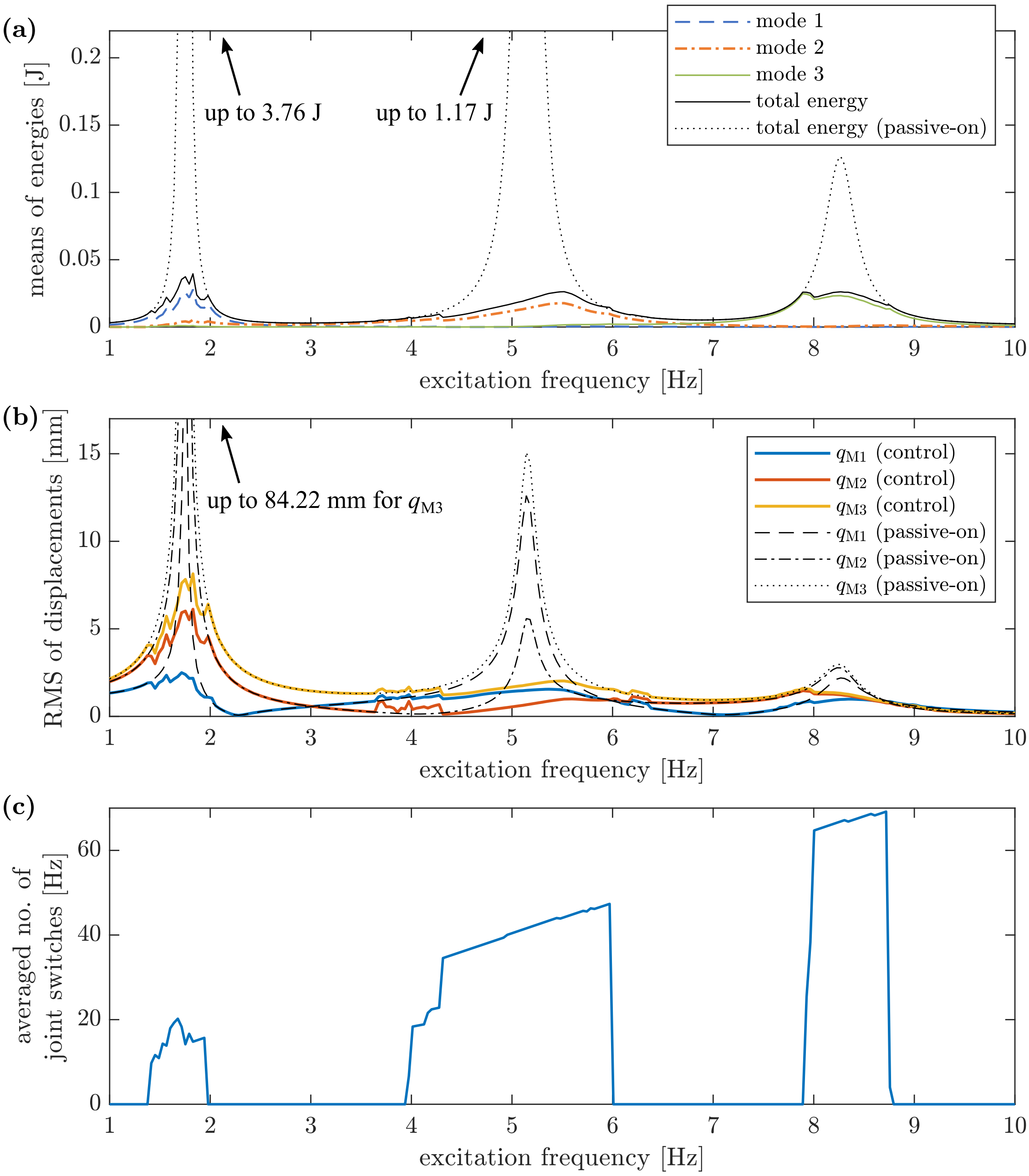

Figure 4.10: Various metrics of performance calculated for PAR control in dependence of the excitation frequency (excitation case 2): (a) mean modal energies, (b) RMS displacement values and (c) mean no. of joint switches per second

on the energy transfer rates which do not depend explicitly on natural frequencies but on monitored modal velocities and bending moments transmitted by the lockable joints. This transfer is accurately estimated independently on the excitation frequency.

Case 3 The last excitation considered in this subsection simulates random motion of the support. Acceleration of the support has Gaussian distribution in each time step. It results in substitution of vector of external disturbances $\mathbf{d}(t)$ in Equa-

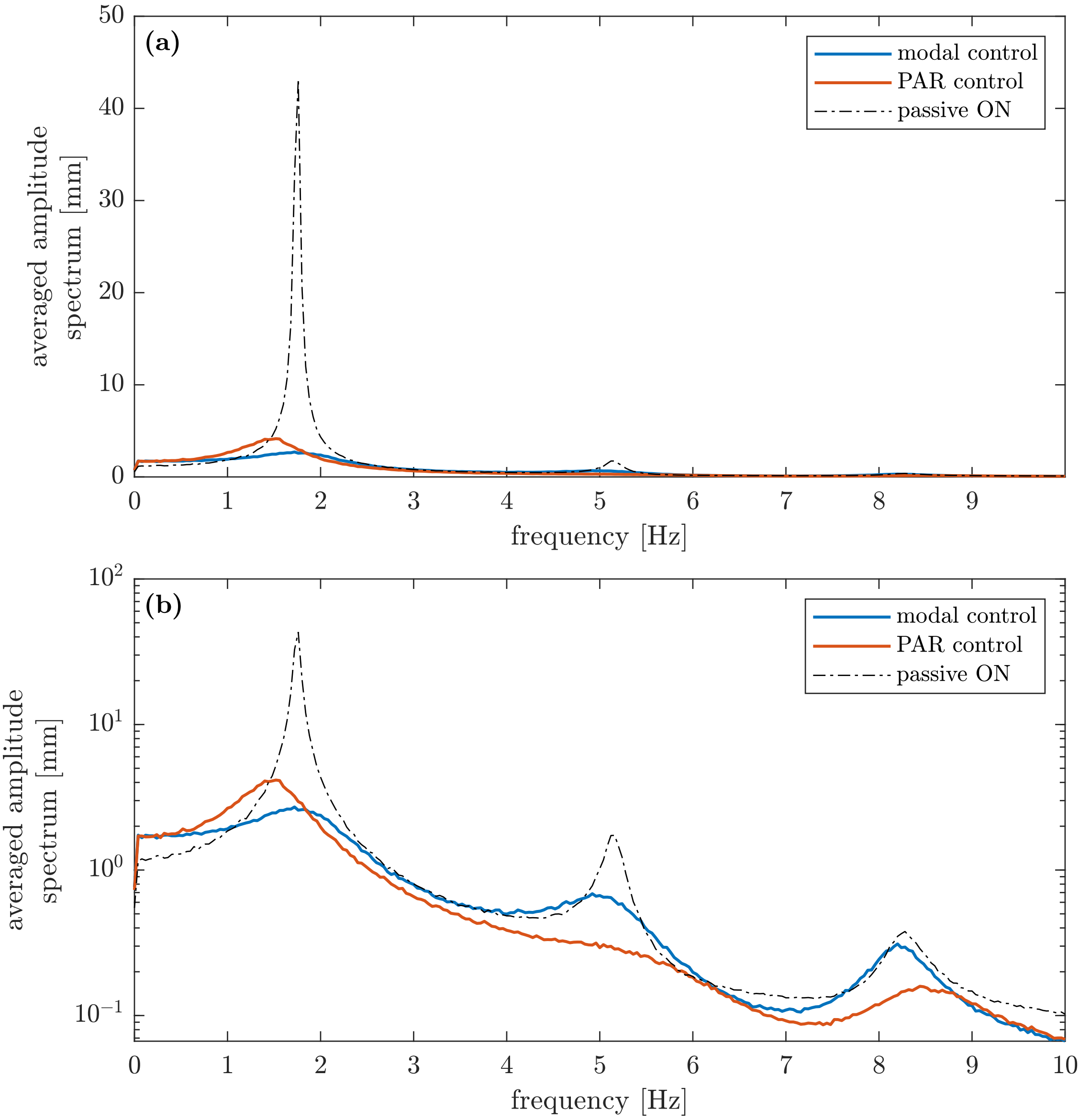

Figure 4.11: Averaged amplitude spectra of structure tip end ($q_{\mathrm{M3}}(t)$) in (a) linear and (b) semilog-y scales for the excitation case 3

Table 4.3: Comparison of various metrics of the control performance for modal PAR approaches and passively locked joints for the excitation case 3 averaged from 1000 simulations

Control type	RMS(q_{M1}) [mm]	RMS(q_{M2}) [mm]	RMS(q_{M3}) [mm]	$\overline{E}$ [J]	$\overline{n}_{\mathrm{J}}$ [Hz]
Modal	5.83	10.71	13.73	0.169	27.82
PAR	7.37	13.45	16.28	0.155	39.65
Passive-on	15.10	39.62	51.46	1.580	0

tion (2.41) with the inertia force

$$\mathbf{d}(t) = -\mathbf{M}\mathbf{l}_{\mathrm{x}}\sigma_a a_{\mathcal{N}(0,1)} \tag{4.8}$$

where $a_{\mathcal{N}(0,1)}$ is random acceleration with normalised Gaussian distribution and σ_a is its magnitude (also standard deviation of the acceleration).

For simulation purposes $\sigma_a = 9$ m/s^2 and duration time of vibration 40 s are selected. 1000 simulations with random accelerations are performed for calculation of various averaged performance metrics. The performance metrics are calculated for each particular simulation analogously to case 2 but using the data from the time interval $\mathbf{T} = [15, 40]$ s. Comparison of the modal control and PAR strategy accompanied with results for the structure with passively locked joints are shown in Figure 4.11 and listed in Table 4.3. $\overline{n}_{\mathrm{J}}$ is no. of switches averaged on the time interval $\mathbf{T}$:

$$\overline{n}_{\mathrm{J}} = n_{\mathrm{J}}/T, \tag{4.9}$$

where T is length of $\mathbf{T}$.

Once again, due to the selected weights α_p proposed modal approach mitigates the first unlocked vibration mode more effectively at the expense of effectiveness of damping of the remaining modes comparing to PAR control. It results in lower RMS values of the structural displacements at sensor locations despite of slightly greater mean vibration energy. Also lower averaged number of joint switches for the modal control is achieved. PAR approach shifts the first resonance peak towards lower frequencies, whereas modal control only mitigates it, without its shifting.

4.1.3 Eight-bay smart structure with two non-optimally placed lockable joints

Candidate locations for optimal placement of actuators or semi-active devices in many situations can be restricted due to possible technical limitations, e.g. limited space for the device, availability of the power supply, safety reasons, etc... Thus, in this subsection performance of modal and PAR approach obtained for non-optimal joint locations is assessed and compared.

Structure under investigation is the same as in previous subsection (Fig. 4.1) but with lockable joints placed at the ends of the fourth transversal beam. The first one is then connected with longitudinal beams as remaining transversal beams. The first three vibration modes calculated for the new arrangement of the lockable joints (both in locked and unlocked state) are shown in Figure 4.12. The optimal sensor locations corresponding with the unlocked modes is shown in Figure 4.13. Strain gauges are located on the beam equipped with lockable joints analogously to Subsection 4.1.2.

The comparison of the proposed methodology and PAR approach is conduced using the same test excitations as introduced in Subsection 4.1.2 (case 1 – case 3). Due to the non-optimally placed lockable joints thresholds $\kappa_1 = 7.5 \cdot 10^{-4}$ W and $\kappa_2 = 0.5$ W are selected, whereas the remaining algorithm parameters keep the same values as for optimally placed lockable joints (Subsection 4.1.2). In the case of PAR approach $\kappa_\varepsilon = 50$. These parameters are selected with the trial-and-error method.

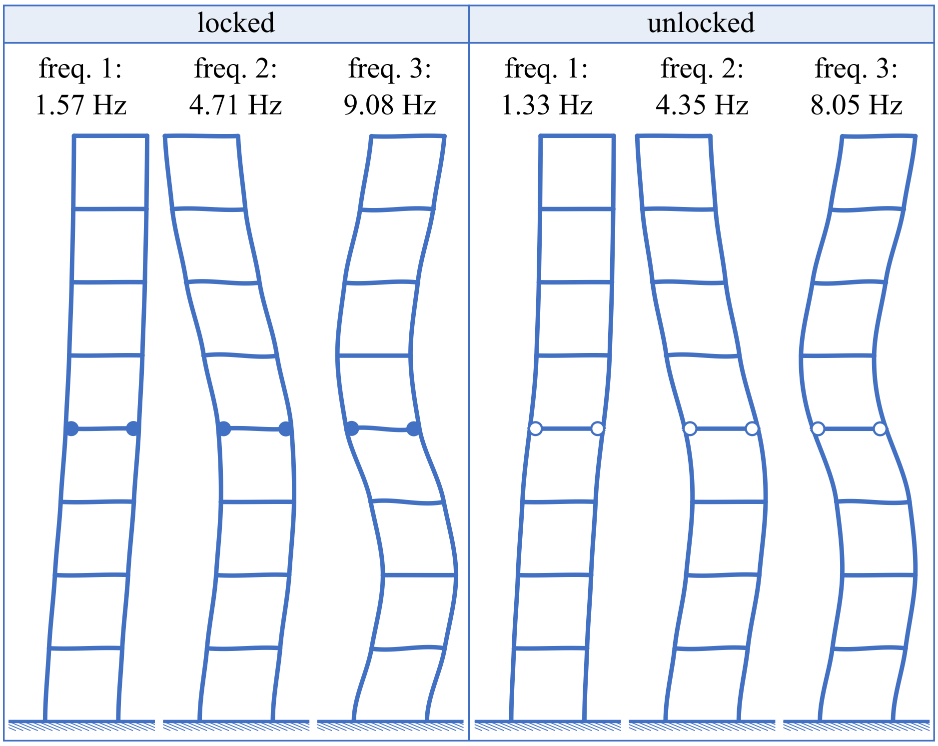

Figure 4.12: Structure with non-optimally placed lockable joints: first three vibration modes for both locked and unlocked joints

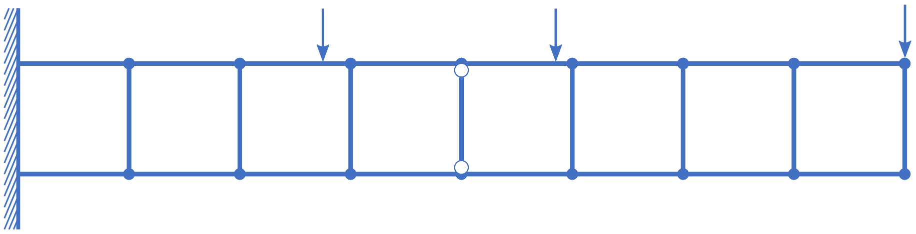

Figure 4.13: FE mesh with optimal sensor locations obtained for structure with non-optimally located lockable joints

Case 1 Simulation results of structural vibration damped with modal approach, obtained for sudden stop of the ground motion (Eq. (4.3)) are shown in Figure 4.14. Non-optimal placement of the lockable joints results in grater number of the local extreme values both of the measured strain signals and the energy associated with the higher-order (not monitored) unlocked vibration modes (Figures 4.14b and c). It results from the fact that in Subsection 4.1.2 the lockable joints are placed to attenuate with the biggest effectiveness mainly the first unlocked modes (controllability weights reciprocal to the natural frequencies, see: Fig. 4.3). For the placement of the lockable joints at the ends of the fourth transversal beam the controllability of the third unlocked mode is greater in relation to the first unlocked vibration mode than for the previous joint arrangement. Thus, the lock of the joints causes relatively more effective interaction between this monitored unlocked vibration mode and the higher-order ones. It results in adding of the local extreme values accordingly to

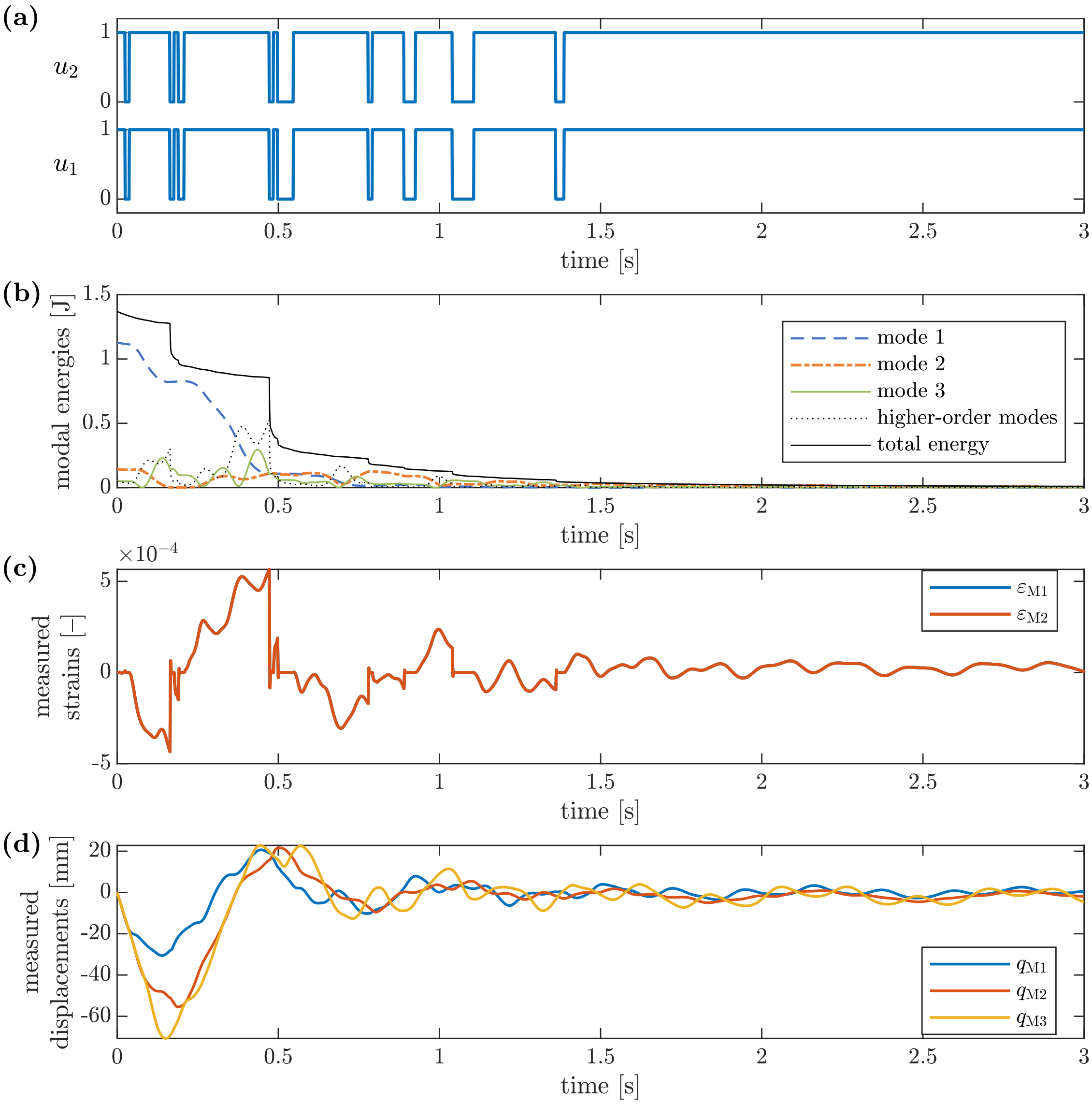

Figure 4.14: Time histories of: (a) control signals, (b) modal energies of the structure, (c) measured strains and (d) structural displacements at sensor locations for case 1 of excitation of the structure with non-optimally placed lockable joints controlled by the modal control algorithm

the greater natural frequency of the third unlocked vibration mode. However, due to the information about global state of the system carried by the estimated modal velocities the control algorithm is robust with respect to these local extremes. Due to the selected weights α_p lockable joints are unlocked mainly in time instants then energy of the first unlocked vibration mode stops decreasing (compare Figs 4.14a and b). The operation of the algorithm accordingly to the pursued priority in mitigating of the monitored unlocked vibration modes results in quick reduction of the main component of the structural displacements that is associated with the first unlocked vibration mode as shown in Figure 4.14d. After transferring majority of the energy from the first unlocked vibration mode and later from the second and third ones only residual vibration is visible due to the selected thresholds κ_1 and κ_2.

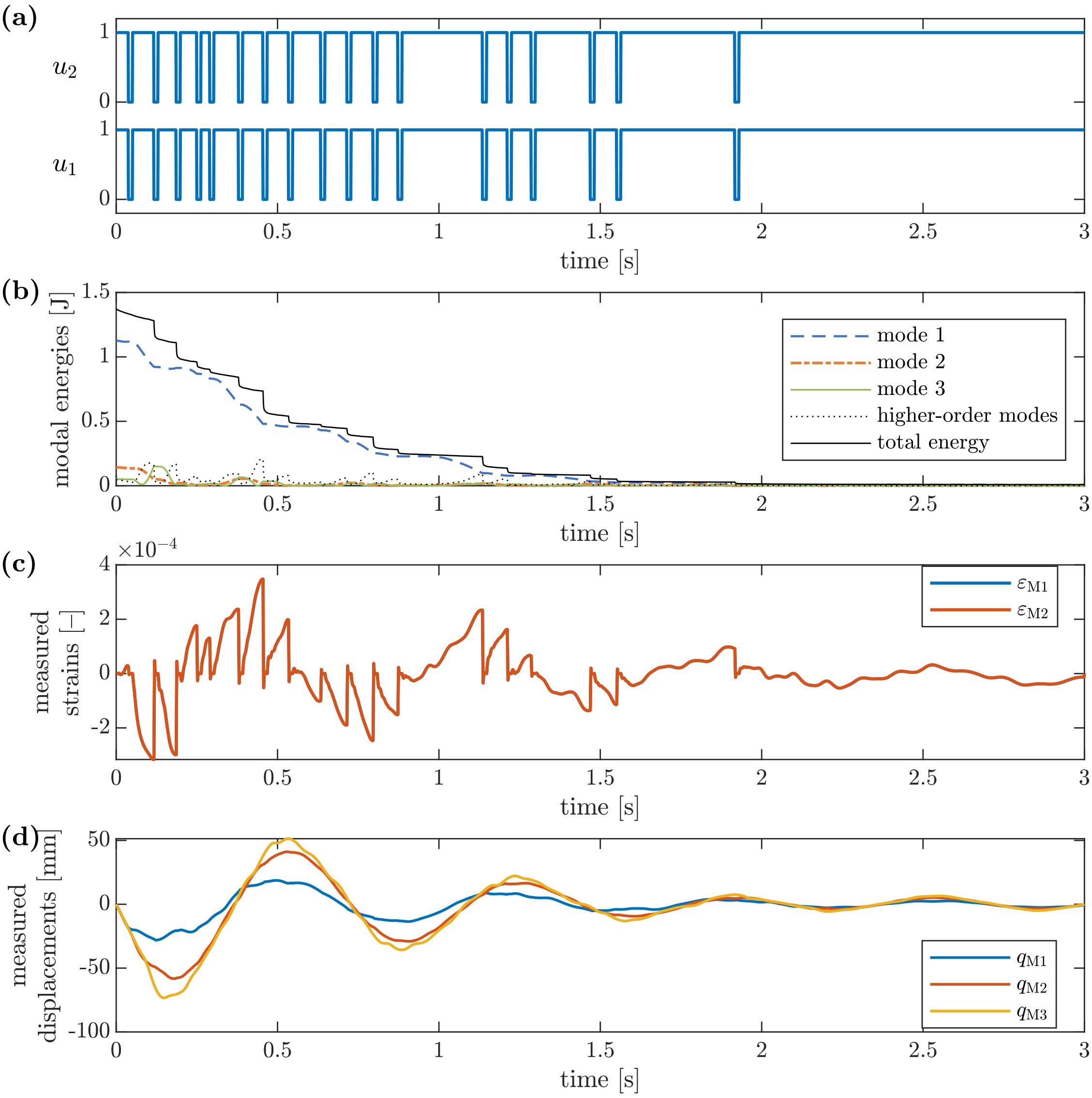

Figure 4.15: Time histories of: (a) control signals, (b) modal energies of the structure, (c) measured strains and (d) structural displacements at sensor locations for case 1 of excitation of the structure with non-optimally placed lockable joints controlled by the PAR algorithm

Results obtained for non-optimally placed lockable joints controlled with PAR strategy and case 1 of excitation are shown in Figure 4.15. As opposed to the modal control, in PAR approach the lockable joints are unlocked each time when the measured control signal goes through its extreme value (compare: Figs 4.15a and c). In the case of selected non-optimal locations of the lockable joints it results in relatively frequent joint unlocks. Then, mitigation of the first unlocked vibration mode is slower than in modal control (see: Figs 4.15b and d).

Comparison of the control signals and structural tip displacements for the modal control, PAR strategy and passive-on case (locked joints) is shown in Figure 4.16. Even for non-optimal lockable joint placement, both vibration damping strategies still achieve satisfactory performance and allows for quick dissipation of the struc-

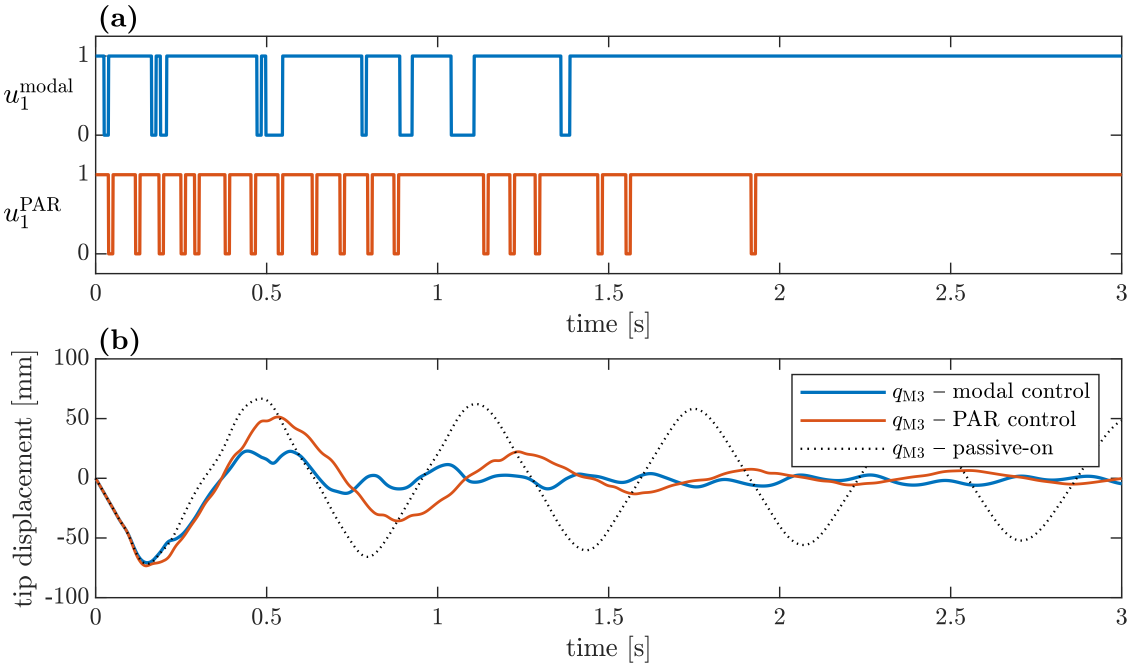

Figure 4.16: Comparison of modal and PAR control strategies for excitation case 1 and non-optimal placement of the lockable joints: (a) control signals and (b) structural tip displacements accompanied with the passive-on case

Table 4.4: Comparison of various metrics of the control performance for modal and PAR approaches, and passively locked joints for their non-optimal locations in case 1 of excitation

Control type	RMS(q_{M1}) [mm]	RMS(q_{M2}) [mm]	RMS(q_{M3}) [mm]	$\overline{E}$ [J]	n_{J} [–]
Modal	8.06	13.96	16.91	0.226	36
PAR	9.20	19.41	23.15	0.257	72
Passive-on	19.95	32.91	40.08	0.949	0

tural energy. However, PAR strategy exhibits its greater sensitivity to the joint placement than the modal approach. It is visible as increased number of cycles of the first unlocked vibration mode until it is mitigated and greater number of the joint switches. Decrement of the efficiency of the proposed modal control strategy is not as distinguishable as of PAR approach. It is visible also in results listed Table 4.4. The increment of the number of joint switches for the modal control in relation to optimally placed lockable joints is below 30 %, whereas for PAR control it is 50 % (compare with Tab. 4.2). For both control methods the RMS values of displacements are slightly higher than for the optimally placed lockable joints. However, the mean energy decreased for the modal control as opposed to the PAR approach. Hence, for the non-optimally placed lockable joints modal control provides lower level of displacements, lower mean energy and smaller number of the joint switches in mitigation of free structural vibration.

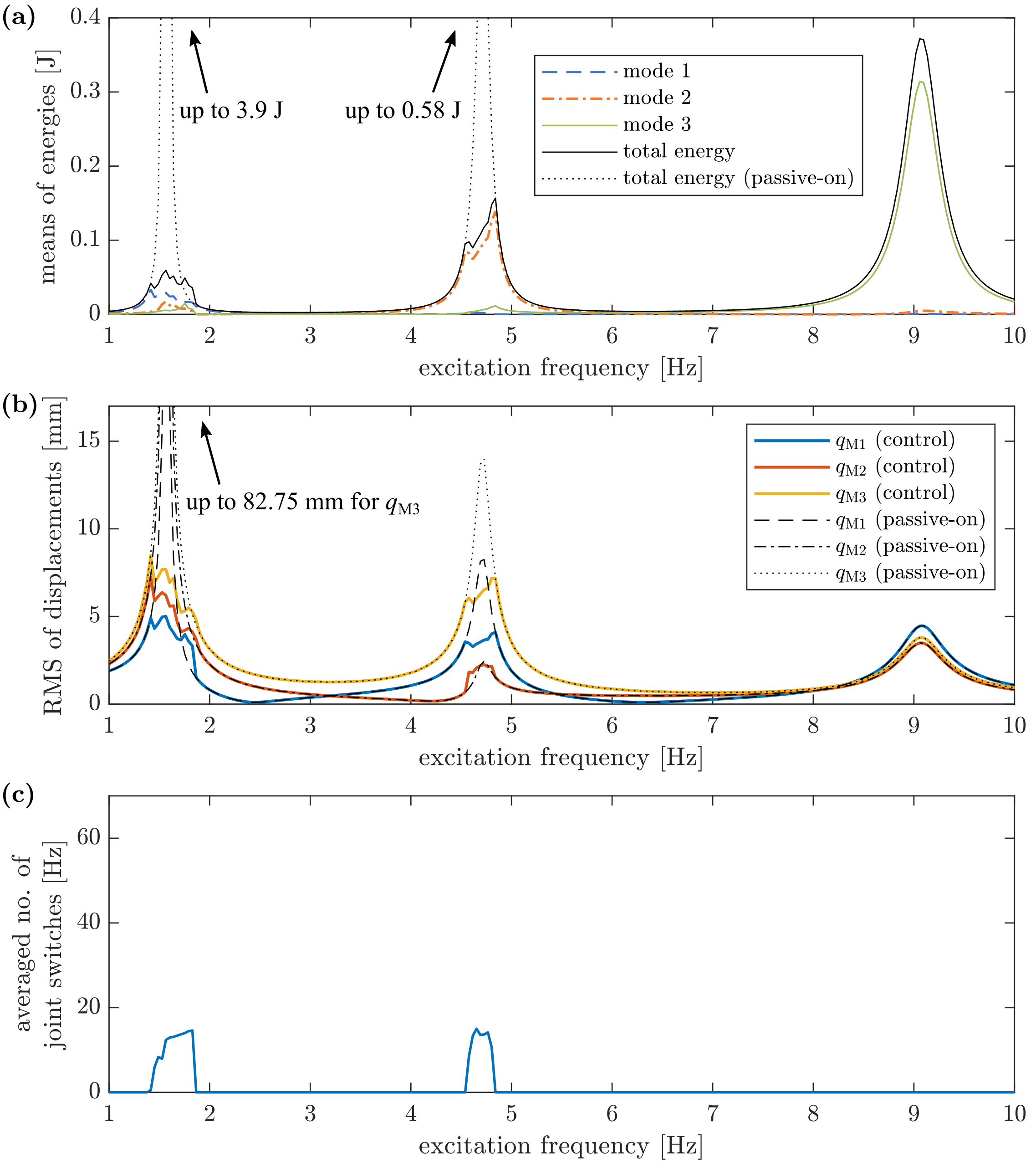

Figure 4.17: Various metrics of performance calculated for modal control in dependence of the excitation frequency (excitation case 2) for non-optimal placement of the lockable joints: (a) mean modal energies, (b) RMS displacement values and (c) mean no. of joint switches per second

Case 2 In this case the structure with non-optimally placed lockable joints is excited accordingly to the case 2 of excitation (Eq. (4.4) in Subsection 4.1.2). Results obtained with modal control are shown in Figure 4.17. It is visible that for non-optimal locations of the lockable joints the averaged number of joint switches is smaller at first two resonances (especially the second one) at the expense of slightly higher amplitudes of motion as comparing to the case with optimally placed lockable joints. The lockable joints also operate in narrower frequency ranges. Vibration in the third resonance is not mitigated by the control. Similarly to the structure with

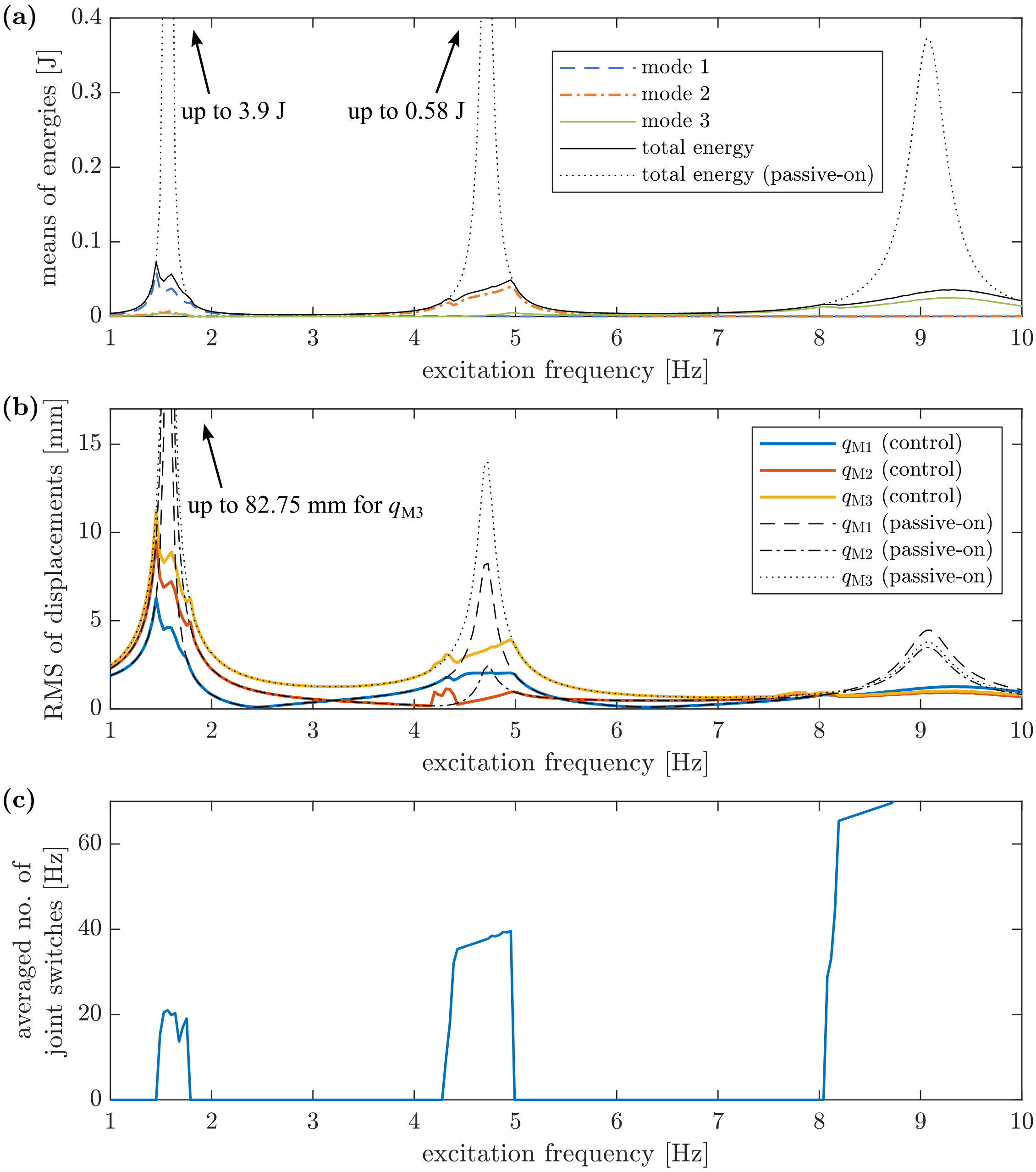

Figure 4.18: Various metrics of performance calculated for PAR control in dependence of the excitation frequency (excitation case 2) for non-optimal placement of the lockable joints: (a) mean modal energies, (b) RMS displacement values and (c) mean no. of joint switches per second

optimally placed lockable joints, the reason of such a behaviour is that the selected thresholds κ_1 and κ_2 are higher than possible energy transfer rate multiplied by α_3 for this level of the excitation.

Analogous results for PAR strategy are shown in Figure 4.18. Due to the higher selected threshold κ_ε PAR control also switches the lockable joints in narrower frequency ranges than for optimally located joints, excepting the third resonance. This behaviour is caused by the placement of the lockable joints providing higher controllability of the third unlocked vibration mode than for the optimal joint placement

Table 4.5: Comparison of various metrics of the control performance for modal and PAR approaches, and passively locked joints for the excitation case 3 and non-optimally placed lockable joints averaged from 1000 simulations

Control type	RMS(q_{M1}) [mm]	RMS(q_{M2}) [mm]	RMS(q_{M3}) [mm]	$\overline{E}$ [J]	$\overline{n}_{\mathrm{J}}$ [Hz]
Modal	7.86	12.55	15.32	0.20	24.42
PAR	8.59	17.28	20.67	0.23	39.52
Passive-on	28.25	46.70	56.84	2.00	0

(see: Fig. 4.3, beam no. 1 vs beam no. 4). The higher modal controllability is the greater strains can be accumulated in the transversal beam equipped with the pair of lockable joints. Hence, also the more potential energy is released during the joint unlock in high-frequency vibrations.

PAR mitigates the first resonance with still satisfactory but slightly less effectiveness than modal approach and require more joint switches. Weights α_p in the modal control algorithm are selected in such a way that the first resonance is mitigated with the highest priority, whereas the remaining ones are mitigated more weakly but also with the lower averaged number of joint switches than PAR. Such a weights are selected in this study because the lower-order unlocked vibration modes usually have predominant participation in the structural motion. PAR approach does not allow for such a selective vibration damping, hence it mitigates vibration in all resonances at the expense of significantly higher number of joint switches.

Case 3 In the present case the structure with non-optimally placed lockable joints is excited by random base motion as described in Subsection 4.1.2, case 3 (see: Eq. 4.8). Analogous results are shown in Figure 4.19.

It is well demonstrated that PAR strategy mitigates vibration at second and third resonance better than modal control at the expense of the first resonance. All metrics of control performance listed in Table 4.5 are better for the modal control, including the averaged number of joint switches. It is mainly due to the fact that the first unlocked vibration mode, which is suppressed by the modal approach with greater effectiveness, takes predominant participation in the structural motion. These results reveal that the possibility of weighing particular vibration modes by weights α_p in the proposed control allows for focusing of the efforts on the most harmful vibration modes, as opposed to PAR whose performance depends mainly on the location of the lockable joints. Once again PAR approach shifts the first mitigated resonance peak towards lower frequencies, whereas in this case modal approach shifts the third resonance peak without its suppression. Also its very small increase is noticeable as result of decrease of the effective stiffness provided by unlocking of the joints. The second resonance peak is shifted towards the higher frequencies in the case of PAR approach.

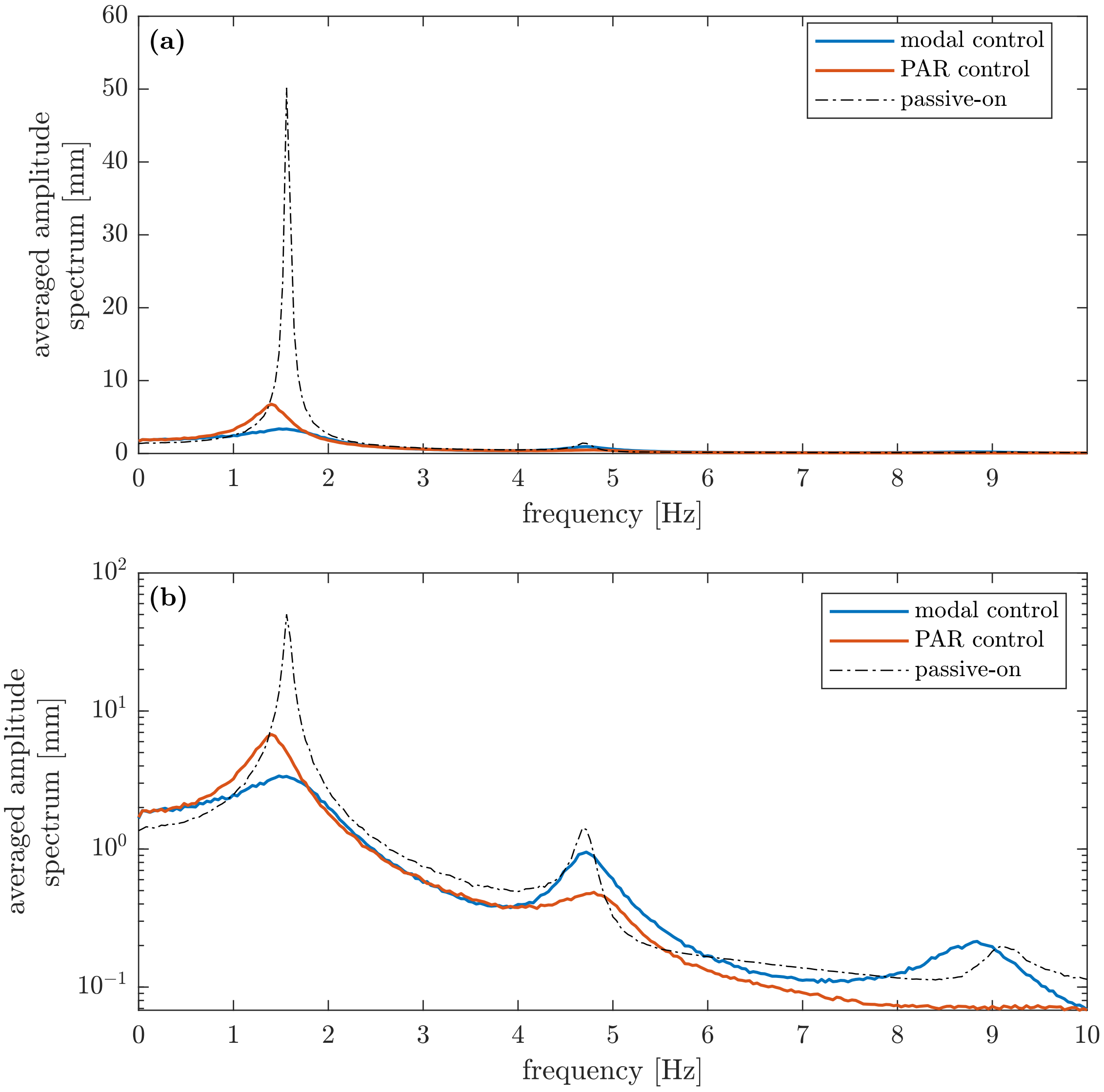

Figure 4.19: Averaged amplitude spectra of structure tip end ($q_{\mathrm{M3}}(t)$) in (a) linear and (b) semilog-y scales for the excitation case 3 and non-optimally placed lockable joints

4.2 Energy harvesting

The proposed control methodology is able not only to transfer mechanical energy from weakly damped vibration modes allowing for efficient mitigation of structural vibration, but also can be used for directed energy transfer to the preselected unlocked vibration mode. In this section numerical results that present the use of this property to enhance energy harvesting process are described and discussed. First, a small structure equipped with lockable joints that is to be controlled is described in the subsection below. This structure is a primary structure to which the energy harvester (EH) is attached as a secondary structure. EH is tuned to one of the unlocked vibration modes of the controlled structure. This mode is referred as the targeted mode to which the vibration energy is to be transferred. It provides that EH works under resonance conditions even if external excitation of the primary structure is

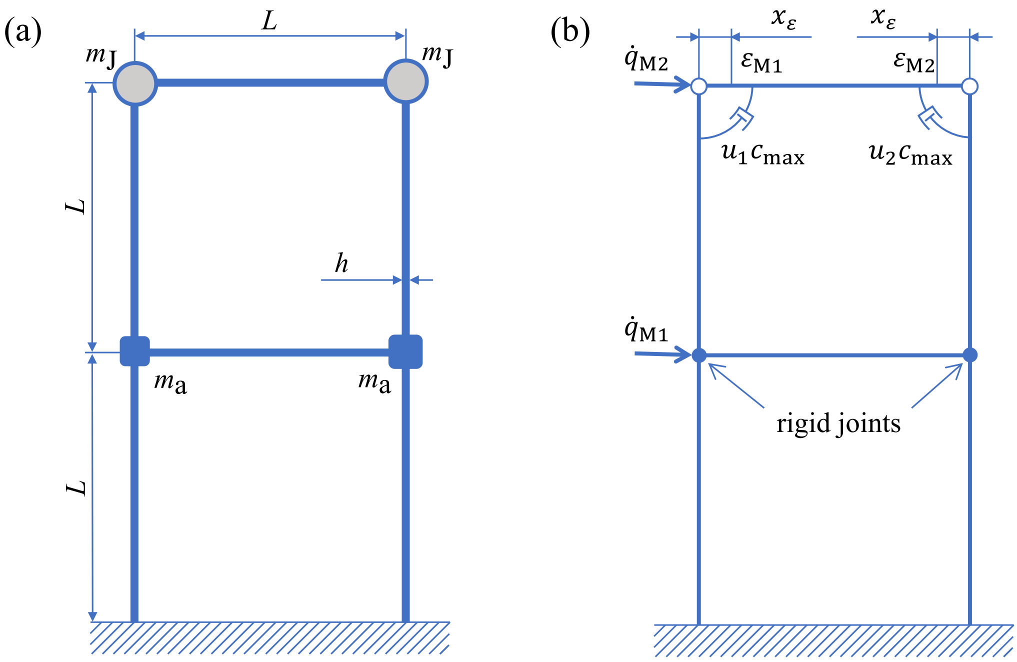

Figure 4.20: Frame structure equipped with two lockable joints: (a) scheme of the structure, (b) finite element mesh and placement of sensors [145]

Table 4.6: Parameters of the two-story frame structure

Quantity	**Symbol**	**Units**	**Value**
length	L	[mm]	400
offset of the strain gauges from semi-active joint	x_ε	[mm]	50
Young modulus (steel)	E	[Pa]	$210 \cdot 10^9$
material density (steel)	ρ	[kg/m^3]	7860
dimensions of the cross-section (height × width)	$h \times b$	[mm]	8×10
mass of the semi-active joint	m_J	[kg]	1.0
mass of the rigid connection	m_a	[kg]	0.4

away from the resonance range of the EH. In Subsection 4.2.2 an electromagnetic energy harvester (EMEH) and its model are discussed. Assembly and mechanical interaction between EH and primary structure are described in Subsection 4.2.3. Location of the EMEH in dependence of the targeted mode also is indicated in Subsection 4.2.4. Further, numerical study of the effectiveness of the proposed modal control for enhancing of the energy harvesting for various excitations is described and discussed in Subsection 4.2.5.

4.2.1 Smart structure enhancing energy harvesting process

A scheme of the controlled frame structure (primary structure of the energy harvesting system) is shown in Figure 4.20a, whereas its FE model is shown in Figure 4.20b. This two-bay structure is fixed in the ground. The lower transversal beam is connected to the longitudinal columns via joints providing rigid (uncontrolled) con-

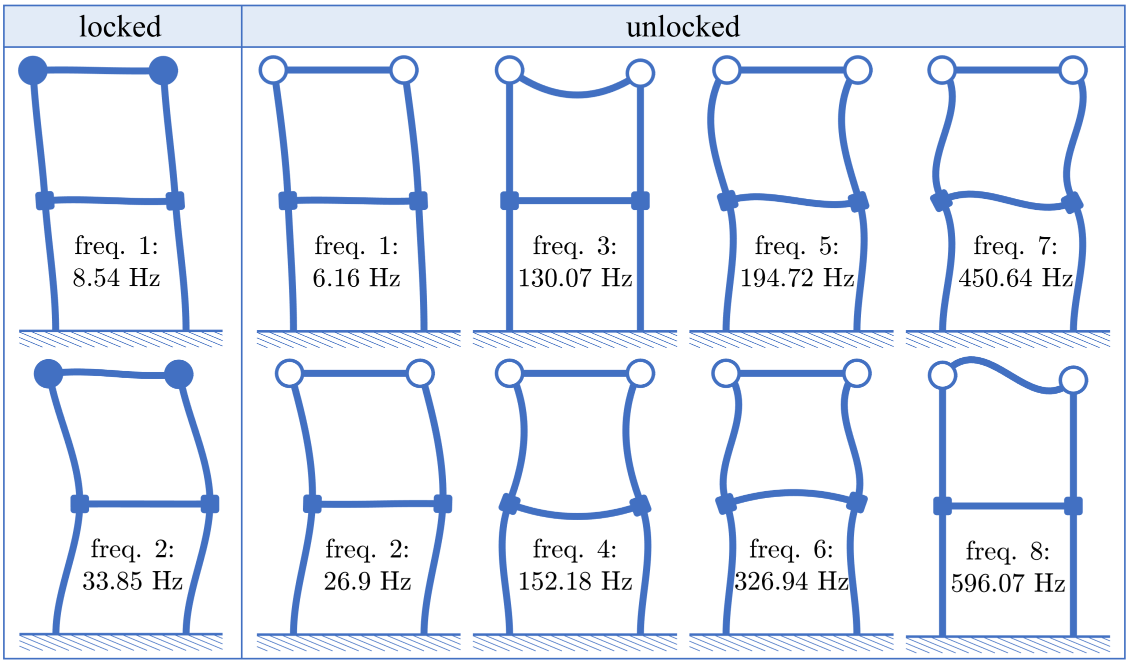

Figure 4.21: Vibration modes of the controlled two-bay structure obtained for unlocked joints accompanied with the first two vibration modes obtained for joints locked at 90° between connected beams

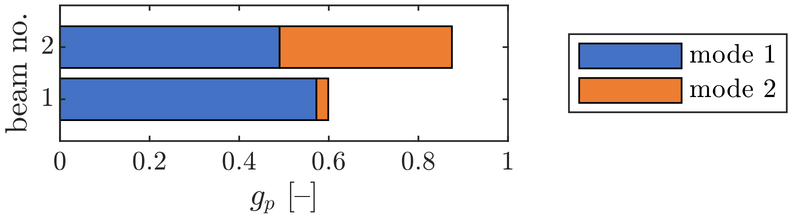

Figure 4.22: Controllability of the monitored unlocked vibration modes for lockable joints placed at the ends of the first and second transversal beam of the structure

nections. The upper transversal beam is is connected to the longitudinal beams via lockable (controlled) joints. Both controlled and rigid joints have non-negligible mass that allows for vibration of the structure in the two predominant low-frequency unlocked vibration modes. This makes it easier to control these modes of vibration and exchange of the energy between them. Dimensions and properties of the structure shown in Figure 4.20 are listed in Table 4.6.

FE model of the structure has 6 beam FEs based on the Euler-Bernoulli beam theory. Each beam FE element is non-strechable (5 DOFs per beam) and have cubic shape functions. FE model has 8 DOFs.

Locations of two sensors for estimation of the first two modal velocities are shown in Figure 4.20b along with locations of the strain gauges. The measured strains are calculated using FE shape functions as described in Section 3.1.

All eight unlocked vibration modes of the structure and the first two locked ones are shown in Figure 4.21. It is visible that the third and higher-order unlocked modes shapes involve mainly local curvatures as opposed to the first two unlocked

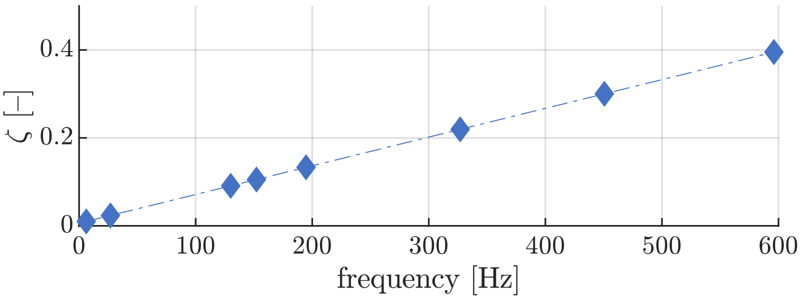

Figure 4.23: Modal damping factors characterising material damping of the two-bay structure in dependence of the natural frequency

vibration modes involving significant displacements of horizontal beams along with massive, both lockable and rigid, joints.

Aiming at the control of the first two unlocked vibration modes the lockable joints are located at the ends of the upper transversal beam instead of the lower one. Controllability of the monitored unlocked vibration modes in dependence of the joint locations is shown in Figure 4.22. In the case of energy harvesting application of the proposed methodology all unlocked vibration modes have to be controllable. If the lockable joints are placed at the ends of first transversal beam the second unlocked vibration mode would be controlled with poor efficiency. Thus, the energy transfer to/from this vibration mode would be not effective. It is due to the fact that for the corresponding locked vibration mode the first beam almost does not accumulate strains (it is not significantly deflected, as shown in Fig. 4.21), hence the joints do not transmit any significant bending moment.

Despite of the fact that non-simplified form of Equation (3.28) is employed to obtain results shown in Figure 4.22 the simplified form would give similar results, since for the first two vibration of the considered structure: $\vartheta_{11} = 0.9897$ and $\vartheta_{22} = 0.987$ have values close to ones. It follows that the simplification proposed in Equation (3.28) is valid even for structures whose size is relatively small if the set of monitored vibration modes is properly selected.

Material damping model is described by modal damping factors analogously to Equation (4.2). For this structure coefficients $\alpha = 0$, $\beta = 0.012$ and $\gamma = 2.0785 \cdot 10^{-4}$ are selected. Corresponding modal damping factors in dependence on the natural frequencies are shown in Figure 4.23. The first two modal damping factors are: $\zeta^{(1)} = 0.01$ and $\zeta^{(2)} = 0.0235$.

4.2.2 Model of electromagnetic energy harvester

Electromagnetic energy harvester (EMEH) is selected, since EMEHs have relative low frequencies of operation that is desired in demonstrated application example. Scheme of the EMEH is shown in Figure 4.24a. The considered EMEH consists of the magnet having mass m attached to the spring heaving stiffness k inside a casing. The casing is covered by an electromagnetic coil. It is assumed that magnet of the

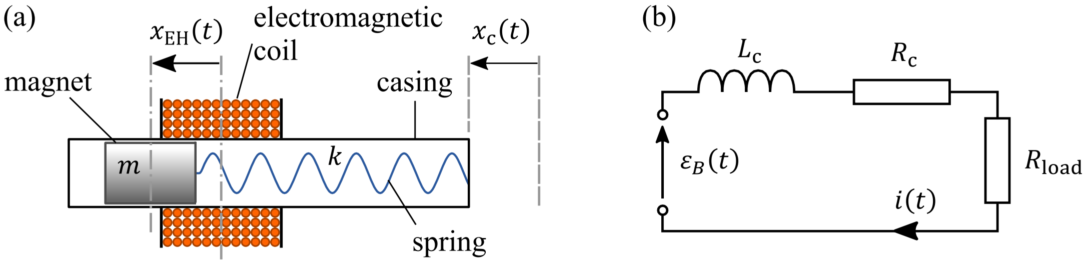

Figure 4.24: EMEH device: (a) scheme of the mechanical part and (b) scheme of the electrical circuit [145]

Table 4.7: Properties of EMEH adopted in present study [145, 147–149]

Quantity	**Symbol**	**Units**	**Value**
mass of the magnet	m	[kg]	$90 \cdot 10^{-3}$
damping coefficient	c	[Ns/m]	0.1
electromechanical coupling	κ_B	[Vs/m]	60
coil inductance	L_c	[H]	1.463
coil resistance	R_c	[Ω]	1200
magnet diameter × magnet height	$D_\mathrm{m} \times H_\mathrm{m}$	[m]	$20 \cdot 10^{-3} \times 35 \cdot 10^{-3}$
coil wire diameter	D_w	[m]	$0.14 \cdot 10^{-3}$
turns of winding	N_turns	[–]	12 740

EMEH is excited kinematically by displacement $x_\mathrm{c}(t)$ of the casing that is mounted to the vibrating structure (more details in the next subsection).

Motion of the magnet inside the electromagnetic coil induces the electromotive force accordingly to the Faraday's law. The electromotive force generally depends nonlinearly on displacement $x_\mathrm{EH}(t)$ and linearly on velocity $\dot{x}_\mathrm{EH}(t)$ of the magnet with respect to the coil. These nonlinearities have strong influence on the dynamics of the electrical circuit when displacements of the magnet are large with respect to the coil dimensions as investigated in [18]. However, for relatively small amplitude of the vibration of the magnet the electromotive force $\varepsilon_B(t)$ can be considered as proportional to the relative magnet velocity:

$$\varepsilon_B(t) = \kappa_B \dot{x}_\mathrm{EH}(t), \tag{4.10}$$

where κ_B is called electromechanical coupling. Then, after proper selection of κ_B EMEH behaviour is similar to that obtained from the rigorous nonlinear model, as investigated in [147].

Scheme of the electrical circuit of the EMEH is shown in Figure 4.24b, where L_c and R_c are inductance (also assumed to be constant) and resistance of the electromagnetic coil, respectively, R_load is resistance of the resistor considered as the energy receiver and $i(t)$ is electrical current. Behaviour of the considered EMEH is described by the equation set below

$$\begin{cases} m\ddot{x}_{\mathrm{EH}}(t) + c\dot{x}_{\mathrm{EH}}(t) + kx_{\mathrm{EH}}(t) = -\kappa_B i(t) - m\ddot{x}_c(t) \\ L_\mathrm{c}\dot{i}(t) + (R_\mathrm{c} + R_\mathrm{load})\, i(t) = \kappa_B \dot{x}_{\mathrm{EH}}(t) \end{cases}. \tag{4.11}$$

For the present study values of parameters describing EMEH properties that are contained in Equation (4.11) are shown in Table 4.7. They are similar to data describing EMEH researched in [147–149]. Stiffness of the model is linearized with respect to the equilibrium point (at zero displacement). Stiffness k is tuned to the targeted vibration mode of the two-bay, primary, structure (see: Subsection 4.2.4).

Power produced by the EMEH device is calculated as

$$P(t) = R_\mathrm{load} i^2(t). \tag{4.12}$$

Power $P(t)$ changes with the frequency equal to twice of EMEH vibration frequency. Thus, it is more informative to use the mean value of the power produced by the EMEH:

$$\overline{P} = \frac{1}{T} \int\limits_{t_0}^{t_0+T} P(t)\mathrm{d}t. \tag{4.13}$$

4.2.3 Interaction between the energy harvester and the structure

In this subsection mechanical interaction between the structure and EMEH is described. It is required for simulation purposes, since from the mechanical point of view magnet on the spring behaves like mass damper.

Displacement of EMEH casing attached to the structure in the inertial reference frame is described by the formula below

$$x_\mathrm{c}(t) = \mathbf{l}_{\mathrm{EH}}^{\mathrm{T}} \mathbf{q}(t) + q_\mathrm{g}(t). \tag{4.14}$$

In the equation above $\mathbf{l}_{\mathrm{EH}}$ is Boolean vector selecting structural DOF to which EMEH is attached, $\mathbf{q}(t)$ is structural displacement vector with respect to the ground and $q_\mathrm{g}(t)$ is displacement of the ground (treated later as the non-inertial reference frame). The ground (or support) motion simulates vibration of the structure on which the whole energy harvesting system (controlled primary structure with attached EMEH) can be mounted.

EMEH acts on the structure with force

$$\mathbf{d}_{\mathrm{EH}}(t) = \mathbf{l}_{\mathrm{EH}} \left(\kappa_B i(t) + c\dot{x}_{\mathrm{EH}}(t) + kx_{\mathrm{EH}}(t) \right). \tag{4.15}$$

In the equation above force $\mathbf{d}_{\mathrm{EH}}(t)$ is equal to the sum of: (1) the Lorentz force $\mathbf{l}_{\mathrm{EH}}\kappa_B i(t)$ that acts on the electromagnetic coil (fixed to the structure through the casing), (2) viscous damping force $\mathbf{l}_{\mathrm{EH}} c \dot{x}_{\mathrm{EH}}(t)$ and (3) the stiffness force $\mathbf{l}_{\mathrm{EH}} k x_{\mathrm{EH}}(t)$ generated by the spring deformed.

The EMEH and the controlled structure can be also considered as the assembled system using primal assembly formulation [150, 151]. The subsystems to be assembled, EMEH and structure, are shown in Figure 4.25. ith DOF of the component 1 (controlled structure) is indicated by vector $\mathbf{l}_{\mathrm{EH}}$. In this Figure the location of the EMEH on the structure is only the example.

Behaviour of the structure and the attached EMEH is described by the equation set below

$$\begin{cases} \mathbf{M}^{(1)}\ddot{\mathbf{q}}^{(1)}(t) + \mathbf{C}^{(1)}(\mathbf{u})\dot{\mathbf{q}}^{(1)}(t) + \mathbf{K}^{(1)}\mathbf{q}^{(1)}(t) = \mathbf{d}^{(1)}(t) + \mathbf{g}^{(1)}(t) \\ \mathbf{M}^{(2)}\ddot{\mathbf{q}}^{(2)}(t) + \mathbf{C}^{(2)}\dot{\mathbf{q}}^{(2)}(t) + \mathbf{K}^{(2)}\mathbf{q}^{(2)}(t) = \mathbf{d}^{(2)}(t) + \mathbf{g}^{(2)}(t) \\ \mathbf{l}_{\mathrm{EH}}^{\mathrm{T}}\mathbf{q}^{(1)}(t) - q_1^{(2)}(t) = 0 \\ \mathbf{l}_{\mathrm{EH}}^{\mathrm{T}}\mathbf{g}^{(1)}(t) + g_1^{(2)}(t) = 0 \end{cases} . \tag{4.16}$$

Superscript (1) refers to the component 1 in Figure 4.25, whereas (2) to the component 2, respectively, $\mathbf{M}^{(1)} = \mathbf{M}$, $\mathbf{C}^{(1)}(\mathbf{u}) = \mathbf{C} + \sum_{k=1}^{N_k} u_k(t)\widetilde{\mathbf{C}}_k$ (see: Eq. 2.43), $\mathbf{K}^{(1)} = \mathbf{K}$, $\mathbf{q}^{(2)}(t) \in \mathbb{R}^3$,

$$\mathbf{M}^{(2)} = \begin{bmatrix} 0 & 0 & 0 \\ 0 & m & 0 \\ 0 & 0 & L_{\mathrm{c}} \end{bmatrix}, \quad \mathbf{C}^{(2)} = \begin{bmatrix} c & -c & -\kappa_B \\ -c & c & \kappa_B \\ \kappa_B & -\kappa_B & R_{\mathrm{c}} + R_{\mathrm{load}} \end{bmatrix}, \quad \mathbf{K}^{(2)} = \begin{bmatrix} k & -k & 0 \\ -k & k & 0 \\ 0 & 0 & 0 \end{bmatrix},$$

vectors $\mathbf{g}^{(1)}(t)$ and $\mathbf{g}^{(2)}(t)$ are the interface forces that stay in equilibrium ($\mathbf{g}^{(1)}(t)$ is equal to $\mathbf{d}_{\mathrm{EH}}(t)$ in Eq. (4.15)). $q_3^{(2)}(t)$ represents electrical charge, whereas its time derivative is equal to the electrical current $i(t)$.

Equations describing interfaces can be rewritten into the form below

$$\mathbf{L}_{\mathrm{EH}} \begin{bmatrix} \mathbf{q}^{(1)}(t) \\ \mathbf{q}^{(2)}(t) \end{bmatrix} = \mathbf{0}, \qquad \mathbf{L}_{\mathrm{N}}^{\mathrm{T}} \begin{bmatrix} \mathbf{g}^{(1)}(t) \\ \mathbf{g}^{(2)}(t) \end{bmatrix} = \mathbf{0}, \tag{4.17}$$

where: $\mathbf{L}_{\mathrm{EH}} = \begin{bmatrix} \mathbf{L}_{\mathrm{EH}}^{(1)} & \mathbf{L}_{\mathrm{EH}}^{(2)} \end{bmatrix}$, $\mathbf{L}_{\mathrm{EH}}^{(1)} = \mathbf{l}_{\mathrm{EH}}^{\mathrm{T}}$, $\mathbf{L}_{\mathrm{EH}}^{(2)} = \begin{bmatrix} -1 & 0 & 0 \end{bmatrix}$ and $\mathbf{L}_{\mathrm{N}}$ is defined as the null space of matrix $\mathbf{L}_{\mathrm{EH}}$. Substituting

$$\begin{bmatrix} \mathbf{q}^{(1)}(t) \\ \mathbf{q}^{(2)}(t) \end{bmatrix} = \mathbf{L}_{\mathrm{N}}\mathbf{q}_{\mathrm{u}}(t), \tag{4.18}$$

where $\mathbf{q}_{\mathrm{u}}(t)$ describes unique DOFs for the total structure, into Equation (4.16) and

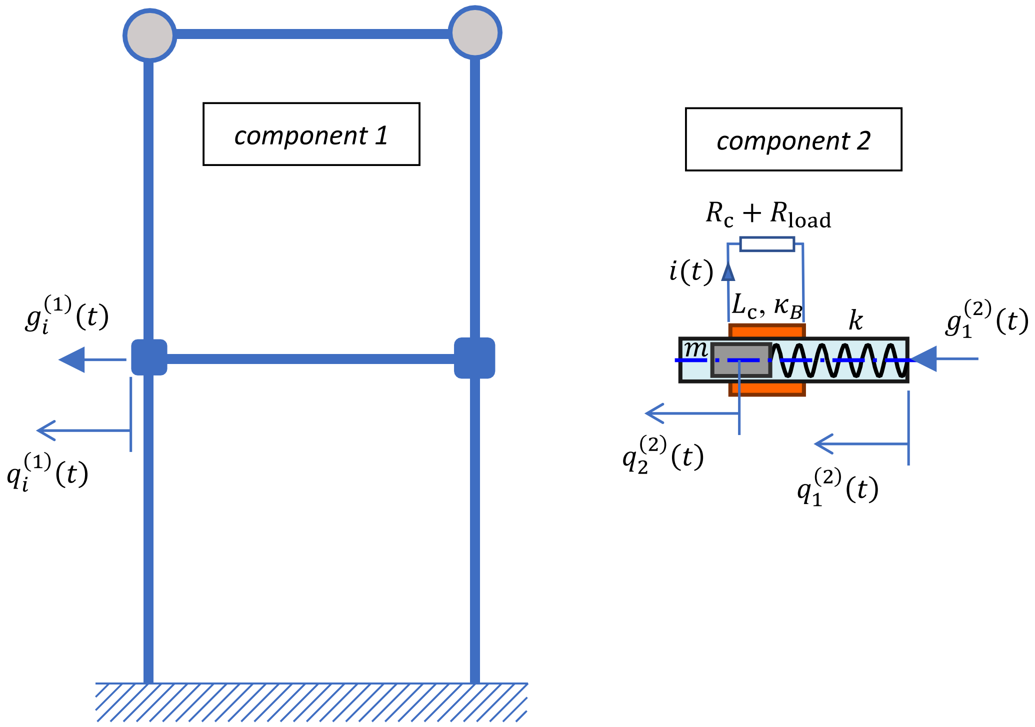

Figure 4.25: Components (controlled structure and EMEH) for primal assembly

left-multiplying by $\mathbf{L}_{\mathrm{N}}^{\mathrm{T}}$ we receive equation of motion below

$$\begin{gathered}\underbrace{\mathbf{L}_{\mathrm{N}}^{\mathrm{T}}\begin{bmatrix}\mathbf{M}^{(1)} & \mathbf{0}\\ \mathbf{0} & \mathbf{M}^{(2)}\end{bmatrix}\mathbf{L}_{\mathrm{N}}}_{\mathbf{M}_{\mathrm{u}}}\ddot{\mathbf{q}}_{\mathrm{u}}(t)+\underbrace{\mathbf{L}_{\mathrm{N}}^{\mathrm{T}}\begin{bmatrix}\mathbf{C}^{(1)}(\mathbf{u}) & \mathbf{0}\\ \mathbf{0} & \mathbf{C}^{(2)}\end{bmatrix}\mathbf{L}_{\mathrm{N}}}_{\mathbf{C}_{\mathrm{u}}(\mathbf{u})}\dot{\mathbf{q}}_{\mathrm{u}}(t)+\\ +\underbrace{\mathbf{L}_{\mathrm{N}}^{\mathrm{T}}\begin{bmatrix}\mathbf{K}^{(1)} & \mathbf{0}\\ \mathbf{0} & \mathbf{K}^{(2)}\end{bmatrix}\mathbf{L}_{\mathrm{N}}}_{\mathbf{K}_{\mathrm{u}}}\mathbf{q}_{\mathrm{u}}(t)=\underbrace{\mathbf{L}_{\mathrm{N}}^{\mathrm{T}}\begin{bmatrix}\mathbf{d}^{(1)}(t)\\ \mathbf{d}^{(2)}(t)\end{bmatrix}}_{\mathbf{d}_{\mathrm{u}}(t)}+\underbrace{\mathbf{L}_{\mathrm{N}}^{\mathrm{T}}\begin{bmatrix}\mathbf{g}^{(1)}(t)\\ \mathbf{g}^{(2)}(t)\end{bmatrix}}_{\mathbf{0}}.\end{gathered} \tag{4.19}$$

Equation of motion above represents the controlled structure and EMEH as one total system (including the state of the electrical circuit of the EMEH).

The assembly of the system components into one total system allows for simulation of the system behaviour by integration of one equation set. Then, Equation (4.19) is integrated as described at the end of Section 2.2.2 (see Eq. (2.44) and (2.45)). The time step $\Delta t = 5 \cdot 10^{-5}$ s is selected for simulations of the behaviour of the EMEH and controlled structure.

4.2.4 Optimal EMEH placement and tuning for preselected targeted unlocked vibration mode

Seeking for the highest efficiency of the energy harvesting system EMEH should be located at the DOF of the biggest displacement value corresponding with the tar-

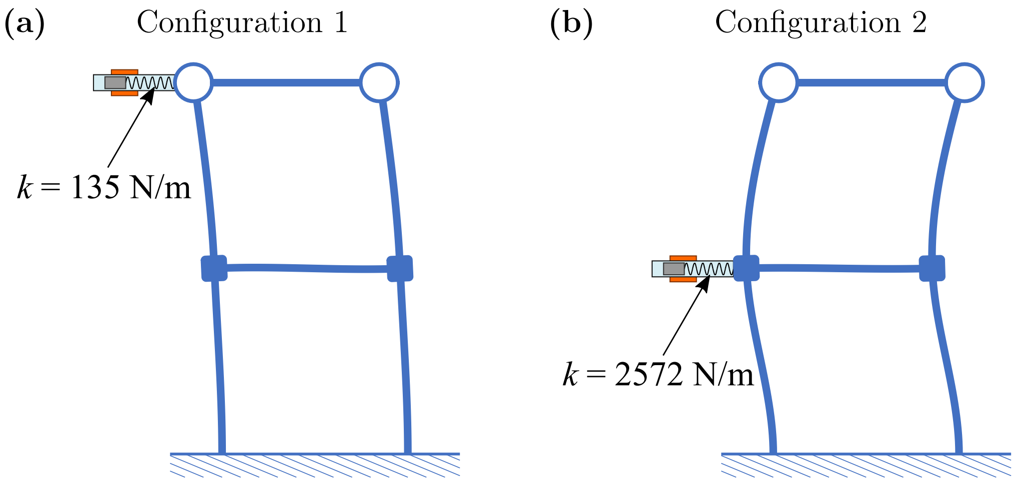

Figure 4.26: Selected EMEH location when tuned to (a) the first and (b) the second unlocked vibration mode, selected as the targeted one

geted mode shape. This DOF is selected by vector $\mathbf{l}^{\star}_{\mathrm{EH}}(r) = \begin{bmatrix} 0 & \cdots & 0 & 1 & 0 & \cdots & 0 \end{bmatrix}^{\mathrm{T}}$ such that

$$\mathbf{l}^{\star\mathrm{T}}_{\mathrm{EH}}(r)\boldsymbol{\phi}^{(r)} = \max_{i \in S_{\mathrm{EH}}} \left| \phi_i^{(r)} \right|, \tag{4.20}$$

where: r is index of the targeted mode and S_{EH} is set of structural DOFs candidate to be EMEH location.

EMEH should be also tuned to the targeted vibration mode. The stiffness of the EMEH spring is selected that EMEH has the same natural frequency as the targeted mode:

$$\frac{k(r)}{m} = \omega^{(r)2}. \tag{4.21}$$

In the present study the energy harvesting system is tested for both the first and the second controlled unlocked vibration mode selected as the targeted one. EMEH placements for both these modes and tuned stiffness k of the spring are shown in Figure 4.26. In the further part of this thesis the system configuration shown in Figure 4.26a is called “configuration 1”, whereas in Figure 4.26b is called “configuration 2”.

4.2.5 Modal energy transfer for enhancement of the energy harvesting process

In this subsection three cases of the kinematic excitations are considered:

case 1 short modulated harmonic ground motion causing transient vibration of the structure,

case 2 harmonic excitation and

case 3 noise excitation.

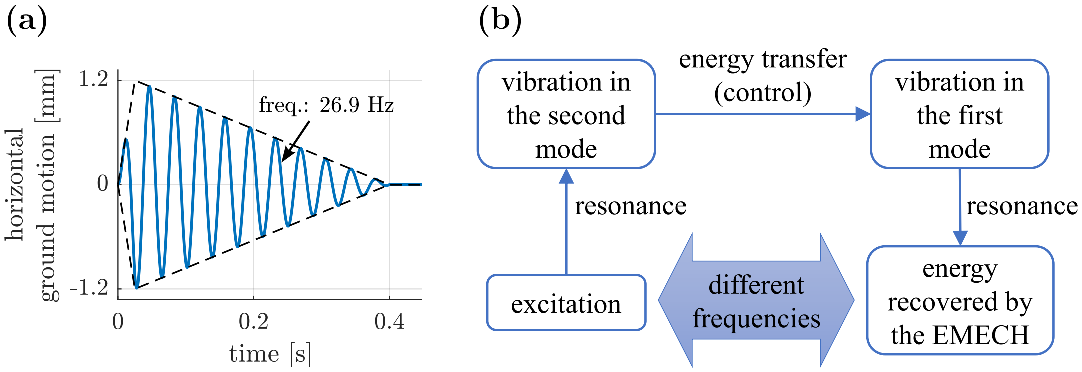

Figure 4.27: (a) time history of kinematic excitation (horizontal ground motion) providing resonance of the second structural unlocked mode and (b) flowchart of the desired energy flow in the system for the configuration 1

Case 1 Modulated horizontal ground motion serving as the kinematic excitation is expressed as

$$q_{\mathrm{g}}(t) = A_{\mathrm{g}}(t) \sin \mathit{\Omega}_{\mathrm{g}} t, \tag{4.22}$$

where: $A_{\mathrm{g}}(t)$ is the motion amplitude depending on the time and $\mathit{\Omega}_{\mathrm{g}}$ is the excitation frequency. The resulting inertia force acting on the structure integrated with the EMEH (see: Eq. (4.19)) is as follows:

$$d_{\mathrm{u}}(t) = -\mathbf{M}_{\mathrm{u}} \mathbf{l}_{\mathrm{xu}} \ddot{q}_{\mathrm{g}}(t), \tag{4.23}$$

where Boolean vector $\mathbf{l}_{\mathrm{xu}}$ selects translational DOFs analogously as $\mathbf{l}_{\mathrm{x}}$ but includes also the motion of the magnet in EMEH.

The ability of the control to transfer the vibration energy to the first unlocked mode (see Fig. 4.26a) is tested first. The test kinematic excitation is modulated and has the same frequency as the second unlocked vibration mode of the structure as shown in Figure 4.27a. This sub-case of the excitation is further called "**case 1-1**". Later, the mechanical energy is to be transferred from the currently excited, the second, unlocked vibration mode of the structure to the first, targeted, unlocked one as shown in Figure 4.27b. Finally, the EMEH tuned to the targeted vibration mode recovers the vibration energy.

The algorithm parameters (see: Algorithm 2) have been select with the trial-and-error method as follows: $\alpha_1 = -1$, $\alpha_2 = 0$, $t_{\mathrm{lock}} = t_{\mathrm{unlock}} = 0$, $\kappa_1 = 300$ W and $\kappa_2 = 0$. The negative first weight and second one equal to zero mean that the control algorithm check only current modal energy transfer rate to the first unlocked vibration mode aiming at making decision to lock or unlock the joints. In this case it is sufficient and provides satisfactory results.

Results are shown in Figure 4.28. It is visible that the second unlocked mode has predominant energy at the beginning due to the resonance with the kinematic excitation (Fig. 4.28b). However, operation of the lockable joints (Fig. 4.28a) causes that the energy is effectively transferred to the first unlocked vibration mode.

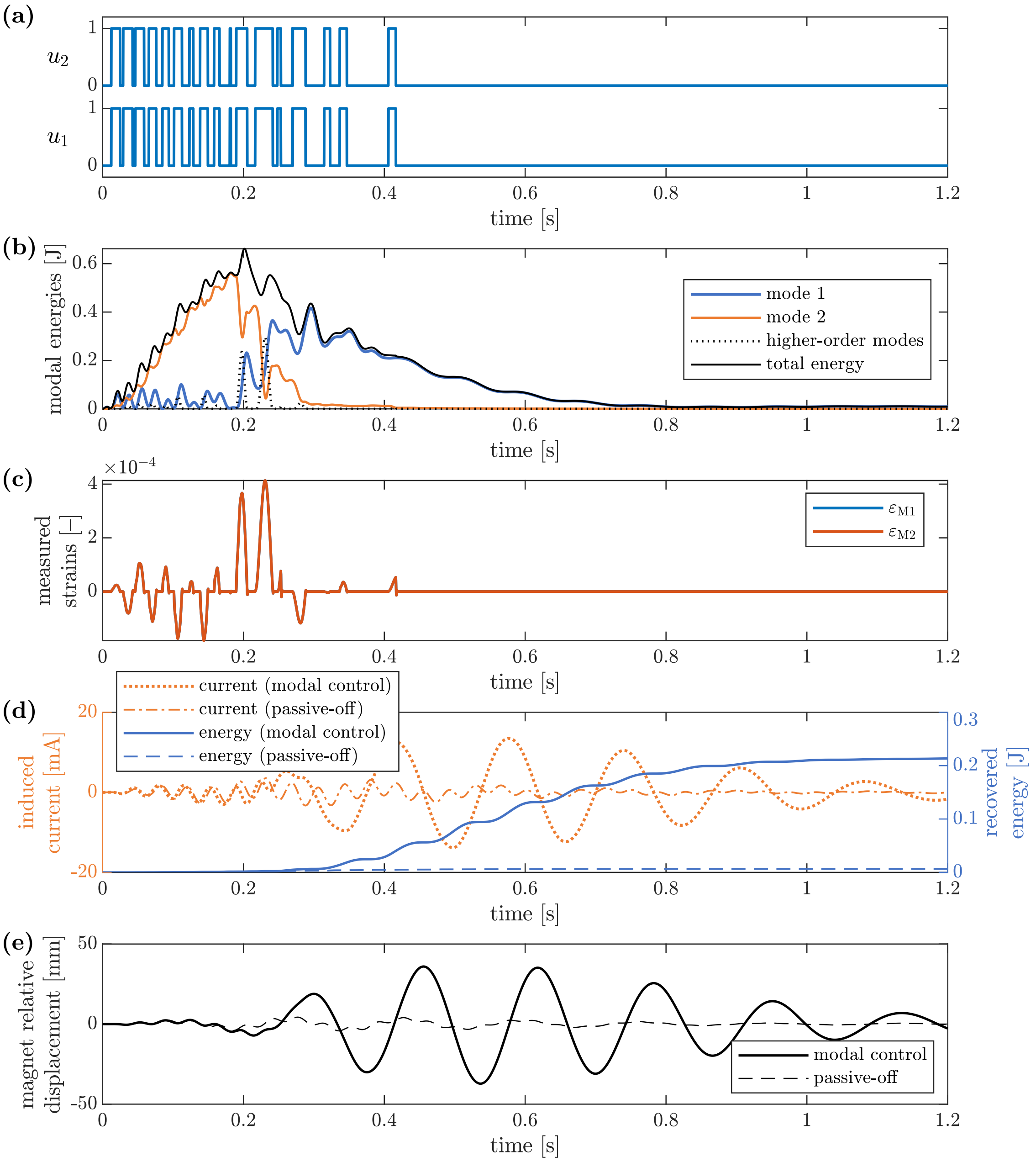

Figure 4.28: Time histories of: (a) control signals, (b) modal energies of the structure, (c) measured strains, (d) electrical current and energy produced by the EMEH displacements compared with passive-off case and (e) relative magnet displacement compared with the passive-off case for case 1-1 of excitation and configuration 1 of the system

In this case the joints are unlocked in time instances when the potential energy of the higher-order unlocked vibration modes is near to zero (dotted line in Fig. 4.28b). It corresponds to near-zero measured strains in Figure 4.28c. Due to that step-like decrements of the structural energy nor measured strains are not visible in after the joint unlocking (compare with the results for vibration attenuation application shown in Section 4.1). In the present case, the strain energy provided by the bending moments transmitted by the lockable joints is transferred back to the targeted mode before the joint unlock, instead of being released in high-frequency vibration. In result, the mechanical energy that is to be recovered by the EMEH is not wasted but kept to be finally recovered by EMEH. The opposite case of the system behaviour could be considered as result of control spillover as opposed to the vibration attenuation application of the control, where dissipation of the energy in the material damping is desired phenomenon.

The energy transferred to the first unlocked vibration mode quickly decreases due to the operation of the EMEH that acts on the controlled structure as TMD. This results in significantly increased amplitude of the magnet relative displacement in comparison to the passive-off case, when the joints are passively unlocked (see: Fig. 4.28e). In consequence, the produced electrical current and energy also are significantly higher in relation to the corresponding quantities obtained for the passive-off case (Fig. 4.28d). In the passive-off case the energy is not transferred to the first unlocked vibration mode, thus EMEH is out of resonance and almost no any energy is produced.

This numerical example shows that the mechanical energy can be effectively transferred to the first unlocked vibration mode from the second one. Here, the energy flow is opposite to the case in which vibration is to be mitigated. It suggest that the proposed control methodology has potential to be used to precisely manage the distribution of mechanical energy among the unlocked vibration modes.

The ability of the proposed control strategy transfer of the energy to the second unlocked vibration mode is investigated below employing configuration 2 of the system (Fig. 4.26b). In this case the kinematic excitation is of the same type but has frequency equal to the natural frequency of the first unlocked vibration mode of the structure and has bigger amplitude. In relation to case 1-1 the amplitude is multiplied by the ratio $\omega^{(2)}/\omega^{(1)}$ that provides the same energy level of the excitation accordingly to the rule

$$A_{\mathrm{g}}^2(t=t_i)\mathit{\Omega}_{\mathrm{g}}^2 = \mathrm{const}, \tag{4.24}$$

where: $A_{\mathrm{g}}(t=t_i)$ is amplitude of the ground motion for any fixed time instant t_i and $\mathit{\Omega}_{\mathrm{g}}$ is its frequency (here: $\mathit{\Omega}_{\mathrm{g}} = \omega^{(2)}$). This sub-case of excitation is called "**case 1-2**" in the further part of this thesis. The test excitation is shown in Figure 4.29a, whereas the desired energy flow is shown in Figure 4.29b.

The algorithm parameters (see: Algorithm 2) have been selected with the trial-and-error method differently from the previous system configuration: $\alpha_1 = 1.5$, $\alpha_2 = -1$, $t_{\mathrm{lock}} = t_{\mathrm{unlock}} = 0$, $\kappa_1 = 800$ W and $\kappa_2 = 0$. In this case the control algorithm checks the weighted sum of current modal energy transfer rates both from the first unlocked vibration mode (the positive first weight) and to the targeted mode (the negative second weight). The reason is explained as follows. The second unlocked modal velocity changes its sign more frequently than the first one in free vibration accordingly to their natural frequencies. In result, if only α_2 is selected nonzero the eventual weighted modal energy transfer rate estimated from Equation (3.39)

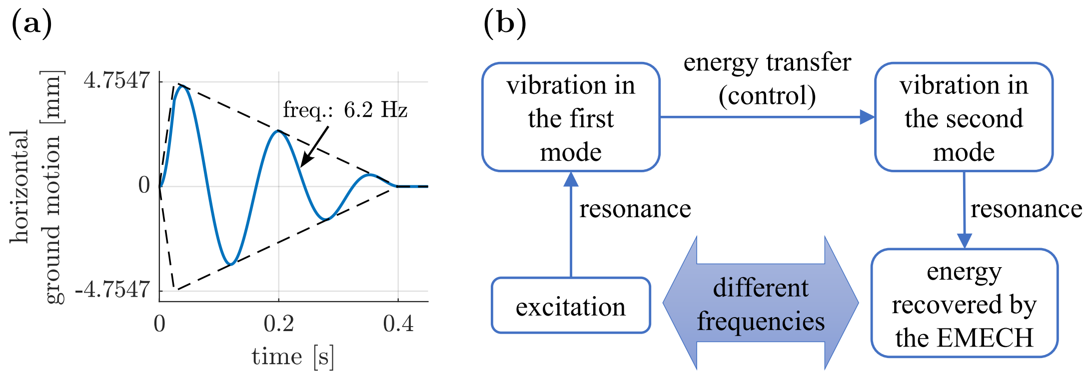

Figure 4.29: (a) time history of kinematic excitation (horizontal ground motion) providing resonance of the first structural unlocked mode and (b) flowchart of the desired energy flow in the system for the configuration 2

also would change its sign more frequently. Such a selection of weights could result in more frequent and less effective switches of the lockable joints. Selecting both weights nonzero allows for decrease of the redundant sign changes. In consequence, it reduces the number of redundant and less effective joint switches.

The results corresponding with case 1-2 of excitation (Fig. 4.29) are shown in Figure 4.30. Similarly to case 1-1 the unlocked mode being under resonance with excitation, but here the first one, is excited. Due to the operation of the lockable joints the energy is transferred to the second, targeted, unlocked vibration mode (see: Figs 4.30a and b). However, in this case the joints mainly are not unlocked at time instances characterised by near-zero strain values resulting in their quick drops (Fig. 4.30c), as opposed to case 1-1. It is due to the fact that the targeted mode has bigger natural frequency than the currently excited unlocked mode, from which energy is transferred. In this situation the targeted mode and remaining higher-order unlocked ones vibrate with frequency lower than their natural frequencies. Thus, the energy transferred to the second and higher-order unlocked vibration modes is accumulated mostly as the strain (potential) energy. This structural behaviour is similar to the vibration attenuation (Section 4.1), where the energy also is transferred from lower-order unlocked vibration modes to the higher order ones. However, in this case due to the negative second weight α_2, the second modal energy usually has predominant participation in the total stain energy to be released after the joint unlock.

Similarly to the case 1-1 the modal energy transfer to the targeted mode results in increase of the: relative magnet displacement amplitude, level of the produced electrical current and recovered energy in relation to the passive-off case (Figs 4.30d and e). However, the produced energy is more than two times smaller than in the case 1-1 despite of the same level of the excitation energy in the sense of Equation (4.24). The control spillover effect is the first reason. Some part of the energy is released in free vibration of the higher-order vibration modes after the joint unlock and later quickly dissipated in the material damping (Fig. 4.30a and b). The second

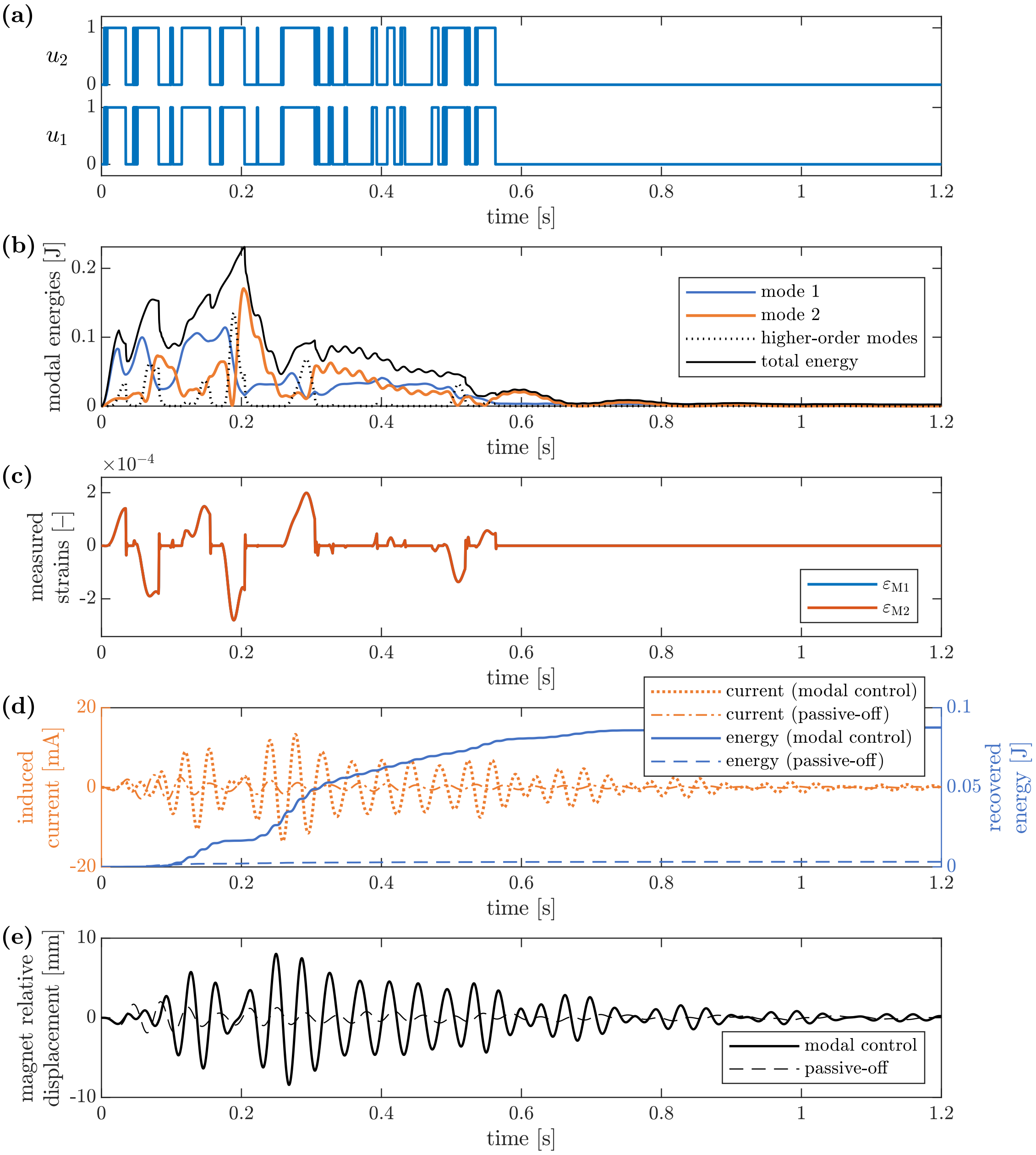

Figure 4.30: Time histories of: (a) control signals, (b) modal energies of the structure, (c) measured strains, (d) electrical current and energy produced by the EMEH displacements compared with passive-off case and (e) relative magnet displacement compared with the passive-off case for case 1-2 of excitation and configuration 2 of the system

reason is that the second unlocked vibration mode has greater damping than the first one, thus the targeted mode loses the energy faster than the first one in case 1-1. Then the less amount of the energy can be recovered by the EMEH.

Case 2 In this case kinematic excitation with the amplitude constant in time is considered. However, the amplitude depends on the frequency that provides constant energy level of the excitation in the sense of Equation (4.24). Horizontal ground displacement is thus described by the equation below

$$q_{\mathrm{g}}(t) = \frac{A_0}{\Omega_{\mathrm{g}}} \sin \Omega_{\mathrm{g}} t. \tag{4.25}$$

Excitation with selected $A_0 = 0.03$ sm/rad is used for both configurations of the system – see: Figure 4.26. The excitation frequencies from range from 1 to 45 Hz is selected. For each frequency of excitation the vibration in the duration time of 10 s is simulated. All results shown in this case are obtained from the last second of this duration in which steady-state of the system is provided.

For both system configurations algorithm parameters remain the same as for case 1 of the excitation.

Comparison of the results obtained both for controlled and passive-off cases for the configuration 1 of the system is shown in Figure 4.31. The two resonance peaks of the structural motion for each sensor location (Fig. 4.20b) are visible near to the natural frequency of the first (targeted) unlocked vibration mode (Fig 4.31a). It is due to the fact that the attached EMEH provides additional mechanical DOF and is tuned to the first unlocked vibration mode. Due to the damping in the system and small mass of the magnet in the EMEH these peaks are not well-separated. In this case the control does not switches the joint state (Fig. 4.31d) and does not transfer energy between unlocked vibration modes, since the targeted mode is naturally excited. Thus, response of the controlled structure is the same as in the uncontrolled case.

For the excitation frequencies in vicinity of the second unlocked natural frequency of the structure the amplitude of q_{M1} is greater than q_{M2} for the passive case. It corresponds with the second unlocked mode shape and is in opposite structural behaviour in vicinity of the first natural frequency of the structure. However, for the controlled structure the amplitude of q_{M1} is lower than q_{M2} as for the first structural unlocked vibration mode. It is evident that the controlled structure vibrates mainly in the first unlocked vibration mode despite of the excitation frequency near to the second unlocked natural frequency. It is result of the energy transfer to the first unlocked vibration mode from the second one.

Phenomenon of the energy transfer is visible also in behaviour of the magnet in EMEH (Fig. 4.31b). In the vicinity of the second natural frequency of the structure the magnet achieves amplitude 2/3 of the amplitude at the first resonance, whereas in the passive-off case it is close to zero. Due to controlled energy transfer the generated power (Fig. 4.31c) in this area also is significantly greater than in the passive-off case for which almost no energy is recovered. For the controlled case maximum mean power produced by EMEH when the energy is transferred from the second unlocked vibration mode to the first one is near to half of the maximum mean power obtained for the first resonance peak. The power peak related to the modal energy transfer has broadened frequency range both in relation to the first power peak and to frequency range of the second unlocked vibration mode.

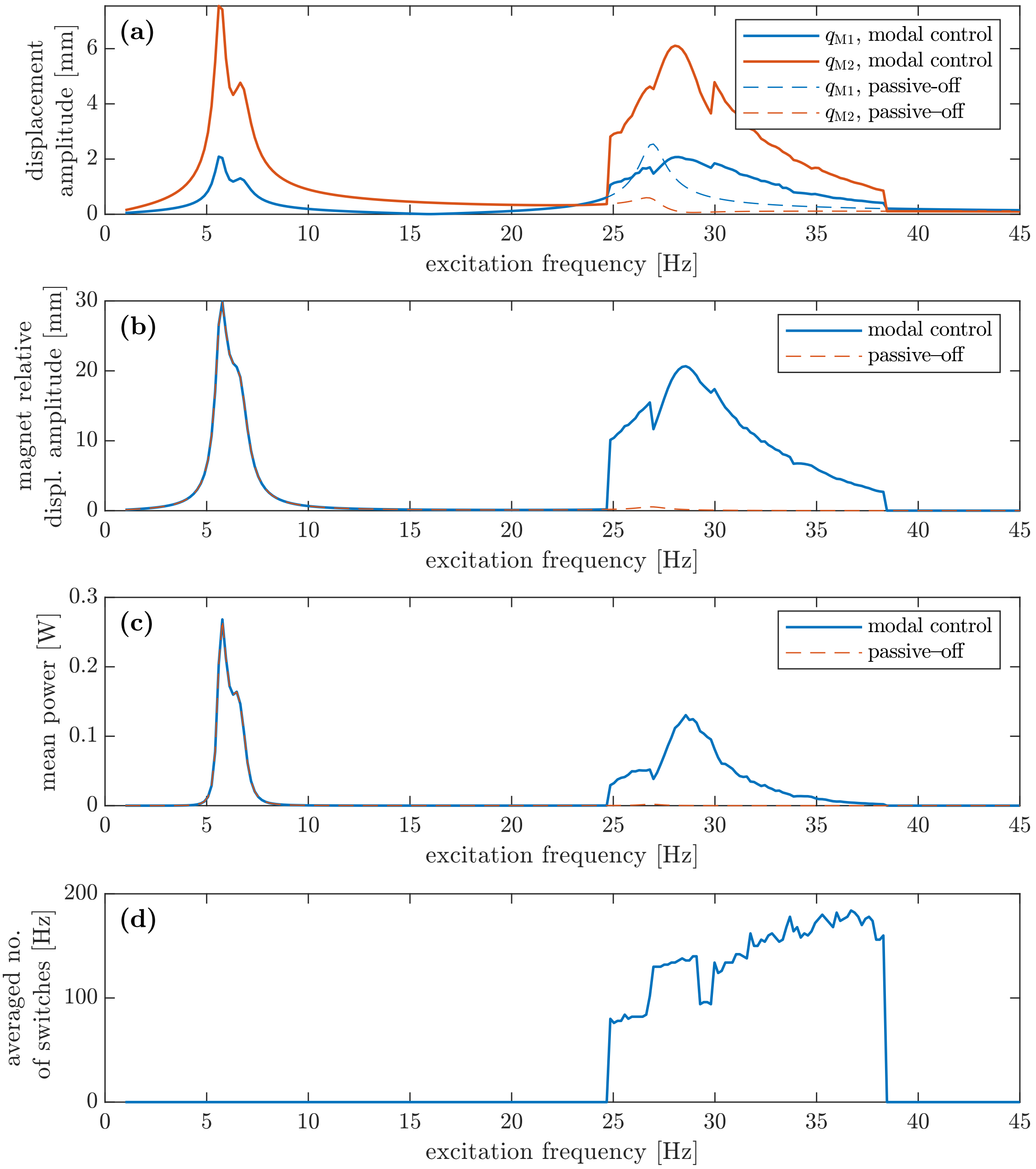

Figure 4.31: Various quantities characterising steady-state system behaviour in dependence on the frequency of kinematic excitation (case 2) obtained for both controlled and passive-off system in configuration 1: (a) amplitudes of structural displacements at sensor locations, (b) amplitude of the relative magnet motion, (c) mean power produced by the EMEH and (d) averaged no. of joint switches $\overline{n}_{\mathrm{J}}$

It is visible that for the frequency range in which modal energy transfer occurs the state of lockable joints is switched with mean frequency below 200 Hz. This quantity increases with the excitation frequency that is typical behaviour. Joints suddenly stop their operation below 25 Hz and above 38 Hz of the excitation frequency. It is due to the selected threshold κ_1 preventing from the frequent joint switches when energy transfer rates are small due to small vibration amplitudes.

Results for the configuration 2 of the system are shown in Figure 4.32. The first

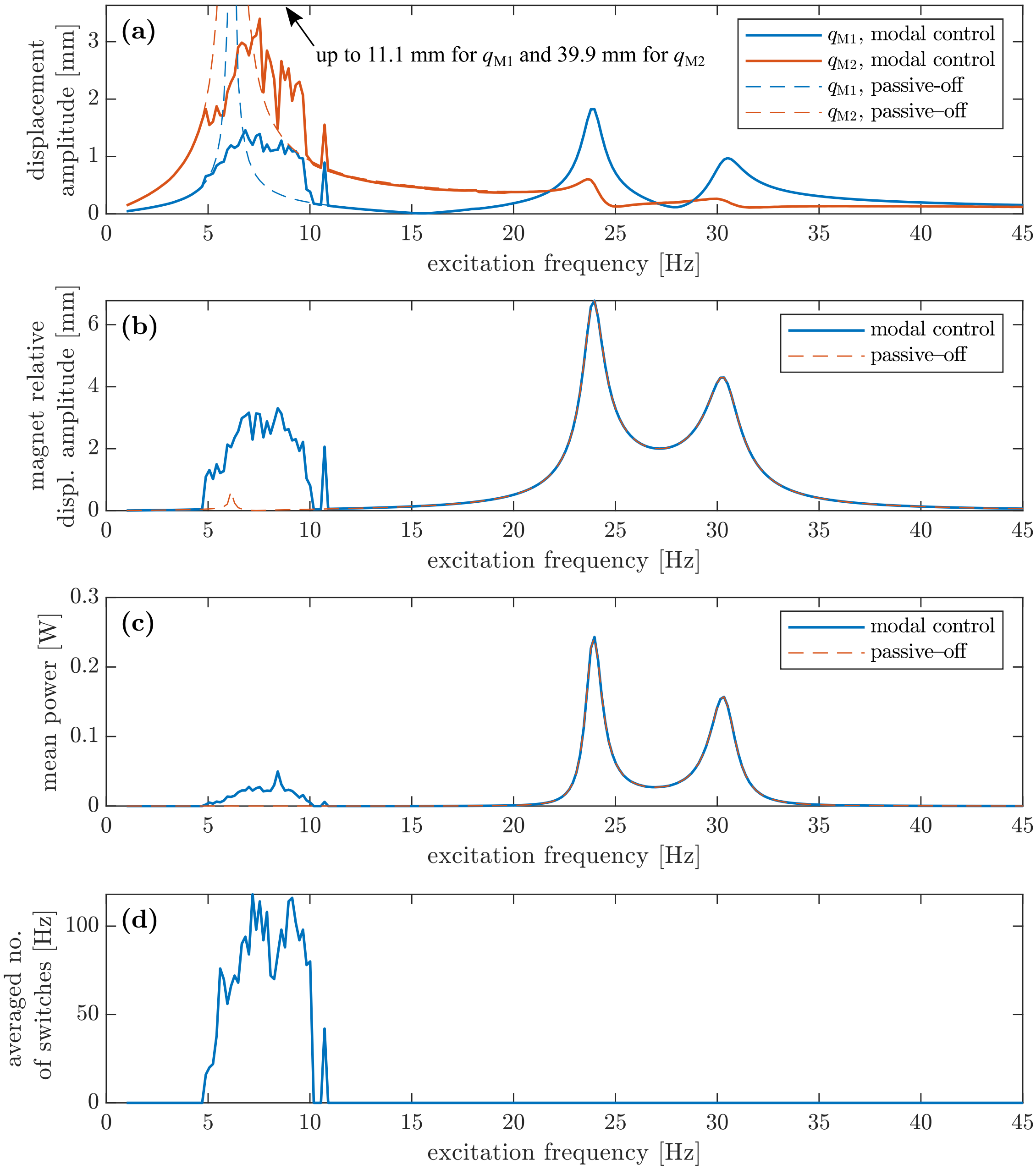

Figure 4.32: Various quantities characterising steady-state system behaviour in dependence on the frequency of kinematic excitation (case 2) obtained for both controlled and passive-off system in configuration 2: (a) amplitudes of structural displacements at sensor locations, (b) amplitude of the relative magnet motion, (c) mean power produced by the EMEH and (d) averaged no. of joint switches $\overline{n}_{\mathrm{J}}$

observation is that the operation of the lockable joints caused significant reduction (near to 10 times) of the vibration amplitude near to the first resonance (Fig. 4.32a). The first reason is that the joints are unlocked at time instances when strains are not equal to zero. Then, some part of energy is released in the higher-order unlocked vibration modes and vibration is mitigated, as described in case 1-2. The second reason is that the amplitude of vibration in the second unlocked vibration mode, to which energy is transferred, is significantly smaller than in the first one for the same level of the mechanical energy. As contrary to the results shown in Figure 4.31a, here after the transfer of the energy to the targeted mode the amplitudes of structural displacements at particular sensor locations do not change their order. It is due to the smaller amplitude of the second, targeted, unlocked vibration mode and still non-negligible participation of the first unlocked mode in the structural vibration.

The two resonance peaks in the vicinity of the second natural frequency of the structure (visible from 20 to 35 Hz) are result of the influence of the EMEH on structural dynamics. Here, EMEH tuned to the second unlocked vibration mode behaves similarly to TMD, analogously to the results for configuration 1 of the system. However, the two new peaks are well-separated for the EMEH tuned to the second unlocked vibration mode. The main reason is the increased stiffness of the EMEH spring aiming at tuning of the EMEH to the second unlocked vibration mode.

The amplitude of the relative magnet displacement in the controlled case is significantly increased with respect to the passive case in the vicinity of the first natural frequency of the structure (Fig. 4.32b). It confirms that energy is transferred to the second unlocked vibration mode to which EMEH is tuned. The amplitude of the relative magnet displacement resulting from the modal energy transfer to the targeted mode is near to half of the maximal amplitude that is achieved in the resonance at 24 Hz.

Regarding the power generated by the EMEH device peak efficiency is slightly smaller than for the previous system configuration but the corresponding operational frequency bandwidth is wider (compare: Fig. 4.31c and Fig. 4.32c). However, both bandwidth and level of the generated power for the configuration 2 of the system when energy is transferred from first unlocked vibration mode are significantly smaller than for configuration 1 when energy is transferred from the second unlocked vibration mode. The corresponding bandwidth is 2.5 times smaller and corresponding generated power level is near to 3 times smaller.

The frequency range in which the modal energy transfer occurs corresponds with the range in which the lockable joints are switched (Fig. 4.32d), analogously to the previous system configuration. Here, the averaged no. of switches achieves level around 100 Hz or is below. It is lower than in the previous system configuration due to the fact that in the present system configuration the joints operate for lower frequencies of excitation aiming at transferring energy in the reversed direction (from the first to the second unlocked mode).

Case 3 In this case the system is excited by the inertia force described analogously to Equation (4.8) but additional DOF related to the EMEH magnet motion is taken into account ($\mathbf{M}_{\mathrm{u}}$ and $\mathbf{l}_{\mathrm{xu}}$ are considered instead of $\mathbf{M}$ and $\mathbf{l}_{\mathrm{x}}$, respectively). Here, the noise magnitude (standard deviation) $\sigma_a = 75$ m/s^2. Results discussed in this case are averaged from 1000 simulations. In each such a simulation the duration time is 30 s, where the last 20 s is taken for calculations of the results. In such a

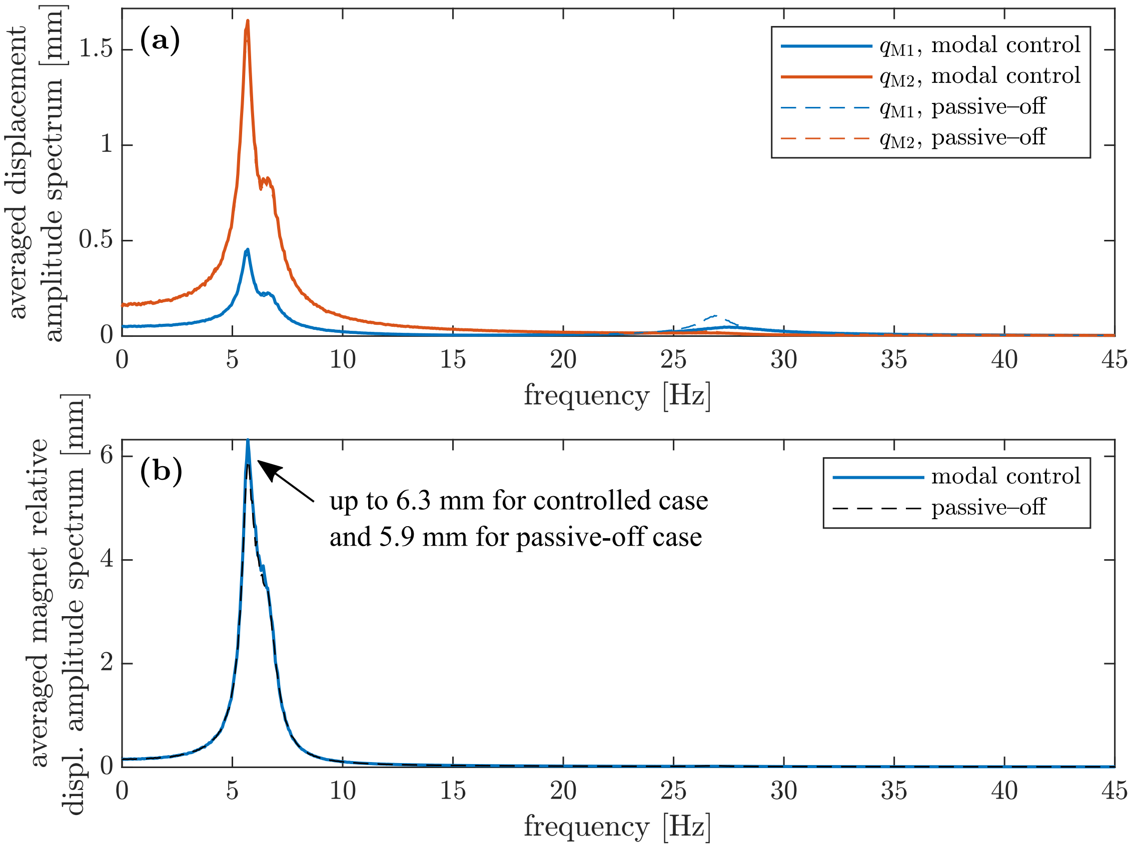

Figure 4.33: Averaged amplitude spectra of: (a) structural displacement at sensor locations and (b) magnet relative displacement obtained for the configuration 1 and excitation case 3, compared with results obtained for uncontrolled structure (passive-off)

way the two structure configurations are tested to assess the ability of the control algorithm to transfer the energy to the first and second unlocked vibration mode. For both system configurations algorithm parameters remain the same as for the case 1 of excitation.

Performance metrics for the configuration 1 of the system are shown in Figure 4.33. In this case the noise kinematic excitation causes vibration mainly in the first unlocked vibration mode (targeted one). Thus, the amount of the energy transferred to this mode is negligible. It is visible in Figure 4.33a, where resonance peaks of the amplitude spectra corresponding with controlled and passive-off case almost overlap in vicinity of the first structural natural frequency. The modal energy transfer is visible in these metrics due to reduction of the resonance peak corresponding with the second structural unlocked vibration mode. Energy from this mode is transferred to the first one that results in small increment of the amplitude of the magnet relative displacement (Fig. 4.33b).

Corresponding performance metrics obtained for the configuration 2 of the system are shown in Figure 4.34. Here, similarly to the case 2 of the excitation, the amplitude spectra for the first structural unlocked vibration mode are significantly reduced (Fig. 4.34a). The first reason is the control spillover effect. The energy

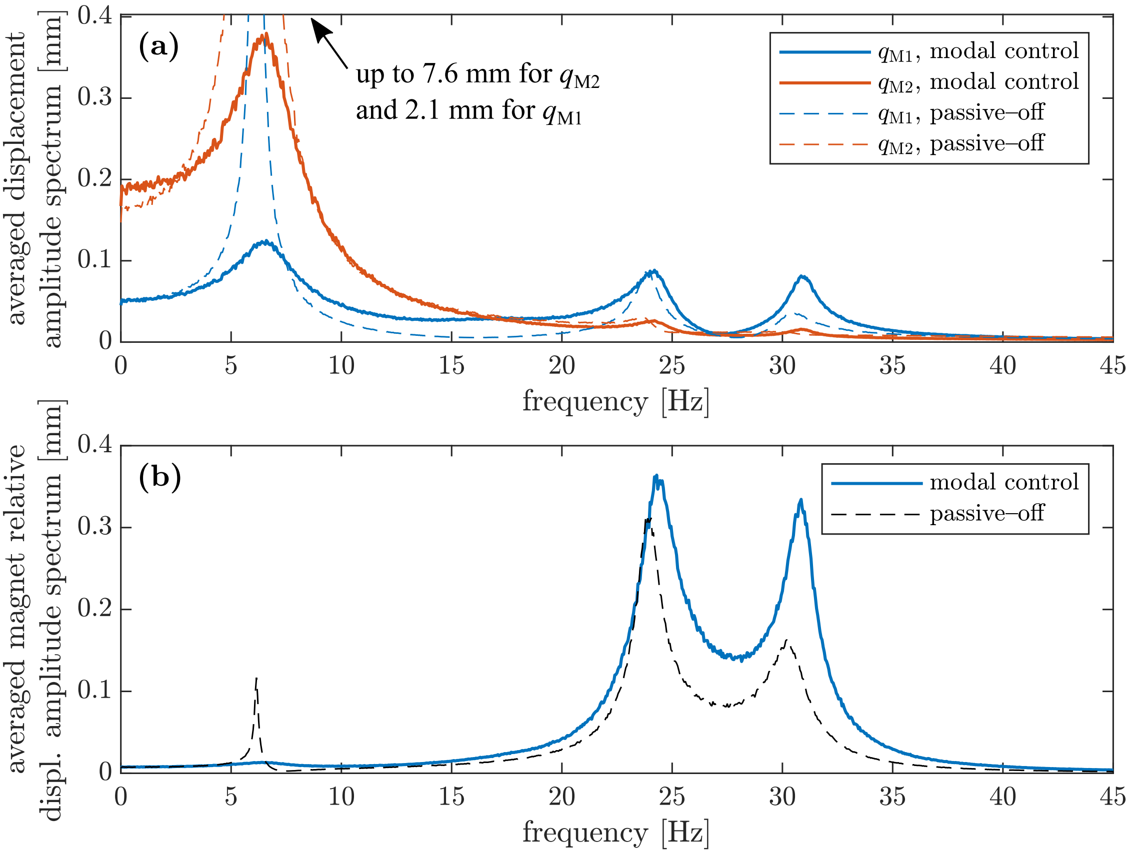

Figure 4.34: Averaged amplitude spectra of: (a) structural displacement at sensor locations and (b) magnet relative displacement obtained for the configuration 2 and excitation case 3 , compared with results obtained for uncontrolled structure (passive-off)

is undesirably transferred to the higher-order unlocked vibration modes and dissipated in the material damping. It is described in detail in cases 1 and 2, where this phenomenon also is observed for the configuration 2. The second reason is, as mentioned in the case 2, disproportion between modal energy and corresponding structural displacement amplitudes for subsequent mode orders. In other words, structural vibration in the second unlocked vibration mode has significantly smaller displacement amplitude than vibration the first one in relation their energy levels. Thus, relatively small but noticeable increment of the amplitude spectra near to the second natural frequency of the structure is achieved at the expense of the large decrement of the first resonance peak due to the modal energy transfer provided by operation of the lockable joints.

Operation of the control algorithm results in the increment of the relative magnet displacement amplitude spectrum in vicinity of the second structural unlocked vibration mode (Fig. 4.34b). It is visible for both resonance peaks related to the operation of the EMEH but the second one is characterised by the greater increment than the first one. A small peak corresponding with the first structural unlocked vibration mode is present in the passive-off case due to the relatively big amplitude

Table 4.8: Comparison of performance metrics of the energy harvesting systems in configuration 1 and 2 the case 3 of excitation, averaged from 1000 simulations

System configuration	**Control state**	$\overline{P}$ [mW]	$\delta\overline{P}$ [%]	$\overline{n}_{\mathrm{J}}$ [Hz]
Configuration 1	controlled	283.0	6.3	79.2
	passive-off	266.2		—
Configuration 2	controlled	88.8	169	134.1
	passive-off	33.0		—

of the structural vibration. For the controlled case the vibration in this mode is significantly reduced and the resonance peak is not distinguishable.

Table 4.8 summarizes effectiveness of the control for both system configurations. $\delta\overline{P}$ is relative increment of the mean power produced by the EMEH (Eq. (4.13)) defined by the equation below.

$$\delta\overline{P} = \frac{\overline{P}_{\mathrm{c}} - \overline{P}_{\mathrm{off}}}{\overline{P}_{\mathrm{off}}}, \tag{4.26}$$

where subscripts "c" and "off" refer to the controlled and passive-off case, respectively.

It is evident that the mean power produced by the EMEH in the controlled case is near three times greater for the configuration 1 of the system than for the configuration 2. It is due to the fact that the first unlocked vibration mode (the targeted one in the configuration 1) of the controlled structure is more sensitive to the kinematic excitation. It can be modal calculation of the modal controllability metric referring to the excitation, as follows: $|\boldsymbol{\phi}^{(1)\mathrm{T}}\mathbf{M}\mathbf{l}_{\mathrm{x}}| = 1.81$ and $|\boldsymbol{\phi}^{(2)\mathrm{T}}\mathbf{M}\mathbf{l}_{\mathrm{x}}| = 0.85$ (see: Eq. (4.8)). Amplitudes referring to the inertial force have greater participation in the first unlocked mode shape than in the second one. Moreover, the first unlocked vibration mode is less damped than the second one (Fig. 4.23). Thus, despite of the fact that for the configuration 2 the 169 % increment of the generated power is achieved the configuration 1 provides significantly better performance of the system even without energy transfer as in passive-off case.

Averaged number of joint switches visible in Table 4.8 is calculated analogously as in Equation (4.9) and averaged from 1000 simulations. It is greater for the configuration 2 than for the configuration 1, as opposed to case 2 of excitation. Case 2 is affected by the excitation frequency for which the transfer occurs (Figs 4.31d and 4.32d), however in the present case excitation for both configurations is of random type. Hence, in this case the other influencing factor is the natural frequency of the targeted mode. Second monitored modal velocity usually (e.g. in free vibration) changes its sign more frequently than the first one, thus the estimated weighted modal energy transfer rates also more frequently cross the selected thresholds in Algorithm 2. In results, Algorithm 2 switches the joint state more frequently for configuration 2.

From the numerical study discussed in this subsection it follows that the energy harvesting system should be designed in such a way that the targeted mode is the most sensitive to the excitations and is within the frequency range of the excitations. Energy transfer from other unlocked vibration modes should be treated as additional possibility for expanding of the operational frequency bandwidth. Moreover, it is also desired that the targeted mode has lower natural frequency than other unlocked vibration modes within the frequency range of the excitation. It is due to the control spillover effect occurring when the energy transferred from the lower-order unlocked vibration modes to higher – targeted one – also is undesirably transferred to not monitored vibration modes. Moreover, lower-order unlocked vibration modes are usually less damped that also is advantage during selection of the targeted mode. However, if the control system is installed on the structure both for the purpose of vibration mitigation and energy recovery, then these recommendations are not the most suitable ones. Here, the one of the highest-order unlocked vibration modes among the monitored ones should be selected as the targeted one. Numerical results obtained for configuration 2 of the system demonstrate that simultaneous vibration mitigation and additional vibration recovery are possible. Vibration mitigation in this configuration occurs even if it is not the purpose of the control. Moreover, weights α_p can be switched during the operation of the control algorithm giving greater flexibility and its adaptation to the current operation purposes or emergency situations where the damping has the biggest priority.

Chapter 5

Experimental verification

In this chapter experimental verification of the proposed control methodology is described and discussed. Experimental results are compared with numerical ones obtained with the aid of updated FE model. The FE model is updated using 10 identified locked vibration modes of the real frame structure. The reason of using locked experimental modal data is described in Subsection 5.1.2. Experimental validation includes both free vibration of the structure (results analysed in the time domain) and forced vibration obtained with frequency sweeps provided by modal shaker (results analysed mainly in the frequency domain). The ability of the control strategy to both attenuate the vibration and transfer the mechanical energy to the preselected unlocked mode is tested.

In this chapter a laboratory-scale frame demonstrator equipped with six lockable joints is introduced and described first (Section 5.1) along with its locked vibration modes. Later, in Section 5.2 FE model of the structure is described that is followed by the model updating procedure using modal data for locked joints. Equipment limitations, hardware control loop and preparation of the control algorithm is described in Section 5.3. In Section 5.4 experimental results of vibration attenuation are analysed and compared with those obtained from numerical simulations using the updated FE model. Analogous comparison for transferring of the energy to the preselected vibration mode is discussed in Section 5.5.

5.1 Experimental setup

5.1.1 Smart structure equipped with 6 semi-active joints

A smart structure under consideration is a laboratory-scale frame equipped with six lockable joints. Its scheme and dimensions are shown in Figure 5.1a, whereas its photo is presented in Figure 5.1b. The locking effect in the joints is provided by clamping force sufficient to stop relative rotation between friction parts. The working principle of the joint and structure is similar to one shown in Figure 2.10b but in employed real lockable joint the friction interface has conical shape. Beams are

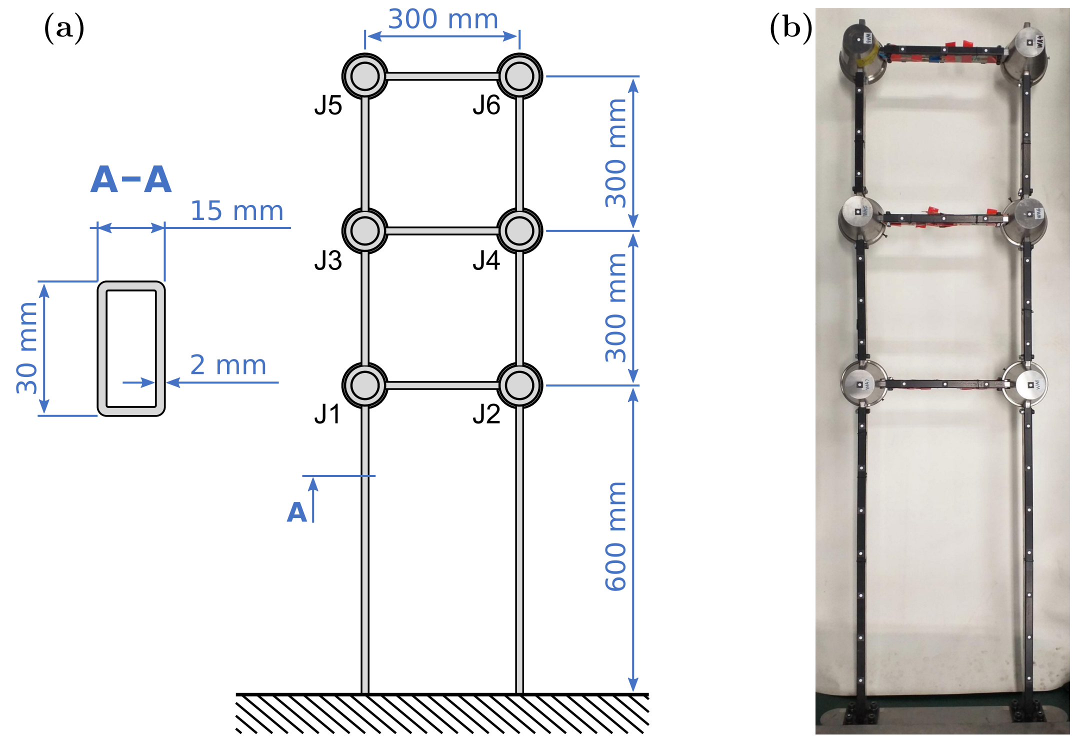

Figure 5.1: Laboratory frame structure: (a) scheme with structural dimensions and numeration of the lockable joints, and (b) its photograph [152]

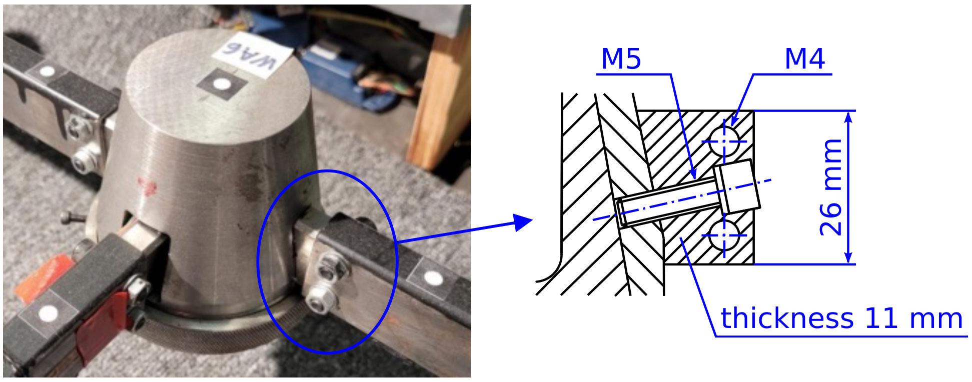

Figure 5.2: Details of the bolted connection between lockable joint and beam [153]

connected to the lockable joints in such a way that rotations of ends of transversal beams can be coupled or decoupled with rotation of longitudinal beams at corresponding locations if the joints are currently locked or unlocked, respectively. The lockable joints always transmit bending moment between longitudinal beams. This also can be deduced from details shown in Figure 5.2, where both adjacent longitudinal beams are connected to one casing, whereas transversal beam is connected to inner part of the joint that can rotate with respect to the casing (when the joint is unlocked).

The lockable joints utilised for the experimental verification are designed in such a way that when they are not supplied with any voltage they are locked by the inner springs providing clamping force between the friction parts. When the appropriate

Table 5.1: Maximal bending moments transmitted by the lockable joints corresponding with their locked and unlocked state

Joint no.	**J1**	**J2**	**J3**	**J4**	**J5**	**J6**
$f_k^{\mathrm{u\,max}}$ [Nm]	2	2.2	1.5	1.5	2	2
$f_k^{\mathrm{l\,max}}$ [Nm]	16	16	38	31	31	37

voltage is supplied then piezo stack unlocks the joint. This action does not change the adopted convention of description of the control signal. Still $u_k(t) = 0$ denotes that the joint is unlocked, whereas $u_k(t) = 1$ denotes the locked state of the joint. The delay in the unlocking of the joint with respect to change in the control signal is 3 ms. The delay of the locking is not known exactly but is assumed to have similar value. Maximal operational frequency of the lockable joints is 300 Hz.

The clamping force provided by the inner springs is sufficient to prevent from the sliding between friction parts if assumed maximal transmitted bending moment $f_k^{\mathrm{l\,max}}$ is not exceeded. Unfortunately, when the joint is in the unlocked state the friction parts are not completely detached. It results in residual friction between friction parts. Thus, for sufficiently small level of vibration the bending moment transmitted by the lockable joint does not exceed the maximal value $f_k^{\mathrm{u\,max}}$ corresponding with maximal value of residual static friction between friction surfaces. In this scenario there is no any difference in behaviour of the unlocked and locked state of the joint. The maximal bending moments $f_k^{\mathrm{l\,max}}$ and $f_k^{\mathrm{u\,max}}$ that can be transmitted by the lockable joints in locked and unlocked state, respectively, without the sliding effect are listed in Table 5.1. Numeration of the lockable joints is consistent with Figure 5.1a. The discrepancies in the transmitted bending moments of particular lockable joints result not only from the operational wear but also from the fact that various generations of the joint prototypes are employed.

The lockable joints are connected with the beams via bolted connections. Details of such a connection are shown in Figure 5.2. The bolted connection should not be modelled as ideally rigid, since it would result in significantly different natural frequencies and mode shapes as demonstrated in [152]. Section 5.2 discusses modelling and parametric identification of the stiffness of the bolted connection aiming at reproduction of the structural behaviour by the FE model. To this end, the modal data (natural frequencies and mode shapes) of the frame structure are used. These data are described in the subsection below.

5.1.2 Experimental modal analysis

Modal data from the frequency range 0-960 Hz are extracted via modal analysis. To this end, four three-directional accelerometers are used. Dense mesh of measurement points distributed with the spatial resolution 75 mm along structural members is achieved with the roving accelerometer technique. It results in 41 sensor locations and 123 measured outputs. The structure is excited using a modal hammer. Hard-

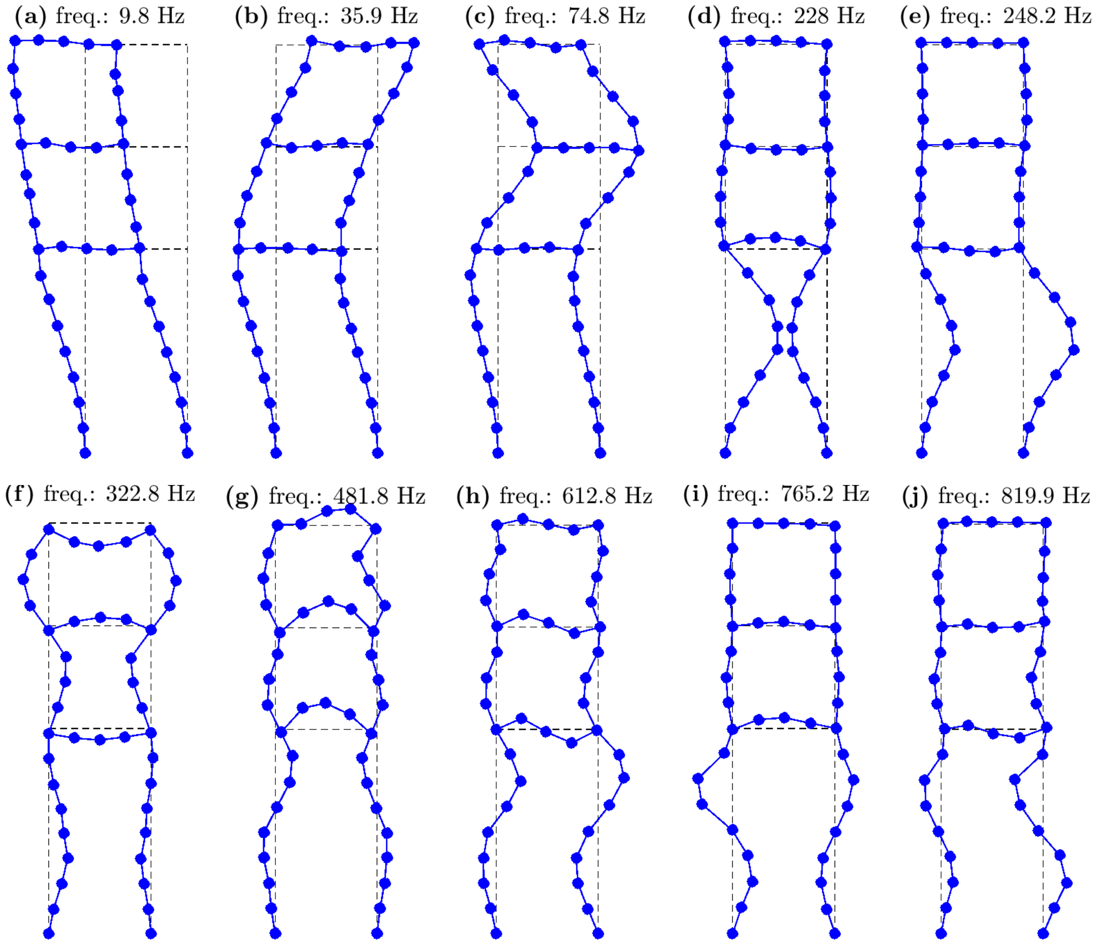

Figure 5.3: Measured locked vibration modes selected for the model updating

ness of the modal hammer tip is increased for subsequent frequency sub-ranges that are: 0-25 Hz, 25-150 Hz, 150-280 Hz, 280-360 Hz, 360-450 Hz, 450-660 Hz and 660-960 Hz. Measurement data are collected and analysed with aid of the LMS SCADAS system integrated with LMS Test.Lab software. Stochastic subspace identification method is used.

Due to the fact that lockable joints keep residual clamping force in the unlocked state they introduce some friction-based bending moment resulting in nonlinearities and strongly non-proportional damping of the system. It is undesirable during identification of the modal parameters. Thus, experimental modal analysis was performed only for the joints in the locked state. FE model is updated only by change of the stiffness of the bolted connections. Thus it can be updated also with joints in the locked state and after unlocking the stiffness of the bolted connections will be preserved.

25 three-dimensional locked mode shapes, natural frequencies and modal damping factors are extracted. They are shown in Appendix A[1]. As described in the

---

[1] The identified modal parameters are slightly different from those shown in [152] due to the fact that the frame has been disassembled, renovated, and reassembled again before modal analysis described in this thesis.

appendix 10 in-plane (IP) vibration modes are selected for the model updating purposes and designing of the controller, since out-of-plane vibration modes are not controllable by the lockable joints. The selected IP modes are shown in Figure 5.3.

Mode shapes shown in Figure 5.3 contain many shape deviations including asymmetry. It shows that bolted connections (Fig. 5.2) are highly uncertain due to the operational wear of the structure and assembly discrepancies.

5.2 Numerical model of the real structure

In this section both the proposed FE model of the real frame and selected model updating method are described. The updated FE model is used both to design the controller (algorithm parameters based on modal data: $\mathbf{F}$, $\boldsymbol{\Gamma}_{\mathrm{MM}k}$, $\boldsymbol{\Delta\phi}_{\mathrm{M}k}$) and numerical simulations.

5.2.1 Initial finite element model

As mentioned, the FE model is to be updated using experimental modal data obtained for the joints in the locked state. Thus, the joints in FE model also are kept in the locked state during model updating. Moreover, modal data obtained from the FE model with the locked joints are required for calculations and comparison with their experimental counterpart. To this end, locking effect is obtained by pursuing exact kinematic constraint on DOFs involved in the lockable joints (Equation (2.37)). The resulting model is reduced by six DOFs (one rotational DOF per lockable joint).

A FE model $(\widetilde{\mathbf{M}}, \widetilde{\mathbf{K}}(\boldsymbol{\theta}))$ of class $\mathcal{C}$ is considered for model updating. Matrices $\widetilde{\mathbf{M}}$ and $\widetilde{\mathbf{K}}(\boldsymbol{\theta})$ refer to the FE model with locked joints and can be obtained with transformation as in Equation (2.59). $\widetilde{\mathbf{M}}$ is assumed to be known, whereas $\widetilde{\mathbf{K}}(\boldsymbol{\theta})$ depends on unknown parameter vector $\boldsymbol{\theta} = \begin{bmatrix}\theta_1 & \theta_2 & \cdots & \theta_{N_\theta}\end{bmatrix}^{\mathrm{T}}$ as follows:

$$\widetilde{\mathbf{K}}(\boldsymbol{\theta}) = \widetilde{\mathbf{K}}_0 + \sum_{t=1}^{N_\theta} \theta_t \widetilde{\mathbf{K}}_t, \tag{5.1}$$

where: $\widetilde{\mathbf{K}}_0$ is matrix representing stiffness of well-known components of the structure, θ_t is unknown parameter scaling matrix $\widetilde{\mathbf{K}}_t$ associated with the components of the structure with uncertain stiffness.

FE model of the structure is shown in Figure 5.4a. Behaviour of the bolted connection is reproduced by nominal rotational stiffness k_{R} scaled by unknown parameter θ_t as shown in the zoomed area. For tth bolted connection matrix $\widetilde{\mathbf{K}}_t$ is defined as follows:

$$\widetilde{\mathbf{K}}_t = k_{\mathrm{R}} \widetilde{\mathbf{b}}_t \widetilde{\mathbf{b}}_t^{\mathrm{T}}, \tag{5.2}$$

where vector

$$\widetilde{\mathbf{b}}_t = \begin{bmatrix}0 & \cdots & 0 & 1 & 0 & \cdots & 0 & -1 & 0 & \cdots & 0\end{bmatrix}^{\mathrm{T}}$$

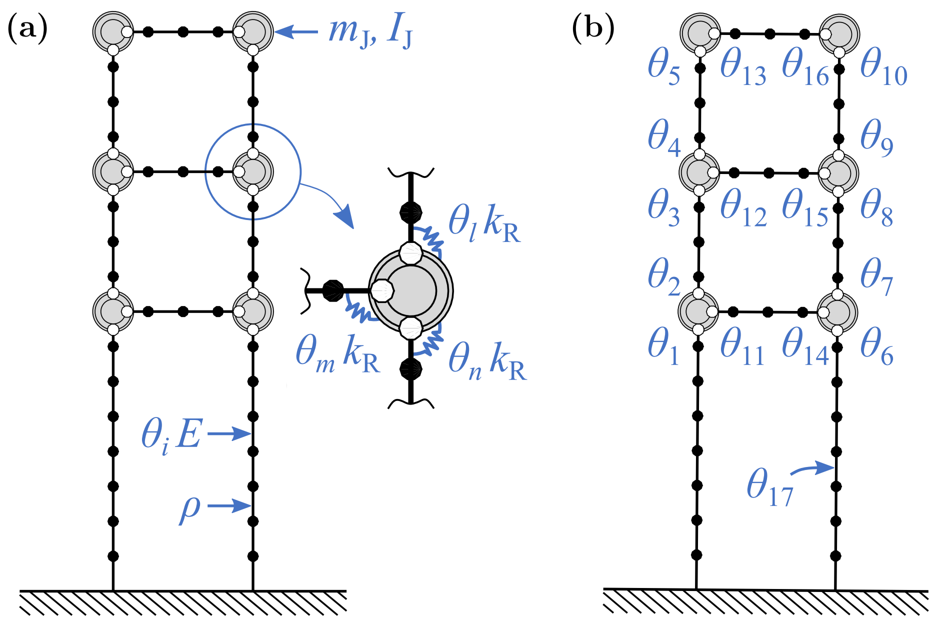

Figure 5.4: Structural FE model to be updated [152]: (a) FE mesh with assigned physical properties and (b) assigning of the unknown parameters to the bolted connections and Young modulus of the beams

Table 5.2: Properties of the FE model of the structure

Quantity	**Symbol**	**Units**	**Value**
Young modulus (steel)	E	[Pa]	$210 \cdot 10^9$
material density (steel)	ρ	[kg/m^3]	7840
geometric moment inertia of the beam cross section	I	[mm^4]	5554
area of the cross section of the beam	A	[mm^2]	164
total mass of the semi-active joint	m_J	[kg]	1.86
total mass moment of inertia of the locked joint	I_J	[kgmm^4]	$1.55 \cdot 10^9$
nominal rotationa stiffness of the bolted connection	k_R	[Nm/rad]	10^4
total no. of DOFs (unlocked joints)	N_d	[–]	145
reduced no. of DOFs (locked joints)	$N_d - N_k$	[–]	139

selects DOFs involved in tth bolted connection (that differ from DOFs selected by vector $\mathbf{l}_k$ described in Subsection 2.2.2).

Additionally, Young modulus of the material of beams is also scaled by the unknown parameter. Finally, the structure is parameterized with 17 unknown parameters: 16 for all bolted connections (each bolted connection is parameterized independently) and one for stiffness of all beams by scaling the Young modulus (common parameter for all beams), as shown in Figure 5.4b.

Physical properties are listed in Table 5.2 along with FE model parameters. Due to the fact that joints are kept in the locked state they are treated as rigid bodies with mass m_J and inertia moment I_J. Beam structural members are represented by beam FEs based on the Euler-Bernoulli beam theory. Each beam FE has 6 DOFs (in-plane motion). Its transversal motion is described by cubic shape functions, whereas longitudinal deformation by linear shape functions. FE mesh nodes on the beams are consistent with accelerometer locations, excepting beam ends (compare Figs 5.4 and 5.3). Then, length of particular FEs belonging to one structural beam is not constant. However, bending moments transmitted by the beams connected to the locked joints is usually greatest at their ends, thus it is desirable to use denser FE mesh in these regions.

Selected value of the nominal rotational stiffness k_{R} (Tab. 5.2) is within the range of highest sensitivity of the numerical modal parameters to the changes of the rotational stiffness of the bolted connections (when $\theta_t = 1$, $t = 1, 2, \ldots 17$). It improves estimation accuracy of the unknown parameters (see: Subsection 5.2.2). k_{R} much below of the selected value could cause behaviour of the bolted connection similar to the hinge, whereas too big k_{R} could cause that the bolted connections behaves like semi-rigid joint. In both cases sensitivity of the numerical modal parameters to the stiffness of the bolted connection is too low to provide reliable model updating [154]. The sensitivity range and selection of the nominal rotational stiffness for the structure under consideration in this thesis is investigated in [152].

After the stage of model updating, when the FE model is used for the controller design and simulation, the joint can be unlocked and, in consequence, the total mass moment of inertia of the locked joint I_{J} (see: Tab. 5.2) is divided into moment of inertia $I_{\mathrm{J1}} = 1.21 \cdot 10^9$ kgmm^4 related to the rotational DOF belonging to the longitudinal beams and $I_{\mathrm{J2}} = 3.41 \cdot 10^8$ kgmm^4 related to the end of transversal beam. Total mass of the lockable joint m_{J} does not have to be divided, since translational DOFs are not decoupled when joint is unlocked as opposed to the rotational ones.

5.2.2 Model updating

Classical model updating methods can be divided into two types according to type of model that is to be updated and the way they find the updated model [155]: direct methods and iterative methods. Direct methods are faster but have many significant disadvantages. They usually tend to exactly reproduce the measurement data, including the measurement noise. Thus, high-accuracy of measurement is the prerequisite. The direct methods often operate on entire matrices representing the updated model, e.g. mass and stiffness matrices. Thus, they require extrapolation of the measurement data from the measurement locations to the configuration space of the FE model or reduction of the FE model to the configuration space related to sensor locations. Moreover, the physical meaning provided by the updated mass and stiffness matrices is limited and updated model often reproduces only the data to which was calibrated, whereas it can be not able to reproduce behaviour of the real system in any other scenario. It is also possibility to introduce the spurious modes. As opposed, the iterative methods operate on the parametric model, whose example is described in Section 5.2, in which enables selection of the parameters that are to be updated. These parameters are physically meaningful. Despite of required higher computational burden and physical insight to select updated parameters the iterative methods are devoid of disadvantages of the direct methods.

Among iterative methods of model updating based on the experimental modal data the two ones are widely accepted: mode matching and Bayesian approach proposed by Yuen et al. Mode matching is based on sensitivity of the modal parameters with respect to $\boldsymbol{\theta}$. It minimises norm of error between numerical and experimental modal data [155, 156]. However, measured modal data can be incomplete (missing some of subsequent modes) and, in addition, numerical vibration modes obtained from the FE model can have order different from the experimental ones. Moreover, the order of numerical vibration modes can be switched during the model updating procedure due to changing unknown parameters representing structural properties. Thus, in each iteration step it requires of matching of the numerical modal data with the corresponding experimental that allows for proper calculation of the error norm and its derivatives. It is reflected in the name of the method. Usually, experimental and numerical mode are matched according to the highest MAC value. Mode matching problem can be avoided using the Bayesian probabilistic framework for parametric identification of the structural stiffness proposed by Yuen et al. [157, 158]. However, identified modal parameters shown in Figure 5.3 have sufficient number of sensor locations for calculation of MAC between experimental modes and their numerical counterparts allowing for reliable mode matching. Moreover, a comprehensive comparison provided by Ostrowski et al. [152] demonstrates that method proposed by Yuen et al., despite of its advantages, should not be recommended for identification of rotational stiffness of the structural members. For the considered class of problems this method is characterised by very slow convergence, resulting in tremendous computational burden required to find stiffness parameter values. Method also yields to numerical problems resulting in unreliable estimation of parameter variances. Mode matching is devoid of these disadvantages: it finds stiffness parameters quickly (tens of iterations vs. hundreds of thousands of iterations) and allows for reliable estimation of variances. Due to its performance in estimation of rotational stiffness parameters mode matching is adopted in this thesis for updating of the considered FE model.

Mode matching: optimisation problem

Mode matching method solves the optimisation problem below.

$$\begin{aligned} &\text{Find} && \boldsymbol{\theta} \in \mathbb{R}_{+}^{N_\theta} \\ &\text{to minimise} && \varepsilon(\boldsymbol{\theta}), \end{aligned} \tag{5.3}$$

where:

$$\varepsilon(\boldsymbol{\theta}) = \mathbf{e}^{\mathrm{T}}(\boldsymbol{\theta})\mathbf{W}_{\mathrm{e}}\mathbf{e}(\boldsymbol{\theta}), \tag{5.4}$$

is the objective function representing square weighted error between numerical and experimental vibration modes. Such a weighted norm is widely accepted error metric for model updating of engineering structures [153, 155, 156, 159–162]. In the equation above $\mathbf{W}_\mathrm{e}$ is selected weighting matrix and vector $\mathbf{e}(\boldsymbol{\theta})$ collects errors between modal parameters including both locked eigenvalues (squares of corresponding natural frequencies) and locked mode shapes:

$$\mathbf{e}(\boldsymbol{\theta}) = \begin{bmatrix} \widetilde{\boldsymbol{\lambda}}_\mathrm{exp} \\ \widetilde{\boldsymbol{\psi}}_\mathrm{exp} \end{bmatrix} - \begin{bmatrix} \widetilde{\boldsymbol{\lambda}}(\boldsymbol{\theta}) \\ \mathbf{L}_\mathrm{o}\widetilde{\boldsymbol{\phi}}(\boldsymbol{\theta}) \end{bmatrix}, \tag{5.5}$$

where: vectors $\widetilde{\boldsymbol{\lambda}}_\mathrm{exp} = \begin{bmatrix} \widetilde{\lambda}^{(1)}_\mathrm{exp} & \cdots & \widetilde{\lambda}^{(N_\mathrm{M})}_\mathrm{exp} \end{bmatrix}^\mathrm{T} \in \mathbb{R}^{N_\mathrm{M}}$, $\widetilde{\lambda}^{(1)}_\mathrm{exp} = \widetilde{\omega}^{(m)2}$, and $\widetilde{\boldsymbol{\psi}}_\mathrm{exp} = \begin{bmatrix} \widetilde{\boldsymbol{\psi}}^{(1)\mathrm{T}}_\mathrm{exp} & \cdots & \widetilde{\boldsymbol{\psi}}^{(N_\mathrm{M})\mathrm{T}}_\mathrm{exp} \end{bmatrix}^\mathrm{T} \in \mathbb{R}^{N_\mathrm{M}N_\mathrm{o}}$ involve N_M experimental locked eigenvalues and experimental locked mode shapes, respectively, N_o is number of measured outputs. Analogously, vectors $\widetilde{\boldsymbol{\lambda}}(\boldsymbol{\theta}) \in \mathbb{R}^{N_\mathrm{M}}$ and $\widetilde{\boldsymbol{\phi}}(\boldsymbol{\theta}) \in \mathbb{R}^{N_\mathrm{M}N_\mathrm{d}}$ contain matched numerical locked eigenvalues $\widetilde{\lambda}^{(k_m)}(\boldsymbol{\theta})$ and scaled numerical locked mode shapes $c_m\widetilde{\boldsymbol{\phi}}^{(k_m)}(\boldsymbol{\theta}) \in \mathbb{R}^{N_\mathrm{d}}$, where c_m is modal scale factor

$$c_m = \frac{\widetilde{\boldsymbol{\psi}}^{(m)\mathrm{T}}_\mathrm{exp}\mathbf{D}\widetilde{\boldsymbol{\phi}}^{(k_m)}}{\left\|\mathbf{D}\widetilde{\boldsymbol{\phi}}^{(k_m)}\right\|^2}. \tag{5.6}$$

Usually, $\mathbf{D} \in \{0,1\}^{N_\mathrm{o}\times N_\mathrm{d}}$ is Boolean matrix selecting the measured DOFs from numerical mode shapes but as mentioned earlier FE mesh is not consistent with all measured locations, thus in this case $\mathbf{D} \in \mathbb{R}^{N_\mathrm{o}\times N_\mathrm{d}}$ is sparse transformation matrix. $\mathbf{L}_\mathrm{o} \in \mathbb{R}^{N_\mathrm{M}N_\mathrm{o}\times N_\mathrm{M}N_\mathrm{d}}$ in Eq. (5.5) is a block-diagonal matrix composed of matrices $\mathbf{D}$. Numerical vibration modes are matched (paired) to the experimental modes according to the highest MAC value. For each mth experimental vibration mode the index k_m of the numerical vibration mode is obtained as follows:

$$k_m = \arg\max_k \left[\mathrm{MAC}\left(\widetilde{\boldsymbol{\psi}}^{(m)}_\mathrm{exp}, \mathbf{D}\widetilde{\boldsymbol{\phi}}^{(k)}(\boldsymbol{\theta})\right)\right]. \tag{5.7}$$

Seeking simplification of notation, indices k_m of the numerical locked vibration modes are replaced with indices of the corresponding experimental locked modes m.

It is recommended to select the weighting matrix as reciprocal to the measurement covariance matrix $\boldsymbol{\Sigma}_\mathrm{M} \in \mathbb{R}^{N_\mathrm{M}(N_\mathrm{o}+1)\times N_\mathrm{M}(N_\mathrm{o}+1)}$ describing uncertainties of measured modal parameters (both eigenvalues and mode shapes). If $\boldsymbol{\Sigma}_\mathrm{M}$ is not known one can assume the following form of the weighting matrix:

$$\mathbf{W} = \mathrm{diag}\left(\begin{bmatrix} \frac{1}{\widetilde{\lambda}^{(1)2}_\mathrm{exp}}, & \cdots & \frac{1}{\widetilde{\lambda}^{(N_\mathrm{M})2}_\mathrm{exp}}, & \frac{w_\psi}{\left\|\widetilde{\boldsymbol{\psi}}^{(1)}_\mathrm{exp}\right\|^2}\mathbf{1}^\mathrm{T}_\mathrm{o}, & \cdots & \frac{w_\psi}{\left\|\widetilde{\boldsymbol{\psi}}^{(N_\mathrm{M})}_\mathrm{exp}\right\|^2}\mathbf{1}^\mathrm{T}_\mathrm{o} \end{bmatrix}^\mathrm{T}\right), \tag{5.8}$$

where: w_ψ is selected coefficient reflecting level of the measurement discrepancies of the mode shapes and $\mathbf{1}_{\mathrm{o}}$ is vector containing N_{o} ones. Such a form of the matrix relates to the fact that variances of eigenvalues are near-proportional to their squared expected values.

Gauss-Newton minimisation for model updating

Optimisation problem shown in Equation (5.3) is a weighted nonlinear least square problem. The nonlinearities result from the nonlinear dependence of the numerical modal parameters in Equation (5.5) on the unknown parameter vector $\boldsymbol{\theta}$. Thus, Gauss-Newton method, which is widely accepted for minimisation of such objective functions, is selected [163]. Friswell and Mottershead adopted this method for various model updating problems discussed in [155]. For the considered case modal parameters in Equation (5.5) are locally linearized with respect to unknown parameters. It results in the following function that is to be minimised with respect to increment of unknown parameter vector $\boldsymbol{\Delta\theta}$ in each iteration step of the optimisation process:

$$J_{\varepsilon}(\boldsymbol{\Delta\theta}) = \left(\mathbf{S}(\boldsymbol{\theta})\boldsymbol{\Delta\theta} - \mathbf{e}(\boldsymbol{\theta})\right)^{\mathrm{T}} \mathbf{W} \left(\mathbf{S}(\boldsymbol{\theta})\boldsymbol{\Delta\theta} - \mathbf{e}(\boldsymbol{\theta})\right), \tag{5.9}$$

where matrix

$$\mathbf{S}(\boldsymbol{\theta}) = \begin{bmatrix} \frac{\partial \widetilde{\lambda}^{(1)}}{\partial \theta_1} & \cdots & \frac{\partial \widetilde{\lambda}^{(1)}}{\partial \theta_{N_\theta}} \\ \vdots & & \vdots \\ \frac{\partial \widetilde{\lambda}^{(N_{\mathrm{M}})}}{\partial \theta_1} & \cdots & \frac{\partial \widetilde{\lambda}^{(N_{\mathrm{M}})}}{\partial \theta_{N_\theta}} \\ c_1 \mathbf{D} \frac{\partial \widetilde{\boldsymbol{\phi}}^{(1)}}{\partial \theta_1} & \cdots & c_1 \mathbf{D} \frac{\partial \widetilde{\boldsymbol{\phi}}^{(1)}}{\partial \theta_{N_\theta}} \\ \vdots & & \vdots \\ c_{N_{\mathrm{M}}} \mathbf{D} \frac{\partial \widetilde{\boldsymbol{\phi}}^{(N_{\mathrm{M}})}}{\partial \theta_1} & \cdots & c_{N_{\mathrm{M}}} \mathbf{D} \frac{\partial \widetilde{\boldsymbol{\phi}}^{(N_{\mathrm{M}})}}{\partial \theta_{N_\theta}} \end{bmatrix} \tag{5.10}$$

represents modal sensitivities to the unknown parameters. In this thesis eigenvalue derivatives $\frac{\partial \widetilde{\lambda}^{(1)}}{\partial \theta_t}$ are calculated using method proposed in [164], whereas eigenvector derivatives $\frac{\partial \widetilde{\boldsymbol{\phi}}^{(m)}}{\partial \theta_t}$ are obtained as described in [165]. $J_{\varepsilon}(\boldsymbol{\Delta\theta})$ is minimised in current iteration step by pursuing $\nabla J_{\varepsilon}(\boldsymbol{\Delta\theta}) = \mathbf{0}$. Then we have the following equation representing weighted least square problem:

$$\mathbf{S}^{\mathrm{T}}(\boldsymbol{\theta})\mathbf{W}\mathbf{S}(\boldsymbol{\theta})\boldsymbol{\Delta\theta} = \mathbf{S}^{\mathrm{T}}(\boldsymbol{\theta})\mathbf{W}\mathbf{e}(\boldsymbol{\theta}), \tag{5.11}$$

that is to be solved with respect to $\boldsymbol{\Delta\theta}$. Finally, for sth iteration step the unknown parameter vector is updated:

$$\begin{aligned} \boldsymbol{\theta}[s+1] &= \boldsymbol{\theta}[s] + \kappa_\theta \boldsymbol{\Delta\theta}[s] = \\ &= \boldsymbol{\theta}[s] + \kappa_\theta \left(\mathbf{S}^{\mathrm{T}}(\boldsymbol{\theta}[s])\mathbf{W}\mathbf{S}(\boldsymbol{\theta}[s])\right)^{-1} \mathbf{S}^{\mathrm{T}}(\boldsymbol{\theta}[s])\mathbf{W}\mathbf{e}(\boldsymbol{\theta}[s]), \end{aligned} \tag{5.12}$$

where κ_θ is scaling factor that is selected with the trial-and-error method.

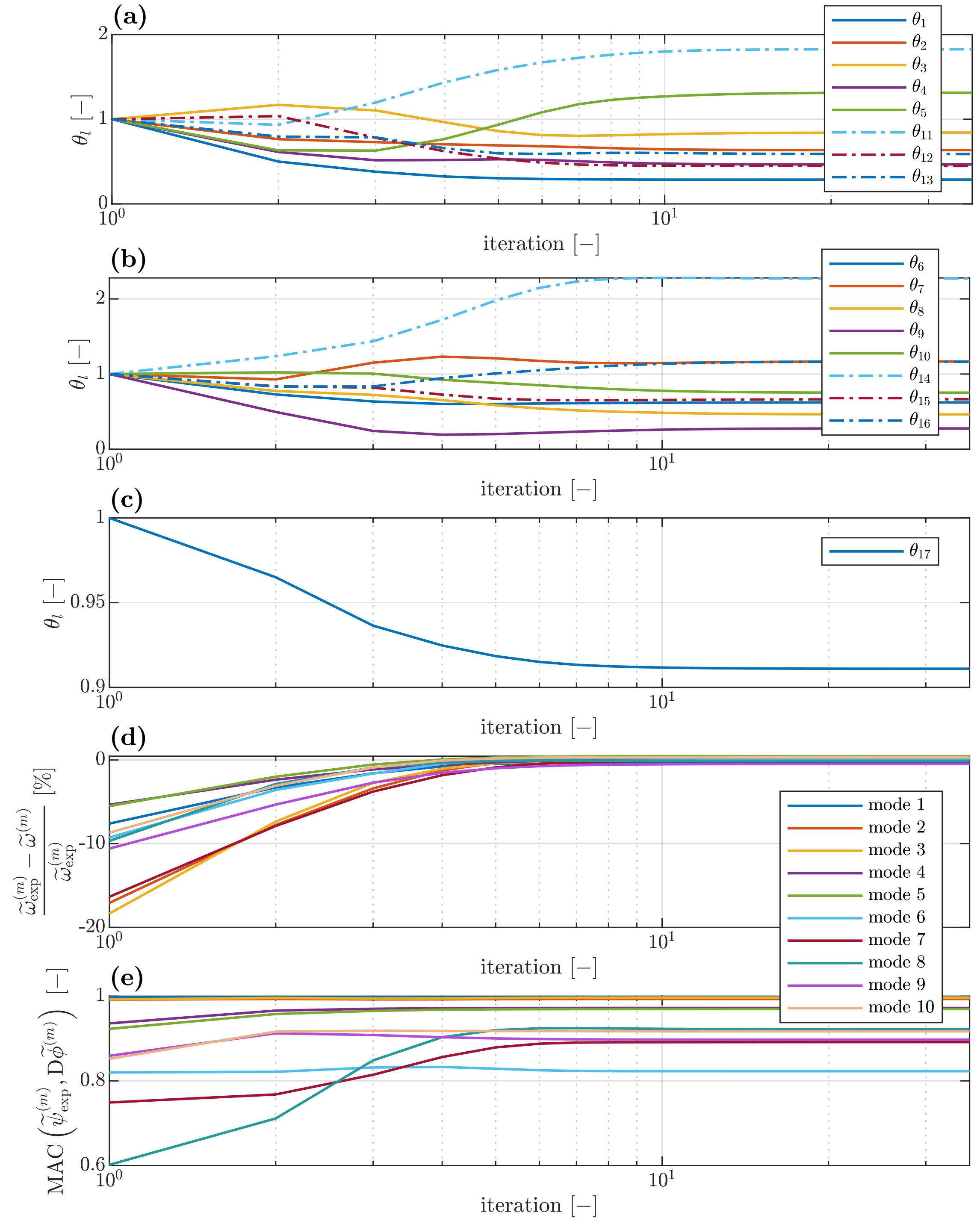

Figure 5.5: Evolution of various parameters during model updating: (a) unknown parameters characterising stiffness of the bolted connections on the left-hand side of the structure, (b) analogous parameters for the right-hand side of the structure, (c) unknown parameter characterising Young modulus of the beams, (d) relative error of the locked natural frequency and (e) MAC between locked experimental and locked numerical mode shapes

Updating of the FE model using identified modal parameters

Experimental modal data described in Subsection 5.1.2 are used for updating FE model shown in Subsection 5.2.1 with initial parameter values $\boldsymbol{\theta}_0 = \begin{bmatrix} 1 & 1 & \cdots & 1 \end{bmatrix}^{\mathrm{T}}$.

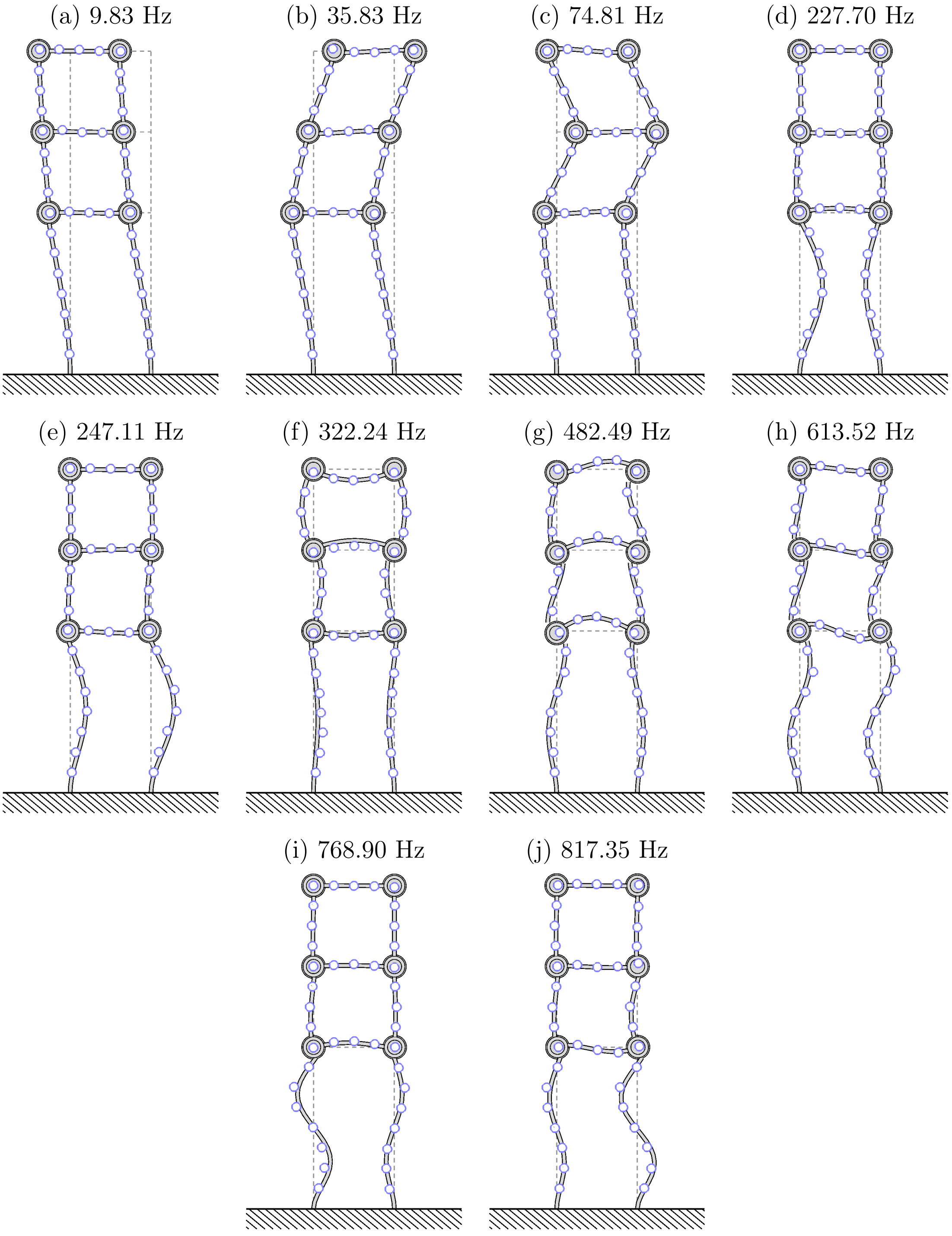

(a) 9.83 Hz (b) 35.83 Hz (c) 74.81 Hz (d) 227.70 Hz

(e) 247.11 Hz (f) 322.24 Hz (g) 482.49 Hz (h) 613.52 Hz

(i) 768.90 Hz (j) 817.35 Hz

Figure 5.6: Numerical locked mode shapes $\boldsymbol{\phi}^{(m)}(\boldsymbol{\theta})$ obtained from the updated FE model (gray solid lines), accompanied with corresponding numerical natural frequencies, compared with experimental locked mode shapes $\boldsymbol{\psi}^{(m)}$ (blue points at sensor locations);

Covariance matrix $\boldsymbol{\Sigma}_{\mathrm{M}}$ describing measurement uncertainties is not available. Thus, weighting matrix is constructed in accordance to Equation (5.8). Coefficient $w_{\psi} = 0.01$ is selected, since standard deviation of measured mode shape typically is greater by one order of magnitude [152, 155]. $\kappa_{\theta} = 0.5$ is selected. Stop condition is selected in such a way that all unknown parameters must have absolute relative increment $\frac{|\Delta\theta_t[s]|}{\theta_t[s]} < 10^{-5}$, $t = 1, 2, \ldots N_\theta$.

Convergence of unknown parameters and error metrics of modal parameters is shown in Figure 5.5. Mode matching finds unknown parameters in 36 iteration steps.

Evolution of relative natural frequency error (Fig 5.5d) shows that natural frequencies are closely reproduced. Absolute values of this error for all vibration modes are below 0.5 %, whereas the absolute value of initial relative error was near to 20 %. Similarly, MAC between experimental and numerical locked mode shapes is significantly improved during model updating. At the initial iteration step the worse MAC is near to 0.6. All MAC for the updated model are above 0.8 and most of them above 0.9 that is satisfactory result. It allows for reproduction of asymmetries and other distortions of experimental mode shapes as demonstrated in Figure 5.6. It is visible especially for mode shapes shown in Figures 5.6d, e, g, i and j. Even high-frequency vibration modes that are characterised by local curvatures in the mode shapes are reproduced by the updated FE model.

Such accurate reproduction of experimental locked mode shapes is possible due to independent parameterization for each bolted connection. Unknown parameters related to bolted connections the right-hand side of the structure are different from the corresponding parameters related to left-hand side (Figs 5.5a, b and 5.4b). Moreover, final values of the unknown parameters are strongly scattered around their initial values. It reveals assembly discrepancies of the bolted connections which affects the mode shapes.

Unknown parameter describing Young modulus of the beams changes significantly less than parameters related to the bolted connections (Figs 5.5c and 5.4b). It is in agreement in expectations, since Young modulus of the beam is the parameter characterised by much lower uncertainty than stiffness of bolted connection whose actual value can be affected by many local effects.

Accurate calibration of the FE model of the controlled frame not only allows for accurate calculation of quantities required by the controller but also improves reliability of the simulation within broad frequency range. It is valuable property of the updated model, since higher-order vibration modes are induced due to operation of the lockable joints.

5.2.3 Material damping

Due to the fact that estimation of the modal damping ratios is highly uncertain the material damping model analogous to one adopted in Chapter 4. The following values coefficients in Equation (4.2) are selected with the trial-and-error method: $\alpha = 0$, $\beta = 0.016$ and $\gamma = 3 \cdot 10^{-5}$. These coefficients are valid for all case considered the next section. As indicated in Subsection 5.3 unlocked vibration modes change depending on the lockable joints selected to be controlled (whereas the remaining ones are passively locked), however the dependence of the modal damping ratios on natural frequency (Eq. (4.2)) is invariant with respect to the selected of the lockable joints to be controlled. It means that for various lockable joints selected to be controlled the modal damping rations corresponding to the unlocked vibration modes will be slightly different but always will be placed on the same curve $\zeta(\omega)$ indicated by β and γ.

5.3 Hardware control loop

5.3.1 Equipment and its limitations

The control algorithm is realised by the embedded real-time controller cRIO-9014 combined with cRIO-9114 CompactRIO Chassis that is based on field-programmable gate array (FPGA)-based processor Virtex-5 LX50. This real-time controller is further called "FPGA controller". Unfortunately, the FPGA controller utilised in the present research has limited memory, thus also the uploaded algorithm is subject to some restrictions.

The main restriction is that the controller is able to produce only one control signal $u(t)$. On the other hand, as shown in Chapter 4 the lockable joints are usually controlled symmetrically (see e.g. Figs 4.5, 4.14, 4.28 and 4.30) due to the symmetry of the structure. Moreover, it is demonstrated one pair of lockable joints is sufficient to provide satisfactory results. Thus, the available control signal can be used to control selected pair of the lockable joints. During the experiments it has been assumed that one pair of the lockable joints among three available ones can be controlled:

- at the ends of the first (bottom, joints J1 and J2) transversal beam (see: Fig 5.1a),
- second (middle, joints J3 and J4) and
- third (top, joints J5 and J6) one.

The lockable joints that are not selected to be controlled always are passively locked at angle 90° between adjacent beams ($\Delta q = 0$). The voltage, determined by the control signal $u(t)$, is supplied to both selected lockable joints to be controlled. The selected pair can be changed for various control scenarios.

Since the pair of the lockable joints is controlled by single signal $u(t)$ it is theoretically sufficient to measure strains in the vicinity of only one lockable joint by the pair of strain gauges accordingly to Equation (3.3). It is confirmed by the simulation results in Figs 4.5, 4.14, 4.28 and 4.30 where due to structural symmetry and character of the excitations the signals of measured strain are the same for the joint on left-hand side and right-hand side of the structure. However, during the experimental validation the quality of the strain measurement is improved by calculation

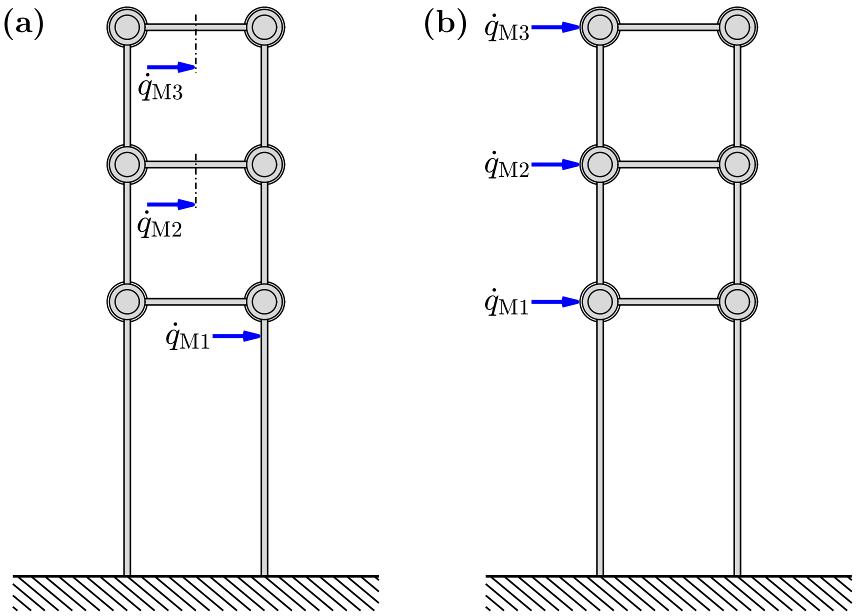

Figure 5.7: Selected sensor locations for modal filtering of first three modal velocities: (a) indicated by CR-based approach and (b) modified that are adopted in experiments

of the mean strain signal from two particular pairs of the strain gauges located in the vicinity of both controlled joints:

$$\varepsilon_{\mathrm{M}}(t) = \frac{1}{2}\left(\varepsilon_{\mathrm{M1}}(t) + \varepsilon_{\mathrm{M2}}(t)\right). \tag{5.13}$$

Each pair of the strain gauges is mounted 7.5 cm from the rotational axis of the corresponding lockable joint. During control of the structure only strain gauges corresponding with the controlled joints are used. Signals $\varepsilon_{\mathrm{M1}}(t)$ and $\varepsilon_{\mathrm{M2}}(t)$ are measured in half-bridge configuration dedicated for bending measurements. These signals are filtered and conditioned.

First three unlocked vibration modes are selected to be monitored, since they are related to the motion of transversal beams along with the lockable joints (similarly to the locked vibration modes shown in Fig. 5.6a-c), whereas any higher-order mode shapes are related to the local curvatures and their natural frequencies are well-separated from the selected ones. This property is valid independently of the state of the lockable joints (locked or unlocked). The third monitored unlocked vibration mode is controlled with poor effectiveness due to the delay of the lockable joints (3 ms) that is near to 1/4 of the mode period. Thus, this mode is only monitored but not controlled in this research ($\alpha_3 = 0$). The FPGA controller updates signal $u(t)$ with the frequency 10 kHz which is independent on the delay of the lockable joint caused by its mechanical properties.

Three laser displacement sensors (LDSs) Baumer OADM-2016 characterized with 10 µm linear resolution are adopted for estimation of first three modal velocities accordingly to Equation (3.10). Velocities $\dot{\mathbf{q}}_{\mathrm{M}}(t)$ are obtained by differentiation of the displacement signal provided by LDSs. Before differentiation the signal is conditioned and filtered.

5.3.2 Modal filtering and unlocked vibration modes

Modal filter matrix $\mathbf{\Phi}^{+}$ depends both on unlocked mode shapes of the structure and sensor locations. Here, unlocked mode shapes refer to the modes obtained for unlocked controlled pair of the lockable joints, whereas the remaining ones are in the locked state. Thus, the unlocked mode shapes are different for each pair of lockable joints selected to be controlled. However, sensor locations are selected once and are not changed during experiments. Fortunately, the first three unlocked mode shapes are well correlated with their locked counterpart for each controlled pair of the lockable joints. All MAC values between unlocked and locked vibration modes are above 0.9. Thus, the locked mode shapes can be used for selection of the senor locations for each considered configuration of the controlled lockable joints. Set of candidate sensor locations coincides with all measurement locations selected to identify locked mode shapes before model updating procedure (Fig 5.3). Sensor locations indicated with Algorithm 1 are shown in Figure 5.7a.

Sensor locations shown in Figure 5.7a maximise determinant of FIM, however such a sensor layout has some drawbacks. First, LDSs require a surfaces for reflection of the laser beam. Thus, locations at the middle of transversal beam require mounting additional surfaces reflecting the laser beam. Another drawback is that sensor location $\dot{q}_{\mathrm{M1}}(t)$ is not the best choice regarding contamination of the measurement signal by higher-order unlocked vibration modes. It is due to the fact that higher-order vibration modes involve local curvatures of the beams connected to the lockable joints and have lower amplitudes at locations related to heavy parts of the structure such like lockable joints along with whole transversal beams. Thus, new near-optimal sensor locations are proposed for experiments as shown in Figure 5.7b, which are devoid of these drawbacks.

5.3.3 Preparation of the control algorithm

After performing model updating the identified parameters $\boldsymbol{\theta}$ describing stiffness of the bolted connections are adopted for further calculations based on the FE model of the frame also for the joints in the unlocked state. It is permitted, since stiffness of the bolted connections does not depend on the state of the joints (locked or unlocked). FE model is used both to calculate parameters for the control algorithm, selection of the lockable joints to be controlled and simulation for comparison with experimental results.

Due to the fact that only one control signal is available for any selected pair of the lockable joints the resulting matrix representing locking effect (see: Eq. 2.43) can be calculated as sum of matrices corresponding with controlled joints:

$$\widetilde{\mathbf{C}} = \widetilde{\mathbf{C}}_1 + \widetilde{\mathbf{C}}_2. \tag{5.14}$$

Resulting matrix is not indexed, since indices k in Equation 2.43 denote particular joints among all controlled ones, whereas here always only one pair (described by one matrix $\widetilde{\mathbf{C}}$) of lockable joints is available to be locked in particular control scenario. Hence, providing of any index depending on the selected pair of the controlled joints could be misleading.

From Equation (5.14) it follows that when $u(t) = 1$ the resulting modal energy transfer rate to the monitored unlocked vibration modes is the sum of particular modal energy transfer rates caused by locking of both joints, accordingly to Equation (2.77). Using Equations (2.78) and 2.79 the resultant modal energy transfer rate to the monitored unlocked vibration modes can be written as follows:

$$\begin{aligned}
\dot{W}_{\mathrm{M}} &= \dot{W}_{\mathrm{M1}} + \dot{W}_{\mathrm{M2}} = \\
&= -u(t)\dot{\boldsymbol{\eta}}_{\mathrm{M}}^{\mathrm{T}}(t)\left(\begin{bmatrix}\boldsymbol{\Gamma}_{\mathrm{MM1}} & \boldsymbol{\Gamma}_{\mathrm{MH1}}\end{bmatrix} + \begin{bmatrix}\boldsymbol{\Gamma}_{\mathrm{MM2}} & \boldsymbol{\Gamma}_{\mathrm{MH2}}\end{bmatrix}\right)\begin{bmatrix}\dot{\boldsymbol{\eta}}_{\mathrm{M}}(t) \\ \dot{\boldsymbol{\eta}}_{\mathrm{H}}(t)\end{bmatrix} = \\
&= \dot{\boldsymbol{\eta}}_{\mathrm{M}}^{\mathrm{T}}(t)\left(\boldsymbol{\Delta\phi}_{\mathrm{M1}} f_1(t) + \boldsymbol{\Delta\phi}_{\mathrm{M2}} f_2(t)\right).
\end{aligned} \tag{5.15}$$

Finally, by taking into account the equations above the estimated weighted modal energy transfer rates used in lines 5 and 11 of control Algorithm 2 (Eqs (3.39) and (3.41), respectively) can be calculated as:

$$\dot{\widehat{V}}_W(t) = -\dot{\widehat{\boldsymbol{\eta}}}_{\mathrm{M}}^{\mathrm{T}}(t)\mathbf{W}_\alpha \boldsymbol{\Gamma}_{\mathrm{MM}} \dot{\widehat{\boldsymbol{\eta}}}_{\mathrm{M}}(t), \tag{5.16}$$

where

$$\boldsymbol{\Gamma}_{\mathrm{MM}} = \boldsymbol{\Gamma}_{\mathrm{MM1}} + \boldsymbol{\Gamma}_{\mathrm{MM2}},$$

and

$$\dot{\widehat{V}}_W(t) = \dot{\widehat{\boldsymbol{\eta}}}_{\mathrm{M}}^{\mathrm{T}}(t)\mathbf{W}_\alpha \boldsymbol{\Delta\phi}_{\mathrm{M}} \widehat{f}(t), \tag{5.17}$$

where:

$$\boldsymbol{\Delta\phi}_{\mathrm{M}} = \boldsymbol{\Delta\phi}_{\mathrm{M1}} + \boldsymbol{\Delta\phi}_{\mathrm{M2}},$$

and $\widehat{f}(t)$ is calculated from the mean strain signal (Eq. (5.13)) analogously to Equation (3.2):

$$\widehat{f}(t) = -\frac{2EI}{h}\varepsilon_{\mathrm{M}}(t). \tag{5.18}$$

In this case number of iterations of the “for” loop $N_k = 1$ (line 2 of the algorithm).

Similarly to the modal filter matrix, $\boldsymbol{\Gamma}_{\mathrm{MM}}$ and $\boldsymbol{\Delta\phi}_{\mathrm{M}}$ also are different depending on the selected pair of the lockable joints to be controlled. Hence, for each pair of the lockable joint selected to be controlled the control algorithm has different parameters based on modal data.

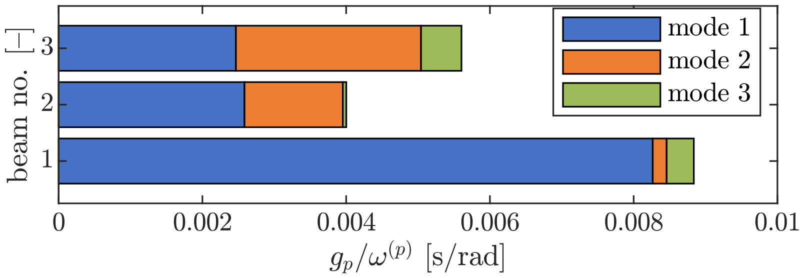

Figure 5.8: Controllability of the monitored unlocked vibration modes for lockable joints placed at the ends particular transversal beams (from the bottom to the top)

In further part of this chapter all algorithm parameters are the same for both experiment and simulation to which experiment is compared. Thresholds κ_1 and κ_2 are selected with the trial-and-error method during experiments. Due to the fact that measured signals are conditioned these thresholds given in this chapter are recalculated to values corresponding with the measured quantities adopted in Algorithm 2. Time integration step $\Delta t = 0.1$ ms (Eq. (2.45)) is selected for the numerical simulation. It corresponds to the sampling frequency of the hardware control loop.

5.4 Vibration attenuation

This section focuses on experimental validation of the proposed control strategy in vibration attenuation. First, controllability of the monitored unlocked vibration modes for various pairs of the lockable joints is evaluated in subsection below. The relevance of the proposed controllability metric is demonstrated on three control scenarios of the updated FE model (three various pairs of the lockable joints selected to be controlled). In Subsection 5.4.2, vibration attenuation is tested for free vibration employing two different pairs of the lockable joints selected to be controlled. Each time experimental results are compared with the simulation. Comparison of experimental and simulation results of forced vibration attenuation for two different pairs of the lockable joints selected to be controlled is discussed in Subsection 5.4.3. Here, vibration was excited by frequency sweeps provided with modal shaker and later analysed mainly in the frequency domain.

5.4.1 Modal controllability by various pairs of lockable joints

Selection of the pair of the controlled lockable joints depends on the priority of damping of particular unlocked vibration modes. Thus, controllability metrics for particular monitored unlocked vibration modes with weights $\beta_p = 1/\omega^{(p)}$ (see: Eq. (3.29)) is calculated for each pair of potentially controlled lockable joints and shown in Figure 5.8. It is obtained using actual unlocked vibration modes for each selection of the lockable joints to be controlled.

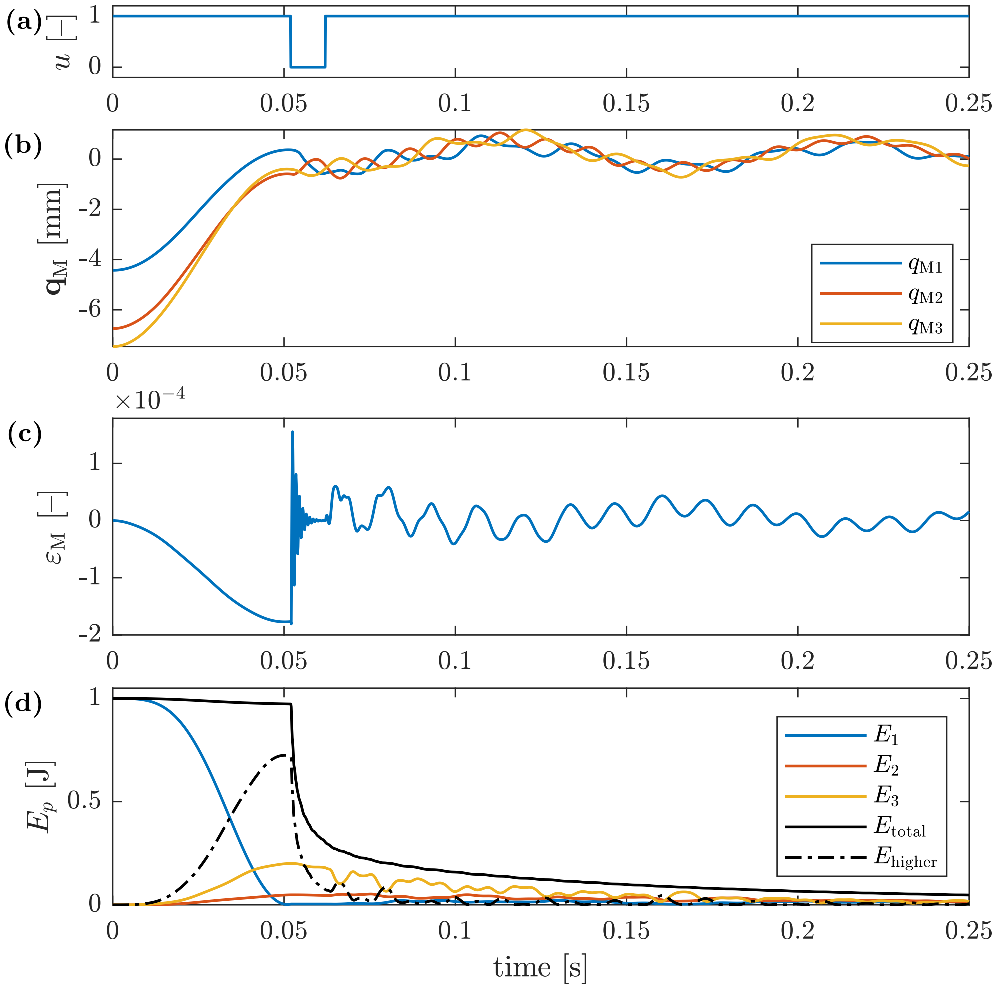

Figure 5.9: Simulation test of the controllability of the first unlocked vibration mode by the lockable joints placed at the first (bottom) transversal beam; time histories of: (a) control signal, (b) measured displacements, (c) measured strain and (d) modal energies of the structure

It is evident that the first unlocked vibration mode is controllable for each pair of lockable joints. However, lockable joints at the ends of the first (bottom) transversal beam cannot control the second unlocked vibration mode effectively. It is in agreement with the observation that this beam accumulate almost no any strains for the second locked mode shape. It can be seen in Figure 5.6b, where the first transversal beam almost does not deform and longitudinal beams are not inclined at the corresponding height due to their maximal transversal displacement. Similarly, the third unlocked vibration mode is almost not-controllable by the lockable joints at the ends of the second (middle) transversal beam.

The agreement between the controllability metrics calculated accordingly to Section 3.3 and modal energy transfer rates is demonstrated achieved in vibration attenuation of the first vibration mode is demonstrated using the updated FE model. To this end, the initial condition that the structure is prestressed in the first unlocked vibration mode, achieving 1 J of potential energy, is pursued. Thus, for each tested

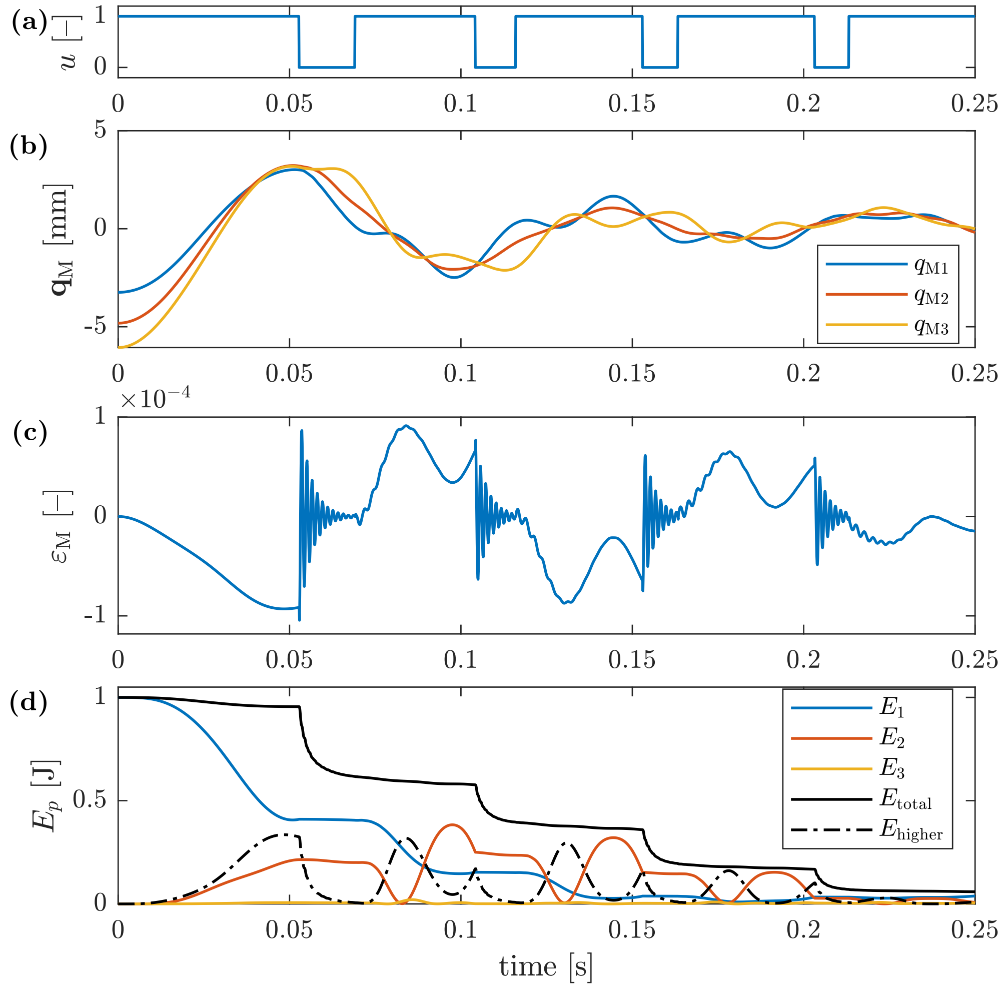

Figure 5.10: Simulation test of the controllability of the first unlocked vibration mode by the lockable joints placed at the second (middle) transversal beam; time histories of: (a) control signal, (b) measured displacements, (c) measured strain and (d) modal energies of the structure

pair of the lockable joints: $\mathbf{q}_0 = \frac{1}{\omega^{(1)}}\boldsymbol{\phi}^{(1)}$, $\dot{\mathbf{q}}_0 = \mathbf{0}$ and the following parameters of the control algorithm are selected: $\alpha_1 = 1$, $\alpha_2 = \alpha_3 = 0$, $t_\mathrm{unlock} = 10$ ms, $t_\mathrm{lock} = 5$ ms, $\kappa_1 = 100$ W and $\kappa_2 = 1$ W. Results for controlled lockable joints at the ends of first, second and third transversal beam of the structure are shown in Figures 5.9, 5.10 and 5.11, respectively.

It is evident that for the first transversal beam almost whole energy associated with the first unlocked vibration mode is transferred out and directed to the remaining vibration modes within one time interval when the joint is locked (Fig. 5.9a and d). Vibration of the first unlocked vibration mode is suppressed within 0.05 s until the first unlock of the currently selected lockable joints that is near to half of the first-mode period (Fig. 5.9b). The strain measured in vicinity of the controlled lockable joints is accumulated monotonically and after the joint unlock high-frequency unlocked vibration modes are demonstrated in the strain signal within short time interval. It is evident that controllability of the first unlocked vibration mode by the

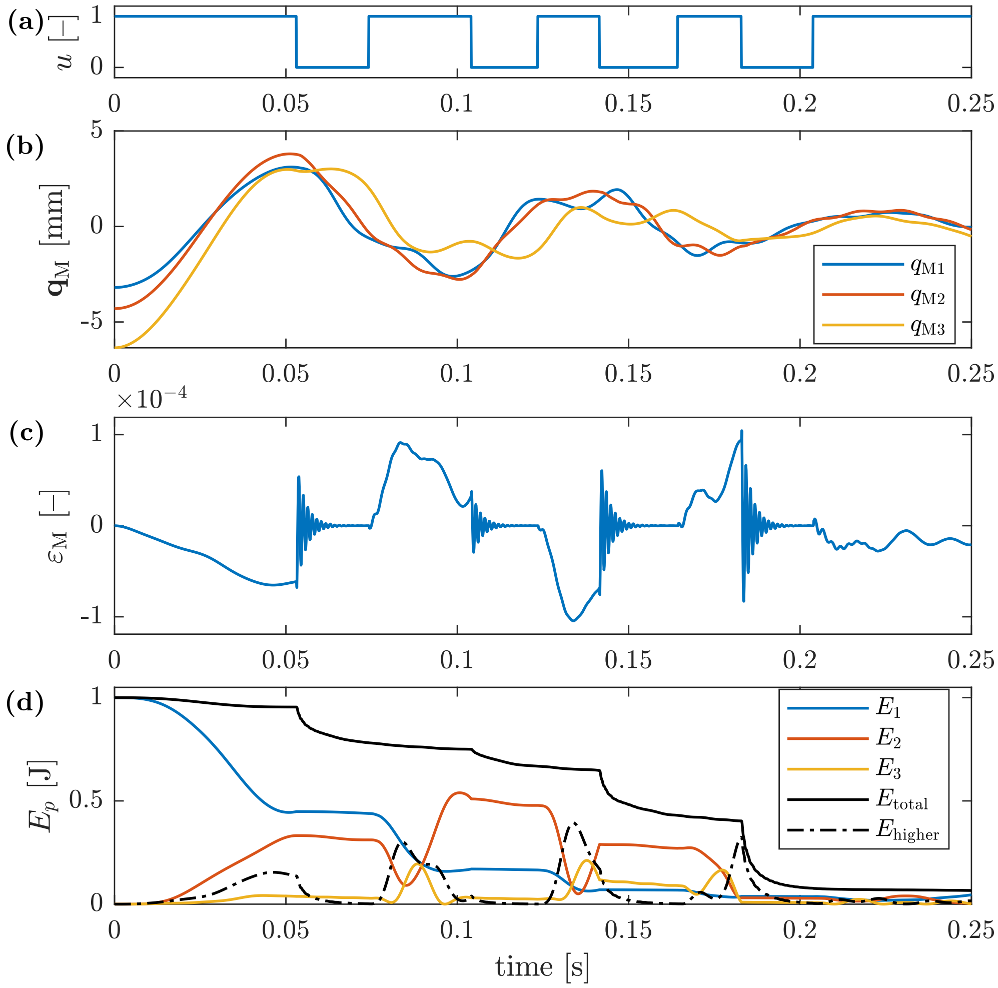

Figure 5.11: Simulation test of the controllability of the first unlocked vibration mode by the lockable joints placed at the third (top) transversal beam; time histories of: (a) control signal, (b) measured displacements, (c) measured strain and (d) modal energies of the structure

currently selected lockable joints is very satisfactory and agrees with results shown in Figure 5.8.

Controllability metrics of the first unlocked vibration mode for the joints belonging to the second and third transversal beam are almost equal and are smaller than for the first transversal beam (Fig. 5.8). This observation is in good agreement with behaviour of the structure controlled by the lockable joints located at the ends of the second and third transversal beam that is presented in Figures 5.10 and 5.11, respectively. In both these cases time history of the first modal energy is very similar (Figs 5.10d and 5.11d) correspondingly to the controllability metrics. The lockable joints are unlocked after 0.05 s, as similar to the first tested case (Fig. 5.9). However, for the second and third transversal beam energy decreases to the value near to 0.5 J as opposed to the first transversal one, where almost whole energy is transferred out from the first unlocked vibration mode before the first joint unlock.

Additional observation is that energy transferred from the first vibration mode is partially transferred to other monitored vibration modes near-proportionally to the controllability metrics presented in Figure 5.8. In Figure 5.9d the second vibration mode is almost not-excited correspondingly with its poor controllability by the lockable joints belonging to the first transversal beam. In results shown in Figures 5.10d and 5.11d energy associated with second unlocked vibration mode achieves level near-proportional to the corresponding controllability metrics for second and third transversal beam: for the third transversal beam (Fig. 5.11) the second modal energy achieves values above 0.5 J, whereas for the second one (Fig. 5.10) slightly below. Similar observations on the controllability of the third monitored vibration mode can be noticed.

Lower values of measured strains for the case of the controlled lockable joints belonging to second and third transversal beam in relation to the first one can be observed. It is due to lower amount of the transferred energy from the first unlocked vibration mode that results in smaller deformations of the structure occurring during single time period when joints are in the locked state. However, high-frequency vibration demonstrated in the measured strain is more noticeable than for the first test of modal controllability. It results from the fact that for various lockable joints selected to be controlled the different higher-order unlocked vibration modes are excited predominantly. Moreover, the same high-frequency modes can be demonstrated differently depending on the location of the strain gauges that changes along with the selected pair of the lockable joints to be controlled.

Although it is not shown in this thesis, a good agreement of the proposed controllability metric with the structural behaviour can be obtained also when the energy is to be transferred out from the modes other than the first unlocked one. However, in the case of experiments the proposed metric of controllability of particular vibration modes does not reflect structural behaviour as relevantly as for simulations using FE model. The reason is that currently used lockable joints are imperfect and do not unlock completely (see: Tab. 5.1). The residual clamping force occurs that results in dry friction. Then, for sufficiently small amplitudes of motion resulting in small bending moments transmitted by the lockable joints they can still operate as locked ones due to residual dry friction even if the control signal imposes the unlocked state. It causes also that some amount of the potential energy to be released in high-frequency free vibration is still kept in strains. This phenomenon especially affects operation of the joints J5 and J6 belonging to the top transversal beam. They are less effective than one could expect from the proposed controllability metrics, thus only the first and second transversal beams are selected to be controlled in the further part of this chapter.

5.4.2 Mitigation of free structural vibration

Two various scenarios of mitigation of free vibrations are investigated and described below. The structure is pre-stressed with the aid of a manual hook attached to the

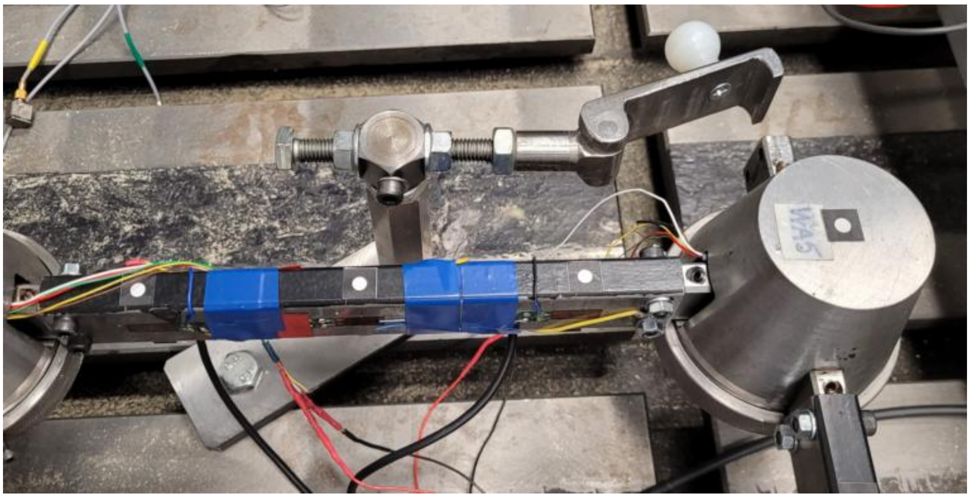

Figure 5.12: Manual hook used in free-vibration testing

end tip of the structure. Later, the structural free vibration is caused by the release of the hook. The hook is shown in Figure 5.12. All joints are in the locked state when the hook is released. Such a way of setting the structure in motion is also simulated with the aid of the FE model by pursuing the following initial conditions:

$$\mathbf{q}_0 = \mathbf{B}\widetilde{\mathbf{K}}^{-1}\mathbf{d}_\mathrm{h}, \qquad \dot{\mathbf{q}}_0 = \mathbf{0}, \tag{5.19}$$

where $\mathbf{d}_\mathrm{h} = \begin{bmatrix} 0 & \cdots & 0 & d_\mathrm{h} & 0 & \cdots & 0 \end{bmatrix}^\mathrm{T}$ is force vector representing prestress of the structure by the hook and has nonzero element at DOF representing location of the hook. The value d_h is selected in such a way that $\mathbf{q}_0$ at the appropriate location is equal to the structural tip displacement imposed by the hook that is 6 mm. Here, matrix $\mathbf{B}$ is obtained for the unlocked modes calculated for only the actually controlled joints in the unlocked state. The first unlocked (and locked) vibration mode has predominant participation in the structural motion excited in this way.

The algorithm controlling the real structure starts working when structural tip end passes preselected displacement value q_ON: $|q_\mathrm{ON}| = 5$ mm. It allows avoiding operation of the algorithm when the hook is not released yet. The same condition is adopted in the simulation.

The two cases of free-vibration mitigation investigated in this subsection:

Case 1: joints J1 and J2 are controlled (the first transversal beam) and

Case 2: joints J3 and J4 are controlled (the second transversal beam).

They differ also in the selected thresholds κ_1 and κ_2. As mentioned, remaining (uncontrolled) joints are passively locked in each control scenario. Parameters of Algorithm 2 that are common for these two cases are: $\alpha_1 = 1$, $\alpha_2 = \alpha_3 = 0$ and $t_\mathrm{lock} = t_\mathrm{unlock} = 15$ ms. Selection of weights α_p corresponds to the fact that mainly first vibration mode is excited with the manual hook.

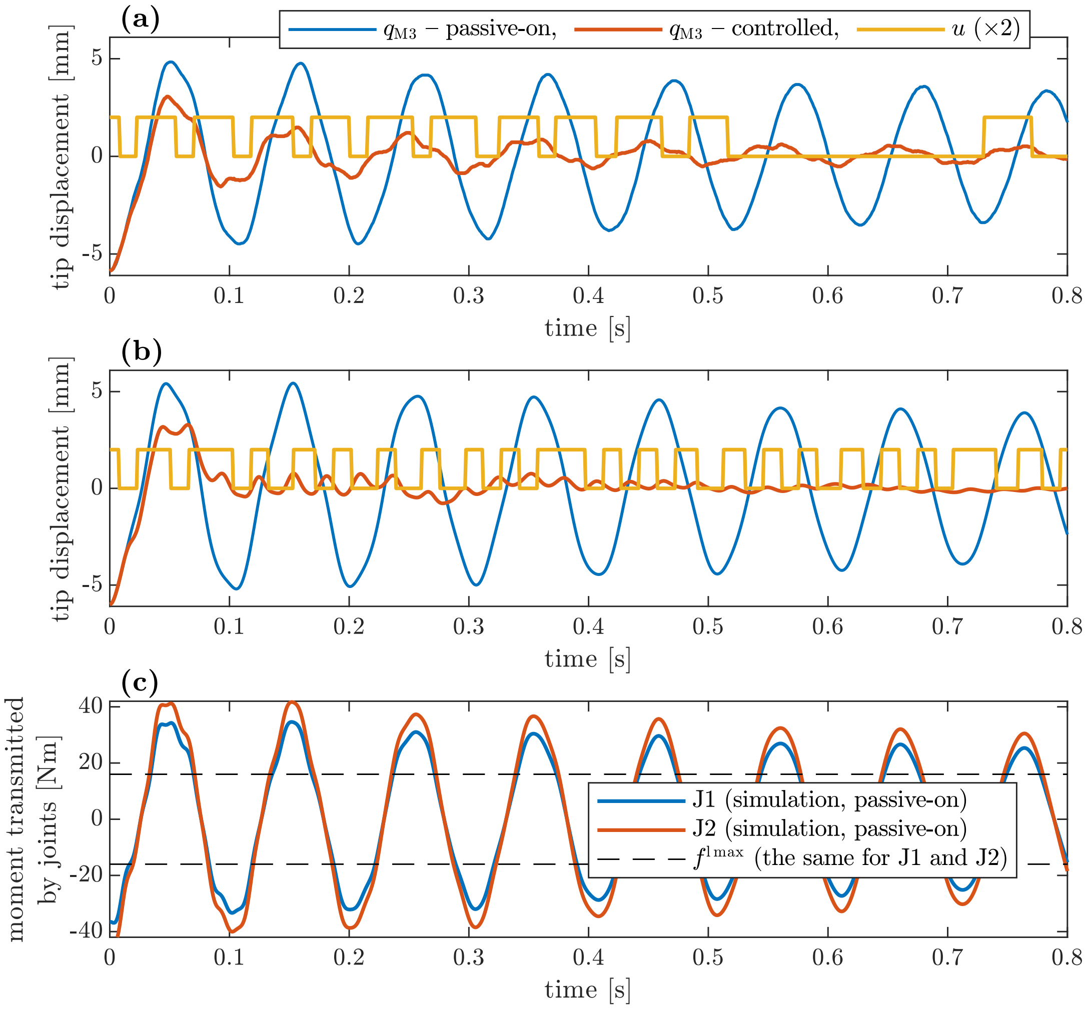

Figure 5.13: Case 1 of free vibration attenuation: structural tip-end displacement for uncontrolled (passive-on) and controlled structure along with the control signal for: (a) experiment, (b) corresponding simulation, and (c) bending moments transmitted by the passively locked joints obtained from the updated FE model compared with maximal bending moments transmitted by the real joints

Case 1 In this case lockable joints J1 and J2 are to be controlled. The thresholds $\kappa_1 = 0.38$ W and $\kappa_2 = 4.2 \cdot 10^{-4}$ W are selected.

Results of the experiment comparing structural response at the tip-end of the controlled and uncontrolled (locked joints) structure along with control signal are shown in Figures 5.13a, whereas analogous results obtained with simulation using updated FE model are shown in Figure 5.13b. The experimental results demonstrate satisfactory performance of the control but noticeably worse in relation to the simulation. Displacement of the structural tip end decays slower in the experiment. In simulation structural displacement related to the first unlocked vibration mode is mitigated quickly whereas second unlocked vibration mode is mitigated very slowly. It is due to the selected weights α_p and small controllability of the second unlocked vibration mode (see: Fig. 5.8). The second unlocked vibration mode also does not decay in experimental results.

Relatively frequent switches of the lockable joints demonstrated in Fig. 5.13b follows from high participation of the second unlocked vibration mode in relation to quickly mitigated first one. It affects the operation of the control algorithm, despite of the fact that weights $\alpha_2 = \alpha_3 = 0$. Such a sensitivity to the second unlocked vibration mode is caused by the thresholds κ_1 and κ_2 that are selected for the best algorithm operation in the experiment, where first unlocked vibration mode participates significantly in the structural motion within the whole investigated time interval.

The differences in behaviour of the controlled structure in simulation and experiment follows from the fact that the lockable joints are prototypes and are imperfect. Figure 5.13c shows bending moments transmitted by the joints J1 and J2 corresponding to the passive-on response shown in Figure 5.13b, which are compared with the maximal transmitted bending moments by real lockable joints (see: Tab. 5.1). These bending moments are not estimated from the strain gauges but calculated using Equation (2.39). It is evident that they exceed maximal transmitted bending moments $f_{\mathrm{J1}}^{\mathrm{l\,max}} = f_{\mathrm{J2}}^{\mathrm{l\,max}}$ characterising the real joints. It follows that friction parts in real joints can slide against each other providing dry friction as opposed to situation when $f^{\mathrm{l\,max}}$ is not reached. When $f^{\mathrm{l\,max}}$ is exceeded Equation (2.71) and thus Equation (2.74) is not valid. Here, the decrease of the energy corresponding to the monitored unlocked vibration modes (that are to be damped) is limited by $f^{\mathrm{l\,max}}$, as follows:

$$\left|\dot{W}_{\mathrm{M}}(t)\right| \leq \left|\dot{\boldsymbol{\eta}}_{\mathrm{M}}^{\mathrm{T}}(t) \sum_{k=1}^{N_k} \boldsymbol{\Delta\phi}_{\mathrm{M}k} f_k^{\mathrm{l\,max}}\right|, \tag{5.20}$$

and then the energy transferred to the higher-order unlocked vibration modes W_{H} is additionally decreased by the energy dissipated in dry fiction between the sliding friction surfaces inside the joints. Despite of the fact that $f^{\mathrm{l\,max}}$ limits the transmitted bending moment even two times, the proposed control still has satisfactory effectiveness. It demonstrates that the proposed control is robust with respect to considerable differences between behaviour of the employed prototypes of real lockable joints and the model.

Apart from its influence on the control performance the dry friction in the lockable joints can cause two more phenomena that should be commented. First, locked natural frequencies are decreased, since the sliding of the friction surfaces in the lockable joints not only provides additional damping to the structure but also has similar influence on the structural dynamics as reduction of the stiffness. The change of the locked natural frequency is visible in of the phase shift between displacement of structural tip end for the experiment and simulation (passive-on), which especially visible at the end of the considered time interval (Figs 5.13a and b). This difference probably follows from the fact that the FE model is updated using experimental modal data obtained for lower amplitudes of motion for which $f^{\mathrm{l\,max}}$ is not exceeded. The second phenomenon is additional nonlinearity related to dry friction. However, its exact influence on structural dynamics is unclear on this stage of the

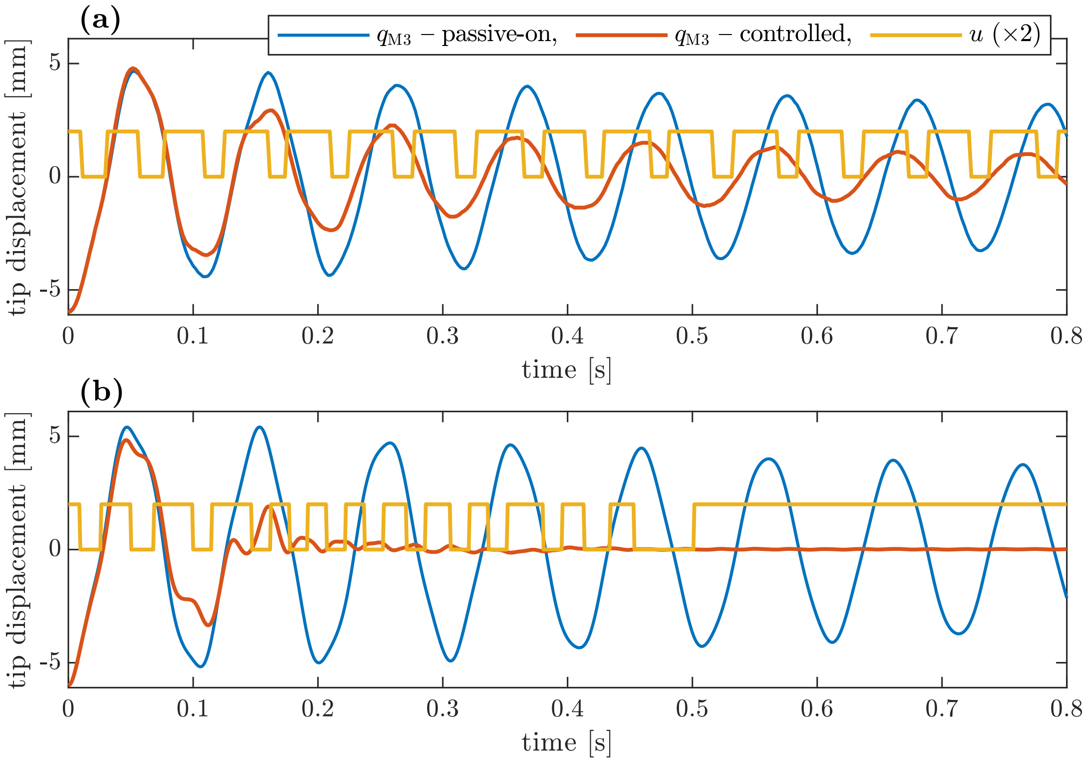

Figure 5.14: Structural tip-end displacement for uncontrolled (passive-on) and controlled structure along with control signal in Case 1 of free vibration attenuation for: (a) experimental results and (b) corresponding simulation ones

research. Coherence for the passively locked joints shown in Figures 5.18b and 5.19b that is discussed in Subsection 5.4.3 suggests that structure behaves near-linearly. This issue is outside of the scope of this thesis focusing around the control strategy being developed. It seems to be interesting topic for the future research.

Bending moment transmitted by the lockable joint J2 achieves greater values than the joint J1 due to the fact that the bolted connection coupling the bottom horizontal beam with the lockable joint J2 is stiffer than one coupling this beam with the joint J1. It is shown in Figures 5.5a and b, where stiffness unknown parameter θ_{14} is greater than θ_{11} (see: Fig. 5.4b).

Case 2 In the second case of free vibration testing the lockable joints belonging to the second transversal beam (J3 and J4) are selected to be controlled. The thresholds $\kappa_1 = 0.38$ and $\kappa_2 = 5.3 \cdot 10^{-4}$ are selected. Corresponding results for experiment and simulation are shown in Figure 5.14a and b, respectively.

Due to location of the controlled lockable joints the effectiveness of the damping of the first unlocked vibration mode is slightly smaller than in Case 1 both for experiment and simulation. It agrees with controllability metrics shown in Figure 5.8. Due to the selected weights α_p the first vibration mode is mitigated first. The second vibration mode is mitigated due to the fact that joint locking/unlocking intended to suppress vibration in the first unlocked mode also acts on the second one. Greater

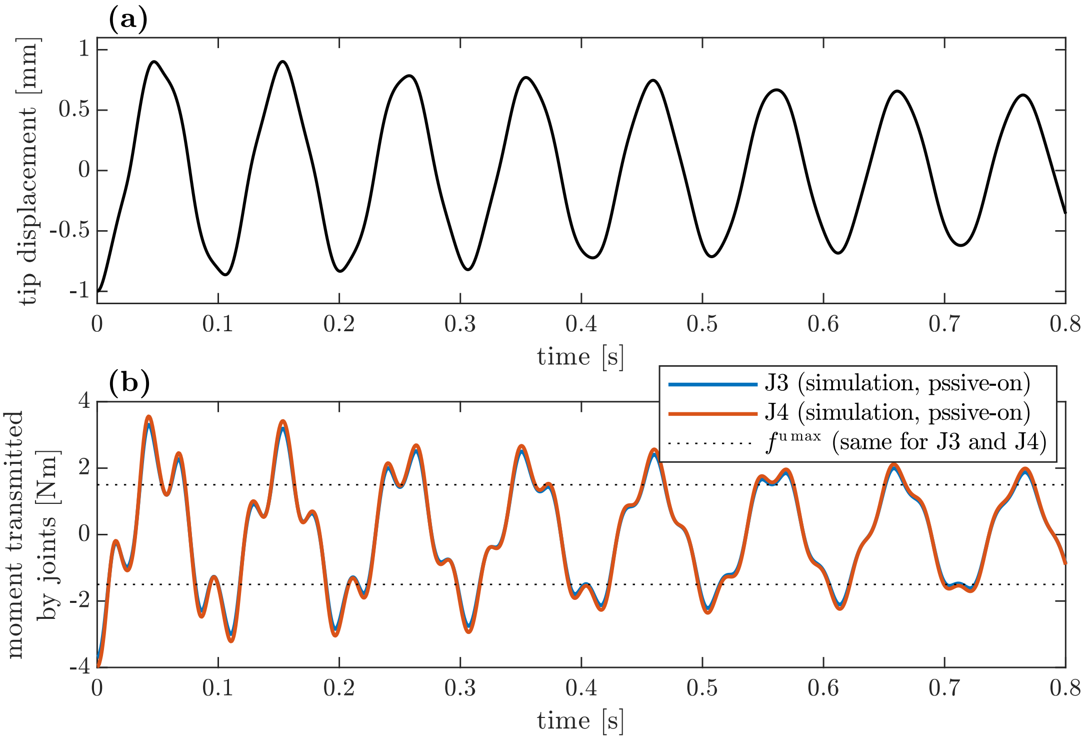

Figure 5.15: Time histories of: (a) structural tip displacement joints in the locked state obtained from the numerical simulation for reduced initial displacement and (b) corresponding bending moments compared with the maximal bending moments transmitted by the real joint in the unlocked state

controllability metric for the second unlocked vibration mode than in Case 1 causes that this non-intentional mitigation of the second vibration mode is relatively more efficient in simulation results (compare with Fig. 5.13b).

Similarly to Case 1, the control achieves worse performance in experiment than in the simulation. In this case bending moments transmitted by the lockable joints do not reach $f^{\mathrm{l\,max}}$, since second transversal beam accumulates lower strains than the first one when the joints are in the locked state. However, efficiency of the joint operation is here degraded by the opposed situation, i.e. residual dry friction when the joints are unlocked. It is caused by the fact that the friction surfaces are not effectively detached. For sufficiently small vibration amplitude the unlocking of the joint provides a little or even no any effect. This situation occurs for the real controlled structure at the end of time duration shown in Figure 5.14a, where the structural tip-end displacement has amplitude lower than 1 mm. An additional simulation with aid of the updated FE model, aiming at comparison of the expected level of transmitted bending moments and maximal transmitted bending moments $f^{\mathrm{u\,max}}$ of the real joints in the unlocked state, is provided. In this simulation all joints are passively locked and initial displacement imposed by the hook is reduced to 1 mm. Corresponding results are shown in Figure 5.15. It is evident that for such an amplitude of vibration the bending moments transmitted by the lockable joints only slightly exceeds $f^{\mathrm{u\,max}}$. It indicates that unlocking of the joints J3 and J4

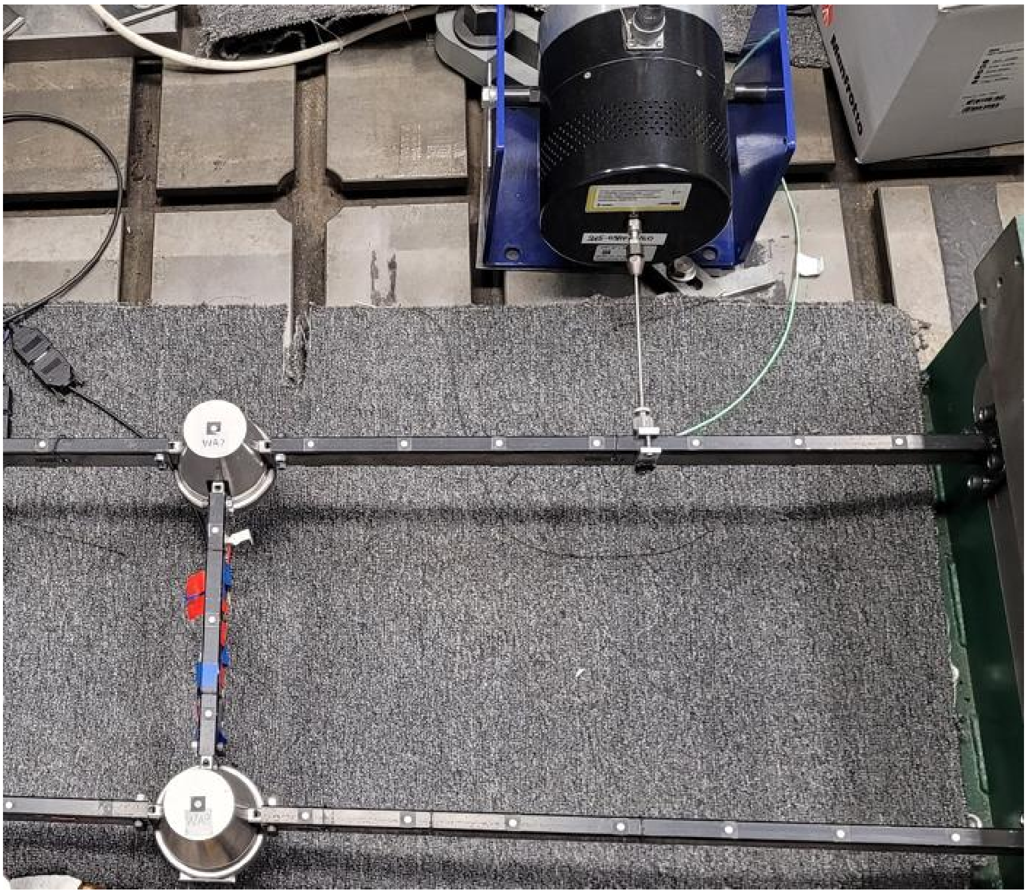

Figure 5.16: Location of the stinger of the modal shaker exciting the structure

in real structure provides almost no effect on vibration damping for this vibration amplitude. Hence, the only a little amount of the strain energy is released in high-frequency free vibrations, whereas the remaining part is still kept in the accumulated strains.

Despite of the decrease decrease of the control performance in experiment it still mitigates the structural response until the the described above imperfectness of the lockable joints does not dominate their behaviour. It confirms the robustness of the proposed control methodology.

5.4.3 Mitigation of the forced structural vibration

In this subsection performance of the proposed control strategy in mitigation of the forced vibrations is tested experimentally. The controlled structure is excited by the modal shaker attached to the structure at location shown in Figure 5.16. Time history of the excitation force provided by the modal shaker is measured with a force sensor located at the end of the stinger. The amplitude of force produced by the modal shaker depends on current structural response. Thus, uncontrolled and controlled structural responses are obtained for different amplitudes of the excitation force due to their different vibration amplitude levels. Hence, frequency response functions (FRFs) are utilised to avoid this problem. They allow to assess the level of the structural response with respect to the level of the excitation.

Aiming at validation of the control performance in vibration attenuation frequency sweeps are performed. Each time the frequency range from 4 to 100 Hz is swept by the modal shaker with the logarithmic increment of the frequency. The duration of each frequency sweep is 32 s. Data demonstrated in frequency domain: power spectral density (PSD), frequency response function (FRF) and coherence function are calculated as the mean value from the corresponding frequency-domain data obtained from 10 frequency sweeps. FRF is calculated using H1 estimator.

In numerical simulation the excitation force is assumed to have constant amplitude $A_\mathrm{d} = 85$ N. Force in single frequency sweep is described by the equations below.

$$\mathbf{d}(t) = \mathbf{L}_\mathrm{d}\boldsymbol{\Xi}(s_\mathrm{d})A_\mathrm{d}\sin F(t), \tag{5.21}$$

where: $\boldsymbol{\Xi}(s_\mathrm{d})$ is column matrix containing values of shape functions of FE at location of the excitation force s_d excepting the longitudinal motion, since the force has direction transversal to the beam, $\mathbf{L}_\mathrm{d}$ is transformation matrix,

$$F(t) = \frac{\Omega_0 T}{\ln\left(\frac{\Omega_1}{\Omega_0}\right)}\left(\frac{\Omega_1}{\Omega_0}\right)^{\frac{t}{T}}, \tag{5.22}$$

$\Omega_0/2/\pi = 4$ Hz, $\Omega_1/2/\pi = 100$ Hz and $T = 32$ s. Function of time $F(t)$ satisfies condition that frequency

$$\Omega_\mathrm{d}(t) = \frac{\mathrm{d}F(t)}{\mathrm{d}t} = \Omega_0\left(\frac{\Omega_1}{\Omega_0}\right)^{\frac{t}{T}} \tag{5.23}$$

grows exponentially from Ω_0 to Ω_1 in time duration T.

Similarly to free vibration testing, two cases of the mitigation of forced vibrations are investigated in this subsection:

Case 1 lockable joints belonging to the first transversal beam (J1 and J2) are controlled and

Case 1 lockable joints belonging to the second transversal beam (J3 and J4) are controlled

The algorithm parameters $t_\mathrm{unlock} = t_\mathrm{lock} = 15$ ms are common for both cases discussed in this subsection, whereas α_p, $p = 1, 2, 3$, κ_1 and κ_2 are selected separately for each case.

Case 1 In this case lockable joints J1 and J2 are selected to be controlled. Weights $\alpha_1 = 1$, $\alpha_2 = \alpha_3 = 0$ and thresholds $\kappa_1 = 0.384$, $\kappa_2 = 0.0011$ are selected.

Time histories of structural tip-end displacement and force produced by the modal shaker obtained in single experimental frequency sweeps both for controlled

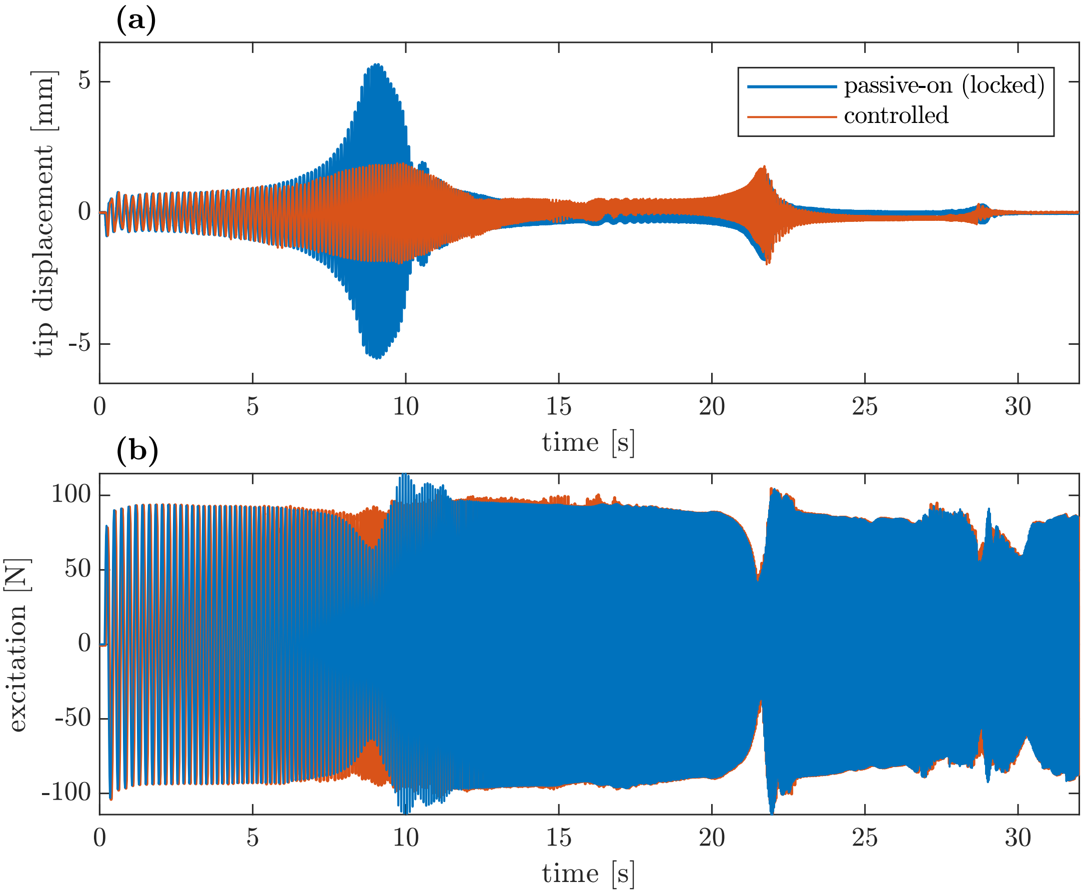

Figure 5.17: Time history of the tip-end displacement of laboratory frame demonstrator and excitation force of controlled (Case 1) and uncontrolled (passively locked) structure obtained from the single frequency sweep

and uncontrolled structure are shown in Figure 5.17. As the frequency of excitation increases and through three locked natural frequencies of the structure three corresponding resonances can be distinguished in structural displacement (Fig. 5.17a). It is visible that amplitude of the structural displacement is significantly reduced for the controlled structure. It is worth to notice that the force amplitude decreases when structural vibration achieves greater amplitude. Hence, controlled structure is excited with greater force values than uncontrolled one in the region of the first resonance (Fig. 5.17b). Thus, damping introduced by the proposed control is greater in reality than presented in Figure 5.17a. Due to the selected weights in the algorithm only the first resonance is intentionally mitigated by the control.

Comparison of frequency response functions $\mathrm{FRF}_{\mathrm{dis}}$ characterising the dependence of the structural tip-end displacement on the excitation force for uncontrolled and controlled laboratory structure is shown in Figure 5.18a. Analogous results obtained from the simulation are shown in Figure 5.18c. As mentioned in previous paragraph the control mitigates only the first resonance peak due to the selected weights in the control algorithm. Similarly to free-vibration tests the control performance in experiment is worse than in the simulation but still satisfactory. The

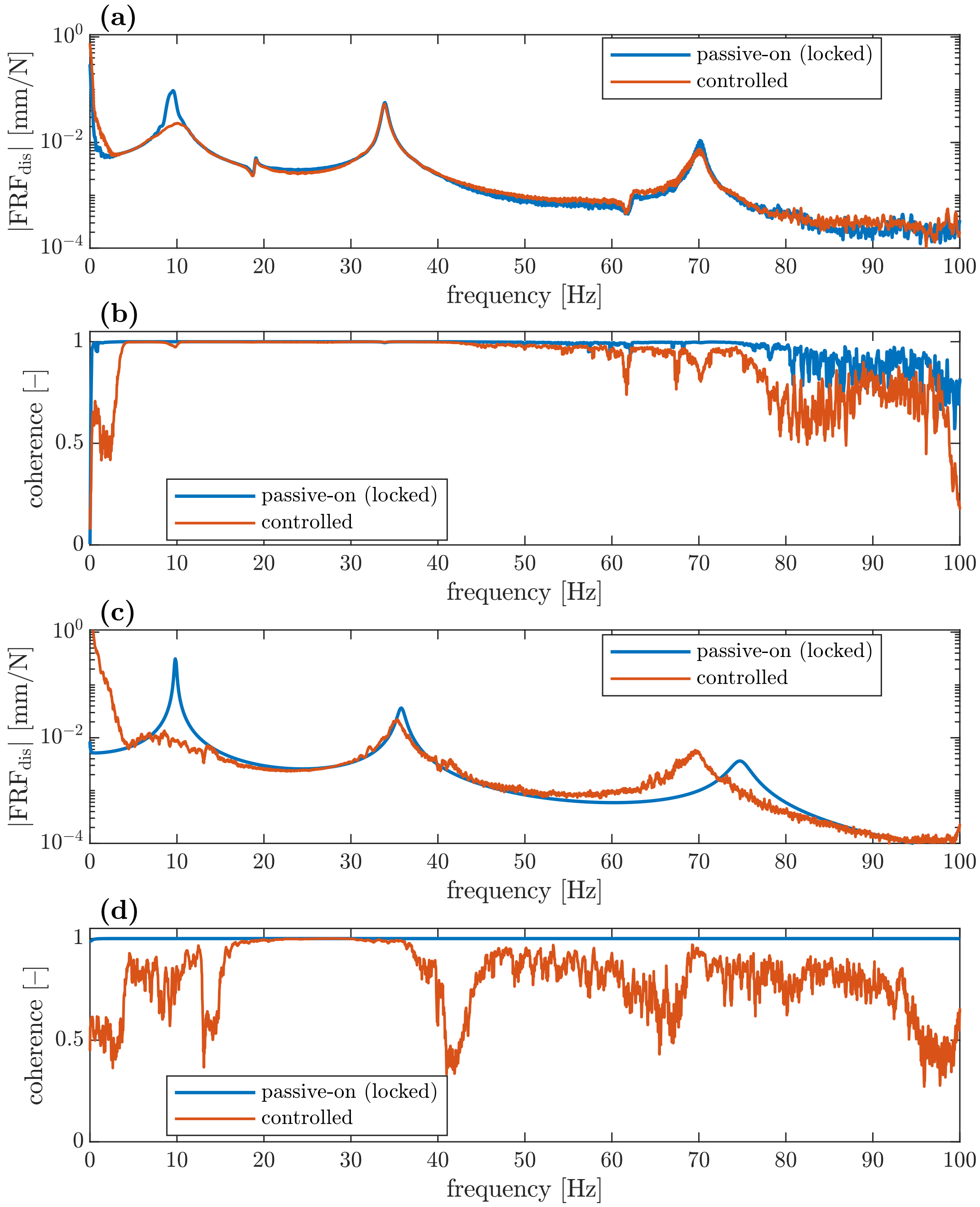

Figure 5.18: Comparison of various frequency-domain characteristics of vibration of controlled (Case 1) and uncontrolled (passively locked) structure: (a) experimental FRF for structural tip-end displacement, (b) corresponding experimental coherence, (c) numerical FRF for structural tip-end displacement and (d) corresponding numerical coherence

reason of the worse performance again is imperfectness of the lockable joints and the fact that level of the transmitted bending moments exceeds maximal bending moments transmitted by the lockable joints, since structural vibration achieves similar displacement amplitude at the first resonance as in the previously tested free vibration (compare Fig. 5.17a and 5.13a, c). Then, dry friction introduces additional damping into the structure even for the locked joints. This results in the fact that

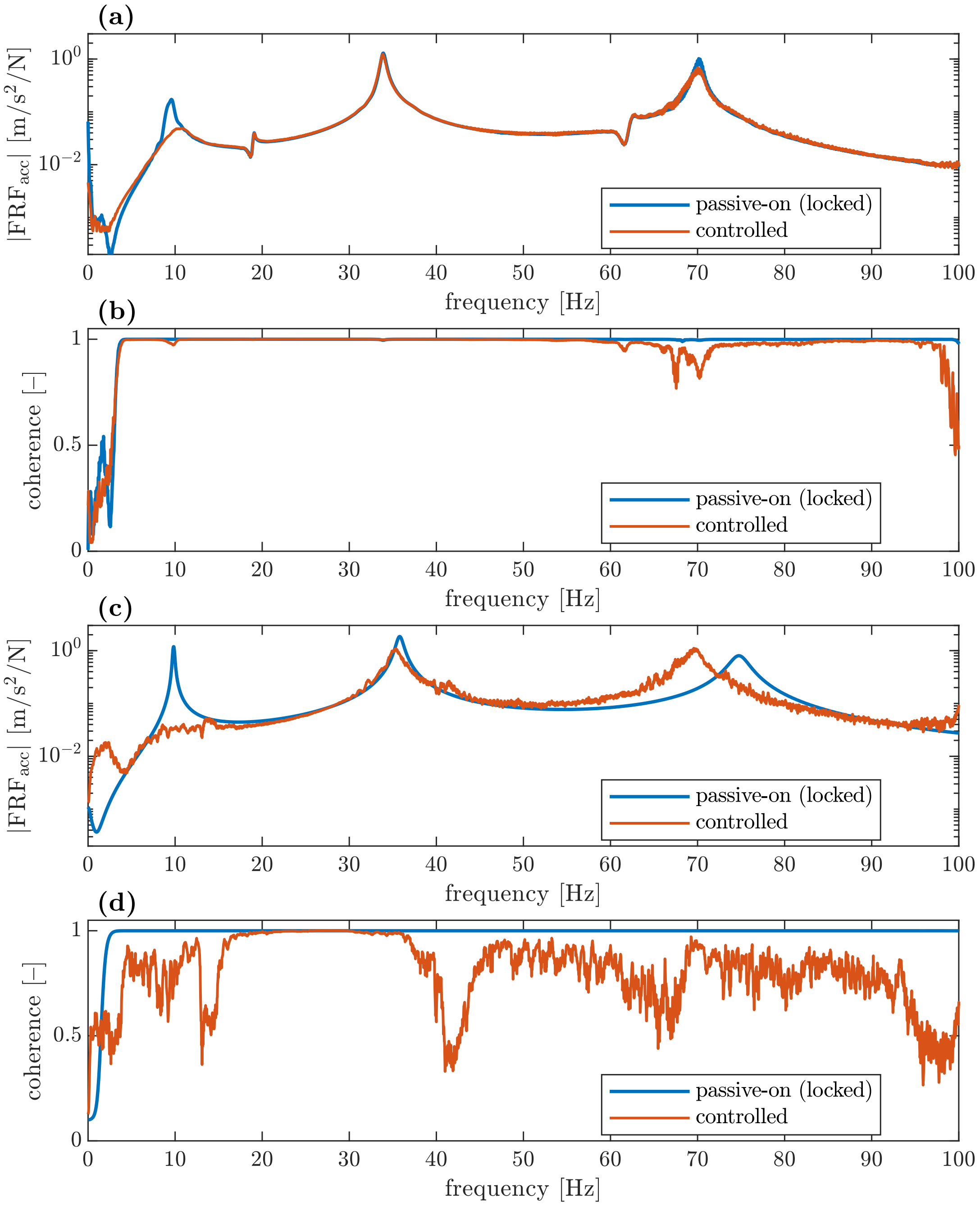

Figure 5.19: Comparison of various frequency-domain characteristics of vibration of controlled (Case 1) and uncontrolled (passively locked) structure: (a) experimental FRF for structural tip-end acceleration, (b) corresponding experimental coherence, (c) numerical FRF for structural tip-end acceleration and (d) corresponding numerical coherence

$\mathrm{FRF}_{\mathrm{dis}}$ obtained from simulation with uncontrolled structure contains bigger the first resonance peak, whereas for the corresponding controlled case is smaller than in experimental case.

Despite of the nonlinear character of dry friction introduced by real lockable joints the coherence functions obtained for laboratory structure with both the passively locked and controlled joints are mainly close to one. Only decreases and noise in

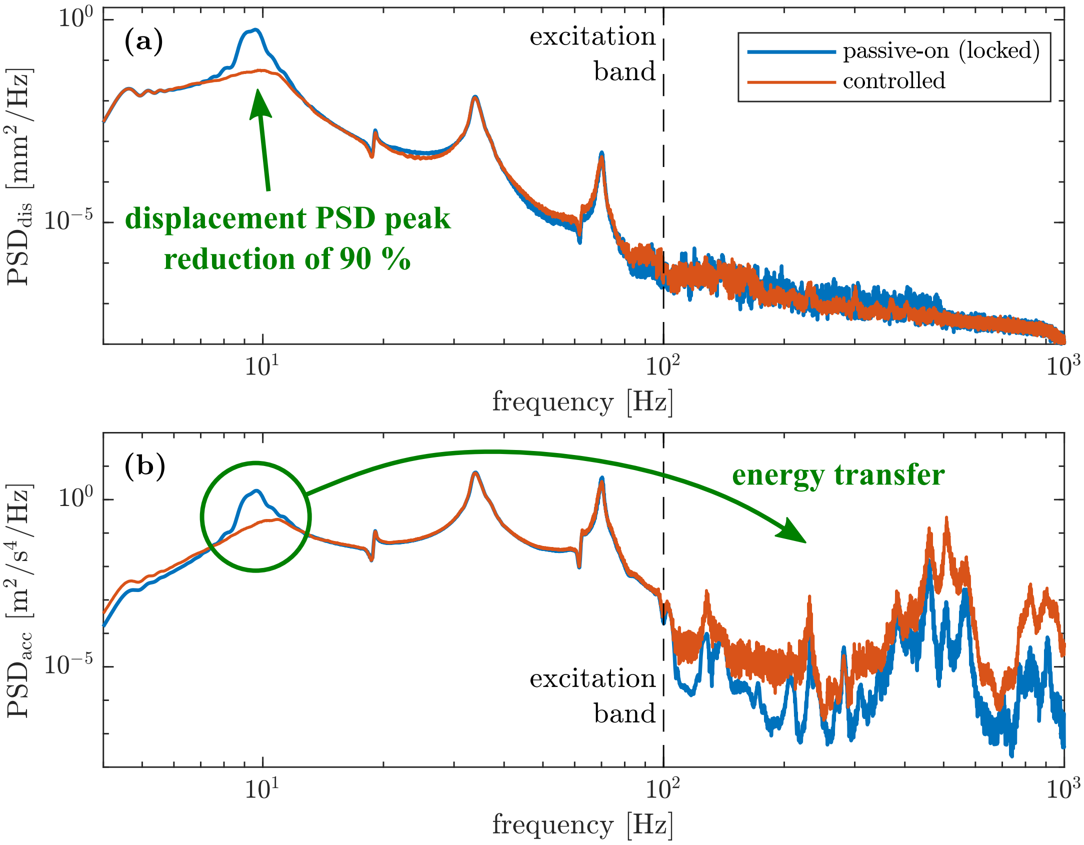

Figure 5.20: Experimental power spectral densities of structural tip-end (a) displacement and (b) acceleration obtained for Case 1

the region close to the upper limit of the excitation bandwidth and near to zero frequency that is outside the excitation bandwidth (4–100 Hz) are noticeable. FRFs for the controlled structure demonstrated in Figures 5.18a and c achieve large values for frequencies close to zero. Due to the excitation frequency starting from 4 Hz these values can be overestimated correspondingly to the decreased coherence functions.

A very interesting observation is that coherence function obtained form the simulation involving updated FE model (Fig. 5.18d) has lower values than one obtained from the experiment (Fig. 5.18b). The reason is that the updated FE model is described by piece-wise linear equation of motion (e.g. Eqs (2.43) and (2.44)). This piece-wise linear character relates to the capability of the joints to be fully locked or fully unlocked. Due to fact that the lockable joints in FE model have no such limitations as the real joints the simulated structure can accumulate and release more energy in the higher-order unlocked vibration modes. This behaviour is visible when comparing experimental and numerical structural response in free-vibration tests, e.g. in Figure 5.14a and b. It is visible that the numerical structural response is more distorted than experimental one that decays more gently. Also behaviour of the FE model is more sensitive to the time instant of the joint unlock. It results in more non-coherent structural response signals than for the experimental case.

The third resonance peak in simulation results (Fig. 5.18c) is not mitigated but is shifted towards lower frequencies. As $\alpha_3 = 0$ the third vibration mode is not mitigated, however relatively small thresholds κ_1 and κ_2 results in additional joint switches. As the structural stiffness is lower when the joint is unlocked the third resonance peak is shifted to the frequency near to 70 Hz that is between unlocked and locked natural frequency of the structure, 66.4 and 74.8 Hz, respectively.

The observations above are relevant also for FRFs calculated for accelerations of the structural tip end and corresponding coherence functions presented in Figure 5.19.

Experimental PSDs of structural tip-end displacements and accelerations are shown in Figure 5.20a and b, respectively. Despite of the fact that the level of the force produced by the modal shaker is relatively greater for the controlled structure than in the passively locked case near the first resonance (see: Fig. 5.17) the PSD of the structural tip-end displacement is reduced by 90 % at the first resonance peak.

PSD of structural tip-end accelerations reveals the phenomenon of the modal energy transfer from the first unlocked vibration mode into the higher-order vibration ones that are outside the frequency range of the excitation (4-100 Hz). It is the essential observation in the conduced experimental validation, since despite of the significant imperfectness of the lockable joints utilised in the laboratory frame demonstrator the proposed control algorithm still operates in agreement with stated thesis. PSD of the structural tip-end accelerations for the controlled structure is increased at the higher frequencies outside the excitation bandwidth at the expense of the first resonance peak accordingly to the selected weights. It is despite of the fact that some amount of mechanical energy is dissipated in friction between friction parts of the lockable joints due to limited clamping force.

Case 2 In this case lockable joints J3 and J4 are selected to be controlled. Selected thresholds and weights are as follows: $\alpha_1 = 1$, $\alpha_2 = 0.05$, $\alpha_3 = 0$, $\kappa_1 = 0.384$ W and $\kappa_2 = 5.3 \cdot 10^{-4}$ W.

Experimental and numerical FRFs accompanied with corresponding coherence functions are presented in Figure 5.21. FRFs depicted in Figures 5.21a and c are additionally plotted in linear scale in Figure 5.22 aiming at demonstration more details in the vicinity of the resonance peaks. Here, not only the first resonance is damped but also the second one. It is interesting that the first resonance peak is reduced significantly more efficiently in numerical simulation than experiment, whereas the control algorithm mitigates the second resonance peak effectively both for experiment and simulation. The reason of this phenomenon can be explained by going back to the consideration on Case 2 of free vibration, where the same pair of joints is controlled (J3 and J4). Case 2 of free vibration tests reveals that significant amount of strain energy accumulated in higher-order unlocked vibration modes is not released in free vibration when the joint is being unlocked. It is due to residual clamping force in the real lockable joints. As in free vibration the release of the manual hook excites vibration mainly in the first vibration mode

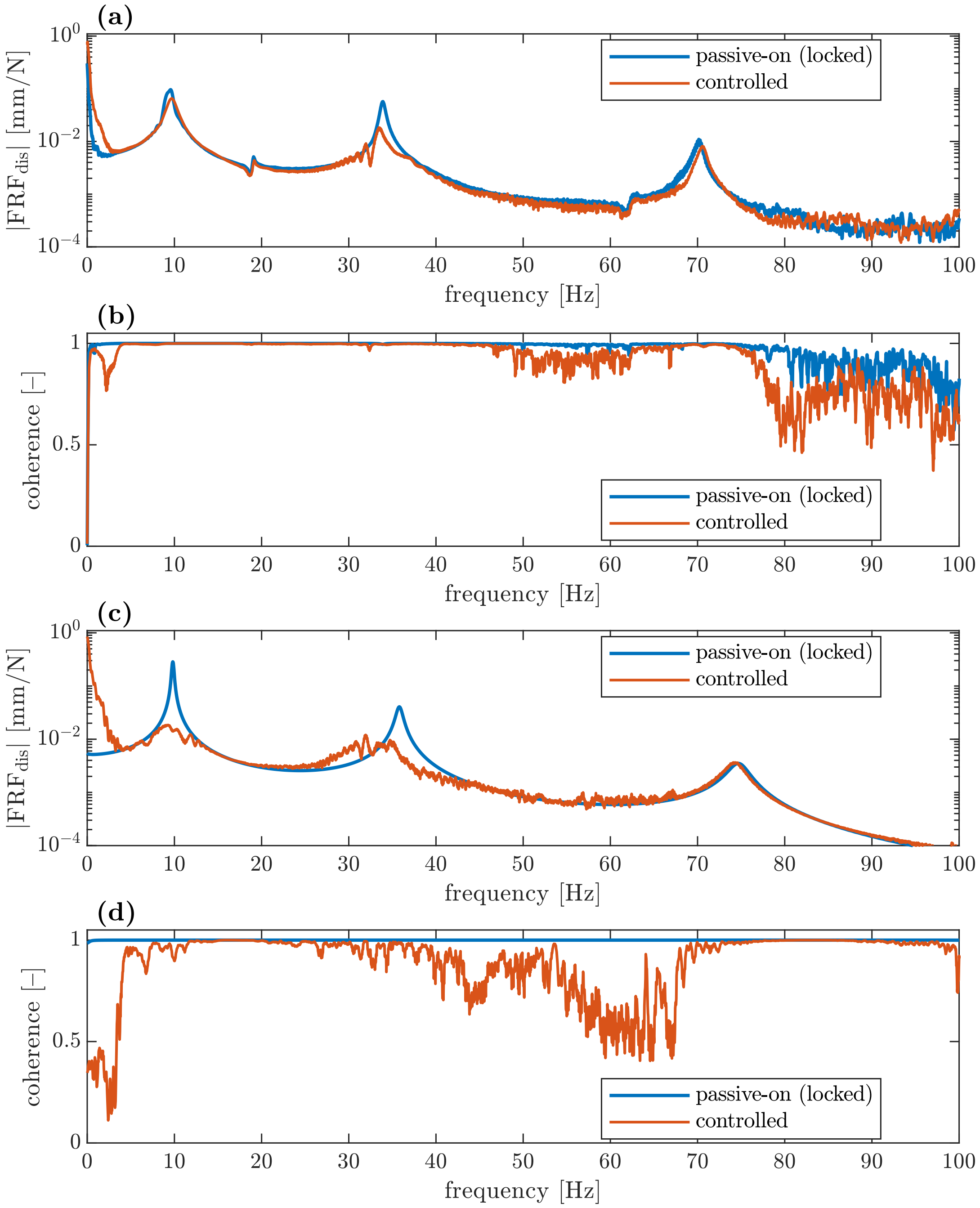

Figure 5.21: Comparison of various frequency-domain characteristics of vibration of controlled (Case 2) and uncontrolled (passively locked) structure: (a) experimental FRF for structural tip-end displacement, (b) corresponding experimental coherence, (c) numerical FRF for structural tip-end displacement and (d) corresponding numerical coherence

this observation is relevant also for the first resonance peak in the present case of the forced vibration. As opposed, the second peak is mitigated efficiently even in experimental case due to the fact that the pair of joints J3 and J4 transmits greater bending moments when modal shaker sweeps the second resonance peak. This is illustrated in Figure 5.23 by using the updated FE model with passively locked joints. The greater level of the transmitted bending moments in relation to

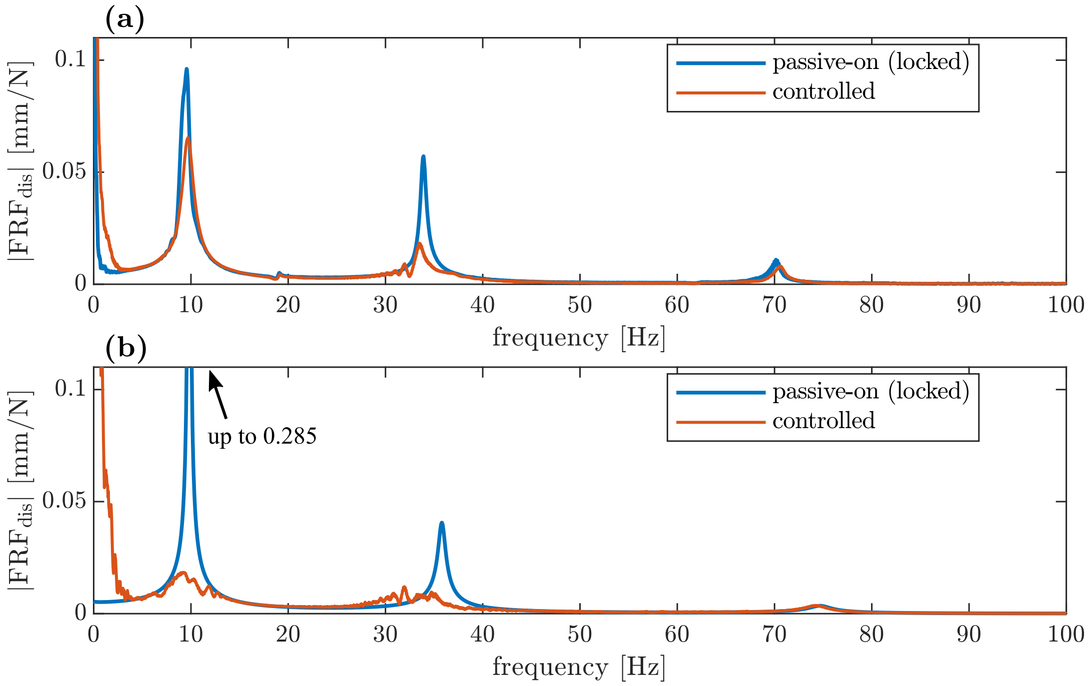

Figure 5.22: Comparison of FRFs for structural tip-end displacement in lin-scale for controlled (Case 2) and uncontrolled (passively locked) structure obtained from: (a) experiment and (b) numerical simulation

moment $f^{\mathrm{u\,max}}$ results in ability to release more strain energy into the free vibration. Structural tip-end displacement obtained with the updated FE model is significantly greater than corresponding displacement obtained experimentally for the passively locked joints (compare Figs 5.17a and 5.23a) due to the additional friction-based damping in real joints, whereas joints in numerical simulations are locked without slipping. It is worth to notice, that despite of the fact that the joints J1 and J2 are not controlled in this case (passively locked), slipping between their friction parts cannot be avoided similarly to Case 1 of both free and forced vibration tests.

It is worth to notice that despite of the lower controllability of the first unlocked vibration mode by the selected pair of the lockable joints (Fig. 5.8) the first resonance peak is still effectively mitigated in the simulation. It stays in agreement with discussion in Section 4.1.3 that even for non-optimal placement of the lockable joints the proposed control methodology is still efficient and insensitive to the local extreme values of measured strains.

In the present case of the forced vibration testing once again experimental coherence is close to one despite of nonlinearity provided by the dry friction (Fig. 5.21b). Coherence has lower values only for frequencies above the third resonance peak and below 4 Hz, which is lower limit of the excitation bandwidth. Numerical coherence (Fig. 5.21d) obtained for the controlled structure tends to be smaller than experimental one at frequencies below 70 Hz. It is consistent with results obtained for Case 1. Similarly to Case 1, in the present case the reason is that joints in simulation are always fully locked when $u(t) = 1$ that results in more efficient modal

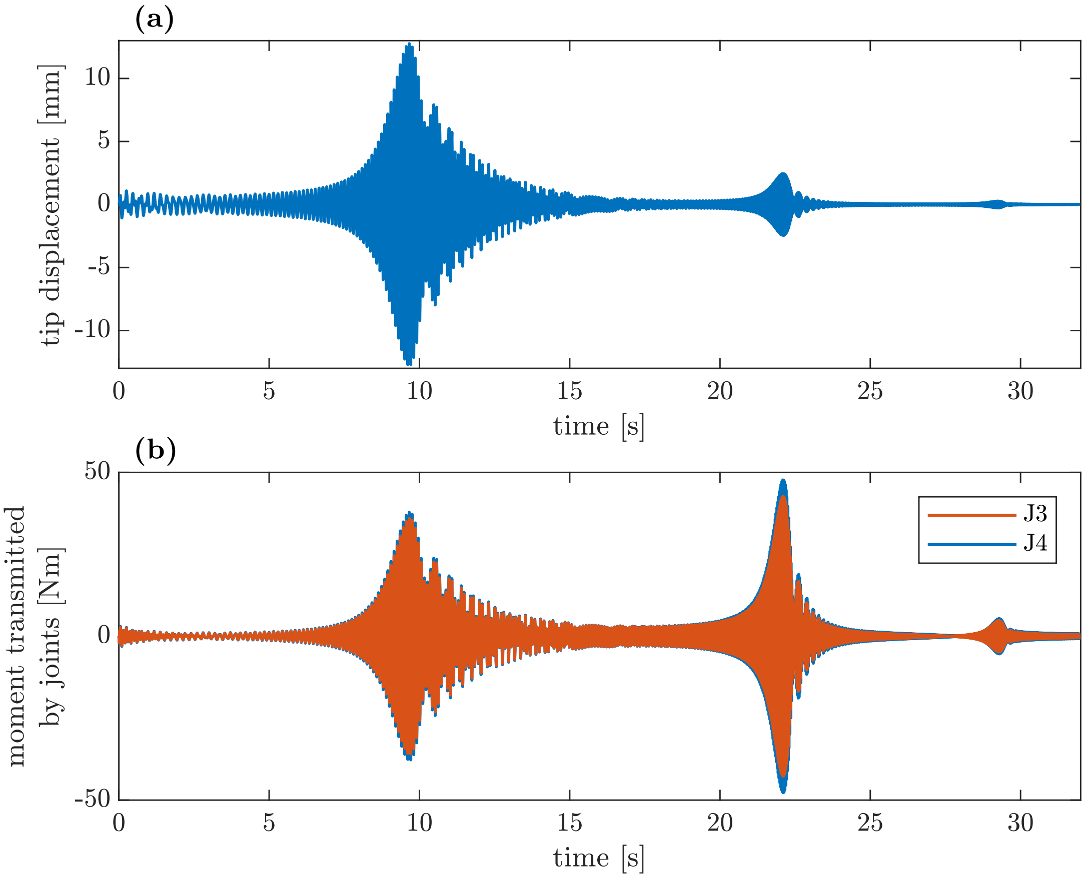

Figure 5.23: Time history of (a) tip-end displacement obtained with the updated FE model with passively locked joints and (b) corresponding bending moments transmitted by the joints J3 and J4 for a single frequency sweep

energy transfer to the higher-order unlocked vibration modes. It results in more distorted response of the structure and lower coherence between the excitation and the structural response.

Experimental PSDs of the structural response both for controlled and uncontrolled case are compared in Figure 5.24. Similarly to FRFs the PSDs of the structural response are reduced more effectively for the second resonance peak (displacement PSD peak reduction of 73 %) than for the first one (reduction of only 45 %). The comparison of PSDs of acceleration of the structural tip end (Fig. 5.24b) demonstrates that mechanical energy is transferred from the fist and second unlocked vibration mode into the higher-order vibration modes. Level of the PSD of the structural tip-end acceleration for the controlled structure outside the excitation frequency range is visibly greater than one obtained for the passively locked joints. This difference is greater than in Case 1 (compare with Fig. 5.20b). The first possible reason is that the energy is transferred out from the two controlled unlocked vibration modes, as opposed to Case 1 when only the resonance first peak is reduced. Additionally, the second resonance peak corresponds with the greater bending moments transmitted by the lockable joints J3 and J4 (see: Fig. 5.23. Other reason is that operation of the pair of lockable joints J3 and J4 provide better accumulation

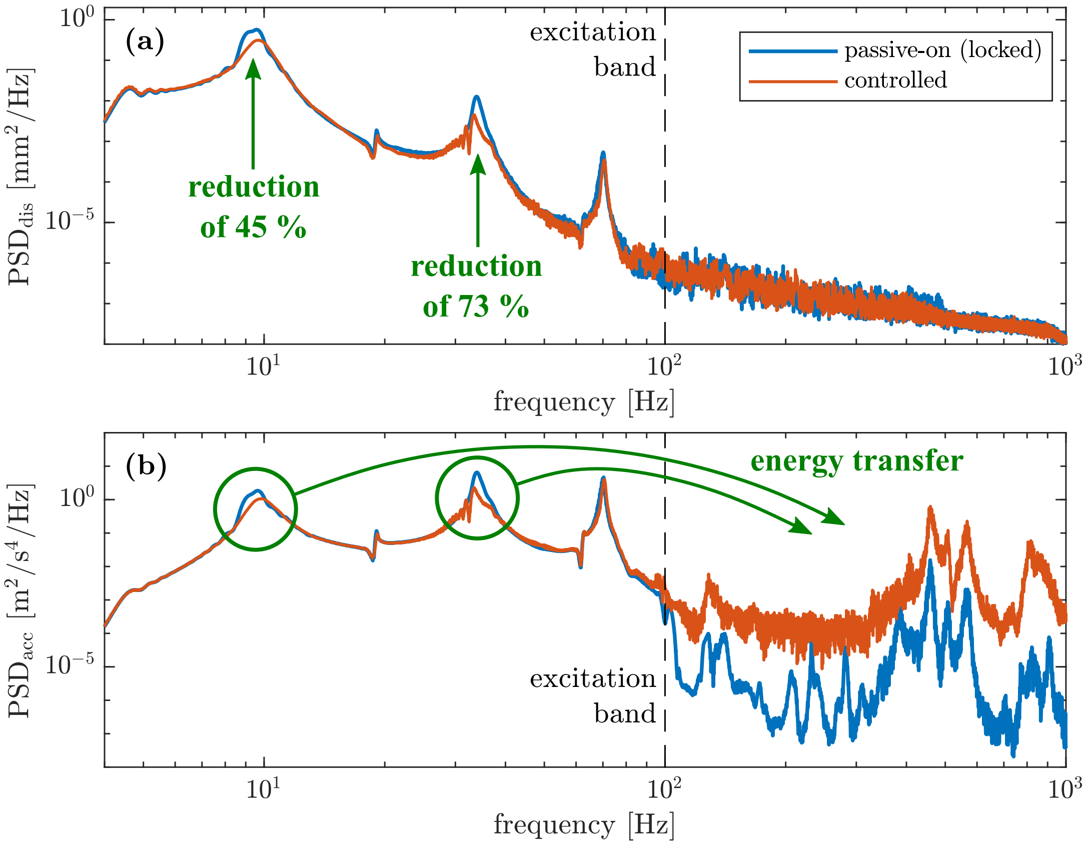

Figure 5.24: Experimental power spectral densities of structural tip end (a) displacement and (b) acceleration obtained for Case 2

of the strain energy than of the joints J1 and J2 due to higher maximal bending moments $f_k^{\mathrm{l\,max}}$ (see: Tab. 5.1).

5.5 Energy transfer to the targeted mode

In this subsection the ability of the proposed control strategy to transfer the mechanical energy from the currently excited unlocked vibration modes into the preselected one is verified experimentally. Experimental results are compared with ones obtained with aid of the updated FE model. Using of the manual hook is insufficient in examination of the control strategy in transferring the mechanical energy in various directions. It excites mainly first vibration mode, whereas the ability to excite various vibration modes is desired. Thus, in this subsection only the forced vibration are tested. Each time the preselected unlocked vibration mode is outside the frequency bandwidth of the excitation aiming at demonstration of the modal energy transfer phenomenon.

Excitation force is provided by the modal shaker whose stinger is connected at the same location as during testing of the control performance in vibration attenuation (see: Fig. 5.16) and the force is measured analogously by the force sensor. Modal shaker sweeps frequency with logarithmic frequency increments in time, analogously to tests of the vibration mitigation. The difference is frequency range that is vary for particular control case and is described below. The frequency sweeps of time duration 32 s are performed. Results discussed below are averaged from five particular frequency sweeps. Excitation in numerical simulation is reproduced analogously to vibration attenuation tests, however new frequency limits from the cases discussed below are substituted into Equation (5.22) and the amplitude $A_\mathrm{d} = 70$ N is adopted in Equation (5.21).

Similarly to vibration attenuation Algorithm 2 is adopted accordingly to Subsection 5.3.3. Algorithm parameters $t_\mathrm{lock} = t_\mathrm{unlock} = 15$ ms, $\kappa_1 = 0.384$ W and $\kappa_2 = 5.25 \cdot 10^{-4}$ W are common for the cases below, whereas the weights α_p are selected separately with the trial-and-error method.

Due to the fact that that energy is transferred to the unlocked vibration mode outside the frequency bandwidth of the excitation FRFs are not used in this subsection. Only PSD functions are utilised to analyse the structural behaviour in the frequency domain.

Case 1 In this case the first unlocked vibration mode is selected as the targeted one. The first unlocked natural frequency of the updated FE model is $f^{(1)} = 8.98$ Hz, whereas its locked counterpart is $\widetilde{f}^{(1)} = 9.83$ Hz. Both of these frequencies are outside the frequency bandwidth of excitation that is 20–100 Hz. The following algorithm weights are selected: $\alpha_1 = -1$, $\alpha_2 = \alpha_3 = 0$.

PSD of structural displacement at the tip end for controlled and passively locked structure obtained from the experiment is shown in log-log and log-lin scales in Figures 5.25a and b, respectively. Figure 5.25b demonstrates increment of the vibration amplitude after transferring the energy into the first unlocked vibration mode, whereas Figures 5.25a demonstrates structural behaviour of all monitored unlocked vibration modes and higher-order ones op to 1 kHz.

It is evident that significant amount of the energy is transferred from the second into the first, targeted, unlocked vibration mode that is outside the excitation frequency range. It results in the significant increment of the vibration amplitude, since it is natural that lower-order vibration modes require less energy to be excited with the same amplitude than the higher-order ones.

As $\alpha_3 = 0$ the third resonance peak is not affected by the lockable joints. Additionally, controllability of this mode is very crude by the currently controlled pair of the lockable joints (see: Fig 5.8).

Analogous results obtained from the numerical simulation are shown in Figure 5.25c. Here the observation that energy is transferred from the second unlocked vibration mode to the first one is also relevant. Due to the fact that the joints locked in the simulation are not subjected to the slip effect the energy transfer is more efficient and results in greater PSD value for the targeted unlocked vibration mode.

Comparison of PSD of structural tip-end accelerations for passively locked and

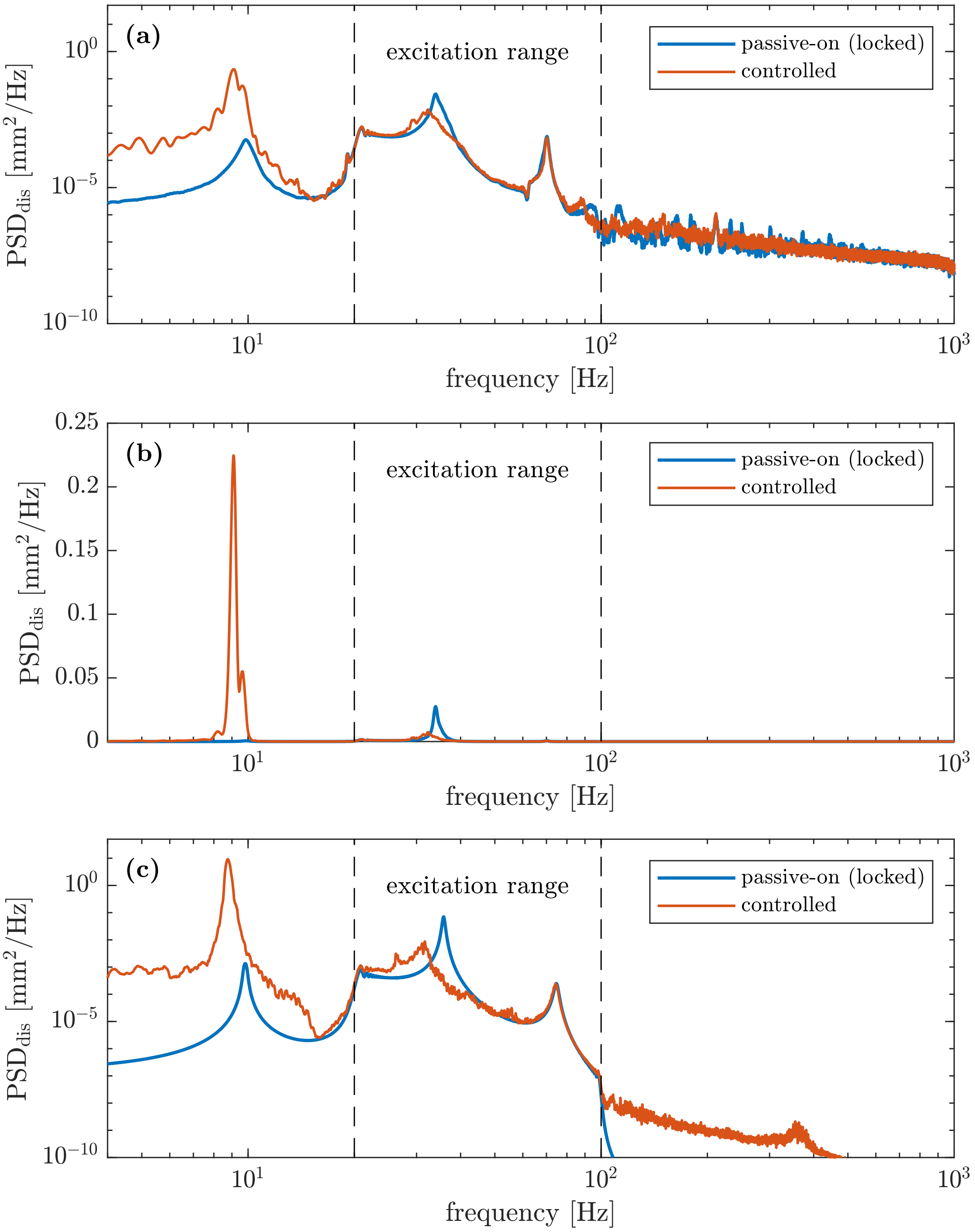

Figure 5.25: Comparison of power spectral densities of structural tip-end displacements for the passively locked and controlled (Case 1) lockable joints J3 and J4 obtained from: (a) experiment, shown in log-log scale, (b) experiment, shown in log-lin scale and (c) numerical simulation, shown in log-log scale

controlled joints is shown in Figures 5.26 both for experiment and numerical simulation. Here, the effect of directed energy flow into the first vibration mode from the second also is clearly demonstrated both for experiment and numerical simulation. Certain amount of the structural energy is unintentionally transferred into the higher-order unlocked vibration modes that is demonstrated by the increment of the PSD values for the controlled structure at frequencies above the excitation

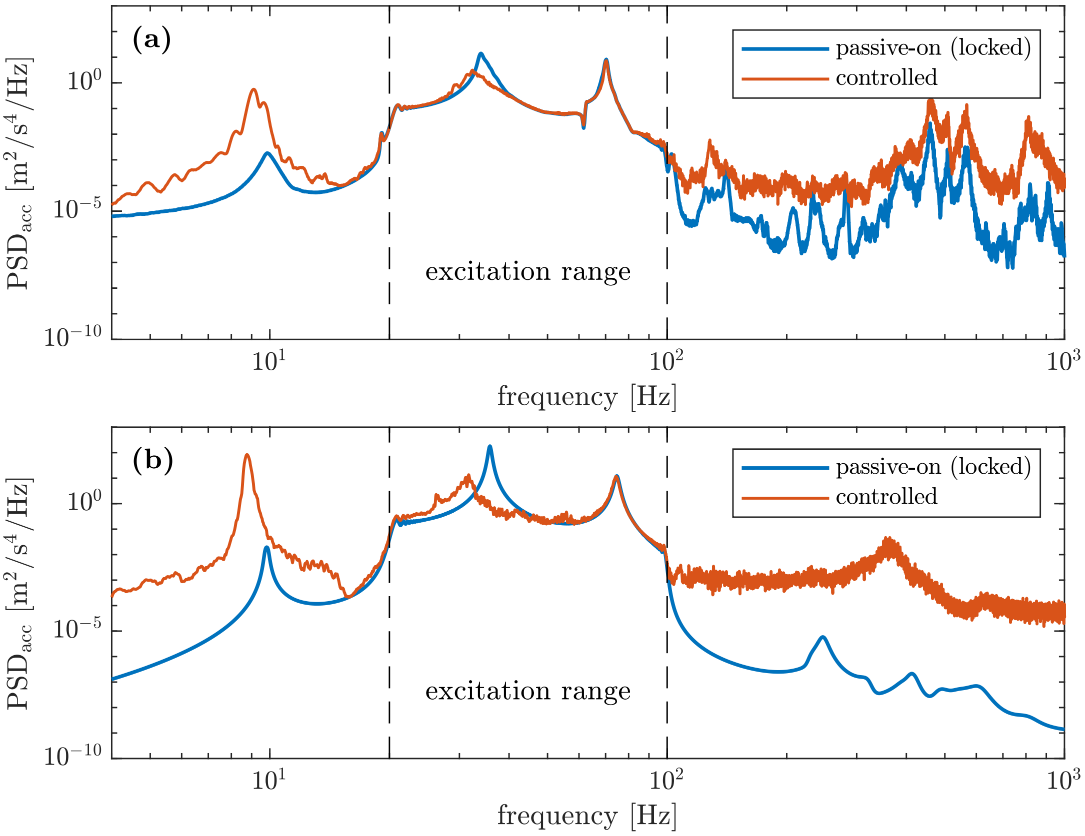

Figure 5.26: Comparison of power spectral densities of structural tip-end accelerations for the passively locked and controlled (Case 1) lockable joints J3 and J4 obtained from: (a) experiment and (b) numerical simulation

range. This can be considered as control spillover effect, as in the energy harvesting application it is undesired phenomenon. The increment PSD for the controlled case corresponding with the targeted vibration mode and the higher-order vibration modes is greater for the numerical simulation due to mentioned limitation of the real lockable joints.

Time history of the structural tip-end displacement obtained from single experimental frequency sweep for uncontrolled (passive-on) and controlled joints J3 and J4 is depicted in Figure 5.27. Two resonance regions visible in Fig. 5.27a relate to the excitation frequency range omitting the first (both locked and unlocked) vibration mode. Results shown the zoomed area (Fig. 5.27b) demonstrate the sudden change of predominant vibration frequency accompanied with the increase of the amplitude. These phenomena are result of the operation of the joints which starts closely before the zoomed area, where the vibration amplitude of the controlled structure stats gently increasing. This change of character of structural vibration confirms that the proposed control causes transfer of the energy from the second to the first unlocked vibration mode. It is despite of the significant imperfectness of the real lockable joints.

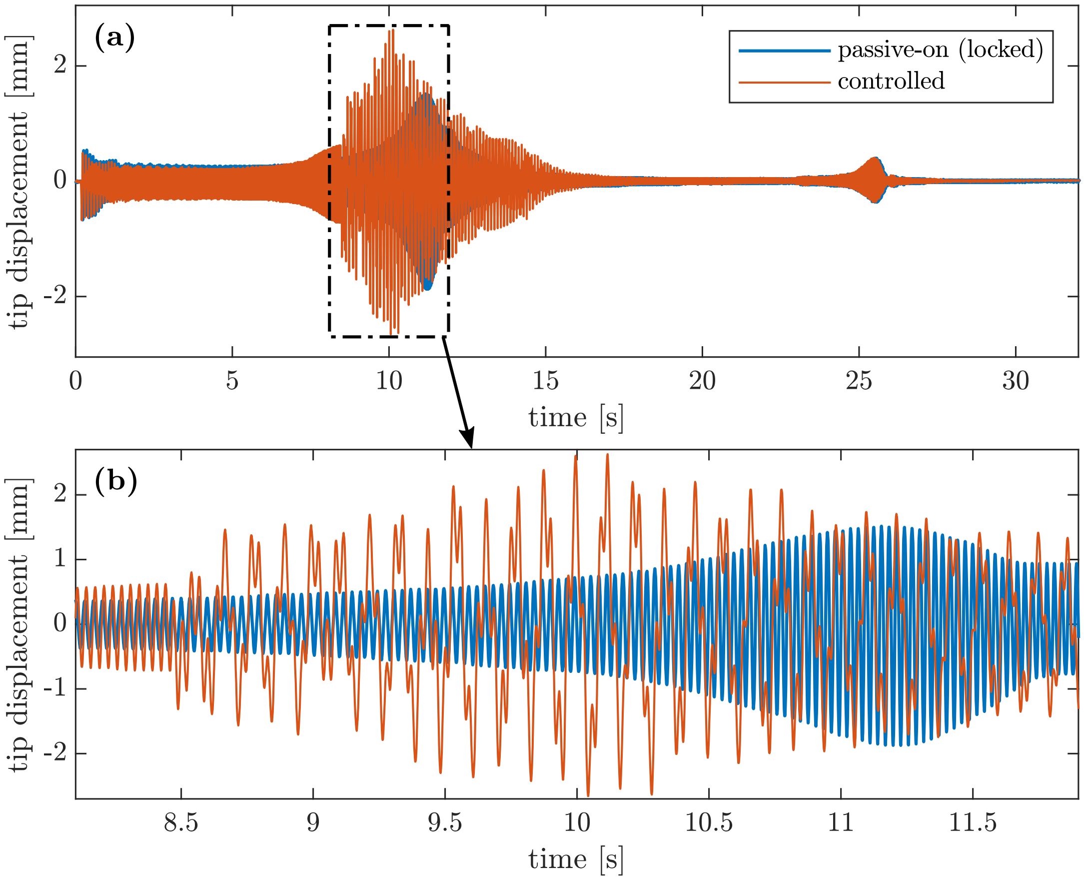

Figure 5.27: Comparison of time histories of structural response on single frequency sweep for the uncontrolled and controlled (Case 1) laboratory frame demonstrator: (a) whole duration and (b) zoomed region

Case 2 In this case the energy is transferred into the second unlocked vibration mode, whose natural frequency is $f^{(2)} = 28.91$ Hz, whereas second locked natural frequency is $\widetilde{f}^{(2)} = 35.83$ Hz. Both of these frequencies are outside the excitation frequency range that is 4-20 Hz. Algorithm weights $\alpha_1 = 0.5$, $\alpha_2 = -1$ and $\alpha_3 = 0$ are selected.

Comparison of PSD of structural tip-end displacements obtained for passively locked and controlled lockable joints both for experiment and simulation are shown in Figure 5.28. It is evident that the second, targeted, unlocked vibration mode has greater participation in the structural motion at the expense of the currently excited, the first one. It is both for experiment and numerical simulation. In the second frequency peak obtained for the controlled structure is placed between second locked and unlocked natural frequency, $f^{(2)}$ and $\widetilde{f}^{(2)}$, respectively. It is difficult to assess whether the doubled peak related to the targeted mode of the controlled case in the numerical results (Fig. 5.28b) relates to locked and unlocked vibration modes shifted in frequency domain or it is result of the leakage effect.

Once again in the experimental study effectiveness of the proposed control strategy is worse than in numerical simulation due to imperfectness of the lockable joints, as described in Subsection 5.4.2. Lower value of the first resonance peak for the

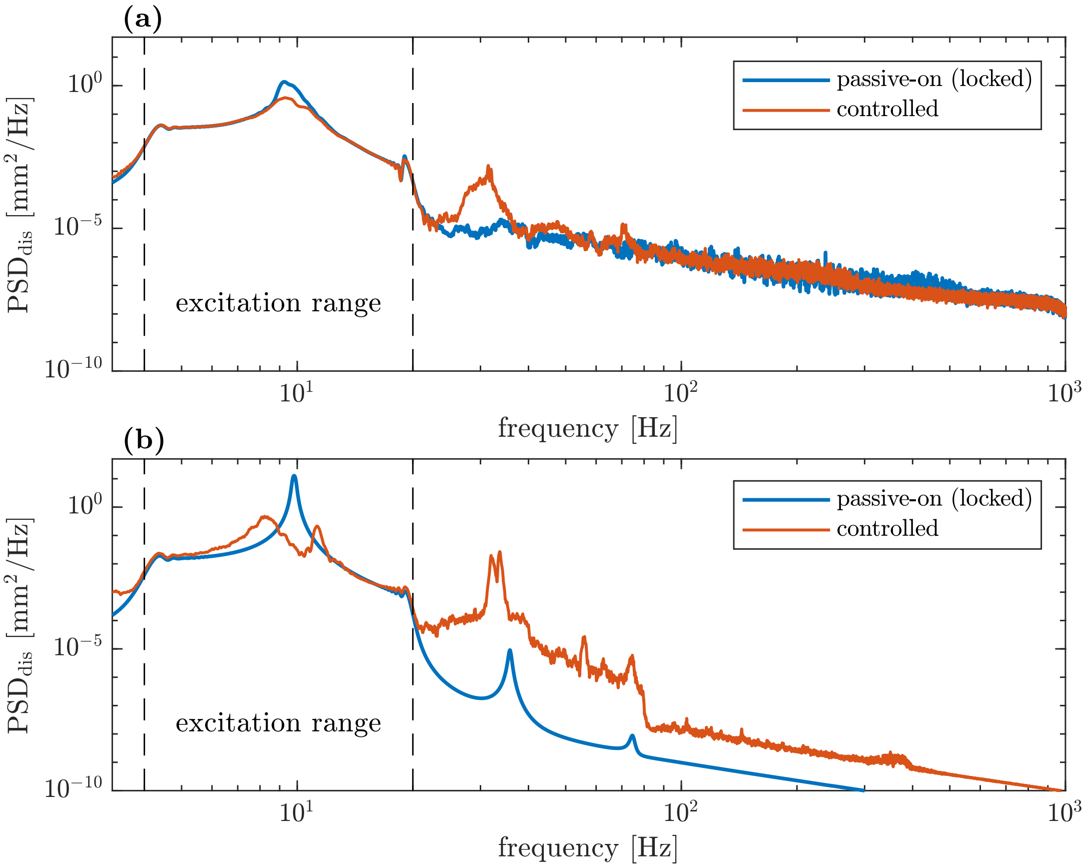

Figure 5.28: Comparison of power spectral densities of structural tip-end displacement for the passively locked and controlled (Case 2) lockable joints J3 and J4 obtained from: (a) experiment and (b) numerical simulation,

passive-on case in the experiment in relation to the corresponding one obtained in numerical simulation is result of both decreased force provided by the modal shaker when the structure is in resonance and additional nonlinear damping provided by the dry friction in real lockable joints (not only currently controlled ones but also J1 and J2).

PSD functions of structural tip-end acceleration corresponding with results discussed above are shown in Figure 5.29. Effect of the transfer of mechanical energy from the first vibration mode to the second one also is clearly demonstrated. PSD of accelerations at frequencies above the second unlocked vibration mode are increased for the controlled case both in experiment and numerical simulation. It shows that certain amount of the energy is unintentionally transferred into the higher-order unlocked vibration modes. Here, this effect seems more pronounced than in Case 1 due to the fact that in the present case high-frequency accelerations of passive structure have lower PSD than in Case 1 but the level of the high-frequency accelerations of the controlled structure is similar (compare with Fig. 5.26). The reason is explained in Case 1-2 of numerical study on energy harvesting applications in Section 4.2.5. As explained, when the mechanical energy is to be transferred from currently excited unlocked vibration mode to the targeted one whose unlocked natural frequency is

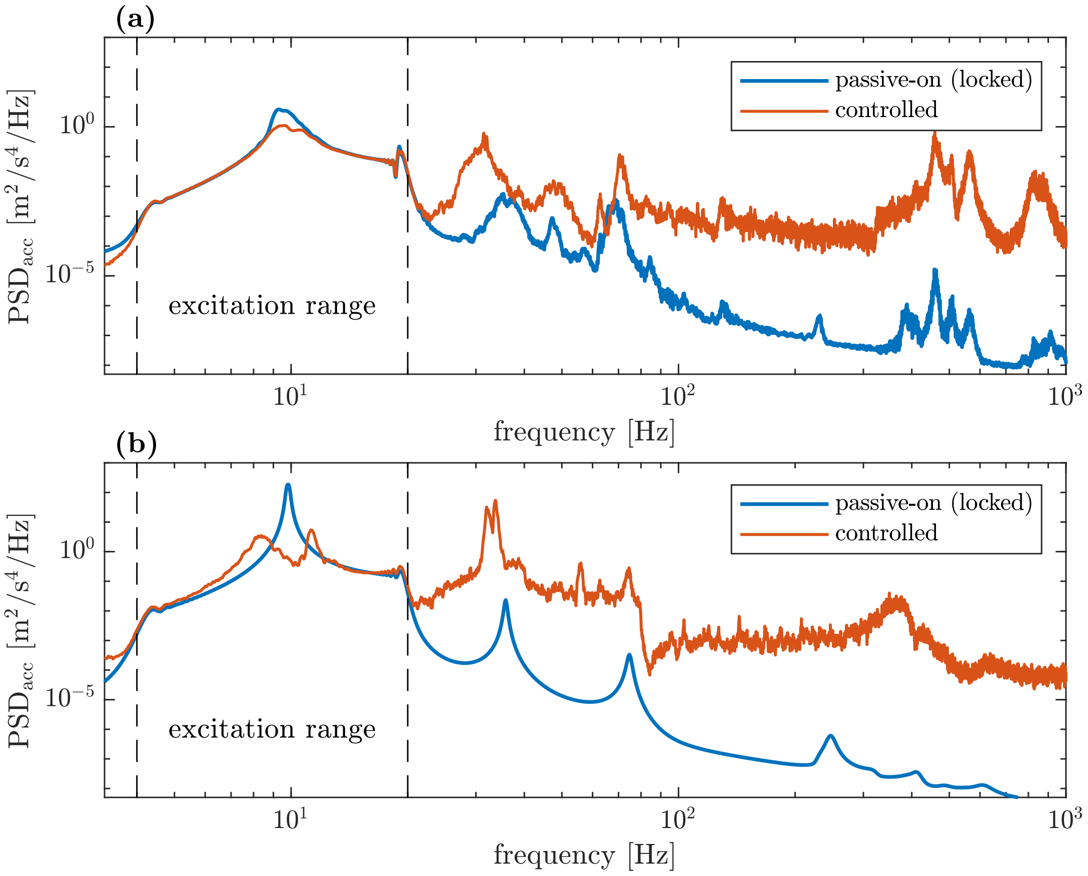

Figure 5.29: Comparison of power spectral densities of structural tip-end acceleration for the passively locked and controlled (Case 2) lockable joints J3 and J4 obtained from: (a) experiment and (b) numerical simulation

relatively greater the joints are unlocked at time instances when measured strains are nonzero (see e.g. Fig. 4.30c). In this case usually some amount of the energy is not only released in free vibration of the targeted unlocked vibration mode but also in the higher-order ones that is undesired effect. However, the negative weight of the targeted mode allows for reduce the escape of the energy into high-frequency oscillations.

Chapter 6

Conclusions

The control methodology that employs controlled structural joints locking/unlocking rotational DOFs between flexible adjacent structural members has been proposed. It causes modal coupling effect resulting in the transfer of the mechanical energy between vibration modes, called in this thesis modal energy transfer. Two potential applications of this original control strategy have been proposed: vibration attenuation and enhancement of the energy harvesting process. In the former application the mechanical energy is to be transferred from the lower-order vibration modes into the higher-order ones. Due to significantly greater damping coefficients of the high-frequency vibration modes the energy is quickly dissipated in the structural volume. In the latter application the energy is to be transferred into the targeted vibration mode to which the energy harvesting device is tuned. Then it operates always under resonance conditions.

The considered class of structure is the subclass of reconfigurable systems, as locking and unlocking of the joints changes: no. of structural DOFs, local stiffness properties of the structure, modal basis and its dimension, as investigated in Chapter 2. It has been demonstrated that it is possible to express structural displacement in unlocked modal basis (obtained for all joints in the unlocked state) even if lockable joints currently are in the locked state, but use the locked modal basis (obtained for joints locked) is insufficient. Locking effect introduces the self-equilibrated pair of moments for each locked joint resulting modal coupling effect between the unlocked vibration modes. It has been also demonstrated that when any joint is locked the coupled unlocked vibration modes exchange their energy. Later, it has been proposed that the constraint describing the joint lock can be relaxed. Then, the locking effect can be represented by large viscous damping between locked rotational DOFs. The conduced analysis shows that for sufficiently large viscous damping factor the viscous-based joint model preserves all important properties of the model based on the kinematic constraint but significantly simplifying the numerical simulation of the structural behaviour and further analytical derivations.

It has been shown that as the joint is locked and does not perform any work over the structure. Hence, the energy transferred from any unlocked vibration mode is equal to the energy transferred to all remaining ones. It is important observation for the vibration mitigation application of the proposed control methodology, since it is sufficient to monitor only lower-order unlocked vibration modes to provide energy transfer into the higher-order vibration modes. Monitoring of the higher-order unlocked vibration modes could be a challenging problem due to the equipment limitations. Another important observation for the control purposes is that total modal energy transfer rate is sum of modal energy transfer rates resulting from locking of each particular joint.

In Chapter 3 various aspects of the control have been discussed. First, quantities to be measured for proper operation of the proposed control have been selected. It results in the hierarchical feedback architecture containing one global control loop that is accompanied with local control loops. In the single global loop modal velocities of the monitored unlocked vibration modes carrying information about global state of the structure are estimated using modal filtering technique. Regarding the local control loops, they are collocated with the lockable joints – bending moment transmitted by each lockable joint is estimated, e.g. by the pair of strain gauges in the vicinity of the lockable joint. In this scheme each joint is controlled independently on each other.

Sensor placement is one of the crucial aspects in modal filtering. Determinant of the Fisher information matrix that is to be maximised has been the selected as an objective function in sensor layout optimisation. Then, optimal solution provides a trade-off between values and linear independence (orthogonality) of mode shapes at sought sensor locations. It is combinatorial problem that in practice can require tremendous computational burden to find optimal solution. Thus, near-optimal solution has been obtained with the new method based on convex relaxation that allows for replace this discrete optimisation problem with its continuous counterpart. This method is not only faster than well-known Kammer's Effective Independence method but is also easy in implementation in a code.

Criterion for optimal placement of the lockable joints, dedicated for the developed control methodology, also has been proposed. As the controlled system equipped with lockable joints is nonlinear, commonly used metrics of modal controllability such as controllability gramian or PBH test can be misleading. The proposed controllability metric describes how much strain energy accumulated in particular mode shape, when joints locked, can be released after the joint unlock into all unlocked vibration modes excepting one the most correlated with mode shape obtained before the joint unlock. In other words it is measure of the amount of the energy that can be distributed among various unlocked vibration modes by the locking the joints.

This chapter has been ended with section introducing the novel control law that is based explicitly on derivations describing the transfer of the energy between unlocked vibration modes. The control law has been adopted for both the proposed potential applications. In the vibration mitigation application the proposed control law is based on Lyapunov function that is weighted sum of energies associated with monitored (lower-order) unlocked vibration modes. Its minimisation results in the transfer of the energy out from these modes into the higher-order vibration modes that are not explicitly included in this function nor monitored. In the energy harvesting application modal energy transfer to the preselected mode is required. Thus, the control law has been modified by switching the weight corresponding with the targeted unlocked vibration mode into the negative value. Then, the objective function cannot be called Lyapunov function because it is not always positive, however it does not affect the minimisation process. Negative value of this weight causes directed transfer of the energy into the preselected vibration mode from the currently excited ones. In both potential applications of the control strategy the fastest decrease of the weighted sum of the modal energies has been provided. The proposed control law has been later adopted into new control algorithm that includes also measured quantities and other practical control issues. Moreover, it has been shown that natural property of the control algorithm is locking of the joints when rotational velocities of the coupled rotational DOFs have the same (or very close) value and direction that reduces the jerking of the structure and operational wear of the lockable joints.

The proposed control methodology has been validated numerically and experimentally. Results of numerical study described in Chapter 4 demonstrate that the developed control methodology allows for efficient transfer of the energy directed to the higher-order unlocked vibration modes or to single preselected vibration mode, depending on the selected application. The proposed control methodology has been compared with PAR method. Both the proposed modal control approach and PAR method achieve satisfactory results for free and forced vibration. When the vibration mitigation is selected as the aim of the proposed methodology it works similarly to PAR approach. However, the proposed control methodology allows for mitigation of particular unlocked vibration modes with priority pursued by the selected algorithm weights as opposed to PAR approach. It results in better performance of the modal control with simultaneous lower number of joint switches (locking/unlocking) than in PAR approach. Moreover, it has been demonstrated that when the joints are not placed optimally (e.g. due to construction limitations) these differences in performance of the compared control methods are getting bigger, especially in number of joints switches.

It has been also demonstrated that the proposed control methodology allows for enhancement of the energy harvesting process. Here, smaller controlled structure plays the role of adaptive energy buffer. The energy harvester attached to this structure has been tuned to one of the unlocked vibration modes that is selected as the targeted one. Numerical results obtained for various types of excitations demonstrate that it is possible to efficiently transfer the vibration energy into the targeted mode. It results in operation of the energy harvester under resonance conditions independently on currently excited monitored modes of the structure. It has been also concluded that if the targeted vibration mode has greater order than currently excited the vibration is mitigated due to energy scattering into higher-order (unmonitored) vibration modes. This phenomenon does not take place when the energy is transferred in opposed direction. Thus, two additional observations are made. First, if the aim of the system is only the energy harvesting, then one of the lowest order unlocked vibration modes should be the targeted one. This mode has has low damping and such a selection of the targeted mode prevents from the energy scattering. Second, if the control is applied to mitigate vibrations with additional simultaneous energy harvesting, then one of the highest-order monitored vibration modes can be targeted providing both effective vibration damping and possibility of the energy recovery from the broadened frequency range of excitations.

Finally, the proposed control methodology has been verified experimentally in Chapter 5 using laboratory-scale frame demonstrator equipped with six lockable joints. Here, the control strategy has been tested in the presence of significant imperfectness of the lockable joints, since they are prototypes yet. These lockable joints have limited maximal bending moment that can be transmitted. If the load exceeds this moment the friction parts (responsible for the locking effect) slide on each other. The second imperfectness is that when the joint is unlocked the friction parts are not fully detached due to the residual clamping force. It results in residual static friction if the joint does not transmit a sufficient bending moment to provide relative rotation of the adjacent beams.

A FE model has been employed aiming at design the control algorithm (calculation of required modal parameters) and numerical simulations for the comparison with experiment. FE model has been updated aiming at reproduction of the behaviour of the real frame demonstrator. 17 uncertain stiffness parameters have been searched using mode-matching (known also as modal sensitivity-based method). The model updating have employed 10 locked vibration modes identified with stochastic identification method within frequency range 0-1 kHz.

Before control validation modal controllability has been evaluated. Free-vibration tests on updated FE model demonstrate that the proposed controllability metric precisely reflects the ability of the joints at particular locations to transfer the mechanical energy between the vibration modes and resulting control performance. In experiment the agreement between controllability metric and structural behaviour is not guaranteed due to the imperfectness of the real joints.

The proposed control has been verified experimentally in attenuation of both free and forced vibration, as well as in the ability to transfer the mechanical energy into the selected unlocked vibration mode. Due to the imperfectness of the real lockable joints experimental results are worse than ones obtained in simulation but still satisfactory. It has been demonstrated in the frequency domain that the proposed control effectively shifts the vibration energy from the monitored unlocked vibration modes towards higher frequencies outside the range provided by the modal shaker acting on the controlled structure. It has been also demonstrated in the frequency domain that the control allows for transfer the energy into the preselected vibration mode that also is outside the excitation bandwidth.

The thesis stated in Section 1.2 has been proven comprehensively: from theoretical considerations and analytical calculations to numerical and experimental validation. The proposed semi-active modal control methodology not only meets the expectations set for it but also is accompanied with deepened theoretical foundation. This allows for understanding better the modal energy transfer in semi-actively controlled systems, the further development of the proposed methodology as well as its adoption to other kinds of structures.

The issues that are not investigated or solved in this thesis but are interesting and worth future research are:

- investigation experimentally the proposed control methodology with improved prototypes of the lockable joints or rearranged currently employed ones in such a way that the joints able to transmit the highest bending moments placed closest to the structural support,
- experimental verification of the control with energy harvester and/or with especially designed primary (controlled) structure,
- development of design techniques of the primary structure for maximisation of recovered energy and operational frequency bandwidth of the system,
- testing analogous semi-active control strategy in three dimensional truss-like structures, where translational DOFs are locked (lockable truss member) instead of rotational ones (lockable joint).

Appendix A

Three dimensional mode shapes of the laboratory-scale frame

In this appendix all identified three-dimensional (3D) mode shapes of the structure described in Section 5.1.1 are shown in Figures A.1-A.25. They are obtained for the joints in the unlocked state. Method of identification is described in Section 5.1.2.

Due to the fact that only in in-plane (IP) vibration modes are controllable by the lockable joints of the structure the 3D vibration modes are divided into IP vibration modes and out-of-plane (OoP) vibration modes. IP vibration modes are used to update the FE model which reproduces only in-plane vibration. IP vibration modes are selected based on visual inspection of 3D mode shapes. Moreover, mode shapes that are strongly distorted are suspected to be spurious modes or highly contaminated by measurement error or error resulting from some nonlinearities. Thus, such vibration modes also are rejected. They could affect the quality of the updated model. The selected IP modes are: 2th, 5th, 7th, 10th, 11th, 13th, 18th, 22th, 23th and 24th one. The fifth 3D mode shape is similar to the fourth one and their natural frequencies also are not well-separated. They are almost orthogonal modes. However, due to the fact that the fifth vibration mode has lower OoP displacement component in relation to the IP displacement component than the fourth vibration mode only the fifth vibration mode is selected for the model updating procedure.

Seeking for the simplicity, after the selection of the IP vibration modes they are numerated from 1 to 10 in this thesis.

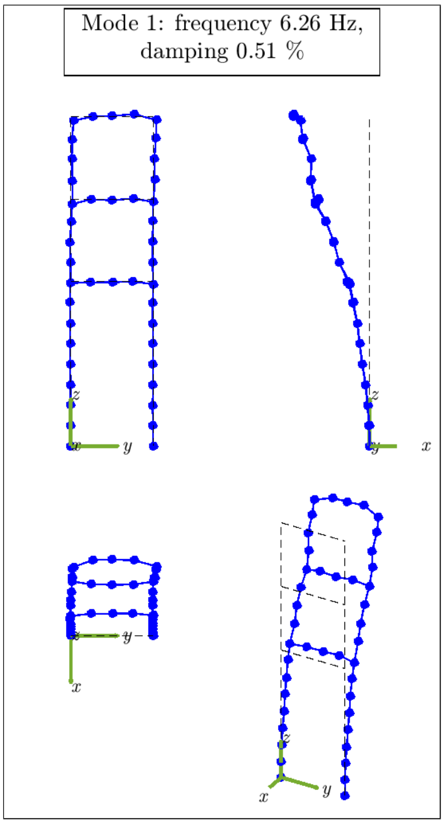

Figure A.1: 3D mode 1

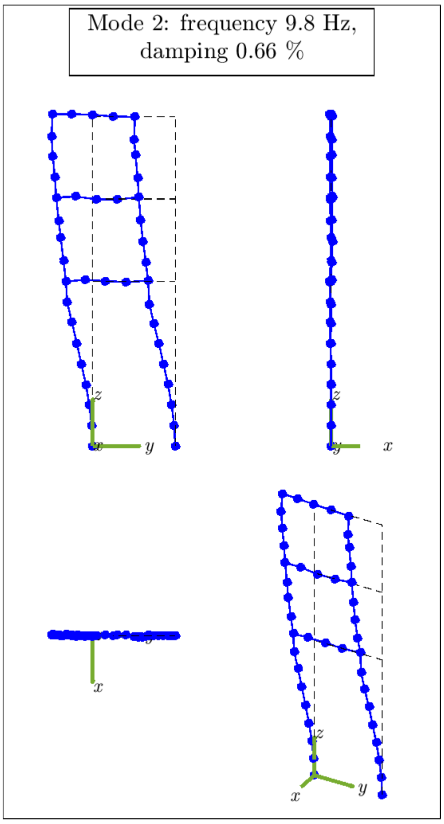

Figure A.2: 3D mode 2

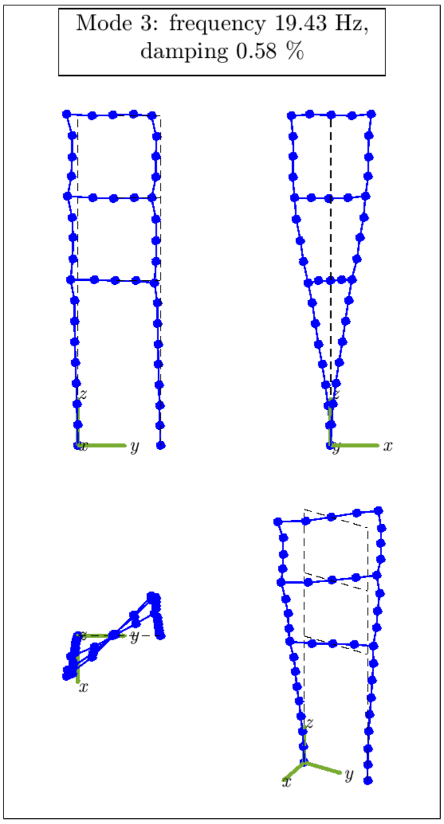

Figure A.3: 3D mode 3

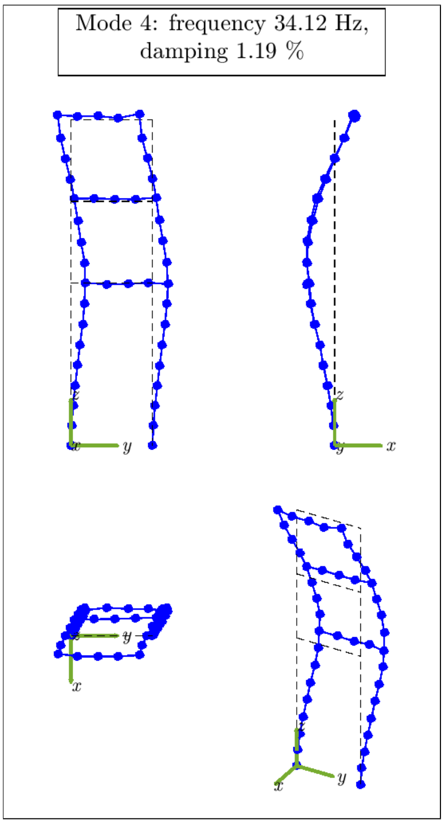

Figure A.4: 3D mode 4

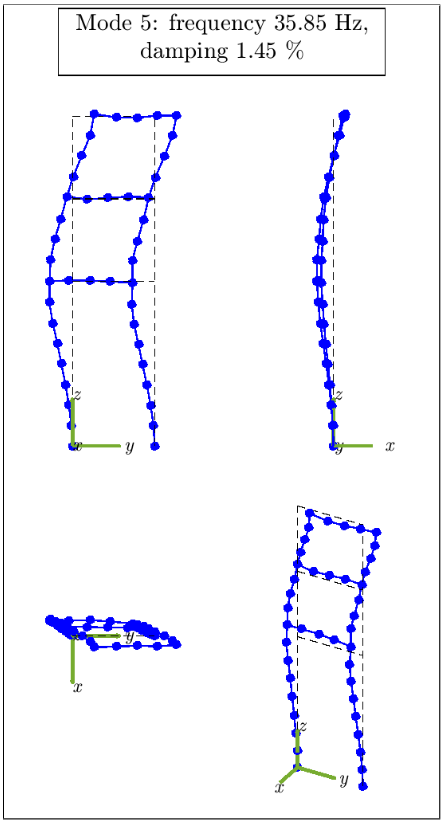

Figure A.5: 3D mode 5

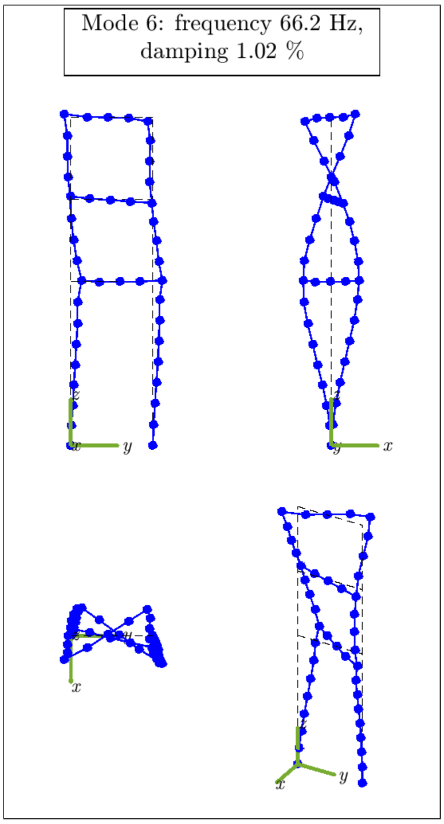

Figure A.6: 3D mode 6

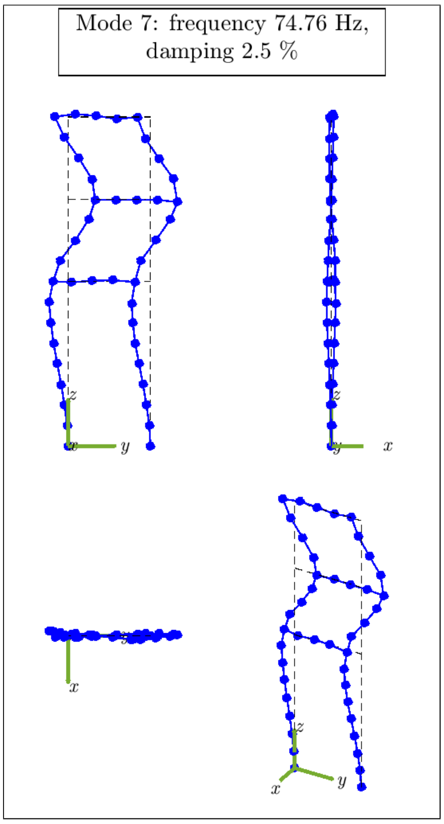

Figure A.7: 3D mode 7

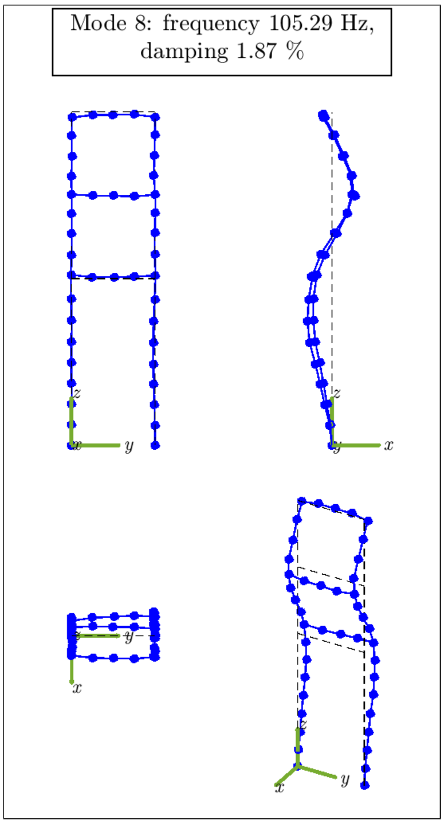

Figure A.8: 3D mode 8

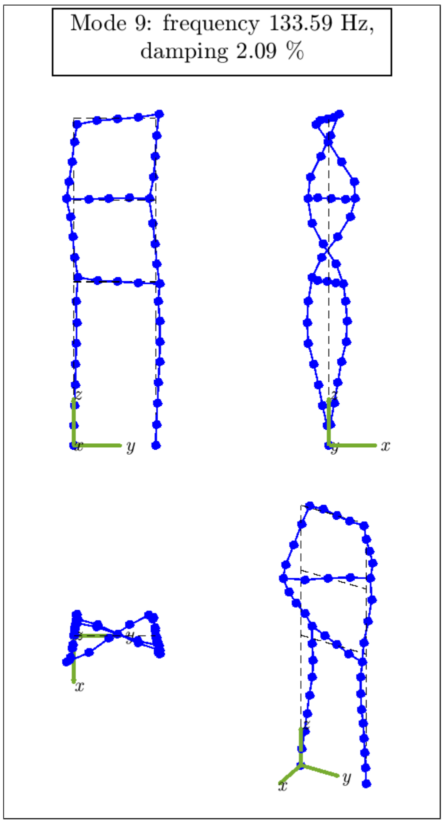

Figure A.9: 3D mode 9

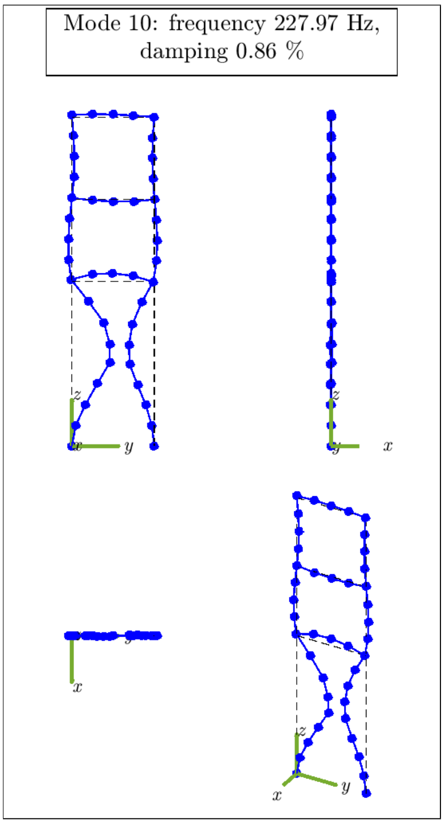

Figure A.10: 3D mode 10

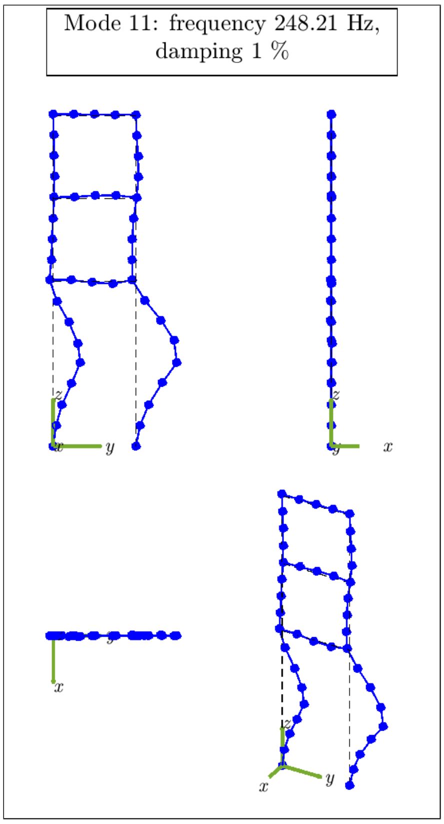

Figure A.11: 3D mode 11

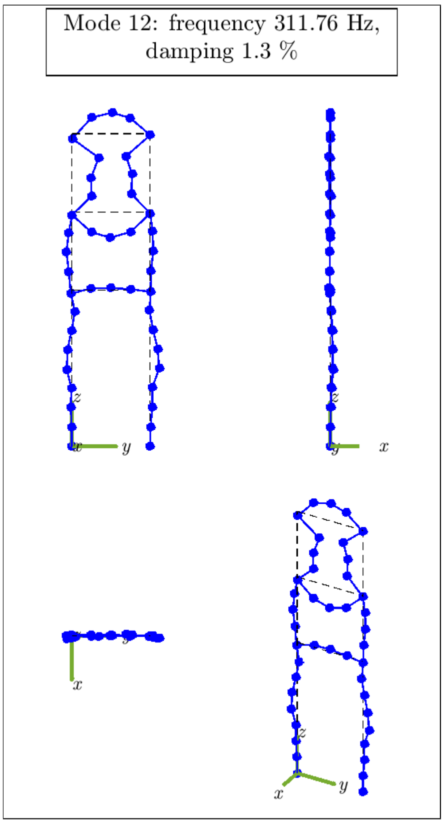

Figure A.12: 3D mode 12

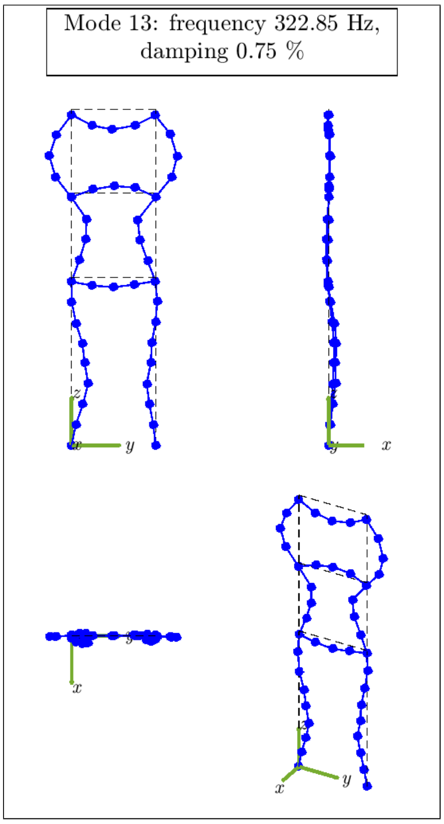

Figure A.13: 3D mode 13

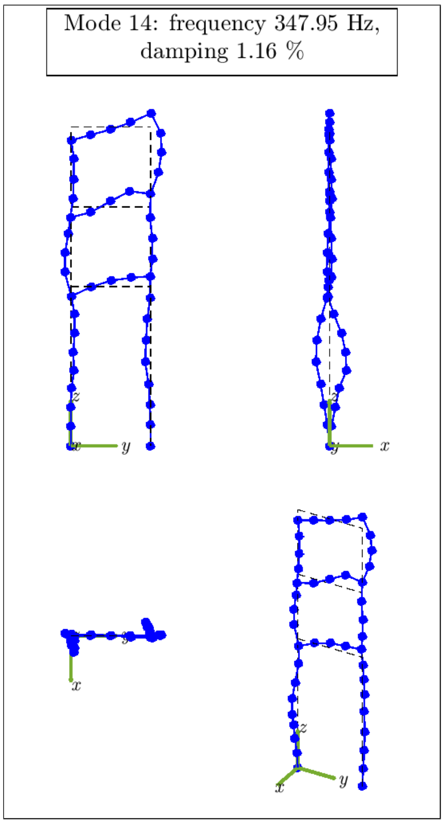

Figure A.14: 3D mode 14

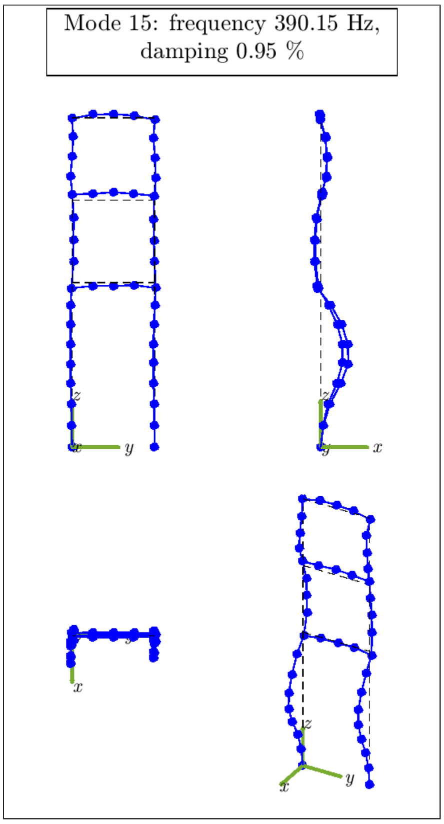

Figure A.15: 3D mode 15

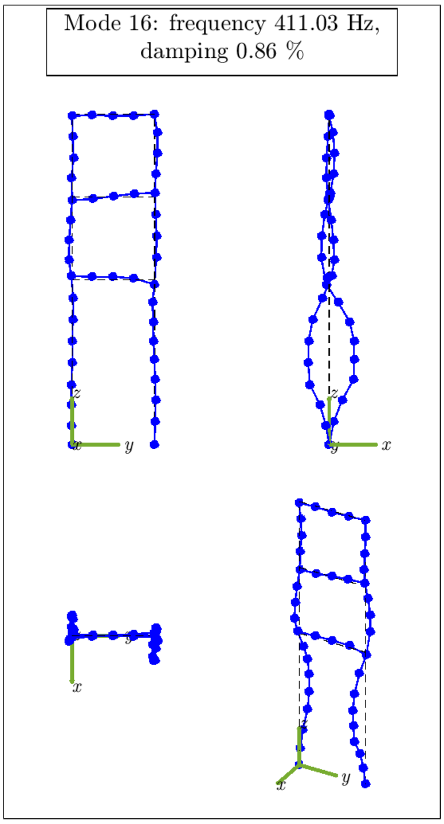

Figure A.16: 3D mode 16

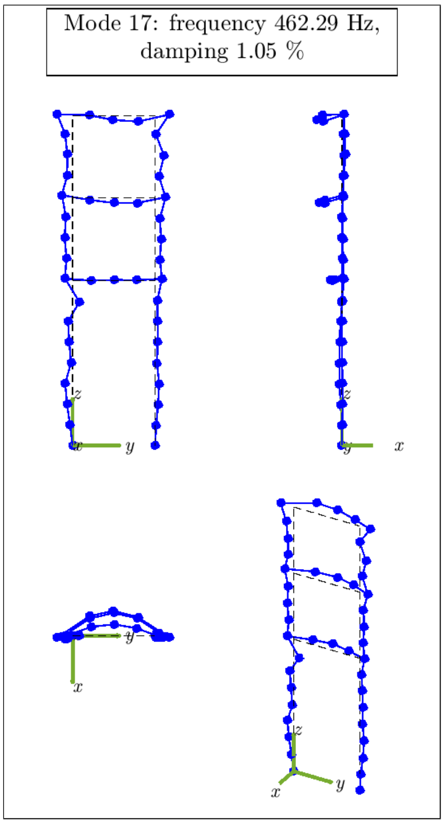

Figure A.17: 3D mode 17

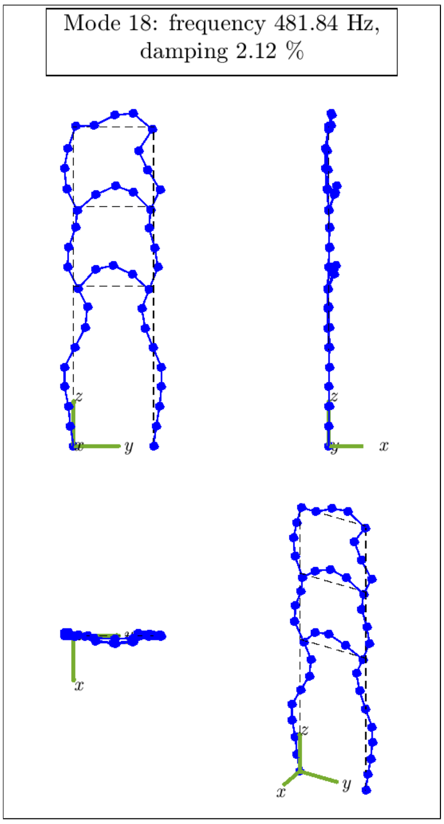

Figure A.18: 3D mode 18

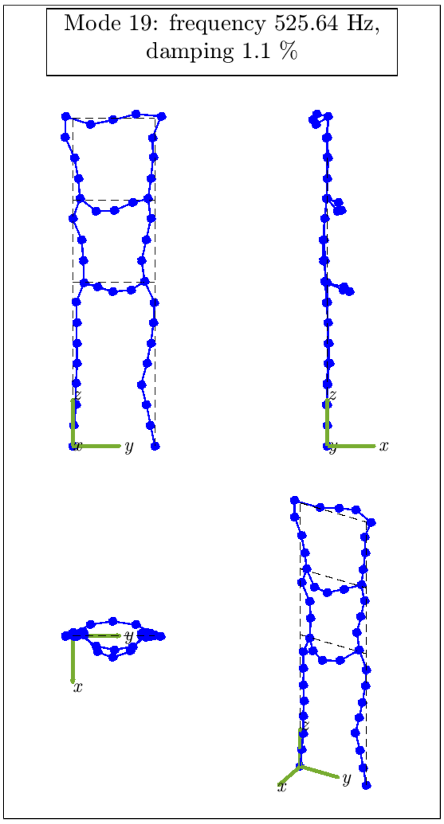

Figure A.19: 3D mode 19

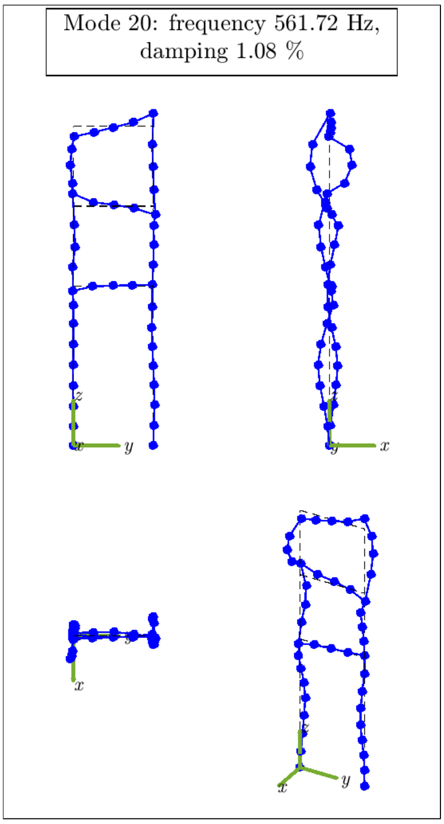

Figure A.20: 3D mode 20

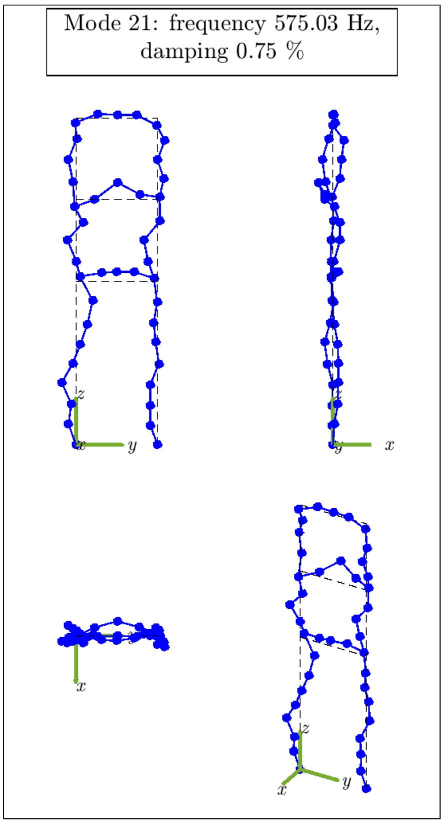

Figure A.21: 3D mode 21

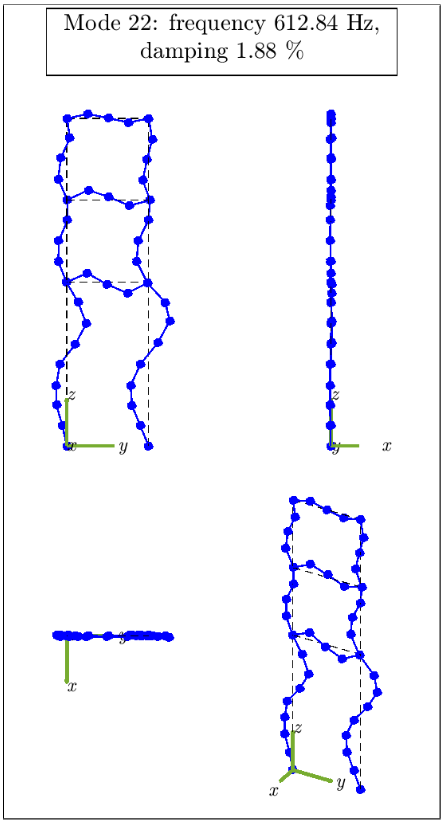

Figure A.22: 3D mode 22

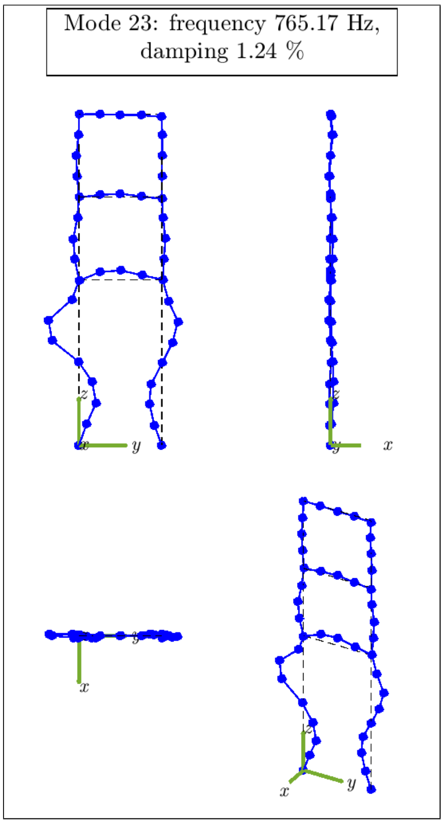

Figure A.23: 3D mode 23

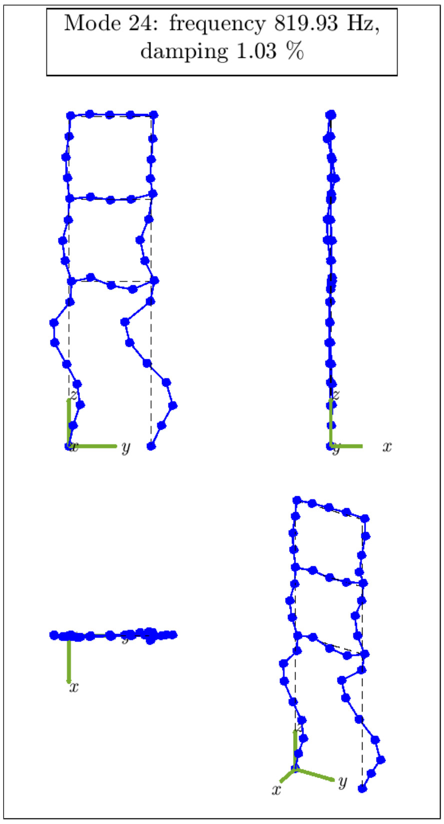

Figure A.24: 3D mode 24

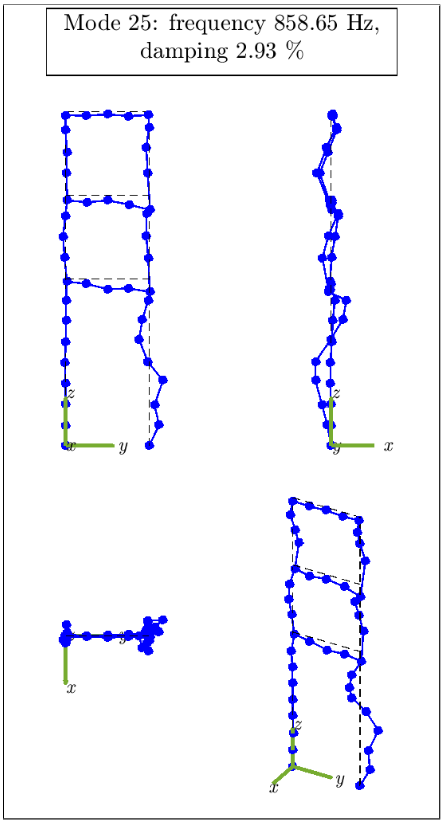

Figure A.25: 3D mode 25

Bibliography

[1] Ghaedi K, Ibrahim Z, Adeli H, Javanmardi A. Invited Review: Recent developments in vibration control of building and bridge structures. Journal of Vibroengineering. 2017;19(5):3564–3580. Available from: `https://doi.org/10.21595/jve.2017.18900`.

[2] Wei C, Jing X. A comprehensive review on vibration energy harvesting: Modelling and realization. Renewable and Sustainable Energy Reviews. 2017;74:1–18. Available from: `https://doi.org/10.1016/j.rser.2017.01.073`.

[3] Li W, Wierschem NE, Li X, Yang T. On the energy transfer mechanism of the single-sided vibro-impact nonlinear energy sink. Journal of Sound and Vibration. 2018;437:166–179. Available from: `https://doi.org/10.1016/j.jsv.2018.08.057`.

[4] Theurich T, Gross J, Krack M. Effects of modal energy scattering and friction on the resonance mitigation with an impact absorber. Journal of Sound and Vibration. 2019;442:71–89. Available from: `https://doi.org/10.1016/j.jsv.2018.10.055`.

[5] Fang B, Theurich T, Krack M, Bergman LA, Vakakis AF. Vibration suppression and modal energy transfers in a linear beam with attached vibro-impact nonlinear energy sinks. Communications in Nonlinear Science and Numerical Simulation. 2020;91:105415. Available from: `https://doi.org/10.1016/j.cnsns.2020.105415`.

[6] Li X, Mojahed A, Chen LQ, Bergman LA, Vakakis AF. Shock response mitigation of a large-scale structure by modal energy redistribution facilitated by a strongly nonlinear absorber. Acta Mechanica Sinica. 2022;38:121464. Available from: `https://doi.org/10.1007/s10409-022-09023-x`.

[7] Lu Z, Zhou M, Zhang J, Huang Z, Masri SF. A semi-active impact damper for multi-modal vibration control under earthquake excitations. Mechanical Systems and Signal Processing. 2024;210:111182. Available from: `https://doi.org/10.1016/j.ymssp.2024.111182`.

[8] Onoda J, Endo T, Tamaoki H, Watanabe N. Vibration Suppression by Variable-Stiffness Members. AIAA Journal. 1991;29(6):977–983. Available from: `https://doi.org/10.2514/3.59943`.

[9] Holnicki-Szulc JE, Marzec Z. New technique of vibration control. Warsaw: Centre of Excellence for Advanced Materials and Structures; 2001. Available from: `https://rcin.org.pl/dlibra/publication/24998/edition/35913/content?ref=L3B1YmxpY2F0aW9uLzI0OTkwL2VkaXRpb24vMzU5MTI`.

[10] Mróz A, Orłowska A, Holnicki-Szulc J. Semi-active damping of vibrations. Prestress Accumulation-Release strategy development. Shock and Vibration. 2010;17:126402. Available from: `https://doi.org/10.3233/SAV-2010-0502`.

[11] Mróz A, Holnicki-Szulc J, Biczyk J. Prestress Accumulation-Release Technique for Damping of Impact-Born Vibrations: Application to Self-Deployable Structures. Mathematical Problems in Engineering. 2015;2015:720236. Available from: `https://doi.org/10.1155/2015/720236`.

[12] Popławski B, Mikułowski G, Mróz A, Jankowski Ł. Decentralized semi-active damping of free structural vibrations by means of structural nodes with an on/off ability to transmit moments. Mechanical Systems and Signal Processing. 2018;100:926–939. Available from: `https://doi.org/10.1016/j.ymssp.2017.08.012`.

[13] Popławski B, Mikułowski G, Wiszowaty R, Jankowski Ł. Mitigation of forced vibrations by semi-active control of local transfer of moments. Mechanical Systems and Signal Processing. 2021;157:107733. Available from: `https://doi.org/10.1016/j.ymssp.2021.107733`.

[14] Orłowska A, Gałęzia A, Swiercz A, Jankowski Ł. Mitigation of vibrations in sandwich-type structures by a controllable constrained layer. Journal of Vibration and Control. 2021;27(13-14):1595–1605. Available from: `https://doi.org/10.1177/1077546320946130`.

[15] Zhang H, Corr LR, Ma T. Issues in vibration energy harvesting. Journal of Sound and Vibration. 2018;421:79–90. Available from: `https://doi.org/10.1016/j.jsv.2018.01.057`.

[16] Cottone F, Frizzell R, Goyal S, Kelly G, Punch J. Enhanced vibrational energy harvester based on velocity amplification. Journal of Intelligent Material Systems and Structures. 2014;25:443–451. Available from: `https://doi.org/10.1177/1045389X13498316`.

[17] Halim MA, Cho H, Park JY. Design and experiment of a human-limb driven, frequency up-converted electromagnetic energy harvester. Energy Conversion

and Management. 2015;106:393–404. Available from: `https://doi.org/10.1016/j.enconman.2015.09.065`.

[18] Ostrowski M, Błachowski B, Bocheński M, Piernikarski D, Filipek P, Janicki W. Design of nonlinear electromagnetic energy harvester equipped with mechanical amplifier and spring bumpers. Bulletin of the Polish Academy of Sciences: Technical Sciences. 2020;68(6):1373–1383. Available from: `https://doi.org/10.24425/bpasts.2020.135384`.

[19] El-Hebeary MMR, Arafa MH, Megahed SM. Modeling and experimental verification of multi-modal vibration energy harvesting from plate structures. Sensors and Actuators A: Physical. 2013;193:35–47. Available from: `https://doi.org/10.1016/j.sna.2013.01.006`.

[20] Chen LQ, Fan Y. Internal resonance vibration-based energy harvesting. Nonlinear Dynamics. 2023;111:11703–11727. Available from: `https://doi.org/10.1007/s11071-023-08464-0`.

[21] Błachowski B, Świercz A, Ostrowski M, Tauzowski P, Olaszek P, Jankowski Ł. Convex relaxation for efficient sensor layout optimization in large-scale structures subjected to moving loads. Computer-Aided Civil and Infrastructure Engineering. 2020;35(10):1085–1100. Available from: `https://doi.org/10.1111/mice.12553`.

[22] Housner GW, Bergman LA, Caughey TK, Chassiakos AG, Claus RO, Masri SF, et al. Structural Control: Past, Present, and Future. Journal of Engineering Mechanics. 1997;123(9):897–971. Available from: `https://doi.org/10.1061/(ASCE)0733-9399(1997)123:9(897)`.

[23] Zhang BL, Han QL, Zhang XM. Recent advances in vibration control of offshore platforms. Nonlinear Dynamics. 2017;89:755–771. Available from: `https://doi.org/10.1007/s11071-017-3503-4`.

[24] Hurlebaus S, Gaul L. Smart structure dynamics. Mechanical Systems and Signal Processing. 2006;20(2):255–281. Available from: `https://doi.org/10.1016/j.ymssp.2005.08.025`.

[25] Johnson CD. Design of Passive Damping Systems. Journal of Vibration and Acoustics. 1995 06;117(B):171–176. Available from: `https://doi.org/10.1115/1.2838659`.

[26] Elias S, Matsagar V. Research developments in vibration control of structures using passive tuned mass dampers. Annual Reviews in Control. 2017;44:129–156. Available from: `https://doi.org/10.1016/j.arcontrol.2017.09.015`.

[27] Soong TT, Spencer BF. Supplemental energy dissipation: state-of-the-art and state-of-the-practice. Engineering Structures. 2002;24(3):243–259. Available from: `https://doi.org/10.1016/S0141-0296(01)00092-X`.

[28] GERB. Tuned mass dampers for bridges, buildings and other tall structures; 2012. Brochure.

[29] Pavic A, Willford M, Reynolds P, Wright JR. Key results of modal testing of the Millennium Bridge, London. In: International Conference on the Design and Dynamic Behaviour of Footbridges. January 2002; 2002. p. 225–233. Available from: `http://vibration.ex.ac.uk/doc/4393_56.pdf`.

[30] Sacks M, Swallow J. Tuned Mass Dampers for Towers and Buildings. In: Structural Engineering in Natural Hazards Mitigation: Proceedings of Papers Presented at the Structures Congress '93n. Amer Society of Civil Engineers; 1993. p. 640–645.

[31] Watts P. On a method of reducing the rolling of ships at sea. In: Transactions of the Institution of Naval Architects 26; 1883. p. 165–190.

[32] Frahm H. Device for Damping Vibrations of Bodies, US Patent US 989958A; 1909.

[33] Gatti G. Fundamental insight on the performance of a nonlinear tuned mass damper. Meccanica. 2018;53(1):111–123. Available from: `https://doi.org/10.1007/s11012-017-0723-0`.

[34] Pisal AY, Jangid RS. Dynamic response of structure with tuned mass friction damper. International Journal of Advanced Structural Engineering. 2016;8(4):363–377. Available from: `https://doi.org/10.1007/s40091-016-0136-7`.

[35] Alkmim MH, Fabro AT, de Morais MVG. Optimization of a tuned liquid column damper subject to an arbitrary stochastic wind. Journal of the Brazilian Society of Mechanical Sciences and Engineering. 2018;40(11):551. Available from: `https://doi.org/10.1007/s40430-018-1471-3`.

[36] Sapsis TP, Dane Quinn D, Vakakis AF, Bergman LA. Effective Stiffening and Damping Enhancement of Structures With Strongly Nonlinear Local Attachments. Journal of Vibration and Acoustics. 2012 01;134(1):011016. Available from: `https://doi.org/10.1115/1.4005005`.

[37] Folkman SL, Bingham JG, Crookston JR, Dutson JD, Ferney BD, Ferney GD, et al.. The Joint Damping Experiment (JDX), NASA Contractor Report 4781; 1997.

[38] Motato E, Haris A, Theodossiades S, Mohammadpour M, Rahnejat H, Kelly P, et al. Targeted energy transfer and modal energy redistribution in automotive drivetrains. Nonlinear Dynamics. 2017;87(1):169–190. Available from: `https://doi.org/10.1007/s11071-016-3034-4`.

[39] Forward RL. Electronic damping of vibrations in optical structures. Appl Opt. 1979 Mar;18(5):690–697. Available from: `https://doi.org/10.1364/AO.18.000690`.

[40] Edwards R, Miyakawa R. Large structure damping task report. Hughes Aircraft Co Report. 1980;(4132.22/1408).

[41] Hagood NW, von Flotow A. Damping of structural vibrations with piezoelectric materials and passive electrical networks. Journal of Sound and Vibration. 1991;146(2):243–268. Available from: `https://doi.org/10.1016/0022-460X(91)90762-9`.

[42] Lossouarn B, Deü JF, Kerschen G. A fully passive nonlinear piezoelectric vibration absorber. Philosophical Transactions of the Royal Society A: Mathematical, Physical and Engineering Sciences. 2018;376(2127):20170142. Available from: `https://doi.org/10.1098/rsta.2017.0142`.

[43] Darleux R, Lossouarn B, Deü JF. Passive self-tuning inductor for piezoelectric shunt damping considering temperature variations. Journal of Sound and Vibration. 2018;432:105–118. Available from: `https://doi.org/10.1016/j.jsv.2018.06.017`.

[44] Sales TP, Rade DA, de Souza LCG. Passive vibration control of flexible spacecraft using shunted piezoelectric transducers. Aerospace Science and Technology. 2013;29(1):403–412. Available from: `https://doi.org/10.1016/j.ast.2013.05.001`.

[45] Tehrani MH, Harvey Jr PS. Enhanced passive control of dual-mode systems under extreme seismic loading: An optimal control approach. Structural Control and Health Monitoring. 2019;26(7):e2367. Available from: `https://doi.org/10.1002/stc.2367`.

[46] Tsai CS, Chiang TC, Chen BJ. Finite element formulations and theoretical study for variable curvature friction pendulum system. Engineering Structures. 2003;25(14):1719–1730. Available from: `https://doi.org/10.1016/S0141-0296(03)00151-2`.

[47] Shahbazi P, Taghikhany T. Sensitivity analysis of variable curvature friction pendulum isolator under near-fault ground motions. Smart Structures and Systems. 2017;20(1):23–33. Available from: `https://doi.org/10.12989/sss.2017.20.1.023`.

[48] Swigert CJ, Forward RL. Electronic damping of orthogonal bending modes in a cylindrical mast - Theory. Journal of Spacecraft and Rockets. 1981;18(1):5–10. Available from: `https://doi.org/10.2514/3.28047`.

[49] Fuller CR, Elliott SJ, Nelson PA, editors. Active Control of Vibration. London: Academic Press; 1996. Available from: `https://doi.org/10.1016/B978-012269440-0/50000-5`.

[50] Alkhatib R, Golnaraghi M. Active Structural Vibration Control: A Review. The Shock and Vibration Digest. 2003 09;35:367–383.

[51] Preumont A. Vibration Control of Active Structures. Springer; 2011. Available from: `https://doi.org/10.1007/978-94-007-2033-6`.

[52] Zhang Y, Li L, Guo Y, Zhang X. Bidirectional wind response control of 76-story benchmark building using active mass damper with a rotating actuator. Structural Control and Health Monitoring. 2018;25(10):e2216. Available from: `https://doi.org/10.1002/stc.2216`.

[53] Yang JN, Agrawal AK, Samali B, Wu JC. Benchmark Problem for Response Control of Wind-Excited Tall Buildings. Journal of Engineering Mechanics. 2004;130(4):437–446. Available from: `https://doi.org/10.1061/(ASCE)0733-9399(2004)130:4(437)`.

[54] Bruijnen D, van Dijk N. Combined input shaping and feedforward control for flexible motion systems. In: 2012 American Control Conference (ACC); 2012. p. 2473–2478. Available from: `https://doi.org/10.1109/ACC.2012.6315055`.

[55] Dhanda A, Vaughan J, Singhose W. Vibration Reduction Using Near Time-Optimal Commands for Systems With Nonzero Initial Conditions. Journal of Dynamic Systems, Measurement, and Control. 2016;138(4). 041006. Available from: `https://doi.org/10.1115/1.4032064`.

[56] Wasilewski M, Pisarski D, Bajer CI. Adaptive optimal control for seismically excited structures. Automation in Construction. 2019;106:102885. Available from: `https://doi.org/10.1016/j.autcon.2019.102885`.

[57] Chopra I. Review of State of Art of Smart Structures and Integrated Systems. AIAA Journal. 2002;40(11):2145–2187. Available from: `https://doi.org/10.2514/2.1561`.

[58] Juang JN, Lim KB, Junkins JL. Robust eigensystem assignment for flexible structures. Journal of Guidance, Control, and Dynamics. 1989;12(3):381–387. Available from: `https://doi.org/10.2514/3.20419`.

[59] Ghandchi Tehrani M, Mottershead JE, Shenton AT, Ram YM. Robust pole placement in structures by the method of receptances. Mechanical Systems and Signal Processing. 2011;25(1):112–122. Available from: `https://doi.org/10.1016/j.ymssp.2010.04.005`.

[60] Wang N, Adeli H. Algorithms for chattering reduction in system control. Journal of the Franklin Institute. 2012;349(8):2687–2703. Available from: `https://doi.org/10.1016/j.jfranklin.2012.06.001`.

[61] Gatti G, Brennan MJ, Gardonio P. Active damping of a beam using a physically collocated accelerometer and piezoelectric patch actuator. Journal of Sound and Vibration. 2007;303(3):798–813. Available from: `https://doi.org/10.1016/j.jsv.2007.02.006`.

[62] Casciati F, Magonette G, Marazzi F. Technology of Semiactive Devices and Applications in Vibration Mitigation. John Wiley & Sons, Ltd; 2006. Available from: `https://doi.org/10.1002/0470022914`.

[63] Pisarski D, Konowrocki R, Jankowski Ł. Scalable distributed optimal control of vibrating modular structures. Structural Control and Health Monitoring. 2020;27(4):e2502. Available from: `https://doi.org/10.1002/stc.2502`.

[64] Saeed MU, Sun Z, Elias S. Research developments in adaptive intelligent vibration control of smart civil structures. Journal of Low Frequency Noise, Vibration and Active Control. 2022;41(1):292–329. Available from: `https://doi.org/10.1177/14613484211032758`.

[65] Błachowski B, Pnevmatikos N. Neural Network Based Vibration Control of Seismically Excited Civil Structures. Periodica Polytechnica Civil Engineering. 2018;62(3):620–628. Available from: `https://pp.bme.hu/ci/article/view/11601`.

[66] Jiang X, Adeli H. Dynamic fuzzy wavelet neuroemulator for non-linear control of irregular building structures. International Journal for Numerical Methods in Engineering. 2008;74(7):1045–1066. Available from: `https://doi.org/10.1002/nme.2195`.

[67] Zorić ND, Tomović AM, Obradović AM, Radulović RD, Petrović GR. Active vibration control of smart composite plates using optimized self-tuning fuzzy logic controller with optimization of placement, sizing and orientation of PFRC actuators. Journal of Sound and Vibration. 2019;456:173–198. Available from: `https://doi.org/10.1016/j.jsv.2019.05.035`.

[68] Cong Le D, Zhang J, Pang Y. A novel pipelined neural FIR architecture for nonlinear adaptive filter. Neurocomputing. 2021;440:220–229. Available from: `https://doi.org/10.1016/j.neucom.2020.11.036`.

[69] Karnopp D, Crosby MJ, Harwood RA. Vibration Control Using Semi-Active Force Generators. Journal of Engineering for Industry. 1974 05;96(2):619–626. Available from: `https://doi.org/10.1115/1.3438373`.

[70] Symans MD, Constantinou MC. Semi-active control systems for seismic protection of structures: a state-of-the-art review. Engineering Structures. 1999;21(6):469–487. Available from: `https://doi.org/10.1016/S0141-0296(97)00225-3`.

[71] Casciati F, Rodellar J, Yildirim U. Active and semi-active control of structures – theory and applications: A review of recent advances. Journal of Intelligent Material Systems and Structures. 2012;23(11):1181–1195. Available from: `https://doi.org/10.1177/1045389X12445029`.

[72] Harvey Jr PS, Gavin HP, Scruggs JT, Rinker JM. Determining the physical limits on semi-active control performance: a tutorial. Structural Control and Health Monitoring. 2014;21(5):803–816. Available from: `https://doi.org/10.1002/stc.1602`.

[73] Spencer BF, Dyke SJ, Sain MK, Carlson JD. Phenomenological Model for Magnetorheological Dampers. Journal of Engineering Mechanics. 1997;123(3):230–238. Available from: `https://doi.org/10.1061/(ASCE)0733-9399(1997)123:3(230)`.

[74] Du H, Yim Sze K, Lam J. Semi-active H_∞ control of vehicle suspension with magneto-rheological dampers. Journal of Sound and Vibration. 2005;283(3):981–996. Available from: `https://doi.org/10.1016/j.jsv.2004.05.030`.

[75] Yang J, Ning D, Sun SS, Zheng J, Lu H, Nakano M, et al. A semi-active suspension using a magnetorheological damper with nonlinear negative-stiffness component. Mechanical Systems and Signal Processing. 2021;147:107071. Available from: `https://doi.org/10.1016/j.ymssp.2020.107071`.

[76] Michajłow M, Jankowski Ł, Szolc T, Konowrocki R. Semi-active reduction of vibrations in the mechanical system driven by an electric motor. Optimal Control Applications and Methods. 2017;38(6):922–933. Available from: `https://doi.org/10.1002/oca.2297`.

[77] Li Y, Li J, Samali B, Wang J. Design considerations and experimental studies on semi-active smart pin joint. Frontiers of Mechanical Engineering in China. 2009;4(4):363. Available from: `https://doi.org/10.1007/s11465-009-0074-1`.

[78] Li Y, Li J. Dynamic characteristics of a magnetorheological pin joint for civil structures. Frontiers of Mechanical Engineering. 2014;9(1):15–33. Available from: `https://doi.org/10.1007/s11465-014-0283-0`.

[79] Dyke SJ, Spencer BF, Sain MK, Carlson JD. Modeling and control of magnetorheological dampers for seismic response reduction. Smart Materials and Structures. 1996 oct;5(5):565–575. Available from: `https://doi.org/10.1088/0964-1726/5/5/006`.

[80] Ha QP, Kwok NM, Nguyen MT, Li J, Samali B. Mitigation of seismic responses on building structures using MR dampers with Lyapunov-based control. Structural Control and Health Monitoring. 2008;15(4):604–621. Available from: `https://doi.org/10.1002/stc.218`.

[81] Kwok NM, Ha QP, Nguyen TH, Li J, Samali B. A novel hysteretic model for magnetorheological fluid dampers and parameter identification using particle swarm optimization. Sensors and Actuators A: Physical. 2006;132(2):441–451. Available from: `https://doi.org/10.1016/j.sna.2006.03.015`.

[82] Bogacz R, Bajer C. Active control of beams under a moving load. Journal of Theoretical and Applied Mechanics. 2000;38:523–530. Available from: `https://www.ptmts.org.pl/jtam/index.php/jtam/article/download/v38n3p523/779`.

[83] Wasilewski M, Pisarski D. Adaptive semi-active control of a beam structure subjected to a moving load traversing with time-varying velocity. Journal of Sound and Vibration. 2020;481:115404. Available from: `https://doi.org/10.1016/j.jsv.2020.115404`.

[84] Kurino H, Tagami J, Shimizu K, Kobori T. Switching Oil Damper with Built-in Controller for Structural Control. Journal of Structural Engineering. 2003;129(7):895–904. Available from: `https://doi.org/10.1061/(ASCE)0733-9445(2003)129:7(895)`.

[85] Ikeda Y. Active and semi-active vibration control of buildings in Japan—Practical applications and verification. Structural Control and Health Monitoring. 2009;16(7-8):703–723. Available from: `https://doi.org/10.1002/stc.315`.

[86] Popławski B, Mikułowski G, Mróz A, Jankowski Ł. Decentralized semi-active damping of free structural vibrations by means of structural nodes with an on/off ability to transmit moments. Mechanical Systems and Signal Processing. 2018;100:926–939. Available from: `https://doi.org/10.1016/j.ymssp.2017.08.012`.

[87] Feng MQ, Shinozuka M, Fujii S. Friction-Controllable Sliding Isolation System. Journal of Engineering Mechanics. 1993;119(9):1845–1864. Available from: `https://doi.org/10.1061/(ASCE)0733-9399(1993)119:9(1845)`.

[88] Inaudi JA. Modulated homogeneous friction: a semi-active damping strategy. Earthquake Engineering & Structural Dynamics. 1997;26(3):361–376. Available from: `https://doi.org/10.1002/(SICI)1096-9845(199703)26:3<361::AID-EQE648>3.0.CO;2-M`.

[89] Laflamme S, Taylor D, Abdellaoui Maane M, Connor JJ. Modified friction device for control of large-scale systems. Structural Control and Health Monitoring. 2012;19(4):548–564. Available from: `https://doi.org/10.1002/stc.454`.

[90] Zhang D, Pan P, Zeng Y, Guo Y. A novel robust optimum control algorithm and its application to semi-active controlled base-isolated structures. Bulletin of Earthquake Engineering. 2020;18(5):2431–2460. Available from: `https://doi.org/10.1007/s10518-019-00761-7`.

[91] Hrovat D, Barak P, Rabins M. Semi-Active versus Passive or Active Tuned Mass Dampers for Structural Control. Journal of Engineering Mechanics. 1983;109(3):691–705. Available from: `https://doi.org/10.1061/(ASCE)0733-9399(1983)109:3(691)`.

[92] Setareh M. Application of semi-active tuned mass dampers to base-excited systems. Earthquake Engineering & Structural Dynamics. 2001;30(3):449–462. Available from: `https://doi.org/10.1002/eqe.19`.

[93] Demetriou D, Nikitas N, Tsavdaridis KD. Performance of fixed-parameter control algorithms on high-rise structures equipped with semi-active tuned mass dampers. The Structural Design of Tall and Special Buildings. 2016;25(7):340–354. Available from: `https://doi.org/10.1002/tal.1261`.

[94] Chu SY, Yeh SW, Lu LY, Peng CH. A leverage-type stiffness controllable mass damper for vibration mitigation of structures. Structural Control and Health Monitoring. 2017;24(4):e1896. E1896 STC-15-0275.R1. Available from: `https://doi.org/10.1002/stc.1896`.

[95] Liu YF, Lin TK, Chang KC. Analytical and experimental studies on building mass damper system with semi-active control device. Structural Control and Health Monitoring. 2018;25(6):e2154. E2154 STC-16-0326.R1. Available from: `https://doi.org/10.1002/stc.2154`.

[96] Brzeski P, Kapitaniak T, Perlikowski P. Novel type of tuned mass damper with inerter which enables changes of inertance. Journal of Sound and Vibration. 2015;349:56–66. Available from: `https://doi.org/10.1016/j.jsv.2015.03.035`.

[97] Brzeski P, Lazarek M, Perlikowski P. Experimental study of the novel tuned mass damper with inerter which enables changes of inertance. Journal of

Sound and Vibration. 2017;404:47–57. Available from: `https://doi.org/10.1016/j.jsv.2017.05.034`.

[98] Altay O, Klinkel S. A semi-active tuned liquid column damper for lateral vibration control of high-rise structures: Theory and experimental verification. Structural Control and Health Monitoring. 2018;25(12):e2270. E2270 stc.2270. Available from: `https://doi.org/10.1002/stc.2270`.

[99] Zhou GY. Shear properties of a magnetorheological elastomer. Smart Materials & Structures. 2003 02;12(1):139–146. Available from: `https://doi.org/10.1088/0964-1726/12/1/316`.

[100] Dyniewicz B, Bajkowski JM, Bajer CI. Semi-active control of a sandwich beam partially filled with magnetorheological elastomer. Mechanical Systems and Signal Processing. 2015;60–61:695–705. Available from: `https://doi.org/10.1016/j.ymssp.2015.01.032`.

[101] Pisarski D, Szmidt T, Bajer CI, Dyniewicz B, Bajkowski JM. Vibration Control of Double-Beam System with Multiple Smart Damping Members. Shock and Vibration. 2016;2016:2438902. Available from: `https://doi.org/10.1155/2016/2438902`.

[102] Pisarski D. Decentralized stabilization of semi-active vibrating structures. Mechanical Systems and Signal Processing. 2018;100:694–705. Available from: `https://doi.org/10.1016/j.ymssp.2017.08.003`.

[103] Li Y, Li J, Li W, Du H. A state-of-the-art review on magnetorheological elastomer devices. Smart Materials and Structures. 2014 nov;23(12):123001. Available from: `https://doi.org/10.1088/0964-1726/23/12/123001`.

[104] Bicos AS, Pak YH, Trent CL, Uitto RJ. Passive And Active Vibration Suppression Of Large Space Structures. In: Udd E, editor. Fiber Optic Smart Structures and Skins II. vol. 1170. International Society for Optics and Photonics. SPIE; 1990. p. 359–371. Available from: `https://doi.org/10.1117/12.963111`.

[105] Ferri AA, Heck BS. Analytical investigation of damping enhancement using active and passive structural joints. Journal of Guidance, Control, and Dynamics. 1992;15(5):1258–1264. Available from: `https://doi.org/10.2514/3.20977`.

[106] Gaul L, Nitsche R. Vibration Control by Interface Dissipation in Semi-Active Joints. ZAMM - Journal of Applied Mathematics and Mechanics / Zeitschrift für Angewandte Mathematik und Mechanik. 2000;80:45–48. Available from: `https://doi.org/10.1002/zamm.20000801312`.

[107] Gaul L, Albrecht H, Wirnitzer J. Semi-Active Friction Damping of Large Space Truss Structures. Shock and Vibration. 2004;11:173–186. Available from: `https://doi.org/10.1155/2004/565947`.

[108] Gaul L, Hurlebaus S, Wirnitzer J, Albrecht H. Enhanced damping of lightweight structures by semi-active joints. Acta Mechanica. 2008;195:249–261. Available from: `https://doi.org/10.1007/s00707-007-0547-4`.

[109] Onoda J, Oh HU, Minesugi K. Semi-active vibration suppression of truss structures by electro-rheological fluid. Acta Astronautica. 1997;40(11):771–779. Available from: `https://doi.org/10.1016/S0094-5765(97)00168-9`.

[110] Segalman DJ. Modelling joint friction in structural dynamics. Structural Control and Health Monitoring. 2006;13(1):430–453. Available from: `https://doi.org/10.1002/stc.119`.

[111] Gaul L, Nitsche R. The Role of Friction in Mechanical Joints. Applied Mechanics Reviews. 2001 03;54(2):93–106. Available from: `https://doi.org/10.1115/1.3097294`.

[112] Minesugi K, Kondo K. Semi-active vibration suppression of large space structures with a variable axial stiffness member. In: 34th Structures, Structural Dynamics and Materials Conference. La Jolla, CA; 1993. Available from: `https://doi.org/10.2514/6.1993-1693`.

[113] Bajkowski JM, Dyniewicz B, Bajer CI. Semi-active damping strategy for beams system with pneumatically controlled granular structure. Mechanical Systems and Signal Processing. 2016;70-71:387–396. Available from: `https://doi.org/10.1016/j.ymssp.2015.09.026`.

[114] Inman DJ. Active modal control for smart structures. Philosophical Transactions of the Royal Society of London Series A: Mathematical, Physical and Engineering Sciences. 2001;359(1778):205–219. Available from: `https://doi.org/10.1098/rsta.2000.0721`.

[115] Simon JD, Mitter SK. A theory of modal control. Information and Control. 1968;13(4):316–353. Available from: `https://doi.org/10.1016/S0019-9958(68)90834-6`.

[116] Magni JF. Robust Modal Control with a Toolbox for Use with MATLAB®. Springer, Boston, MA; 2002. Available from: `https://doi.org/10.1007/978-1-4615-0637-9`.

[117] Gould L, Murray-Lasso M. On the modal control of distributed systems with distributed feedback. IEEE Transactions on Automatic Control. 1966;11(4):729–737. Available from: `https://doi.org/10.1109/TAC.1966.1098463`.

[118] Balas MJ. Active control of flexible systems. Journal of Optimization Theory and Applications. 1978;25:415–436. Available from: `https://doi.org/10.1007/BF00932903`.

[119] Öz H, Meirovitch L. Optimal Modal-Space Control of Flexible Gyroscopic Systems. Journal of Guidance and Control. 1980;3(3):218–226. Available from: `https://doi.org/10.2514/3.55975`.

[120] Meirovitch L, Baruh H. Control of self-adjoint distributed-parameter systems. In: AIAA Guidance and Control Conference; 1980. Available from: `https://doi.org/10.2514/6.1980-1707`.

[121] Meirovitch L, Baruh H. Control of self-adjoint distributed-parameter systems. Journal of Guidance, Control, and Dynamics. 1982;5:60–66. Available from: `https://doi.org/10.2514/3.56140`.

[122] Meirovitch L, Baruh H. Robustness of the independent modal-space control method. Journal of Guidance, Control, and Dynamics. 1983;6(1):20–25. Available from: `https://doi.org/10.2514/3.19797`.

[123] Lu LY. Seismic test of modal control with direct output feedback for building structures. Structural Engineering and Mechanics. 2001 12;12(6):633–656. Available from: `https://doi.org/10.12989/sem.2001.12.6.633`.

[124] Lu LY. Semi-active modal control for seismic structures with variable friction dampers. Engineering Structures. 2004;26(4):437–454. Available from: `https://doi.org/10.1016/j.engstruct.2003.10.012`.

[125] Basu B, Nielsen SRK. A multi-modal control using a hybrid pole-placement–integral resonant controller (PPIR) with experimental investigations. Structural Control and Health Monitoring. 2011;18(2):191–206. Available from: `https://doi.org/10.1002/stc.367`.

[126] Belyaev AK, Fedotov AV, Irschik H, Nader M, Polyanskiy VA, Smirnova NA. Experimental study of local and modal approaches to active vibration control of elastic systems. Structural Control and Health Monitoring. 2018;25(2):e2105. Available from: `https://doi.org/10.1002/stc.2105`.

[127] Etedali S. A new modified independent modal space control approach toward control of seismic-excited structures. Bulletin of Earthquake Engineering. 2017;15(10):4215–4243. Available from: `https://doi.org/10.1007/s10518-017-0134-6`.

[128] Ostrowski M, Jedlińska A, Popławski B, Błachowski B, Mikułowski G, Pisarski D, et al. Sliding Mode Control for Semi-Active Damping of Vibrations Using on/off Viscous Structural Nodes. Buildings. 2023;13(2):348. Available from: `https://doi.org/10.3390/buildings13020348`.

[129] Chepuri SP, Leus G. Sensor selection for estimation, filtering, and detection. In: 2014 International Conference on Signal Processing and Communications (SPCOM); 2014. p. 1–5. Available from: `https://doi.org/10.1109/SPCOM.2014.6983912`.

[130] Papadimitriou C, Beck JL, Au SK. Entropy-Based Optimal Sensor Location for Structural Model Updating. Journal of Vibration and Control. 2000;6(5):781–800. Available from: `https://doi.org/10.1177/107754630000600508`.

[131] Schedlinski C, Link M. An approach to optimal pick-up and exciter placement. In: 14th International Modal Analysis Converence, IMAC; 1996. p. 376–382. Available from: `https://doi.org/10.13140/2.1.3105.6327`.

[132] Kammer DC. Sensor placement for on-orbit modal identification and correlation of large space structures. Journal of Guidance, Control, and Dynamics. 1991;14(2):251–259. Available from: `https://doi.org/10.2514/3.20635`.

[133] Gawronski WK. Advanced Structural Dynamics and Active Control of Structures. 1st ed. New York, NY: Springer;. Available from: `https://doi.org/10.1007/978-0-387-72133-0`.

[134] Li Y, Wang X, Huang R, Qiu Z. Actuator placement robust optimization for vibration control system with interval parameters. Aerospace Science and Technology. 2015;45:88–98. Available from: `https://doi.org/10.1016/j.ast.2015.04.017`.

[135] Moloudian G, Hosseinifard M, Kumar S, Simorangkir RBVB, Buckley JL, Song C, et al. RF Energy Harvesting Techniques for Battery-Less Wireless Sensing, Industry 4.0, and Internet of Things: A Review. IEEE Sensors Journal. 2024;24:5732–5745. Available from: `https://doi.org/10.1109/JSEN.2024.3352402`.

[136] Siang J, Lim MH, Leong MS. Review of vibration-based energy harvesting technology: Mechanism and architectural approach. International Journal of Energy Research. 2018;42:1866–1893. Available from: `https://onlinelibrary.wiley.com/doi/abs/10.1002/er.3986`.

[137] Zuo L, Tang X. Large-scale vibration energy harvesting. Journal of Intelligent Material Systems and Structures. 2013;24:1405–1430. Available from: `https://doi.org/10.1177/1045389X13486707`.

[138] Sun R, Zhou S, Cheng L. Ultra-low frequency vibration energy harvesting: Mechanisms, enhancement techniques, and scaling laws. Energy Conversion and Management. 2023;276:116585. Available from: `https://doi.org/10.1016/j.enconman.2022.116585`.

[139] Kundu S, Nemade HB. Piezoelectric vibration energy harvester with tapered substrate thickness for uniform stress. Microsystem Technologies. 2021;27:105–113. Available from: `https://doi.org/10.1007/s00542-020-04922-6`.

[140] Anand A, Kundu S. Design of a spiral-shaped piezoelectric energy harvester for powering pacemakers. Nanomaterials and Energy. 2019;8(2):139–150. Available from: `https://doi.org/10.1680/jnaen.19.00016`.

[141] Shahosseini I, Najafi K. Mechanical Amplifier for Translational Kinetic Energy Harvesters. vol. 557. Awaji Island, Hyogo: IOP Publishing; 2014. p. 012135. Available from: `https://doi.org/10.1088/1742-6596/557/1/012135`.

[142] Wang C, Zhang Q, Wang W. Low-frequency wideband vibration energy harvesting by using frequency up-conversion and quin-stable nonlinearity. Journal of Sound and Vibration. 2017;399:169–181. Available from: `https://doi.org/10.1016/j.jsv.2017.02.048`.

[143] Alevras P, Theodossiades S. Vibration energy harvester for variable speed rotor applications using passively self-tuned beams. Journal of Sound and Vibration. 2019;444:176–196. Available from: `https://doi.org/10.1016/j.jsv.2018.11.007`.

[144] Wilson EL. Three Dimensional Static and Dynamic Analysis of Structures: A Physical Approach with Emphasis on Earthquake Engineering. 3rd ed. Berkeley, CA: Computers and Structures, Inc; 2000.

[145] Ostrowski M, Błachowski B, Popławski B, Pisarski D, Mikułowski G, Jankowski Ł. Semi-active modal control of structures with lockable joints: general methodology and applications. Structural Control and Health Monitoring. 2021;28(5):e2710. Available from: `https://doi.org/10.1002/stc.2710`.

[146] Poston WL, Tolson RH. Maximizing the determinant of the information matrix with the effective independence method. Journal of Guidance, Control, and Dynamics. 1992;15(6):1513–1514. Available from: `https://doi.org/10.2514/3.11419`.

[147] Kęcik K, Mitura A, Lenci S, Warmiński J. Energy harvesting from a magnetic levitation system. International Journal of Non-Linear Mechanics. 2017;94:200–206. Available from: `https://doi.org/10.1016/j.ijnonlinmec.2017.03.021`.

[148] Kęcik K. Energy Recovery from a Non-Linear Electromagnetic System. Acta Mechanica et Automatica. 2018;12(1):11–18. Available from: `https://doi.org/10.2478/ama-2018-0002`.

[149] Kęcik K. Assessment of energy harvesting and vibration mitigation of a pendulum dynamic absorber. In: Mechanical Systems and Signal Processing. vol. 106; 2018. p. 198–209. Available from: `https://doi.org/10.1016/j.ymssp.2017.12.028`.

[150] De Klerk D, Rixen DJ, Voormeeren SN. General Framework for Dynamic Substructuring: History, Review and Classification of Techniques. AIAA Journal. 2008;46(5):1169–1181. Available from: `https://doi.org/10.2514/1.33274`.

[151] Allen MS, Rixen D, van der Seijs M, Tiso P, Abrahamsson T, Mayes RL. Preliminaries: Primal and Dual Assembly of Dynamic Models. In: Substructuring in Engineering Dynamics: Emerging Numerical and Experimental Techniques. Cham: Springer International Publishing; 2020. p. 5–24. Available from: `https://doi.org/10.1007/978-3-030-25532-9_2`.

[152] Ostrowski M, Mikułowski G, Błachowski B, Jankowski Ł. Experimental assessment of Bayesian and mode matching approaches for parametric identification of bolted connections. Mechanical Systems and Signal Processing. 2023;201:110652. Available from: `https://doi.org/10.1016/j.ymssp.2023.110652`.

[153] Ostrowski M, Błachowski B, Mikułowski G, Jankowski Ł. Influence of Noise in Computer-Vision-Based Measurements on Parameter Identification in Structural Dynamics. Sensors. 2023;23(1):291. Available from: `https://doi.org/10.3390/s23010291`.

[154] Błachowski B, Świercz A, Gutkiewicz P, Szelążek J, Gutkowski W. Structural damage detectability using modal and ultrasonic approaches. Measurement. 2016;85:210–221. Available from: `https://doi.org/10.1016/j.measurement.2016.02.033`.

[155] Friswell M, Mottershead JE. Finite Element Model Updating in Structural Dynamics. Springer, Dordrecht; 1995. Available from: `https://doi.org/10.1007/978-94-015-8508-8`.

[156] Mottershead JE, Link M, Friswell MI. The sensitivity method in finite element model updating: A tutorial. Mechanical Systems and Signal Processing. 2011;25(7):2275–2296. Available from: `https://doi.org/10.1016/j.ymssp.2010.10.012`.

[157] Yuen KV, Beck JL, Katafygiotis LS. Efficient model updating and health monitoring methodology using incomplete modal data without mode matching. Structural Control and Health Monitoring. 2006;13(1):91–107. Available from: `https://doi.org/10.1002/stc.144`.

[158] Yuen KV. Bayesian Methods for Structural Dynamics and Civil Engineering. John Wiley & Sons, Ltd; 2010. Available from: `https://doi.org/10.1002/9780470824566`.

[159] Hermansen MB, Thomsen JJ. Vibration-based estimation of beam boundary parameters. Journal of Sound and Vibration. 2018;429:287–304. Available from: `https://doi.org/10.1016/j.jsv.2018.05.016`.

[160] Brøns M, Thomsen JJ. Vibration-based estimation of boundary stiffness and axial tension in beams using added mass. Journal of Sound and Vibration. 2020;487:115617. Available from: `https://doi.org/10.1016/j.jsv.2020.115617`.

[161] Ostrowski M, Błachowski B, Wójcik B, Żarski M, Tauzowski P, Jankowski Ł. A framework for computer vision-based health monitoring of a truss structure subjected to unknown excitations. Earthquake Engineering and Engineering Vibration. 2023;22(1):1–17. Available from: `https://doi.org/10.1007/s11803-023-2154-3`.

[162] Błachowski B. Modal Sensitivity Based Sensor Placement for Damage Identification Under Sparsity Constraint. Periodica Polytechnica Civil Engineering. 2019;63(2):432—445. Available from: `https://doi.org/10.3311/PPci.13888`.

[163] Beck JV, Arnold KJ. Parameter estimation in engineering and science. John Wiley & Sons; 1977. Available from: `https://doi.org/10.1002/aic.690240233`.

[164] Fox RL, Kapoor MP. Rates of change of eigenvalues and eigenvectors. AIAA Journal. 1968;6(12):2426–2429. Available from: `https://doi.org/10.2514/3.5008`.

[165] Nelson RB. Simplified calculation of eigenvector derivatives. AIAA Journal. 1976;14(9):1201–1205. Available from: `https://doi.org/10.2514/3.7211`.